RIGID BODY SPRING NETWORK AND MATERIAL POINT METHOD FOR THE ELASTOPLASTIC ANALYSIS OF STRUCTURES

DOCTORAL DISSERTATION

For the title of Doctor of Philosophy in Engineering

Christos D. Sofianos

NATIONAL TECHNICAL UNIVERSITY OF ATHENS

SCHOOL OF CIVIL ENGINEERING

DEPARTMENT OF STRUCTURAL ENGINEERING

INSTITUTE OF STRUCTURAL ANALYSIS & ASEISMIC RESEARCH

Athens, June 2020

Οι Διακριτες Μεθοδοι Υλικου Σημειου και Δικτυου Στερεων Σωματων και Ελατηριων στην Ελαστοπλαστικη Αναλυση Κατασκευων

ΔΙΔΙΑΚΤΟΡΙΚΗ ΔΙΑΤΡΙΒΗ

Για τον επιστημονικό τίτλο του Διδάκτορος Μηχανικού

Χρήστος Δ. Σοφιανός

ΕΘΝΙΚΟ ΜΕΤΣΟΒΙΟ ΠΟΛΥΤΕΧΝΕΙΟ

ΣΧΟΛΗ ΠΟΛΙΤΙΚΩΝ ΜΗΧΑΝΙΚΩΝ

ΤΟΜΕΑΣ ΔΟΜΟΣΤΑΤΙΚΗΣ

ΕΡΓΑΣΤΗΡΙΟ ΣΤΑΤΙΚΗΣ & ΑΝΤΙΣΕΙΣΜΙΚΩΝ ΕΡΕΥΝΩΝ

Αθήνα, Ιούνιος 2020

Εκτεταμενη περιληψη στην Ελληνικη Γλωσσα

1. Εισαγωγή

Οι αριθμητικές μέθοδοι τα τελευταία χρόνια έχουν αναδειχθεί σε νέο πυλώνα της Μηχανικής. Παράλληλα με τη θεωρία και τα πειράματα, η αριθμητική ανάλυση παρέχει έναν αποτελεσματικό τρόπο για την εξεύρεση λύσεων σε πολύπλοκα προβλήματα. Μάλιστα, υπάρχουν περιπτώσεις όπου η θεωρία αδυνατεί να παρέχει αναλυτικές λύσεις και δεν είναι δυνατή η εκτέλεση πειραμάτων. Ειδικά σε προβλήματα σχεδιασμού, οι αριθμητικές μέθοδοι δίνουν τη δυνατότητα μοντελοποίησης πολύπλοκων γεωμετριών και προσομοίωσης της μη γραμμικής συμπεριφοράς του υλικού, προβλήματα για τα οποία οι συμβατικές μέθοδοι δεν είναι σε θέση να δώσουν πάντα απαντήσεις. Οι αριθμητικές μέθοδοι μπορούν να κατηγοριοποιηθούν με βάση το κινηματικό πλαίσιο αναφοράς στο οποίο αναφέρονται, με το αν προσομοιώνουν το υλικό ως συνεχές μέσο ή ως διακριτά σωματίδια, και τέλος ανάλογα με το αν η ανάλυση είναι γραμμική ή μη γραμμική.

Όσον αφορά την περιγραφή της κίνησης και της παραμόρφωσης, οι αριθμητικές μέθοδοι μπορούν να διαχωρισθούν σε τέσσερις κατηγορίες. Αυτές είναι οι μέθοδοι Lagrange, μέθοδοι Euler, υβριδικές μέθοδοι και μέθοδοι χωρίς πλέγμα. Το Δίκτυο Στερεών Σωμάτων και Ελατηρίων (ΔΣΣΕ) ανήκει στην κατηγορία των μεθόδων που χρησιμοποιούν την περιγραφή κατά Lagrange και είναι η πρώτη διακριτή μέθοδος που εξετάζεται σε αυτή τη διατριβή. Η κατασκευή χωρίζεται σε κυρτά πολύγωνα που αποτελούν τα στερεά σώματα του μοντέλου τα οποία συνδέονται μεταξύ τους με ελατήρια. Αντίστοιχα, η Μέθοδος Υλικού Σημείου (ΜΥΣ) είναι η δεύτερη αριθμητική μέθοδος που χρησιμοποιείται και είναι μια μικτή/υβριδική μέθοδος με την έννοια ότι βασίζεται και στις δύο περιγραφές κατά Lagrange και Euler. Οι τάσεις και οι παραμορφώσεις αποθηκεύονται στα υλικά σημεία, πράγμα το οποίο διευκολύνει την προσομοίωση υλικών των οποίων η απόκριση εξαρτάται από την ιστορία τους. Τα υλικά σημεία ακολουθούν την περιγραφή Lagrange και εμπεριέχουν όλες τις φυσικές

πληροφορίες και ιδιότητες του υλικού, ενώ η μέθοδος χρησιμοποιεί και ένα πλέγμα που δεν παραμορφώνεται, το οποίο ακολουθεί την περιγραφή Euler, και στο οποίο επιλύονται οι εξισώσεις.

Οι αριθμητικές μέθοδοι μπορούν να κατηγοριοποιηθούν επίσης ανάλογα με τη θεώρηση του υλικού ως συνεχές μέσο ή ως ένα σύνολο διακριτών σωματιδίων τα οποία αλληλοεπιδρούν μεταξύ τους. Οι μέθοδοι της παρούσας διατριβής, το ΔΣΣΕ και η ΜΥΣ, παρότι διαφορετικές στην θεωρητική τους διατύπωση, μπορούν να θεωρηθούν ως διακριτές μέθοδοι. Στο ΔΣΣΕ υπάρχουν στερεά σώματα που συνδέονται με ελατήρια στις διεπιφάνειες τους, ενώ στη ΜΥΣ τα υλικά σημεία φέρουν όλες τις πληροφορίες του υλικού σε διακριτά σωματίδια.

Σχετικά με τη συμπεριφορά του υλικού, η θεωρία της γραμμικής ελαστικότητας μπορεί να προβλέψει με ακρίβεια περιπτώσεις που το υλικό συμπεριφέρεται ελαστικά και η σχέση τάσεων παραμορφώσεων είναι γραμμική. Παρόλα αυτά, τα περισσότερα υλικά εμφανίζουν μόνιμες παραμορφώσεις κατά την αποφόρτιση, όταν το φορτίο ξεπεράσει ένα όριο και συμπεριφέρονται ανελαστικά. Ένα σύστημα είναι υστερητικό όταν η απόκρισή του καθορίζεται από την ιστορία των καταστάσεων που έχει βρεθεί και όχι μόνο από την τωρινή του κατάσταση. Τα προηγούμενα χρόνια έχουν αναπτυχθεί διάφορα υστερητικά μοντέλα που μπορούν να διαχωρισθούν σε δύο κύριες κατηγορίες, τα πολυγραμμικά μοντέλα και τα ομαλά υστερητικά μοντέλα. Τα πολυγραμμικά μοντέλα διαχωρίζουν τη συμπεριφορά σε επιμέρους γραμμικά τμήματα, τα οποία αντιπροσωπεύουν τα διάφορα στάδια της υστερητικής συμπεριφοράς (κύκλοι φόρτισης – αποφόρτισης, απομειώσεις αντοχής και δυσκαμψίας κτλ.). Αντίθετα, τα ομαλά υστερητικά μοντέλα προσπαθούν να συμπεριλάβουν όλη την υστερητική συμπεριφορά σε μια ομάδα διαφορικών εξισώσεων, οι οποίες εκφράζονται συχνά σε επίπεδο ρυθμών μεταβολής. Όλα τα στάδια της υστερητικής συμπεριφοράς, όπως απομείωση αντοχής και δυσκαμψίας, κράτυνση ή χαλάρωση και κυκλική απόκριση εμπεριέχονται σε ένα ομαλό

μοντέλο και ελέγχονται μέσω παραμέτρων. Τα ανωτέρω οδηγούν στην περιγραφή του κύριου σκοπού της διατριβής, ο οποίος είναι η προσομοίωση της ανελαστικής – υστερητικής συμπεριφοράς κατασκευών με τη χρήση διακριτών αριθμητικών μεθόδων.

2. Ομαλό υστερητικό προσομοίωμα

Η υστέρηση είναι ένα άκρως μη γραμμικό φαινόμενο και απαντάται σε αρκετά επιστημονικά πεδία. Ένα σύστημα είναι υστερητικό όταν η απόκρισή του εξαρτάται από την ιστορία των καταστάσεών του και όχι μόνο από τη τωρινή του κατάσταση. Αυτό είναι ιδιαίτερα εμφανές στα ελαστοπλαστικά υλικά, όπου η τωρινή παραμόρφωση εξαρτάται από το σύνολο της ιστορίας της φόρτισης. Αντίθετα, στα ελαστικά υλικά οι παραμορφώσεις βασίζονται μόνο στο τωρινό επίπεδο των τάσεων. Τις προηγούμενες δεκαετίες το υστερητικό μοντέλο του Bouc- Wen έχει χρησιμοποιηθεί ευρέως. Χρησιμοποιεί εσωτερικές μεταβλητές οι οποίες ελέγχονται από εξελικτικές εξισώσεις. Αυτές περιγράφονται ως προς τους ρυθμούς μεταβολής και αναπτύσσονται με βάση τις ενδοχρονικές θεωρήσεις της πλαστικότητας. Έτσι, το υστερητικό μοντέλο, είναι σε θέση να περιγράφει την πλαστικότητα σε φαινομενολογικό επίπεδο. Οι παράμετροι του προσομοιώματος μπορούν να προσδιορισθούν με διάφορες μεθόδους που έχουν προταθεί κατά καιρούς στη βιβλιογραφία.

Το μονοαξονικό μοντέλο Bouc- Wen

Μέσα από τη διατύπωση των εξισώσεων για ένα μονοβάθμιο σύστημα και την περιγραφή του μηχανικού ανάλογου, παρουσιάζονται οι ιδιότητες και η συμπεριφορά του μοντέλου. Η μαθηματική του διατύπωση έχει ως εξής:

$$\begin{cases} m\ddot{u} + c\dot{u} + F^{BW} = p \\ F^{BW} = F^{el} + F^{pl} = aku + (1-a)kz \\ \dot{z} = \dot{u}\left[1 - \left|\dfrac{z}{z_y}\right|^n \left(\beta + \gamma \operatorname{sgn}(z\dot{u})\right)\right] \end{cases} \tag{E-1}$$

όπου m είναι η μάζα του συστήματος, c είναι η απόσβεση, p η εξωτερική δύναμη, F^{BW} η υστερητική δύναμη κατά Bouc-Wen, z η υστερητική παράμετρος (εν προκειμένω, το υστερητικό μέρος των μετατοπίσεων) και $\dot{z}$ η παράγωγός της ως προς το χρόνο, sgn η συνάρτηση signum, u η μετατόπιση του συστήματος, $\dot{u}$ η ταχύτητα, $\ddot{u}$ η επιτάχυνση and a το πηλίκο της μετελαστικής δυσκαμψίας k_{pl} προς την αρχική ελαστική k δυσκαμψία:

$$a = \frac{k_{pl}}{k} \tag{E-2}$$

Τέλος n, β και γ είναι παράμετροι του μοντέλου που ελέγχουν τη μορφή των βρόχων. Το μοντέλο βασίζεται σε μία μη γραμμική διαφορική εξίσωση πρώτης τάξης ως προς την υστερητική παράμετρο z. Για ένα μονοβάθμιο σύστημα η δύναμη επαναφοράς αποτελείται από ένα ελαστικό F^{el} και ένα πλαστικό μέρος F^{pl} ως:

$$F = F^{el} + F^{pl} = F_y\left[a\frac{u}{u_y} + (1-a)\frac{z}{u_y}\right] = \alpha ku + (1-\alpha)kz \tag{E-3}$$

Το μηχανικό ανάλογο των εξισώσεων μπορεί να οπτικοποιηθεί ως η παράλληλη ένωση δύο στοιχείων το ένα γραμμικό με μειωμένη δυσκαμψία ak και το άλλο μη γραμμικό όπως φαίνεται στην ακόλουθη εικόνα:

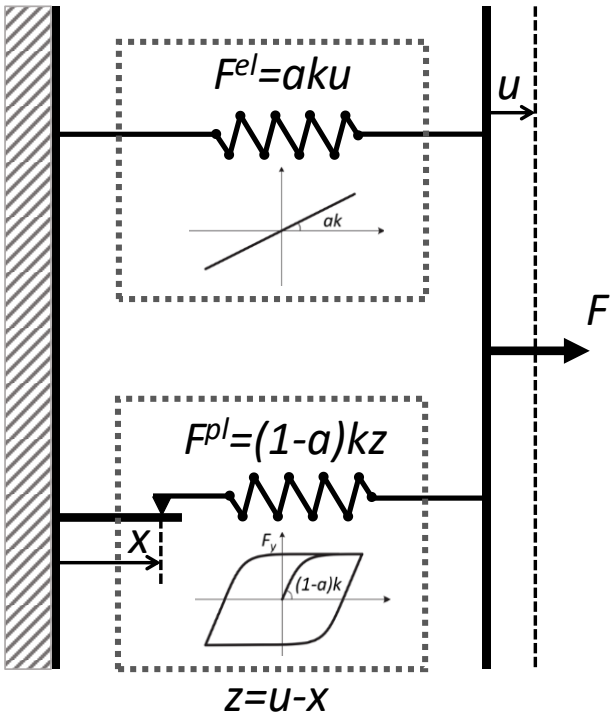

Εικόνα 1: Μηχανικό ανάλογο του μοντέλου Bouc-Wen.

<u>Παράμετροι του ομαλού υστερητικού μοντέλου</u>

Σχετικά με τις παραμέτρους της προηγούμενης παραγράφου, n είναι ένα βαθμωτό μέγεθος που ελέγχει την ομαλότητα της μετάβασης από τον ελαστικό στο μετελαστικό κλάδο. Όσο το n αυξάνει, η συμπεριφορά πλησιάζει τη διγραμμική και για μικρές τιμές της παραμέτρου, μπορεί να επιτευχθεί μια ομαλή μετάβαση.

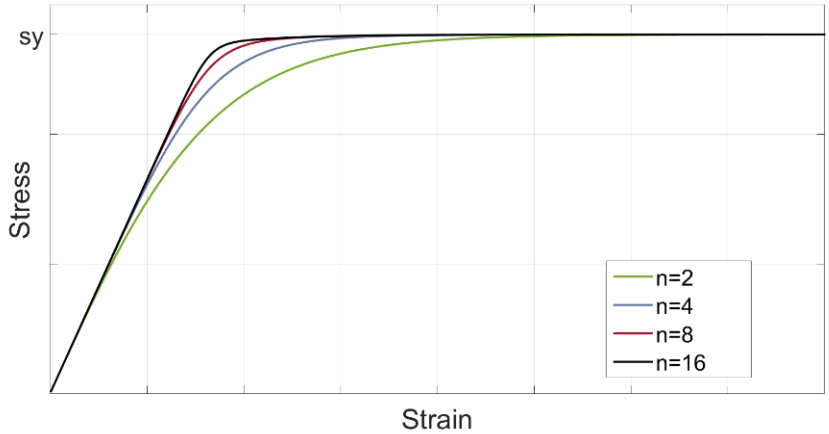

Εικόνα 2: Επίδραση της παραμέτρου n

Οι παράμετροι β και γ ελέγχουν τη μορφή των υστερητικών βρόχων κατά την αποφόρτιση και για να είναι το μοντέλο θερμοδυναμικά συμβατό πρέπει: $-\beta \le \gamma \le \beta$ και $\beta + \gamma = 1$. Η επίδρασή τους φαίνεται στην Εικόνα 3:

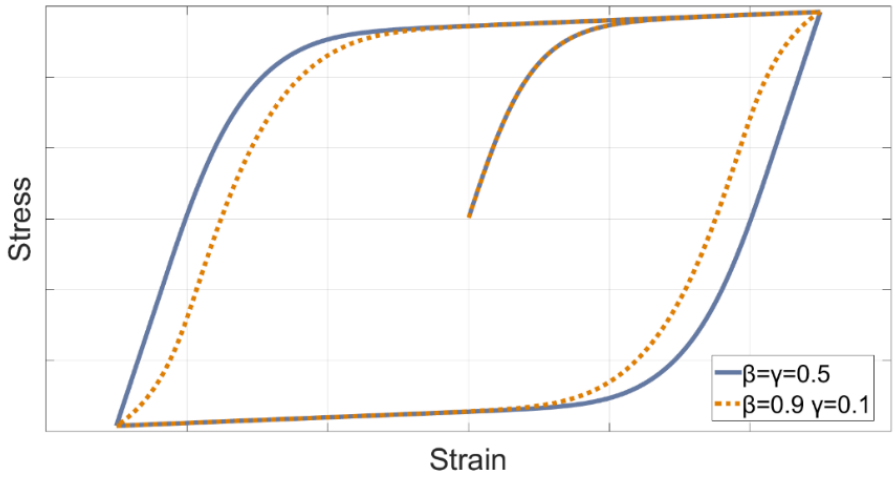

Εικόνα 3: Επίδραση των παραμέτρων β και γ

<u>Γενικευμένη τριαξονική περίπτωση</u>

Ένα ελαστικό υλικό δεν έχει μνήμη των προηγουμένων καταστάσεων που έχει βρεθεί και μετά την αποφόρτιση επιστρέφει σε κατάσταση μηδενικών τάσεων - παραμορφώσεων. Τα περισσότερα υλικά όμως υπόκεινται σε μόνιμες παραμορφώσεις όταν ξεπεραστεί το φορτίο διαρροής τους. Υπάρχει μια επιφάνεια στο χώρο των τάσεων που περικλείει τον χωρίο που το υλικό συμπεριφέρεται ελαστικά, η επιφάνεια διαρροής. Επιπρόσθετη φόρτιση οδηγεί σε διαρροή (ή πλαστική ροή) και στην εμφάνιση πλαστικών παραμορφώσεων. Σύμφωνα με τη θεωρία της κλασσικής πλαστικότητας οι εξισώσεις που διέπουν το πρόβλημα είναι ο νόμος πλαστικής ροής, η συνάρτηση διαρροής και η συνθήκη συνέπειας μαζί με το νόμο της κράτυνσης. Συνεπώς, με βάση αυτές τις εξισώσεις οι οποίες έχουν κοινό τον πλαστικό πολλαπλασιαστή, μπορούμε να καταλήξουμε στην ακόλουθη μορφή του πλαστικού πολλαπλασιαστή:

$$\dot{\lambda} = \lambda_1 \left(\frac{\partial \Phi}{\partial \{\sigma\}} \right)^T [D] \{\dot{\varepsilon}\} \tag{E-4}$$

όπου:

$$\lambda_1 = \left(-(1-m) \left(\frac{\partial \Phi}{\partial \{a^{kin}\}} \right)^T \{G\} - m \frac{\partial \Phi}{\partial \varepsilon_{ps}^{iso}} B + \left(\frac{\partial \Phi}{\partial \{\sigma\}} \right)^T [D] \frac{\partial \Phi}{\partial \{\sigma\}} \right)^{-1} \tag{E-5}$$

Η σχέση του πλαστικού πολλαπλασιαστή ισχύει μόνο όταν το υλικό έχει διαρρεύσει. Η σχέση γενικεύεται για όλο τον χώρο των τάσεων, καθώς και ομαλοποιείται η μετάβαση από την ελαστική στη μετελαστική περιοχή, με τη χρήση των ακόλουθων συναρτήσεων τύπου Heaviside:

$$\dot{\lambda} = H_1 H_2 \lambda_1 \left(\frac{\partial \Phi}{\partial \{\sigma\}} \right)^T [D] \{\dot{\varepsilon}\} \tag{E-6}$$

όπου:

$$H_1 = \left| \frac{f\left(\{\sigma\} - \{a^{kin}\} \right)}{\sigma_y \left(\varepsilon_{ps}^{iso} \right)} \right|^n \qquad H_2 = \beta + \gamma sign \left(\left\{ \frac{\partial \Phi}{\partial \{\sigma\}} \right\}^{\mathrm{T}} [D] \{\dot{\varepsilon}\} \right) \tag{E-7}$$

Τέλος αντικαθιστώντας τη σχέση του πλαστικού πολλαπλασιαστή στη σχέση του νόμου πλαστικής ροής, εξάγεται το εφαπτομενικό μητρώο στιβαρότητας:

$$\begin{gathered} \{\dot{\sigma}\} = [E_t] \{\dot{\varepsilon}\} \\ [E_t] = [D]\left([I] - H_1 H_2 [R] \right) \end{gathered} \tag{E-8}$$

όπου $[R]$ είναι το μητρώο αλληλεπίδρασης:

$$[R] = \lambda_1 \left\{ \frac{\partial \Phi}{\partial \{\sigma\}} \right\} \left\{ \frac{\partial \Phi}{\partial \{\sigma\}} \right\}^{\mathrm{T}} [D] \tag{E-9}$$

Στην Εικόνα 4 παρουσιάζονται οι τιμές των ομαλών συναρτήσεων Heaviside για τα διάφορα στάδια κυκλικής υστερητικής συμπεριφοράς.

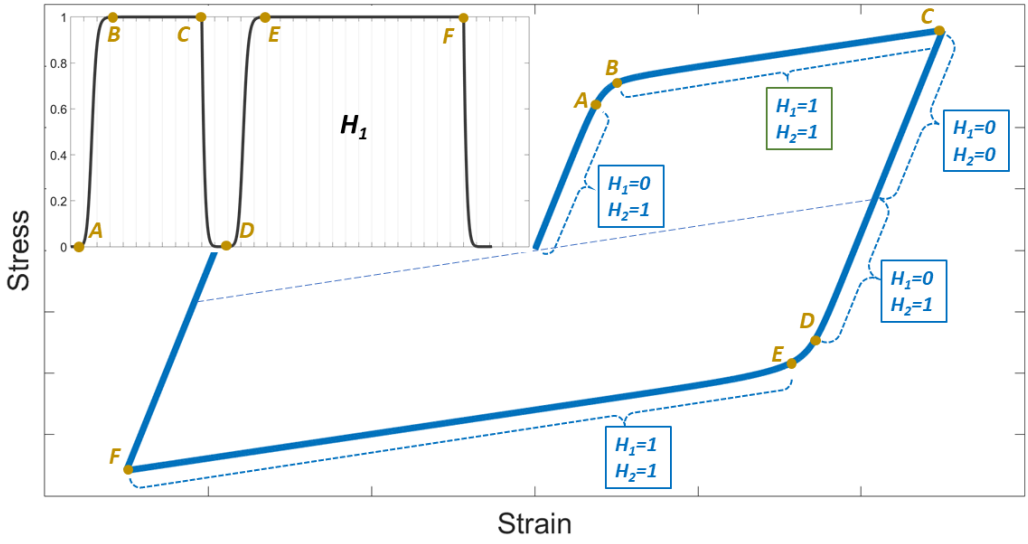

Εικόνα 4: Συμπεριφορά ομαλών συναρτήσεων Heaviside

<u>Απομείωση αντοχής και δυσκαμψίας</u>

Για την προσομοίωση των φαινομένων της απομείωσης της αντοχής και της δυσκαμψίας εισάγονται στο μοντέλο δύο νέες παράμετροι n_s , v_s και η τελική μορφή των εξισώσεων δίνεται στην σχέση (Ε-10). Με αυτόν τον τρόπο, οι νόμοι απομείωσης αντοχής και δυσκαμψίας εισάγονται στο μοντέλο χρησιμοποιώντας μια επιπρόσθετη εξελικτική εξίσωση η οποία επιλύεται ταυτόχρονα με τις υστερητικές εξισώσεις Bouc – Wen. Η επίδραση των παραμέτρων στην υστερητική απομειούμενη κυκλική συμπεριφορά παρουσιάζεται στην Εικόνα 5.

$$\{\dot{\sigma}\} = [D]\frac{1}{\eta}\left([I] - v_s H_1 H_2 [R]\right)\{\dot{\varepsilon}\}$$

$$\dot{\eta} = c_\eta \left(\frac{1}{\eta}\right)^{m_u} \beta H_1 \left(1 + \frac{\gamma}{\beta}\operatorname{sgn}\left(\{\sigma\}^T \{\dot{\varepsilon}\}\right)\right)\left|\{\sigma\}^T \{\dot{\varepsilon}\}\right|$$

$$v_s = 1 + c_v e^h \qquad \text{(E-10)}$$

$$H_1 = \left|\frac{f\left(\{\sigma\} - \{a^{kin}\}\right)}{\sigma_y\left(\varepsilon_{ps}^{iso}\right)}\right|^n$$

$$H_2 = \beta + \gamma sign\left(\left\{\frac{\partial \Phi}{\partial \{\sigma\}}\right\}^{\mathrm{T}} [D]\{\dot{\varepsilon}\}\right)$$

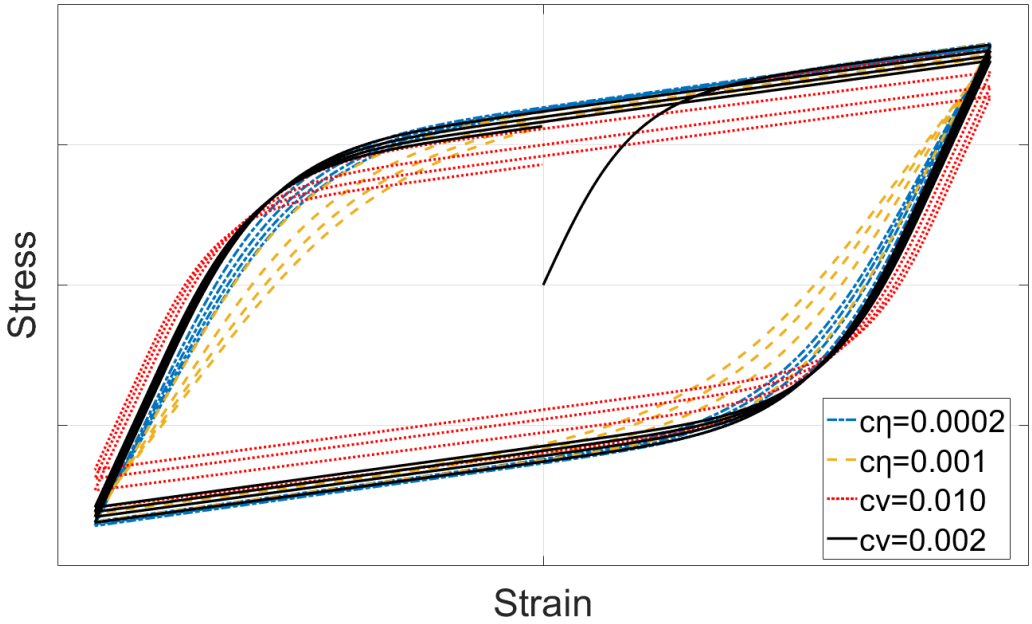

Εικόνα 5: Επίδραση παραμέτρων στην απομείωση αντοχής και δυσκαμψίας

3. Δίκτυο Στερεών Σωμάτων και Ελατηρίων

Τα μοντέλα πλέγματος ελατηρίων έχουν χρησιμοποιηθεί ευρέως σε αριθμητικές προσομοιώσεις σε διάφορα επιστημονικά πεδία, από την προσομοίωση της ύλης σε ατομικό επίπεδο, μέχρι την κίνηση πλανητών. Στη Μηχανική, έχουν χρησιμοποιηθεί επιτυχώς στη θραυστομηχανική, στη διάδοση ελαστικών κυμάτων, στη μηχανική των ρευστών κτλ. Το δίκτυο Στερεών Σωμάτων και Ελατηρίων αποτελεί ένα διακριτό προσομοίωμα και αναπτύχθηκε αρχικά από τον Kawai. Η βασική του ιδέα είναι ο διαχωρισμός της κατασκευής σε ένα σύνολο στερεών σωμάτων που συνδέονται με ελατήρια στις διεπιφάνειες τους. Στην παρούσα διατριβή, χρησιμοποιείται η διακριτοποίηση με διαγράμματα Voronoi για τη δημιουργία κυρτών πολυγώνων και στερεών σωμάτων, η οποία αποτελεί σημαντικό κομμάτι του μοντέλου.

Διαγράμματα Voronoi

Το πρώτο βήμα στη διακριτοποίηση με διαγράμματα Voronoi είναι η τυχαία διασπορά σημείων εντός του χωρίου. Αυτά τα σημεία αποτελούν τους κόμβους του διαγράμματος Voronoi και τους υπολογιστικούς κόμβους του μοντέλου. Στην Εικόνα 6 παρουσιάζεται το διάγραμμα Voronoi καθώς και το δυικό του γράφημα, δηλ. η τριγωνοποίηση Delaunay. Με το διάγραμμα Voronoi δημιουργούνται κυρτά πολύγωνα τα οποία και αποτελούν τα στερεά σώματα του αριθμητικού μοντέλου.

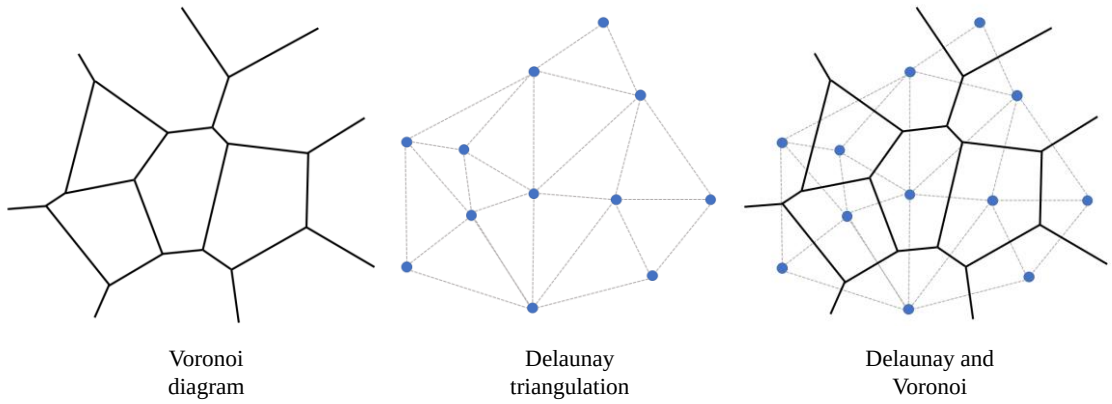

Εικόνα 6: Voronoi Διάγραμμα και τριγωνοποίηση Delaunay

Τα στερεά σώματα συνδέονται στο μέσο της διεπιφάνειας τους με μηδενικού μήκους ελατήρια, όπως φαίνεται στην Εικόνα 7, δύο μετακινησιακά και ένα στροφικό.

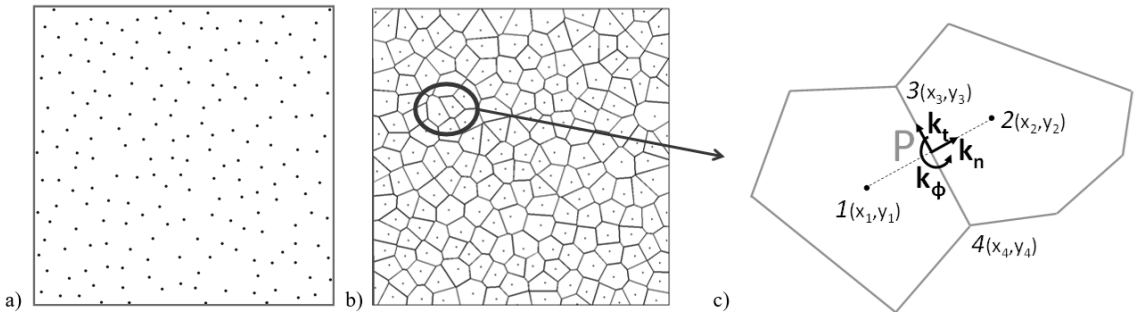

Εικόνα 7: Δίκτυο Στερεών Σωμάτων και Ελατηρίων, a) αρχική κατανομή σημείων, b) διάγραμμα Voronoi, c) στοιχείο του μοντέλου

Η παραμόρφωση της κατασκευής βασίζεται μόνο στις παραμορφώσεις αυτών των εσωτερικών ελατηρίων, και τα στερεά σώματα μπορούν να απομακρύνονται το ένα από το άλλο, αλλά ακόμη και να επικαλύπτουν το ένα το άλλο. Στο μέσο της διεπιφάνειας βρίσκονται δύο μετακινησιακά ελατήρια και ένα στροφικό με αντίστοιχες δυσκαμψίες k_n, k_t και k_φ στο τοπικό σύστημα αναφοράς. Μορφώνεται έτσι το διαγώνιο μητρώο:

$$[D]=\begin{bmatrix} k_n & 0 & 0 \\ 0 & k_t & 0 \\ 0 & 0 & k_\varphi \end{bmatrix} \tag{E-11}$$

Οι σχετικές μετατοπίσεις του μέσου της διεπιφάνειας (σημείο *P*) είναι:

$$\{d\}^T=\begin{bmatrix}\delta_n & \delta_t & \varphi\end{bmatrix} \tag{E-12}$$

και οι μετατοπίσεις των υπολογιστικών κόμβων *1* και *2*:

$$\{u_e\}^T=\begin{bmatrix}u_1 & v_1 & \theta_1 & u_2 & v_2 & \theta_2\end{bmatrix} \tag{E-13}$$

και συνδέονται μεταξύ τους με το μητρώο $[B]$:

$$\{d\}=[B]\{u_e\} \tag{E-14}$$

Το οποίο έχει διαστάσεις (3×6) και προκύπτει από γεωμετρικούς υπολογισμούς:

$$[B]=\frac{1}{l_{43}}\begin{bmatrix} y_{43} & -x_{43} & (-x_{43}x_{P1}-y_{43}y_{P1}) & -y_{43} & x_{43} & (x_{43}y_{P2}+y_{43}y_{P2}) \\ x_{43} & y_{43} & (y_{43}x_{P1}-x_{43}y_{P1}) & -x_{43} & -y_{43} & (-y_{43}x_{P2}+x_{43}y_{P2}) \\ 0 & 0 & -l_{43} & 0 & 0 & l_{43} \end{bmatrix} \quad \text{(E-15)}$$

όπου l_{43} είναι το μήκος της διεπιφάνειας και $x_{ij}=x_i-x_j$. Επιπρόσθετα, οι εσωτερικές δυνάμεις των ελατηρίων μπορούν να υπολογισθούν ως:

$$\{q\}=\begin{Bmatrix} F_n \\ F_t \\ M \end{Bmatrix}=[D]\{d\} \quad \text{(E-16)}$$

όπου F_n, F_t είναι η δύναμη στο ορθό και εφαπτομενικό ελατήριο και M η ροπή του στροφικού ελατηρίου. Για την προσομοίωση των ελαστικών ιδιοτήτων του υλικού οι δυσκαμψίες των ελατηρίων κλιμακώνονται βάση του διαγράμματος Voronoi και σύμφωνα με τις σχέσεις:

$$k_n=\frac{Etl_{43}}{\left(1-\nu^2\right)h}, k_t=\frac{Etl_{43}}{\left(2\left(1+\nu\right)\right)h}, \quad k_\varphi=\frac{k_n l_{43}^2}{12} \quad \text{(E-17)}$$

όπου, E είναι το μέτρο ελαστικότητας, ν ο λόγος Poisson, t το πάχος του χωρίου και h η απόσταση των δύο κόμβων. Το μητρώο δυσκαμψίας στοιχείου προκύπτει από την αρχή των δυνατών έργων και έχει διαστάσεις (6×6):

$$[K]_e=[B]^T[D][B] \quad \text{(E-18)}$$

Όλα τα μητρώα δυσκαμψίας των στοιχείων συγκεντρώνονται στο μητρώο δυσκαμψίας της κατασκευής χρησιμοποιώντας τη μέθοδο άμεσης δυσκαμψίας. Το μητρώο δυσκαμψίας της κατασκευής είναι διαστάσεων $(3n\times 3n)$ όπου n ο συνολικός αριθμός των κόμβων του μοντέλου.

Σε ένα δισδιάστατο ορθογωνικό χωρίο ο μέγιστος αριθμός κόμβων που μπορούν να

τοποθετηθούν, χρησιμοποιώντας μια τυχαία διαδικασία και ένα κριτήριο ελάχιστης απόστασης, είναι: $\hat{n} = 0.68ab / d_m^2$ όπου a και b είναι το ύψος και το πλάτος του ορθογωνικού χωρίου και d_m είναι η ελάχιστη απόσταση μεταξύ των σημείων. Επιλέγοντας $n \to \hat{n}$ η διακριτοποίηση γίνεται περισσότερο κανονική και τα σημεία κατανέμονται περισσότερο ομοιόμορφα. Αυτό επιλέγεται διότι οδηγεί σε μεγαλύτερη ομοιομορφία, όσον αφορά τις ελαστικές ιδιότητες του υλικού, καθώς και σε μείωση της εξάρτησης της πορείας της ρωγμής από τη διακριτοποίηση.

<u>Ενσωμάτωση ομαλού υστερητικού προσομοιώματος στο Δίκτυο Στερεών Σωμάτων και Ελατηρίων</u>

Οι δυνάμεις των εσωτερικών ελατηρίων και των υπολογιστικών κόμβων συνδέονται μεταξύ τους με την ακόλουθη σχέση:

$$\begin{Bmatrix} F_x^1 \\ F_y^1 \\ M^1 \\ F_x^2 \\ F_y^2 \\ M^2 \end{Bmatrix} = [B]^T \begin{Bmatrix} F_n \\ F_t \\ M \end{Bmatrix} \tag{E-19}$$

Σύμφωνα με το ομαλό υστερητικό προσομοίωμα οι δυνάμεις των εσωτερικών ελατηρίων χωρίζονται σε ένα ελαστικό και ένα υστερητικό μέρος ως:

$$\begin{aligned} F_n &= ak_n\delta_n + (1-\alpha)k_n z_n \\ F_t &= ak_t\delta_t + (1-\alpha)k_t z_t \\ M &= ak_\varphi\varphi + (1-\alpha)k_\varphi z_\varphi \end{aligned} \tag{E-20}$$

ή αντίστοιχα σε μητρωική μορφή:

$$\begin{Bmatrix} F_n \\ F_t \\ M \end{Bmatrix} = \begin{bmatrix} ak_n & 0 & 0 \\ 0 & ak_t & 0 \\ 0 & 0 & ak_\varphi \end{bmatrix} \begin{Bmatrix} \delta_n \\ \delta_t \\ \varphi \end{Bmatrix} + \begin{bmatrix} (1-a)k_n & 0 & 0 \\ 0 & (1-a)k_t & 0 \\ 0 & 0 & (1-a)k_\varphi \end{bmatrix} \begin{Bmatrix} z_n \\ z_t \\ z_\varphi \end{Bmatrix} \tag{E-21}$$

όπου οι υστερητικές δυνάμεις είναι:

$$\left\{F^h\right\}=\begin{Bmatrix}F_n^h\\F_t^h\\M^h\end{Bmatrix}=\begin{bmatrix}(1-a)k_n & 0 & 0\\0 & (1-a)k_t & 0\\0 & 0 & (1-a)k_\varphi\end{bmatrix}\begin{Bmatrix}z_n\\z_t\\z_\varphi\end{Bmatrix} \qquad \text{(E-22)}$$

Σύμφωνα με τις εξισώσεις (E-14), (E-21) και αντικαθιστώντας στην (E-19) προκύπτει:

$$\begin{Bmatrix}F_x^1\\F_y^1\\M^1\\F_x^2\\F_y^2\\M^2\end{Bmatrix}=[B]^T\begin{bmatrix}ak_n & 0 & 0\\0 & ak_t & 0\\0 & 0 & ak_\varphi\end{bmatrix}[B]\begin{Bmatrix}u_1\\w_1\\\theta_1\\u_2\\w_2\\\theta_2\end{Bmatrix}+[\mathrm{B}]^T\begin{bmatrix}(1-a)k_n & 0 & 0\\0 & (1-a)k_t & 0\\0 & 0 & (1-a)k_\varphi\end{bmatrix}\begin{Bmatrix}z_n\\z_t\\z_\varphi\end{Bmatrix} \qquad \text{(E-23)}$$

όπου το υστερητικό μέρος ακολουθεί τις εξελικτικές εξισώσεις Bouc-Wen, ως μη γραμμικές διαφορικές εξισώσεις πρώτης τάξης της μορφής:

$$\begin{cases}\dot{z}_n=\dot{\delta}_n\left[1-\left|\dfrac{z_n}{z_y^n}\right|^n\left(\gamma+\beta\,\mathrm{sgn}\left(z_n\dot{\delta}_n\right)\right)\right]\\[2ex]\dot{z}_t=\dot{\delta}_t\left[1-\left|\dfrac{z_t}{z_y^t}\right|^n\left(\gamma+\beta\,\mathrm{sgn}\left(z_t\dot{\delta}_t\right)\right)\right]\\[2ex]\dot{z}_\varphi=\dot{\varphi}\left[1-\left|\dfrac{z_\varphi}{z_y^\varphi}\right|^n\left(\gamma+\beta\,\mathrm{sgn}\left(z_\varphi\dot{\varphi}\right)\right)\right]\end{cases} \qquad \text{(E-24)}$$

Το υστερητικό μητρώο προκύπτει ως

$$[H]=[B]^T\begin{bmatrix}(1-a)k_n & 0 & 0\\0 & (1-a)k_t & 0\\0 & 0 & (1-a)k_\varphi\end{bmatrix} \qquad \text{(E-25)}$$

Συνδυάζοντας όλα τα υστερητικά μητρώα των στοιχείων προκύπτει το υστερητικό μητρώο δυσκαμψίας της κατασκευής $[H]_s$, με διαστάσεις $(3\times n, 3\times n_{el})$ όπου n_{el} είναι ο αριθμός των στοιχείων και n είναι ο συνολικός αριθμός των κόμβων. Η εξίσωση κίνησης διατυπώνεται ως:

$$[M]_s\{\ddot{u}\}+[C]_s\{\dot{u}\}+[K]_s\{u\}+[H]_s\{z\}=\{P(t)\} \qquad \text{(E-26)}$$

και επιλύεται ταυτόχρονα με τις εξελικτικές εξισώσεις Bouc – Wen για κάθε στοιχείο.

Αναπαράσταση ρωγμών στο Δίκτυο Στερεών Σωμάτων και Ελατηρίων

Το ΔΣΣΕ προσφέρει μια διακριτή αναπαράσταση της κατασκευής. Το άνοιγμα και η διάδοση της ρωγμής συνεπώς, περιορίζεται στις διεπιφάνειες των στερεών σωμάτων όπως φαίνεται στην Εικόνα 8. Αυτό σημαίνει ότι η διάδοση της ρωγμής επηρεάζεται από τη διακριτοποίηση. Για τη μείωση της επίδρασης αυτής, χρησιμοποιείται το διάγραμμα Voronoi μαζί με το κριτήριο ελάχιστης απόστασης, που οδηγούν σε περισσότερο ομοιόμορφη διακριτοποίηση.

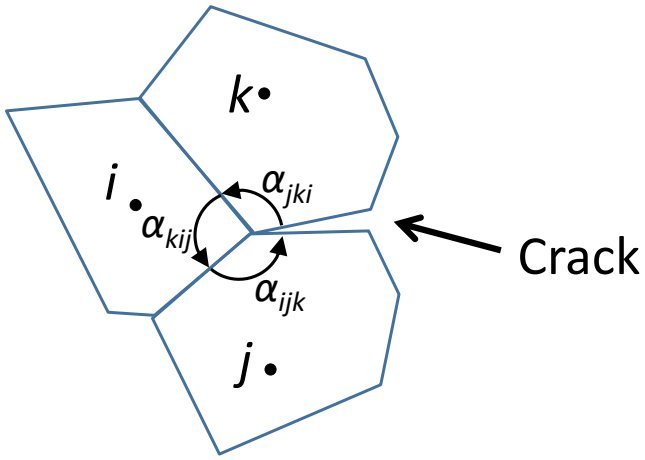

Εικόνα 8: Άνοιγμα ρωγμής μεταξύ των στερεών σωμάτων *k* και *j*.

Με το διάγραμμα Voronoi και το κριτήριο ελάχιστης απόστασης, οι ακμές των στερεών σωμάτων συναντώνται συνήθως σε τριάδες, με μέση τιμή των γωνιών τις 120° και μικρή διασπορά. Αυτό οδηγεί σε μικρότερο βαθμό ανισοτροπίας σχετικά με την κατεύθυνση της ρωγμής. Στην παρούσα διατριβή η έναρξη και διάδοση της ρηγμάτωσης ακολουθούν ένα απλό νόμο τύπου Mohr-Coulomb για τις ορθές και διατμητικές τάσεις, όπως παρουσιάζεται στην Εικόνα 9. Σε κάθε υπολογιστικό κύκλο υπολογίζονται οι τάσεις από τις δυνάμεις των ελατηρίων, και συγκρίνονται με το κριτήριο. Αν οι τάσεις βρίσκονται

εκτός του κριτηρίου τότε θεωρούμε ότι έχουμε θραύση. Σε αυτή την περίπτωση οι δυνάμεις των ελατηρίων απελευθερώνονται και οι δυσκαμψίες τους μηδενίζονται.

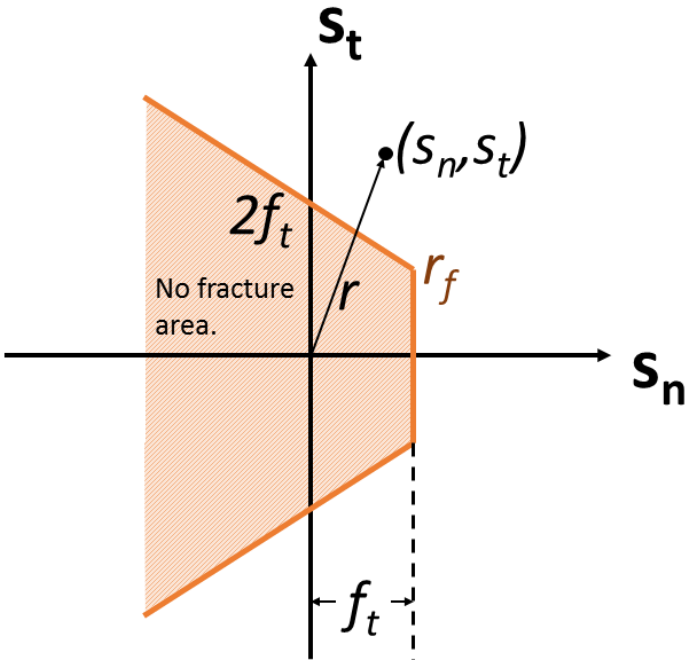

Εικόνα 9: Κριτήριο θραύσης τύπου Mohr-Coulomb

4. Μέθοδος Υλικού Σημείου

Η Μέθοδος Υλικού Σημείου (ΜΥΣ) είναι μια υβριδική μέθοδος με την έννοια ότι εκμεταλλεύεται την περιγραφή κατά Lagrange και την περιγραφή κατά Euler. Όλες οι πληροφορίες του υλικού, όπως ταχύτητα, τάση, παραμόρφωση κτλ., αποθηκεύονται στα διακριτά σωματίδια ενώ χρησιμοποιείται ένα υπολογιστικό πλέγμα στο παρασκήνιο, για την επίλυση των εξισώσεων της ορμής.

Ο αλγόριθμος της ΜΥΣ

Στη ΜΥΣ το χωρίο διακριτοποιείται σε έναν αριθμό υλικών σημείων (σωματιδίων) τα οποία μετακινούνται μέσα σε ένα πλέγμα που παραμένει σταθερό κατά την ανάλυση (Εικόνα 10). Το χωρίο Ω που αντιπροσωπεύει το υλικό μπορεί να αναπαρασταθεί από N_p αριθμό υλικών σημείων. Κάθε υλικό σημείο αντιπροσωπεύει ένα υποχωρίο Ω_p και

φέρει όλες τις ιδιότητες όπως μάζα m_p, θέση x_p, ταχύτητα v_p, παραμόρφωση ε_p και τάση σ_p. Το υπολογιστικό πλέγμα που ακολουθεί την περιγραφή κατά Euler χρησιμοποιείται για την επίλυση των εξισώσεων και τον υπολογισμό των χωρικών παραγώγων των διαφόρων μεγεθών, και αποτελείται από N_g κόμβους. Η αρχή διατήρησης της μάζας ικανοποιείται αυτόματα στη μέθοδο, αφού η συνολική μάζα χωρίζεται στα υλικά σημεία και παραμένει σταθερή κατά τη διάρκεια της ανάλυσης.

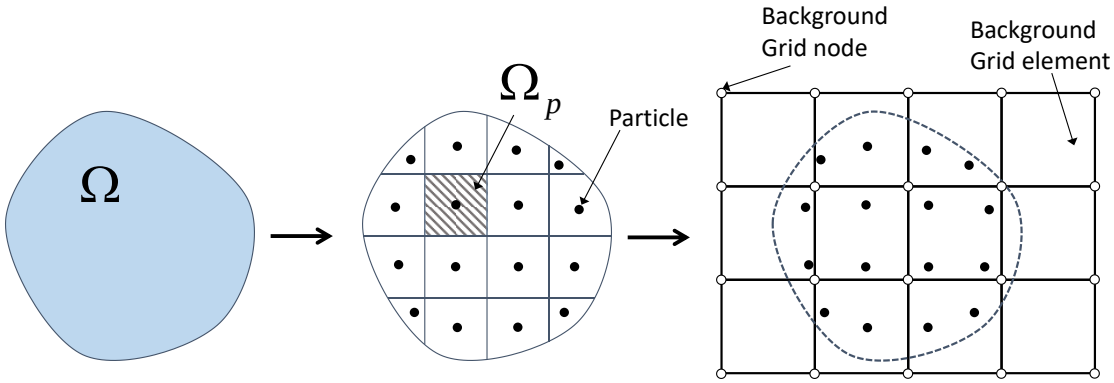

Εικόνα 10: Διακριτοποίηση με τη Μέθοδο Υλικού Σημείου

Η μέθοδος χρησιμοποιεί επίσης συναρτήσεις σχήματος για την προβολή ιδιοτήτων από τα υλικά σημεία προς το υπολογιστικό πλέγμα και αντίστροφα (Εικόνα 11). Στην παρούσα διατριβή εξετάζονται δύο ειδών συναρτήσεις σχήματος, οι γραμμικές και τα κυβικά B-Splines. Τα τελευταία εξαιτίας της ανώτερης τάξης και της συνέχειας των παραγώγων τους, οδηγούν σε μείωση των σφαλμάτων ολοκλήρωσης καθώς και εξαλείφουν τα αριθμητικά σφάλματα που δημιουργούνται όταν ένα υλικό σημείο μετακινείται από ένα στοιχείο του υπολογιστικού κόμβου σε ένα άλλο.

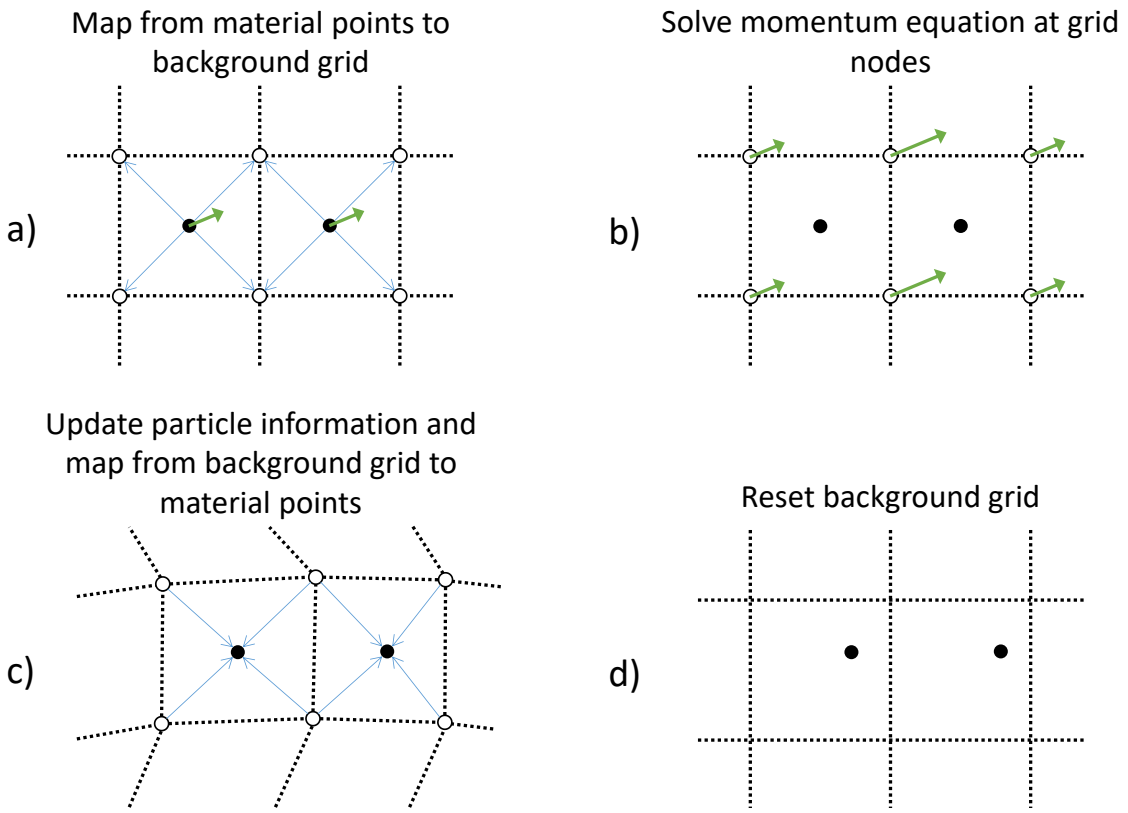

Εικόνα 11: Σχηματική αναπαράσταση υπολογιστικού βήματος της ΜΥΣ

Ο βασικός αλγόριθμος που χρησιμοποιείται συνοψίζεται στα ακόλουθα βήματα (Εικόνα 11):

1. Επαναφορά του υπολογιστικού πλέγματος στην αρχική του κατάσταση. Όλες οι μεταβλητές του μηδενίζονται (όπως μάζα, ορμή, δυνάμεις κτλ.).
2. Ταυτοποίηση του αριθμού του στοιχείου του υπολογιστικού πλέγματος στο οποίο βρίσκεται κάθε υλικό σημείο. Η διαδικασία αυτή είναι απλή και υπολογιστικά ανέξοδη για δομημένα πλέγματα.
3. Υπολογισμός των συναρτήσεων σχήματος και των παραγώγων τους. Για κάθε υλικό σημείο υπολογίζονται 16 συναρτήσεις σχήματος στις δύο διαστάσεις και 32 παράγωγοι, όταν χρησιμοποιούνται κυβικά B-Splines. Οι ιδιότητες κάθε υλικού σημείου προβάλλονται στους κόμβους του στοιχείου στο οποίο ανήκει καθώς και στους κόμβους των γειτονικών στοιχείων. Αντίθετα στις γραμμικές συναρτήσεις σχήματος, υπολογίζονται τέσσερις συναρτήσεις σχήματος και οκτώ

παράγωγοί τους, καθώς το υλικό σημείο προβάλλει τις ιδιότητές του μόνο στους κόμβους του στοιχείου στο οποίο ανήκει.

4. Η μάζα, η ορμή και οι εσωτερικές δυνάμεις προβάλλονται στους κόμβους του υπολογιστικού πλέγματος σύμφωνα με τις ακόλουθες εξισώσεις:

$$
\begin{aligned}
m_i &= \sum_{p=1}^{N_p} M_p N_i \\
(mv)_i &= \sum_{p=1}^{N_p} (Mv)_p N_i \\
F_i^{\text{int}} &= -\sum_{p=1}^{N_p} \frac{M_p}{p_p} \sigma_p \nabla N_i
\end{aligned}
\tag{E-27}
$$

5. Οι εξωτερικές δυνάμεις προβάλλονται στους κόμβους του πλέγματος ως:

$$
F_i^{ext} = \sum_{p=1}^{N_p} N_i b_{ip} \tag{E-28}
$$

6. Υπολογίζεται το διάνυσμα των επικόμβιων δυνάμεων του πλέγματος:

$$
F_i = F_i^{ext} + F_i^{int} \tag{E-29}
$$

7. Υπολογίζονται οι ανανεωμένες ορμές στους κόμβους του πλέγματος:

$$
(mv)_i = (mv)_i + F_i dt \tag{E-30}
$$

8. Επιβάλλονται οι συνοριακές συνθήκες.

9. Από τις ανανεωμένες ορμές στους κόμβους του υπολογιστικού πλέγματος, υπολογίζονται οι ταχύτητες και οι νέες θέσεις των σωματιδίων:

$$
\begin{aligned}
v(x_p) &= v(x_p) + \left(\sum_{i=1}^{N} \frac{F_i N_i}{m_i} \right) dt \\
x_p &= x_p + \left(\sum_{i=1}^{N} \frac{(mv)_i N_i}{m_i} \right) dt
\end{aligned}
\tag{E-31}
$$

10. Το τελευταίο βήμα είναι ο επανυπολογισμός των επικόμβιων ορμών του πλέγματος από τις νέες ταχύτητες των σωματιδίων και με βάση αυτές ο τελικός υπολογισμός των επαυξητικών παραμορφώσεων και τάσεων:

$$
\begin{aligned}
(mv)_i &= \sum_{p=1}^{N_p} M_p v(x_p) N_i \\
v_i &= \frac{(mv)_i}{m_i} \\
\Delta\varepsilon_p &= \sum_{i=1}^{N} v(x_p) \nabla N_i dt \\
\Delta\sigma_p &= [D] \Delta\varepsilon_p
\end{aligned}
\qquad \text{(E-32)}
$$

<u>Διερεύνηση συναρτήσεων σχήματος</u>

Σε αυτή την παράγραφο διερευνάται η επίδραση των συναρτήσεων σχήματος στην υπολογιστική ακρίβεια της μεθόδου και χρησιμοποιούνται κυβικά B-Splines. Δύο περιπτώσεις εξετάζονται. Στην πρώτη διερευνάται η επίδρασή τους στον υπολογισμό της παραγώγου της ταχύτητας (gradient velocity), ενώ στη δεύτερη, η ακρίβεια τους στην ολοκλήρωση για την περίπτωση της πλαστικότητας.

Το χωρίο που εξετάζεται έχει διαστάσεις *0.5m* x *5.0m*, μέτρο ελαστικότητας *E*=10000*Pa*, λόγο Poisson *v=0* και πυκνότητα 1000kg/m^3. Γίνονται διάφορες αναλύσεις και το χωρίο διακριτοποιείται με διαφορετικό αριθμό στοιχείων και με διαφορετικό αριθμό υλικών σημείων ανά στοιχείο. Στη μια ομάδα αναλύσεων ο αριθμός των στοιχείων του υπολογιστικού κόμβου διατηρείται σταθερός και αυξάνεται ο αριθμός των υλικών σημείων ανά στοιχείο. Ο αριθμός των στοιχείων είναι 10, 20 και 40 στοιχεία, ενώ ο αριθμός των υλικών σημείων ανά στοιχείο ποικίλει από 1, 4, 9 έως 16 υλικά σημεία. Σε όλες τις αναλύσεις η αρχική ταχύτητα είναι ημιτονοειδής και δίνεται από την ακόλουθη σχέση:

$$
pVEL = 0.01\cos\left(\frac{\pi}{5}(x_p - 0.5)\right) \qquad \text{(E-33)}
$$

η παράγωγος μπορεί να υπολογισθεί αναλυτικά ως:

$$L_p = (0.01\frac{\pi}{5})\sin\left(\frac{\pi}{10} - \frac{\pi}{5}x_p\right) \qquad \text{(E-34)}$$

και συγκρίνεται με τα αποτελέσματα από την ανάλυση με τη Μέθοδο Υλικού Σημείου. Τα αποτελέσματα παρουσιάζονται στον παρακάτω πίνακα:

N. elements	**Particles per element**	**Computational time (x)**	**L2 norm**
10	1	1	0.0193
10	4	3.86	0.0166
10	9	8.73	0.0164
10	16	15.36	0.0164
20	1	1.97	0.004225
20	4	7.73	0.004111
20	9	17.76	0.004108
20	16	30.88	0.004106
40	1	4.03	0.0010319
40	4	15.8	0.0010282
40	9	35.02	0.0010280
40	16	62.62	0.0010280

Πίνακας 1: Υπολογιστικός χρόνος και ακρίβεια ΜΥΣ

Από τα αποτελέσματα εξάγονται ορισμένα συμπεράσματα τόσο ως προς την ακρίβεια όσο και ως προς τον υπολογιστικό χρόνο. Όσον αφορά τον υπολογιστικό χρόνο, ως βάση θεωρείται η πρώτη ανάλυση με 10 στοιχεία και 1 υλικό σημείο ανά στοιχείο, δηλ. σύνολο 10 υλικά σημεία. Παρατηρείται ότι ο υπολογιστικός χρόνος είναι σχεδόν ανάλογος του αριθμού των υλικών σημείων.

Όσον αφορά το σφάλμα του υπολογισμού των παραγώγων της ταχύτητας, φαίνεται ότι η αύξηση είτε του αριθμού των στοιχείων, είτε του αριθμού των υλικών σημείων ανά

στοιχείο, οδηγεί σε μείωση του σφάλματος. Παρόλα αυτά, η μείωση του σφάλματος είναι μεγαλύτερη στην περίπτωση αύξησης των στοιχείων.

Εφαπτομενικό μητρώο

Το εφαπτομενικό μητρώο της σχέσης (Ε-8) , υπολογίζεται για κάθε υλικό σημείο και έχει πρωτεύοντα ρόλο στην διαμόρφωση της Υστερητικής Μεθόδου Υλικού Σημείου. Αντικαθιστά το μητρώο της ελαστικότητας στην εξίσωση (Ε-32) που συσχετίζει το ρυθμό μεταβολής των παραμορφώσεων με το ρυθμό μεταβολής των τάσεων. Έτσι οι τάσεις στο τέλος κάθε χρονικού βήματος μπορούν να υπολογισθούν βάση των ολικών παραμορφώσεων. Το μητρώο αυτό για δισδιάστατα προβλήματα έχει διαστάσεις (3×3). Μπορεί να προσομοιώσει ισοτροπική, κινηματική και μικτή κράτυνση καθώς και διάφορες συναρτήσεις διαρροής, παρέχοντας ομαλούς υστερητικούς βρόχους. Επίσης στην περίπτωση που λαμβάνεται υπόψη το φαινόμενο της απομείωσης της αντοχής και της δυσκαμψίας, το εφαπτομενικό μητρώο υπολογίζεται ως:

$$
\begin{aligned}
&[E_t] = [D]\frac{1}{\eta}\left([I] - v_s H_1 H_2 [R]\right) \\
&H_1 = \left|\frac{f\left(\{\sigma\} - \{a^{kin}\}\right)}{\sigma_y\left(\varepsilon_{ps}^{iso}\right)}\right|^n \\
&H_2 = \beta + \gamma\, sign\left(\left\{\frac{\partial\Phi}{\partial\{\sigma\}}\right\}^{\mathrm{T}}[D]\{\dot{\varepsilon}\}\right) \qquad \text{(E-35)} \\
&[R] = \lambda_1\left\{\frac{\partial\Phi}{\partial\{\sigma\}}\right\}\left\{\frac{\partial\Phi}{\partial\{\sigma\}}\right\}^{\mathrm{T}}[D] \\
&\lambda_1 = \left((1-m)\frac{3}{2}C_p + mH' + \left(\frac{\partial\Phi}{\partial\{\sigma\}}\right)^T[D]\frac{\partial\Phi}{\partial\{\sigma\}}\right)^{-1}
\end{aligned}
$$

όπου οι παράμετροι για τις απομειώσεις αντοχής και δυσκαμψίας δίνονται από τις σχέσεις:

$$\dot{\eta} = c_\eta \left(\frac{1}{\eta}\right)^{m_u} \beta H_1 \left(1 + \frac{\gamma}{\beta} \operatorname{sgn}\left(\{\sigma\}^T \{\dot{\varepsilon}\}\right)\right) \left|\{\sigma\}^T \{\dot{\varepsilon}\}\right| \qquad \text{(E-36)}$$
$$v_s = 1 + c_v e^h$$

Το εφαπτομενικό μητρώο στην εξίσωση (Ε-35) υπολογίζεται για κάθε υλικό σημείο ξεχωριστά. Οι εξελικτικές σχέσεις (Ε-36) πρέπει να επιλυθούν ταυτόχρονα με τις υπόλοιπες σχέσεις σε μη πεπλεγμένη (explicit) μορφή. Το μοντέλο είναι σε θέση να προσομοιώσει την υστερητική συμπεριφορά με κινηματική, ισοτροπική και μικτή κράτυνση, καθώς και με απομειώσεις αντοχής και δυσκαμψίας.

Πλεονέκτημα της ανωτέρω διατύπωσης αποτελεί το γεγονός ότι όλη η υστερητική συμπεριφορά, εμπεριέχεται στον υπολογισμό του εφαπτομενικού μητρώου για κάθε υλικό σημείο. Η ενσωμάτωσή του σε υπάρχοντες κώδικες της ΜΥΣ είναι απλή και ο υπολογισμός του εφαπτομενικού μητρώου μπορεί να γίνει ανεξάρτητα και παράλληλα για κάθε υλικό σημείο, σε υπολογιστές με πολλούς πυρήνες.

Οι συναρτήσεις σχήματος στην πλαστικότητα

Για τη διερεύνηση της επιρροής των συναρτήσεων σχήματος στην πλαστικότητα εξετάζεται μία αμφιέρειστη δοκός, με συγκεντρωμένο φορτίο στο μέσον της. Το υλικό είναι χάλυβας με μέτρο ελαστικότητας 210*GPa*, τάση διαρροής 240*MPa* και πυκνότητα 7850kg/m^3. Η κράτυνση είναι κινηματικού τύπου με κλίση 5%. Για την διακριτοποίηση χρησιμοποιούνται 1280 υλικά σημεία που αντιστοιχούν σε 4 σωματίδια ανά στοιχείο. Το υπολογιστικό πλέγμα έχει μήκος στοιχείου 0.025m. Πραγματοποιούνται δύο αναλύσεις με τη χρήση γραμμικών συναρτήσεων σχήματος και κυβικών B-Splines.

Στην Εικόνα 12 παρουσιάζονται τα διαγράμματα ορθών τάσεων – παραμορφώσεων για ένα σημείο που βρίσκεται στο μέσο της δοκού στο κάτω τμήμα της. Μπορεί να επισημανθεί ότι για τις γραμμικές συναρτήσεις σχήματος, εμφανίζονται ταλαντώσεις και θόρυβος όσο οι τάσεις πλησιάζουν την τάση διαρροής. Αντίθετα, για τα κυβικά B-Splines

το διάγραμμα είναι ομαλό φανερώνοντας τις ανώτερες ιδιότητές τους. Επίσης στην Εικόνα 13 παρουσιάζονται οι κατανομές των διατμητικών τάσεων για τη δοκό. Οι γραμμικές συναρτήσεις σχήματος εμφανίζουν μια οδοντωτή συμπεριφορά και δεν μπορούν να προσομοιώσουν τη σωστή κατανομή. Αντίθετα τα κυβικά B-Splines υπολογίζουν σωστά την κατανομή των διατμητικών τάσεων με ομαλό τρόπο.

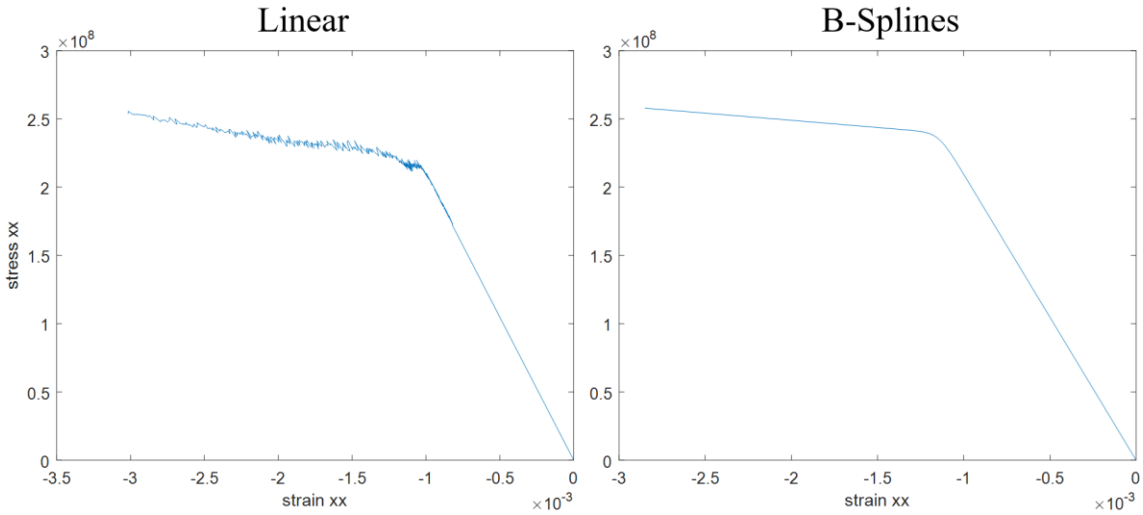

Εικόνα 12: Διαγράμματα ορθών τάσεων – παραμορφώσεων για γραμμικές συναρτήσεις σχήματος (αριστερά) και για κυβικά B-Splines (δεξιά)

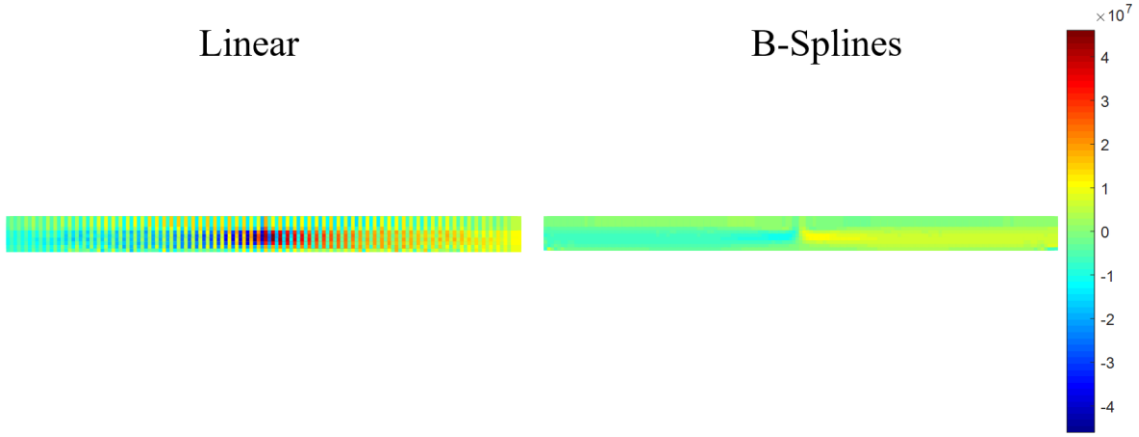

Εικόνα 13: Κατανομή διατμητικών τάσεων για γραμμικές συναρτήσεις σχήματος (αριστερά) και για κυβικά B-Splines (δεξιά)

Συμπεραίνεται ότι όταν υπεισέρχεται η πλαστικότητα, η χρησιμοποίηση γραμμικών συναρτήσεων σχήματος δεν ενδείκνυται. Αυτές ενδέχεται να οδηγήσουν σε μη

ρεαλιστικές τάσεις σε μεμονωμένα υλικά σημεία και σε μικρό-ταλαντώσεις στις τάσεις μετά τη διαρροή. Υπάρχουν επίσης περιπτώσεις που τα υλικά σημεία μπορεί να οδηγηθούν σε διαρροή εξαιτίας της λανθασμένης κατανομής των τάσεων εντός ενός γραμμικού στοιχείου. Για αυτό το λόγο η συμπεριφορά του υλικού δεν αποδίδεται με ακρίβεια και στη περίπτωση της πλαστικής συμπεριφοράς θα πρέπει να χρησιμοποιούνται συναρτήσεις σχήματος ανώτερης τάξης.

5. Εφαρμογές

5.1 ΔΣΣΕ – Πλαστική θραύση πλάκας τιτανίου

Σε αυτό το παράδειγμα εξετάζεται η πλαστική θραύση μιας πλάκας από τιτάνιο. Τα αποτελέσματα συγκρίνονται με αποτελέσματα από άλλες διακριτές μεθόδους (DVIB και DLSM) καθώς και με πειραματικά δεδομένα. Το μέτρο ελαστικότητας του υλικού είναι 115 *GPa*, ο λόγος Poisson είναι 0.28, η εφελκυστική αντοχή σ_t είναι1007 *MPa*, και η τάση διαρροής έχει την τιμή σ_y=955 *MPa*. Αυτές οι τιμές των παραμέτρων προκύπτουν από πείραμα μονοαξονικού εφελκυσμού και χρησιμοποιούνται στις αριθμητικές προσομοιώσεις.

Στην Εικόνα 14 παρουσιάζεται η γεωμετρία του φορέα καθώς και η διακριτοποίηση του με το Δίκτυο Στερεών Σωμάτων και Ελατηρίων. Οι μετακινήσεις των δύο σημείων, που εμφανίζονται με κόκκινο χρώμα, καταγράφονται και η μεταξύ τους απόσταση μετριέται και χαρακτηρίζεται ως Μετατόπιση Ανοίγματος Ρωγμής (Crack Opening Displacement). Το διάγραμμα αυτής της μετατόπισης και των δυνάμεων αντίδρασης χρησιμοποιείται για τη σύγκριση των αποτελεσμάτων. Τα αποτελέσματα παρουσιάζονται στην Εικόνα 15 για τις διάφορες μεθόδους και για το ΔΣΣΕ. Θα πρέπει να σημειωθεί πως για το ΔΣΣΕ η δύναμη επιβάλλεται σταδιακά σε ένα μεγάλο χρονικό διάστημα, αφού η ανάλυση είναι δυναμική.

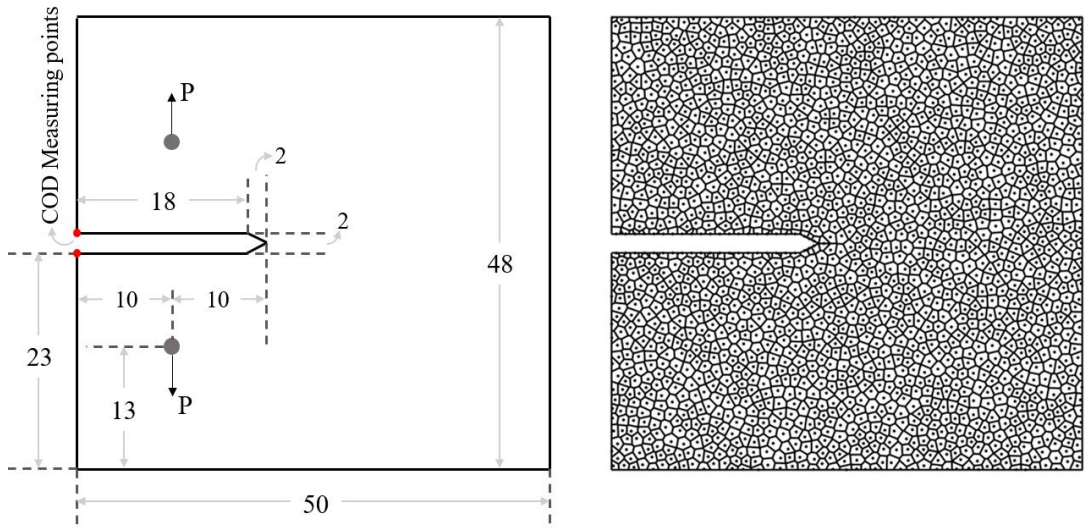

Εικόνα 14: Πλάκα τιτανίου και διακριτοποίηση με το ΔΣΣΥ

Στο ΔΣΣΕ χρησιμοποιούνται δύο διαφορετικές διακριτοποιήσεις, η μία χρησιμοποιώντας ένα κριτήριο ελάχιστης 3mm και η άλλη χρησιμοποιώντας κριτήριο 0.9mm. Αυτό οδηγεί σε 218 και 1949 κόμβους για κάθε διακριτοποίηση. Στην Εικόνα 14 παρουσιάζεται η διακριτοποίηση με 1949 κόμβους.

Στην Εικόνα 15 φαίνεται πως τα αποτελέσματα του ΔΣΣΕ προσεγγίζουν τα πειραματικά δεδομένα με ικανοποιητική ακρίβεια, για την περίπτωση της πλαστικής θραύσης. Διαφορετικές διακριτοποιήσεις οδηγούν σε ελαφρώς διαφοροποιημένα αποτελέσματα σχετικά με την καμπύλη δύναμης – μετατόπισης. Παρόλα αυτά η μορφή της ρωγμής είναι παρόμοια σε όλες τις περιπτώσεις. Η τελική μορφή της ρωγμής παρουσιάζεται στην Εικόνα 16 για όλες τις αριθμητικές μεθόδους και το πείραμα.

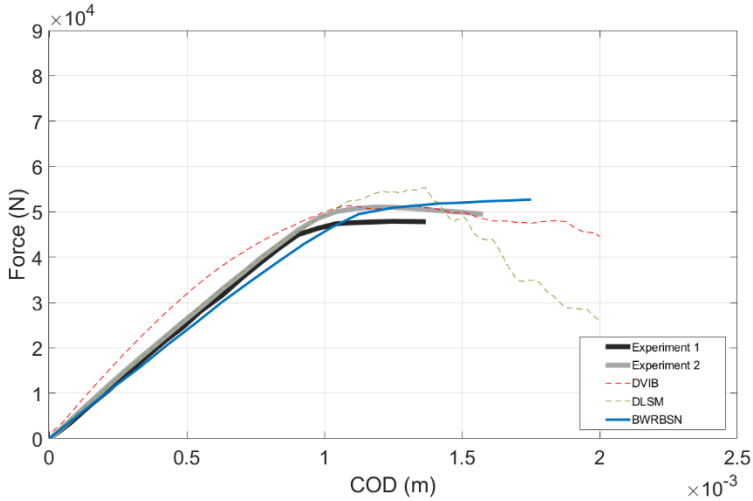

Εικόνα 15: Σύγκριση αριθμητικών και πειραματικών αποτελεσμάτων

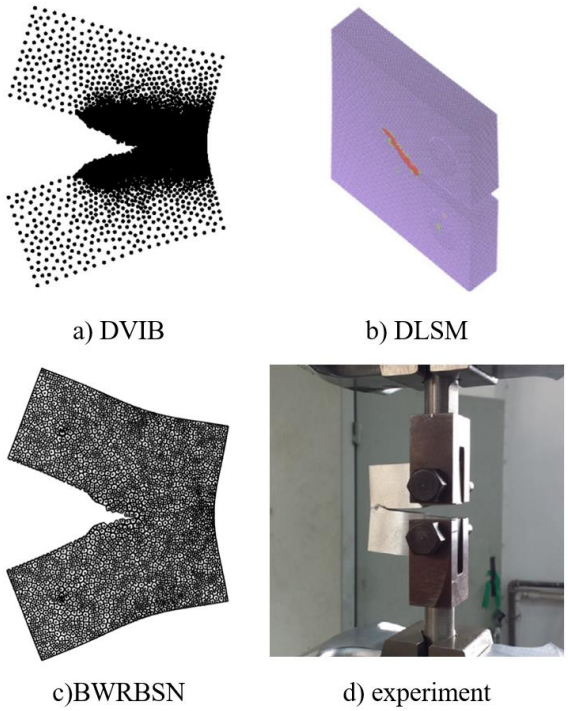

Εικόνα 16: Τελική μορφή της ρωγμής a)με τη μέθοδο DVIB, b) με τη μέθοδο DLSM c) με το ΔΣΣΥ και d) πειραματικά αποτελέσματα

5.2 ΜΥΣ – Γωνιακή σύνδεση

Σε αυτό το παράδειγμα εξετάζεται η μη γραμμική συμπεριφορά γωνιακής σύνδεσης επίπεδου πλαισίου. Η πειραματική διάταξη καθώς και η γεωμετρία της γωνιακής σύνδεσης φαίνονται στην Εικόνα 17. Η διατομή των μελών είναι W30×108 και

υπάρχουν και ενισχύσεις. Το υλικό είναι χάλυβας ποιότητας A36. Για την προσομοίωση του σχήματος διπλού ταυ των διατομών και των ενισχύσεων, δίνονται διαφορετικά πάχη στα αντίστοιχα υλικά σημεία, b_{f} για τα πέλματα και t_w για τον κορμό, όπως φαίνεται στην Εικόνα 17. Το μήκος του στοιχείου του πλέγματος καθώς και ο αριθμός των υλικών σημείων ανά στοιχείο καθορίζουν την τιμή του πλάτους των πελμάτων t_{f} (που προσομοιώνεται από τα περιφερειακά υλικά σημεία που φαίνονται με κόκκινο στην Εικόνα 17). Όλα τα υπόλοιπα σημεία έχουν πάχος ίσο με το πάχος του κορμού t_w. Εξισώνοντας τη ροπή αδρανείας της διατομής με την αρχική ροπή αδρανείας, το πάχος των περιφερειακών υλικών σημείων b_{f} μπορεί να υπολογισθεί:

$$I_{xx} = I_w + I_{\mathrm{f}} = \frac{t_w\left(D-2t_{\mathrm{f}}\right)^2}{12} + 2b_{\mathrm{f}}t_{\mathrm{f}}\left(\frac{D}{2}-\frac{t_{\mathrm{f}}}{2}\right)^2 + 2\frac{b_{\mathrm{f}}t_{\mathrm{f}}^{\,3}}{12} \qquad \text{(E-37)}$$

Για την ανάλυση με τη Μέθοδο Υλικού Σημείου χρησιμοποιήθηκαν 1296 υλικά σημεία και 9 υλικά σημεία ανά στοιχείο. Το διάγραμμα φορτίου μετατόπισης παρουσιάζεται στην Εικόνα 18. Τα αποτελέσματα από την υστερητική ΜΥΣ συγκρίνονται με πειραματικά δεδομένα και με αποτελέσματα από μία μέθοδο χωρίς πλέγμα (Meshfree method). Τα αποτελέσματα έχουν ικανοποιητική ακρίβεια και προσομοιώνουν σωστά την ανελαστική συμπεριφορά μέχρι του σημείου που αρχίζει να εμφανίζεται χαλάρωση στο υλικό. Σε αυτό το σημείο εμφανίζονται φαινόμενα τοπικού λυγισμού στα πέλματα.

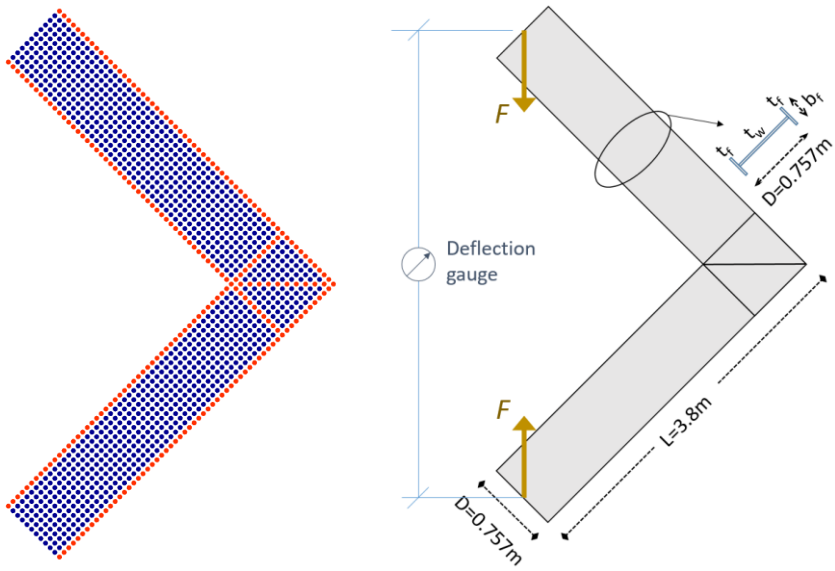

Εικόνα 17: Γεωμετρία γωνιακής σύνδεσης

Τέλος, οι τάσεις που αναπτύσσονται στη γωνιακή σύνδεση παρουσιάζονται στην Εικόνα 19 και συγκρίνονται με αυτές από τη μέθοδο χωρίς πλέγμα. Τα αποτελέσματα σχεδόν ταυτίζονται και οδηγούν σε ορισμένες παρατηρήσεις. Η πρώτη αφορά στη δημιουργία πλαστικής άρθρωσης κοντά στο σημείο σύνδεσης. Η δεύτερη, στην μετατόπιση του ουδέτερου άξονα της διατομής εξαιτίας της ταυτόχρονης καταπόνησης με αξονική δύναμη και ροπή.

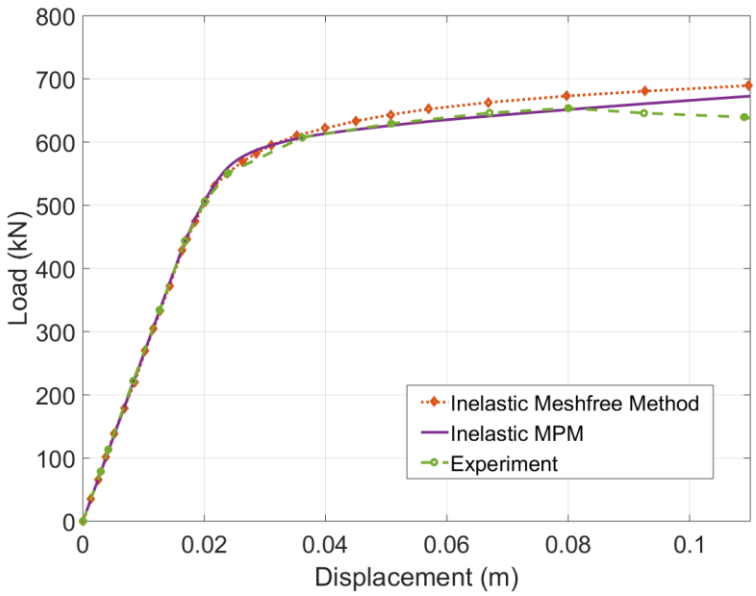

Εικόνα 18: Διάγραμμα φορτίου μετατόπισης για τη γωνιακή σύνδεση

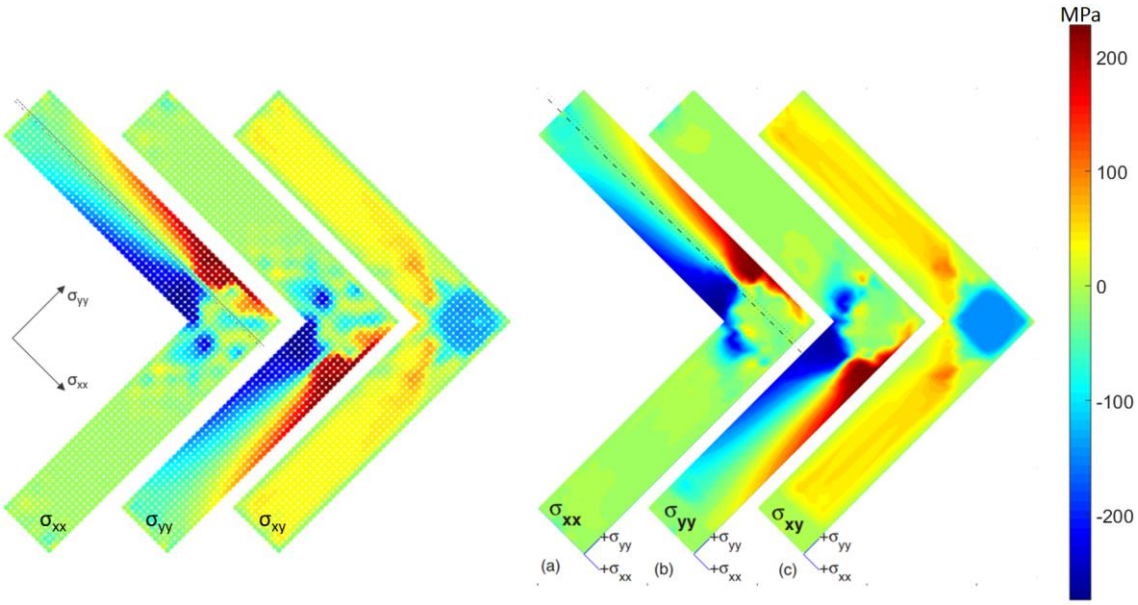

Εικόνα 19: Κατανομές τάσεων (MPa). Αριστερά ΜΥΣ δεξιά Μέθοδος χωρίς πλέγμα

<u>ΜΥΣ – Τεστ κρούσης Taylor</u>

Αυτό το παράδειγμα αφορά ένα κλασσικό τεστ κρούσης που στην βιβλιογραφία αναφέρεται ως Taylor test. Μία χαλύβδινη ράβδος προσκρούει σε ένα άκαμπτο τοίχο με μεγάλη ταχύτητα. Το υλικό είναι αλουμίνιο 6061-T6 με πυκνότητα $p=2700kg/m^3$ και μέτρο ελαστικότητας $E=78.2GPa$. Ο λόγος Poisson είναι $\nu=0.3$ και η τάση διαρροής Von Mises είναι $\sigma_y=0.29GPa$, ενώ ακολουθεί ισοτροπική κράτυνση. Το μήκος της ράβδου είναι τριπλάσιο της διαμέτρου όπου $L_o=2.346cm$ το μήκος και $R_o=0.782cm$ η διάμετρος. Η αρχική γεωμετρία και η διακριτοποίηση με τη Μέθοδο Υλικού Σημείου φαίνονται στην Εικόνα 20.

Η ράβδος έχει αρχική ταχύτητα προς τα κάτω ίση με $v_0=-373m/sec$. Αυτή η ταχύτητα εφαρμόζεται ως αρχική ταχύτητα σε όλα τα υλικά σημεία για τον αλγόριθμο της ΜΥΣ. Επίσης χρησιμοποιείται ένα ορθογωνικό πλέγμα με τετραγωνικά στοιχεία τα οποία έχουν διαστάσεις πλευράς $L_{el}=0.0782\ cm$. Η ράβδος διακριτοποιείται σε 1200 υλικά σημεία με

4 υλικά σημεία ανά στοιχείο. Οι συνοριακές συνθήκες στον αμετακίνητο τοίχο είναι κυλίσεις επιτρέποντας την οριζόντια μετακίνηση και δεσμεύοντας την κατακόρυφη.

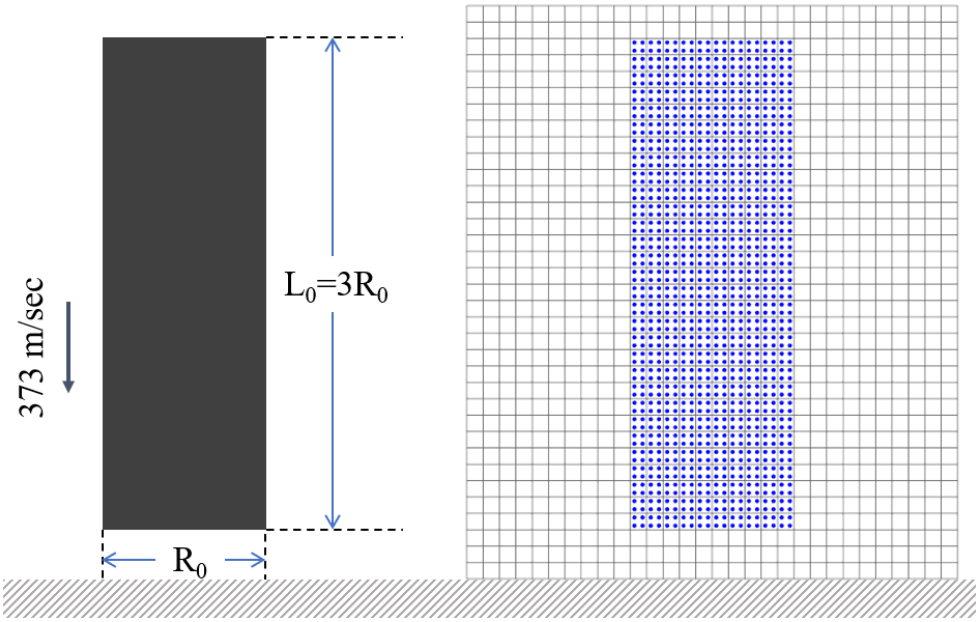

Εικόνα 20: Αρχική γεωμετρία κυλίνδρου και διακριτοποίηση με τη ΜΥΣ

Το ίδιο πρόβλημα αναλύεται στη βιβλιογραφία χρησιμοποιώντας μια αξονοσυμμετρική διατύπωση της ΜΥΣ σε κυλινδρικές συντεταγμένες καθώς και με άλλες μεθόδους. Στον Πίνακα 2 παρουσιάζονται τα τελικά αποτελέσματα όσον αφορά το τελικό μήκος της ράβδου L_f και την τελική της διάμετρο D_f. Επίσης μετριέται η τελική διάμετρος της ράβδου σε ένα ύψος 0.25cm από τη βάση της $D_{h=0.25}$, για τον προσδιορισμό του τελικού της σχήματος. Τα αποτελέσματα συγκρίνονται με αυτά από τις άλλες μεθόδους και δείχνουν ικανοποιητική σύγκλιση. Το παράδειγμα αυτό δείχνει επίσης τη δυνατότητα της Μεθόδου Υλικού Σημείου να διαχειρίζεται φαινόμενα επαφής χωρίς κάποια μεταβολή ή άλλη προσθήκη στον αλγόριθμο επίλυσης. Επιπρόσθετα, στην Εικόνα 21 παρουσιάζεται η τελική μορφή της ράβδου και συγκρίνεται με τις υπόλοιπες μεθόδους. Στην Εικόνα 22 φαίνεται η κατανομή των ισοδύναμων πλαστικών παραμορφώσεων. Όπως αναμένεται η περιοχή με τη μεγαλύτερη πλαστικοποίηση είναι αυτή που βρίσκεται κοντά στην περιοχή της επαφής.

	L_f (cm)	D_f (cm)	$D_{h=0.25}$(cm)
FLIP	1.63	1.480	0.98
HEMP	1.652	1.484	1.106
CSQ	1.605	1.440	1.106
Experiment	1.651	-	
BWMPM	1.595	1.452	1.103

Πίνακας 2: Αποτελέσματα υστερητικής ΜΥΣ και σύγκριση με άλλες μεθόδους

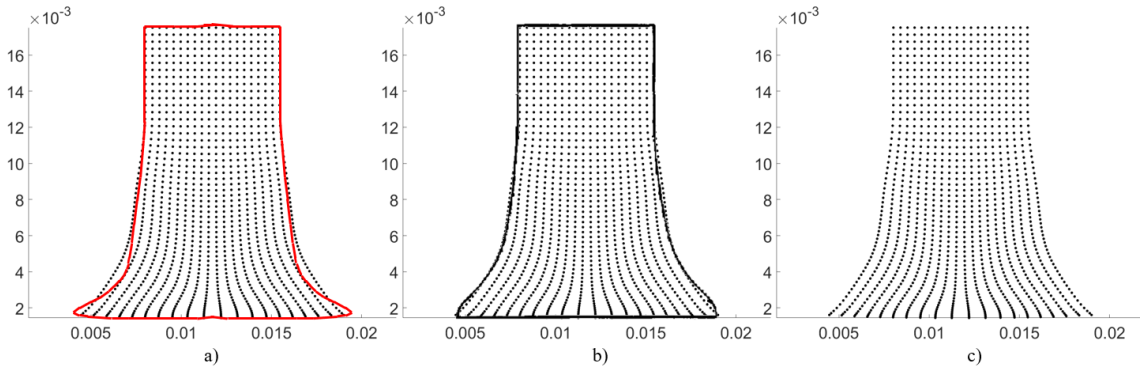

Εικόνα 21: Τελική μορφή της ράβδου: a) Αξισυμμετρική ΜΥΣ , b) μέθοδος CSQ c) Υστερητική ΜΥΣ (μονάδες m)

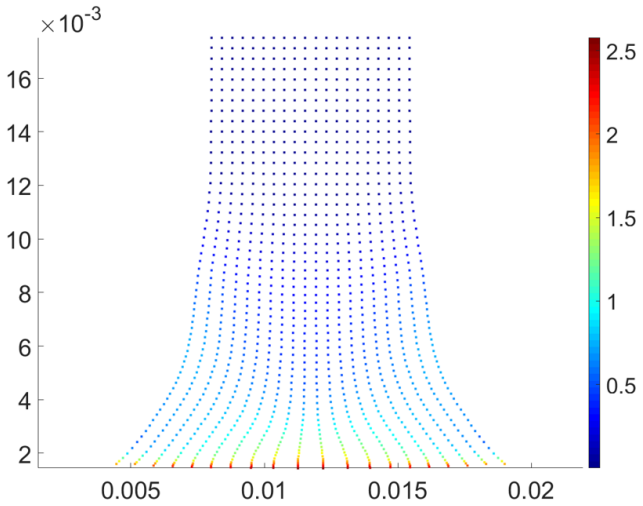

Εικόνα 22: Κατανομή ισοδύναμων πλαστικών παραμορφώσεων (μονάδες m)

Η μέγιστη τιμή των ισοδύναμων πλαστικών παραμορφώσεων που καταγράφεται στη βιβλιογραφία είναι 2.732. Στην Εικόνα 23 παρουσιάζεται η χρονική εξέλιξη των ισοδύναμων πλαστικών παραμορφώσεων για το υλικό σημείο που βρίσκεται στο μέσο της κάτω επιφάνειας της ράβδου. Η Υστερητική Μέθοδος Υλικού Σημείου είναι σε θέση

να προσεγγίσει το τελικό σχήμα της παραμορφωμένης ράβδου, με ορισμένες διαφορές στο σχήμα της σε ύψος 0.25cm από την επιφάνεια κρούσης.

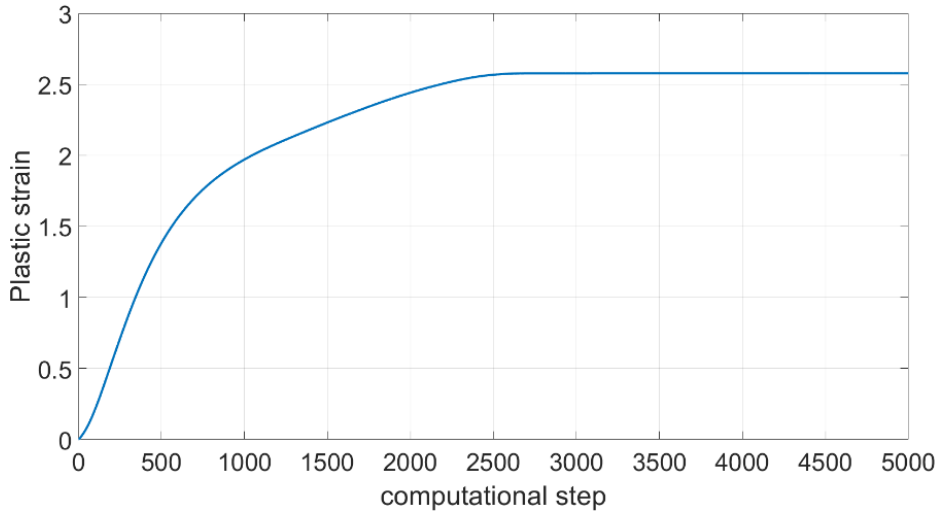

Εικόνα 23: Χρονική εξέλιξη ισοδύναμων πλαστικών παραμορφώσεων

6. Συμπεράσματα – Προτάσεις για μελλοντική έρευνα

Στην παρούσα διατριβή προτείνονται ομαλά υστερητικά προσομοιώματα, βασισμένα στις σχέσεις του Bouc-Wen για την πλαστικότητα ανεξάρτητη του ρυθμού μεταβολής. Τα μοντέλα αυτά προκύπτουν τόσο βάση μιας προσέγγισης ως προς ένα μονοβάθμιο σύστημα και το μηχανικό του ανάλογο, όσο και ως προς τις αρχές της κλασικής πλαστικότητας. Το κύριο πλεονέκτημα της διατύπωσης κατά Bouc-Wen είναι η χρήση ομαλών συναρτήσεων τύπου Heaviside, που λειτουργούν ως διακόπτες και ελέγχουν όλα τα στάδια της υστερητικής συμπεριφοράς. Η διατύπωση είναι γενική και το μοντέλο μπορεί να δεχθεί διαφόρων τύπων κριτήρια διαρροής και νόμους κράτυνσης. Έτσι, διατυπώνονται οι εξελικτικές εξισώσεις Bouc-Wen που επιτρέπουν την προσομοίωση ισοτροπικής, κινηματικής και μικτής κράτυνσης καθώς και απομειώσεις αντοχής και δυσκαμψίας.

Η μέθοδος του Δικτύου Στερεών Σωμάτων και Ελατηρίων επεκτείνεται με τη ενσωμάτωση των υστερητικών μοντέλων σε επίπεδο στοιχείου. Τόσο οι γραμμικές

διαφορικές εξισώσεις κίνησης όσο και οι μη γραμμικές υστερητικές εξισώσεις επιλύονται ταυτόχρονα. Αυτό επιτυγχάνεται με τη μετατροπή του συστήματος σε μορφή χώρου κατάστασης. Για κάθε στοιχείο μορφώνεται το υστερητικό μητρώο και με τη μέθοδο άμεσης δυσκαμψίας το υστερητικό μητρώο της κατασκευής. Αυτό έχει ως αποτέλεσμα την εύκολη ενσωμάτωση του προτεινόμενου μοντέλου σε υπάρχοντες κώδικες του Δικτύου Στερεών Σωμάτων και Ελατηρίων με τη διαμόρφωση του υστερητικού μητρώου της κατασκευής και τη διατύπωση των εξελικτικών υστερητικών εξισώσεων. Παρουσιάζονται αριθμητικά παραδείγματα και εφαρμογές που αναδεικνύουν την ικανότητα του μοντέλου να προσομοιώνει ένα πλήθος υστερητικών συμπεριφορών. Διαμορφώνεται έτσι ένα άμεσο φυσικό μοντέλο που εμπεριέχει τα κύρια χαρακτηριστικά υστερητικών συστημάτων για δισδιάστατα προβλήματα. Αυτό, δίνει τη δυνατότητα κατά τη διάρκεια του σχεδιασμού, για τη μελέτη της υστερητικής συμπεριφοράς διαφόρων κατασκευών, τον εντοπισμό περιοχών ενδιαφέροντος σχετικά με την πλαστικότητα και τον ακριβή υπολογισμό της παραμορφωμένης κατάστασης της κατασκευής.

Στη συνέχεια εξετάζεται η Μέθοδος Υλικού Σημείου, σε μη πεπλεγμένη μορφή για την προσομοίωση δυναμικών προβλημάτων, σε υλικά που συμπεριφέρονται ανελαστικά. Η διατύπωση λαμβάνει υπόψη την ομαλή μετάβαση από την ελαστική στη μετελαστική περιοχή και εμπεριέχει ισοτροπική, κινηματική και μικτή κράτυνση καθώς και απομειώσεις αντοχής και δυσκαμψίας. Η διατύπωση αφορά κάθε υλικό σημείο μορφώνοντας το εφαπτομενικό μητρώο που συσχετίζει τις συνιστώσες των τάσεων και ομαλοποιεί τη συμπεριφορά. Η επίλυση των εξισώσεων γίνεται σε μη πεπλεγμένη μορφή, και τα αριθμητικά αποτελέσματα δείχνουν ότι μπορεί να χρησιμοποιηθεί αποτελεσματικά χωρίς την ανάγκη για έναν αλγόριθμο πρόβλεψης-διόρθωσης ή ακτινικής επιστροφής. Επιπρόσθετα το σφάλμα μειώνεται όσο πιο ομαλή γίνεται η μετάβαση από την ελαστική στην πλαστική περιοχή. Παρουσιάζονται επίσης παραδείγματα και αριθμητικές εφαρμογές, και τα αποτελέσματα συγκρίνονται με πειραματικά δεδομένα, αποτελέσματα

από κώδικες Πεπερασμένων Στοιχείων καθώς και από άλλες αριθμητικές μεθόδους χωρίς πλέγμα, επαληθεύοντας την ικανότητα του μοντέλου να προσομοιώσει υστερητικές συμπεριφορές. Τέλος, ο υπολογισμός του εφαπτομενικού μητρώου γίνεται για κάθε υλικό σημείο ξεχωριστά και συνεπώς η μέθοδος είναι κατάλληλη για το σύγχρονο μαζικό παράλληλο προγραμματισμό. Στον Πίνακα 3 παρουσιάζεται εποπτικά η σύγκριση μεταξύ των δύο μεθόδων της διατριβής.

	Επιλύτης	**Ακρίβεια μετατοπίσεων**	**Ακρίβεια τάσεων**	**Εξάρτηση από τη διακριτοποίηση**	**Ευκολία διακριτοποίησης**
ΔΣΣΕ	Πεπλεγμένη	✓✓✓	✓	✓	✓✓
ΜΥΣ	Μη-πεπλεγμένη	✓✓✓	✓✓✓	✓✓	✓✓✓

Πίνακας 3: Σύγκριση των δύο διακριτών μεθόδων

Ορισμένες προτάσεις για μελλοντική έρευνα είναι:

1. Επέκταση του Δικτύου Στερεών Σωμάτων και Ελατηρίων με νόμους θραύσης που βασίζονται σε ενεργειακές θεωρήσεις τόσο για μονοτονικές όσο και για κυκλικές φορτίσεις.
2. Ένα ενδιαφέρον σημείο μελλοντικής έρευνας θα μπορούσε να είναι η ενσωμάτωση ομαλών προσομοιωμάτων για την περίπτωση της βισκοπλαστικότητας (πλαστικότητα εξαρτώμενη του ρυθμού μεταβολής).
3. Ενσωμάτωση νόμων θεωρίας Βλαβών και ομαλοποίησή τους, για τη προσομοίωση της πλαστικής συμπεριφοράς με χαλάρωση (softening).
4. Ανάπτυξη μοντέλου θεωρίας Βλαβών για τη Μέθοδο υλικού Σημείου, που να μην επηρεάζεται από την ανάλυση του πλέγματος.
5. Κατά την ανάλυση επιμήκων μελών, και χρησιμοποιώντας τετραγωνικό πλέγμα, ο αριθμός των στοιχείων κατά μήκος του μέλους είναι πολύ μεγαλύτερος από τα στοιχεία στην κάθετη στον άξονα του μέλους διεύθυνση. Αυτό οδηγεί σε

μεγάλους υπολογιστικούς χρόνους για την επίτευξη ικανοποιητικής ακρίβειας. Για το σκοπό αυτό θα ήταν ενδιαφέρουσα η ενσωμάτωση στοιχείων δοκού στη Μέθοδο Υλικού Σημείου, τόσο για τη μοντελοποίηση δοκών όσο και για τη μοντελοποίηση οπλισμού.

Dedicated to my parents,

Maria and Dimitris

COMMITTEES

DISCRETE SYSTEMS IN THE ELASTO-PLASTIC ANALYSIS OF STRUCTURES

DOCTORAL DISSERTATION

For the title of Doctor of Philosophy in Engineering submitted in the School of Civil Engineering, National Technical University of Athens

Christos D. Sofianos

ADVISORY COMMITTEE	EXAMINATION COMMITTEE
1. Vlasis Koumousis *Em. Professor N.T.U.A.* *(Supervisor)*	1. Vlasis Koumousis *Em. Professor N.T.U.A.* *(Supervisor)*
2. Evangelos Sapountzakis *Professor N.T.U.A.*	2. Evangelos Sapountzakis *Professor N.T.U.A.*
3. Nikos Lagaros *Assoc. Professor N.T.U.A.*	3. Nikos Lagaros *Assoc. Professor N.T.U.A.*
	4. Charis Gantes *Professor N.T.U.A.*
	5. Christofer Provatidis *Professor N.T.U.A.*
	6. Konstantinos Spiliopoulos *Professor N.T.U.A*
	7. Savvas Triantafyllou *Asst. Professor N.T.U.A.*

ABSTRACT

Hysteresis is a highly nonlinear phenomenon and can be found in many scientific fields. A system is considered to be hysteretic when its state depends not only on its current configuration but also on its history. This is especially true in inelastic – plastic materials, where the current deformation depends on the complete history of the loading of the material. Hysteretic models have been widely applied within the Finite Element Method while little research has been carried out in discrete and particle methods, which is in contrast with their nature since the tracking of history dependent materials is innate in most of these methods. In this work smooth hysteretic models of Bouc – Wen type have been applied in two discrete methods, the Rigid Body Spring Network (RBSN) and the Material Point Method (MPM). The strains are decomposed into an elastic and an inelastic part according to the additive decomposition of the strain tensor of classical plasticity. Two Heaviside-type functions are introduced to account for the different phases of a hysteretic cycle and a smooth transition from the elastic to inelastic regime. These act as switches and can accommodate various yield functions and hardening laws to control the entire cyclic behavior. A single expression is established for the plastic multiplier for the entire stress space. This overcomes the need for a piecewise linear approach and a demanding bookkeeping mechanism especially when multilinear models are concerned that account for stiffness and strength degradation.

The RBSN is based on a physical model rather than a mathematical one, such as to divide the structure into discrete rigid bodies that are connected with springs. Discretization is based on Voronoi tessellation, dividing the structure into convex polygons, which are treated as rigid bodies. Voronoi tessellation is used to ensure uniformity. The rigid bodies are connected with three zero length springs (normal, tangential and rotational) located at the middle of their common facets. The springs follow the smooth hysteretic Bouc–Wen

model, which efficiently incorporates classical plasticity. Numerical results are presented that validate the proposed formulation and verify the model's applicability on determining primarily the displacement field and areas of plastic zones. Moreover, the model is extended by incorporating a Mohr-Coulomb type of stress law to simulate fracture during monotonic loading, and by releasing the stiffness of the spring elements that have ruptured. Even though the formulation is not based on fracture energy calculations or variational formulations, it is capable of identifying areas of fracture and crack paths, through its discrete nature.

The Material Point Method (MPM) is a hybrid method that employs both a Lagrangian and an Eulerian description. In MPM, all the information and state variables are carried by the particles (such as position, mass, velocity, acceleration, stress, strains, etc.). This presents a significant advantage in the simulation of history dependent materials. Moreover, the MPM is based on a weak form formulation being consistent with the FEM. In this work, the standard explicit MPM is extended to account for smooth elastoplastic material behavior with mixed isotropic and kinematic hardening and stiffness and strength degradation. The final form of the constitutive stress rate–strain rate relation incorporates the tangent modulus, which now includes the Heaviside functions and gathers all the governing behavior, facilitating considerably the simulation of nonlinear response in the MPM framework.

ACKNOWLEDGEMENTS

I would like to express my most sincere gratitude to my advisor, Emeritus Professor Vlasis Koumousis. He has been a valuable guide and an example throughout the course of this research. He is a source of inspiration both in terms of his scientific accomplishments as well as his character and integrity, and his contribution extends beyond his academic roles.

I would also like to thank Professor Evangelos Sapountzakis and Associate Professor Nikos Lagaros for serving on my supervising committee and for being ever available for consultation as well as for their lessons taught at the Department of Civil Engineering of the National Technical University of Athens.

Special thanks are also due to Professor Charis Gantes, Professor Christofer Provatidis, Professor Konstantinos Spiliopoulos and Assistant Professor Savvas Triantafyllou for serving on the defense committee of my dissertation.

Most of all, I would like to thank my parents Maria and Dimitris. This work would not have been accomplished without their selfless support, continuous encouragement and love.

CONTENTS

LIST OF TABLES

LIST OF FIGURES

LIST OF ABBREVIATIONS AND ACRONYMS

Abbreviation	Description
MPM	Material Point Method
FEM	Finite Element Method
RBSN	Rigid Body Spring Network
VM	Von Mises
sdof	single degree of freedom
PIC	Particle In Cell
FLIP	Fluid Implicit Particle
FDM	Finite Difference Method
PDE	Partial Differential Equation
MUSL	Modified Update Stress Last
USF	Update Stress First
USL	Update Stress Last
GIMP	Generalized Interpolation Material Point
CPDI	Convected Particle Domain Integrator
CFL	Courant–Friedrichs–Lewy
DDMPM	Dual Domain Material Point Method
BSMPM	B-Spline Material Point Method
SPH	Smoothed Particle Hydrodynamics
DEM	Discrete Element Method
HELP	Hydrodynamic Elastic Plastic
ALE	Arbitrary Lagrangian - Eulerian
IBM	Immersed Boundary Method
FDM	Fictitious Domain Method
LSM	Lattice Spring Models

FVM	Finite Volume Method
LBM	Lattice Boltzmann Method
CA	Cellular Automata
MTS	Maximum Tangential Stress
MSED	Minimum Strain Energy Density
MERR	Maximum Energy Release Rate

LIST OF APPENDICES

1 INTRODUCTION

1.1 Problem statement

Numerical methods have become over the last years a new pillar in engineering. After theory and experiments, numerical analysis provides an effective way to seek solutions to complex problems. In fact, there are cases where the existing theories cannot provide analytical solutions neither is it possible to perform experiments. Especially in design problems, numerical methods provide the means to model complex geometries, simulate nonlinear material behaviors etc., for which conventional methods are not capable of providing answers. This begins with the formulation of the mathematical model and ends with the solution of the governing equations. Therefore, the term modeling implies the representation of a physical system through a mathematical interpretation, whereas simulation refers to the process of solving the equations that resulted from model development [7, 25]. Numerical methods can be categorized based on the frame of reference they employ, whether they represent the material discretely or as a continuum and whether the analysis is linear or nonlinear.

1.1.1 Frames of reference

Numerical methods are divided into four main categories based on how they describe motion and deformation. These are the Lagrangian methods, the Eulerian methods, hybrid methods and meshfree methods. The advantages and disadvantages of these methods are presented in detail below, together with a brief summary in Table 1-1.

In Lagrangian methods the material and the mesh are firmly linked. Individual elements are connected through the mesh, which is a topological map. The mass of each element is constant during the computations, and its volume varies as it deforms. Lagrangian methods are simpler than Eulerian methods in the sense that there is no advection term in the governing equations, since there is no flow of material between element boundaries.

In addition, interfaces can be easily defined and tracked since they coincide with element boundaries. The most notable method in this category is the Finite Element Method (FEM) [12, 15]. The Rigid Body-Spring Network (RBSM) [77] also belongs in this category and is one of the methods used in this thesis. It was formulated as a numerical model in the context of limit analysis in plasticity. The structure is discretized into rigid bodies that are connected by normal, tangential and rotational springs. Similar to FEM, element stiffness matrices are formed, and a connectivity matrix is employed.

In the Eulerian description the mesh is stationary and does not move or deform. This has the evident advantage that the problem of element distortion is alleviated. The material carries physical properties such as mass and momentum and is allowed to move between element boundaries. This gives rise to an advection term in the governing equations rendering them more computationally expensive as compared to Lagrangian methods. In these methods, the volume of the element remains constant and its density changes with time. The Finite Volume Method (FVM) is an Eulerian method applied to fluid simulations where the flow of the material is observed through a fixed mesh in space. The lattice Boltzmann method (LBM) [34] and cellular automata (CA) [2, 102] are notable examples of Eulerian descriptions for the flow of discrete objects. The main difference between the two approaches is that in a Lagrangian (or material) approach, the positions of specific material points are tracked with time; while on an Eulerian (or spatial) approach, the flow through fixed points in space, is measured.

Hybrid Methods. There have been several attempts to formulate new methods to take advantage of the positive features of both the Lagrangian and Eulerian methods. These methods are termed as Hybrid methods. One such method is the Arbitrary Lagrangian – Eulerian method (ALE) that has been applied in Finite Difference (FD) [55] and Finite Element context [43]. Another popular method especially in fluid mechanics is the Particle In Cell (PIC) method [65, 64]. In this method the material is discretized into

particles using the Lagrangian description and carrying some of its properties. An Eulerian mesh is also employed but is reset to its initial configuration at the end of each time step. The method is not purely Lagrangian because some properties are still stored in the background grid. In Fluid Implicit Particle method (FLIP) [23], an extension of PIC, the particles carry all of the properties. This way numerical diffusion, which is present in PIC is eliminated. PIC and FLIP are the precursors of the Material Point Method (MPM) [120] that is the second method used in this thesis. In MPM, contrary to FLIP, the strain and stresses are carried by the material points, while in FLIP they are stored at the cell centers. This allows for the effective simulation of history dependent materials. In addition, the MPM is formulated on the basis of the weak form, like FEM. The MPM employs the two main formulations previously developed in PIC i.e., the use of Lagrangian material points that carry all the physical information, and a background Eulerian grid used for the discretization of continuous fields and gradient calculations. Therefore, the MPM combines the advantages of both Eulerian and Lagrangian methods

	Method	**Advantages**	**Disadvantages**
Lagrangian	FEM	+Simpler to conceptualize +Easy imposition of boundary conditions +Easier to implement history dependent materials	-Element distortion -Time steps in explicit schemes could approach zero
	RBSN		
Eulerian	HELP	+No element distortion	-Don’t explicitly track the position of material -Don’t follow moving boundaries
	IBM		
	FDM		
	FVM		
Hybrid	ALE	+No element distortion +Mesh can be move or be fixed +Higher resolution than Eulerian	-Convective terms still present -Higher computational cost
	MPM		
	PIC		
	FLIP		
Meshfree	SPH	+Can handle large deformations +Ease of refinement	-Usually higher computational cost
	DEM		

Table 1-1: Spatial discretization methodologies

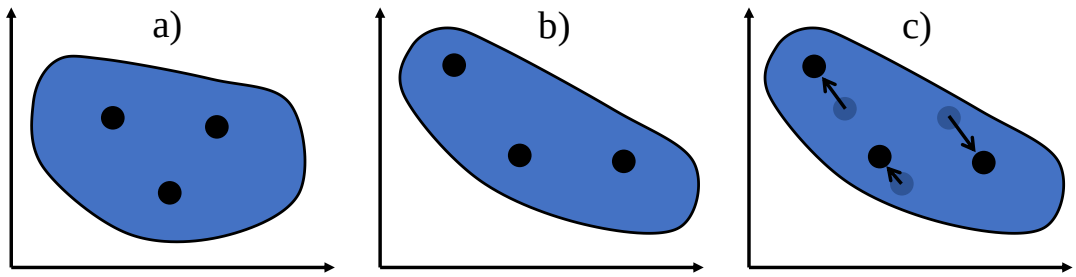

Figure 1.1: a) Reference configuration, b) Lagrangian description, c) Eulerian description

Meshfree Methods. This category includes methods that in general do not employ a mesh but are based on the interaction between neighbor particles. They can simulate challenging problems such as crack propagation, fragmentation and localization problems. They can handle large deformations and use local refinement if a higher accuracy is needed. However, in general the computational cost of these methods is higher. Some examples in this category are the Discrete Element Method DEM [40] and the Smoothed Particle Hydrodynamics [86, 58]. The difference of Lagrangian and Eulerian description from a kinematic standpoint can be seen in Figure 1.1.

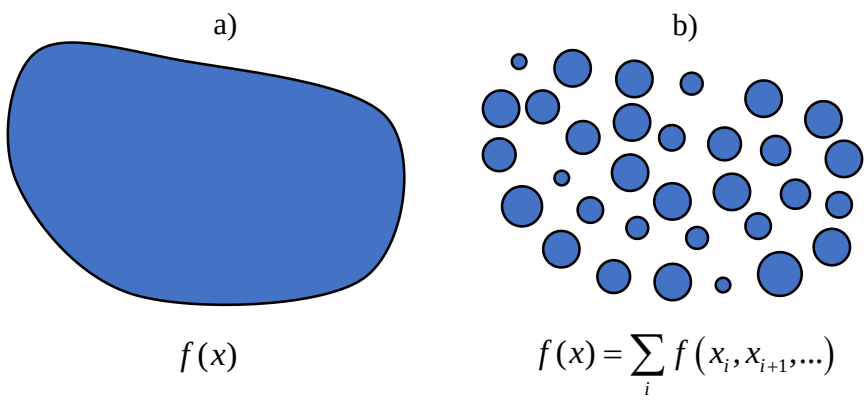

Figure 1.2: Continuum vs discrete

1.1.2 Continuum - discrete

In addition to the method used to describe motion and deformation, another key categorization of the numerical methods is by considering the way the material is being

modelled. The material can be regarded either as a continuum or as a set of discrete objects interacting with each other (Figure 1.2). In the continuum, the constitutive law that describes its behavior is valid within the whole domain and is described by a partial differential equation (PDE) in most engineering problems. On the contrary, in discrete systems there are discrete elements or particles interacting with their surrounding particles. The effect on each particle is the sum of all the interactions with other particles.

		Kinematics	
		Lagrangian	Eulerian
Constitutive topology	Continuous	FEM	FVM
	Discrete	MPM	
		RBSN	CA

Table 1-2: Kinematics and topology categorization of numerical methods

In this thesis the RBSN and MPM methods are employed and examined. Although they are different in their theoretical development, they fall into the category of discrete methods. In RBSN there are discrete rigid particles interconnected with springs while in MPM there are discrete material points that carry all the physical properties of the material.

1.1.3 Linear – nonlinear analyses

So far, the various formulations for kinematic descriptions and continuum or discrete modelling have been addressed. Another aspect refers to the structural analysis, which can be mathematically either linear or nonlinear. The common types of nonlinearities in structural analysis are:

- Material nonlinearities. The stress-strain law may be nonlinear elastic or inelastic, where permanent deformation is manifested upon unloading.
- Nonlinear deformations. To account for large deformations equilibrium is established at the deformed configuration. They can be divided to large

displacements and rotations with small strains, or large displacements and rotations with finite strains. Different strain and stress measures are employed in each case.

- Nonlinearity in Boundary Conditions. Nonlinear support conditions or structures in contact are few examples.

Considering material behavior, the theory of linear elasticity [82] is able to accurately predict the behavior of a material that returns to its initial configuration after the loads are removed. However, most materials exhibit permanent deformations after a certain level of loading is surpassed. These permanent deformations involve the dissipation of energy and therefore cannot be retrieved and are irreversible. The actual dissipative mechanisms are manifested in the molecular and atomic level and are studied through a micromechanical approach [89]. In order to circumvent these actual mechanisms in the atomic level and facilitate the study of nonlinearities at the mesoscale, the phenomenological approach to irreversible processes is developed.

The phenomenological approach is based on internal variables that are associated with the dissipative behavior in microstructure. Some examples of these internal variables are the plastic strains for plasticity or the damage variable for damage theories. Hysteresis is a basic attribute of the dissipation process in solid mechanics and can be studied from a phenomenological point of view. A system is hysteretic when its behavior depends not only on its current state but also on the history of its previous states. There have been several hysteretic models proposed through the years and can be divided into two main categories: the multi segmental linear models and the smooth hysteretic models. The multilinear models are divided into linear segments to account for the different stages of hysteretic phenomena (cyclic behavior, degradations, pinching). Although simpler in their derivation, they require a demanding bookkeeping mechanism, rendering them impractical. Smooth hysteretic models try to encapsulate the entire hysteretic behavior

through a set of nonlinear equations, often expressed in rate form. All the different stages of cyclic phenomena like stiffness degradation, strength deterioration or hardening/softening behavior is incorporated into a single smooth model with varying parameters.

In this section, a general overview of numerical methods in engineering, hysteresis and discrete methods has been presented. More information about the state-of-the-art research on each particular topic is provided in the respective chapter in order to facilitate its presentation.

1.2 Research objectives

The overarching aim of this research to develop an efficient and robust simulation framework for the analysis of the inelastic - hysteretic response of structures. In order to achieve this, the following Research Objectives are identified:

- R.O.1: Formulate the hysteretic Bouc – Wen model in its uniaxial and triaxial form. Extend it to account for stiffness degradation and strength deterioration. Verify it against experimental and published results.
- R.O.2: Implement the Bouc – Wen hysteretic model in the Rigid Body Spring Network framework. Extend the framework with plasticity and fracture for monotonic loading. Examine the effectiveness and accuracy of the proposed methodology in simulating hysteretic phenomena up to the point of fracture and compare against published results.
- R.O.3: Implement the Bouc – Wen hysteretic model in the Material Point Method incorporating stiffness degradation and strength deterioration. Compare basic linear shape functions with higher order ones both with regard to their accuracy in velocity gradient calculations as well as when plasticity is concerned. Examine

the effectiveness and accuracy of the proposed methodology in accurately describing hysteretic behavior with and without degradations. Compare against published data and experimental results.

- R.O.4: Compare the two methodologies and identify their advantages as well as their weak points.

1.3 Methodology

In order to accomplish the Research Objectives, the research has been divided into the following tasks. All computer codes were developed for the purpose of this research. The software used is Matlab for its ease in rapid code generation and benchmarking. In Figure 1.3 the methodology of the research is briefly presented.

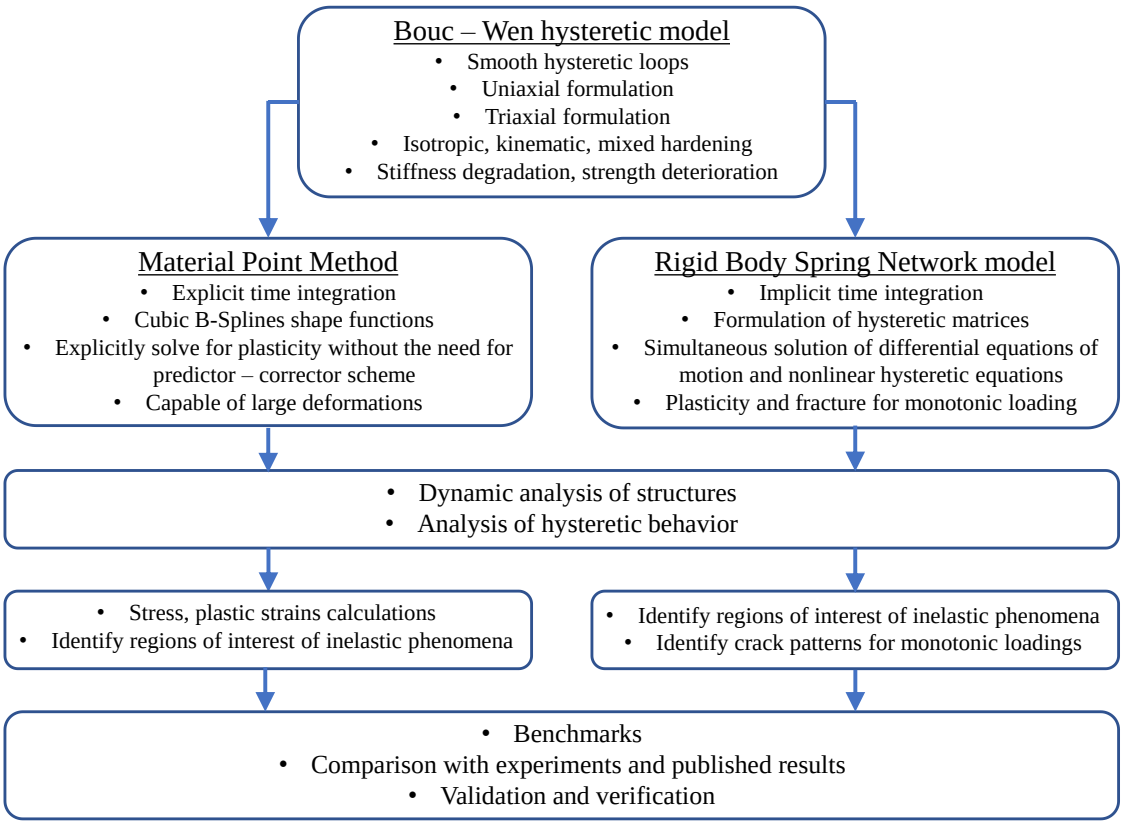

Figure 1.3: Research methodology

- Task 1: Development of the Bouc – Wen model with an in-house computer code. Formulation of the uniaxial model and incorporation of stiffness and strength degradation. Investigation of the model parameters and the hysteretic behaviors it can simulate.
- Task 2: Development of the triaxial Bouc – Wen model with an in-house computer code. Incorporate stiffness degradation and strength deterioration for the general triaxial case.
- Task 3: Development of an in-house computer code for the Rigid Body Spring Network model. Investigation of its properties. Solutions both for the elastic – static case as well as the case of hysteresis with dynamic loading. Access the developed model's ability to effectively identify regions of interest with regard to plastic phenomena as well as crack patterns.
- Task 4: Incorporation of Bouc-Wen hysteretic model in the Rigid Body Spring Network framework. Examination of its behavior, and formulation of an efficient solution process for the differential equations in their matrix form.
- Task 5: Incorporation of a fracture criterion into the model for the simulation of plasticity and fracture during monotonic loading.
- Task 6: Development of an in-house computer code for the Material Point Method in an explicit time integration scheme. Exploration of the most suited shape function choice for plasticity. Examination of its capability in simulating hysteretic behavior for dynamic loading. Examination of its ability in solving for plasticity in an explicit time integration algorithm.
- Task 7: Comparison of the two methods and assessment of their advantages and disadvantages.

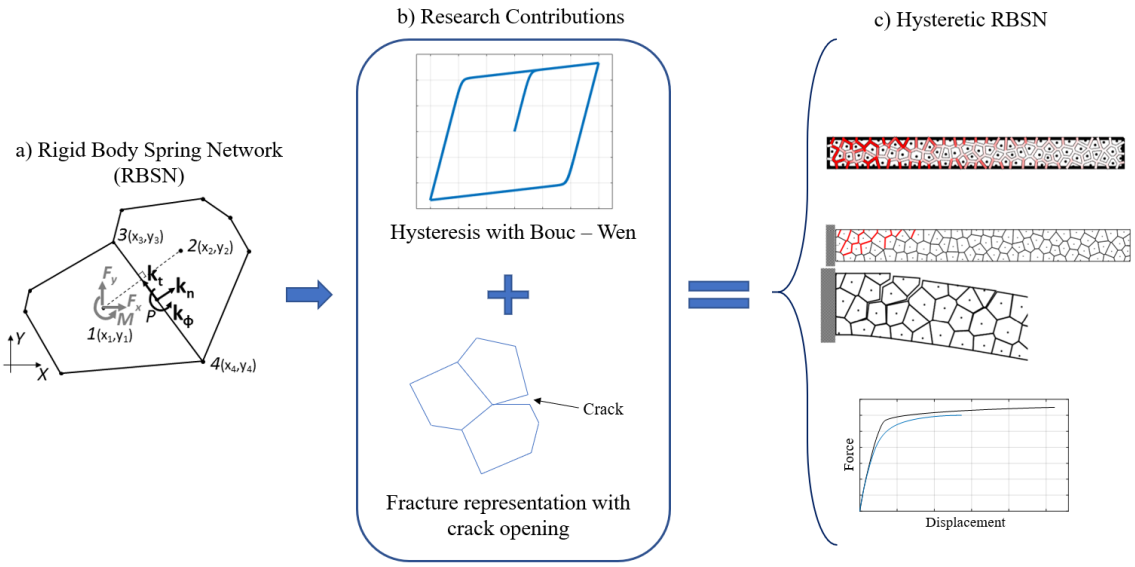

Figure 1.4: Development methodology for the hysteretic RBSN model with fracture

Figure 1.4 and Figure 1.5 depict the development methodology of the two hysteretic discrete models of RBSN and MPM and the research contributions in those areas in a visual representation.

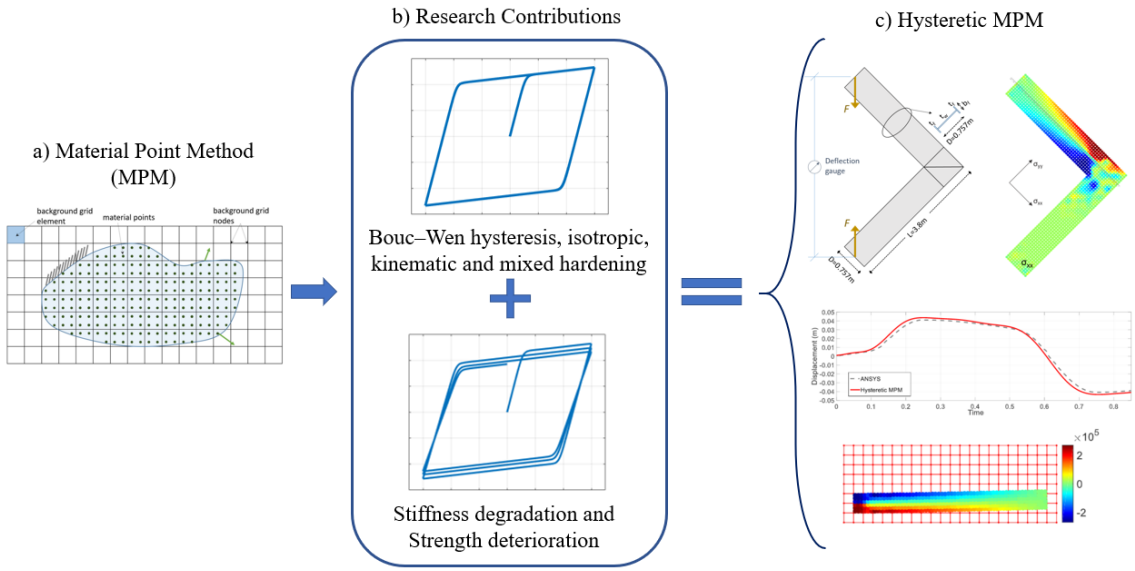

Figure 1.5: Development methodology for the hysteretic MPM model with degradations

1.4 Outline

This thesis is organized in six chapters. In Chapter 2 the development of the Bouc – Wen hysteretic model is presented. Starting from a phenomenological approach to hysteresis and a simple mechanical analogue, the mathematical theory and differential equations describing hysteretic behavior are formulated. The main parameters that govern the shape of the hysteretic loops are explored. The model is extended into the three – dimensional stress space, following the foundations of classical plasticity theory. Moreover, stiffness degradation and strength deterioration are incorporated into the model, with the addition of two parameters. For the general triaxial case, the formulation leads to an additional evolution equation for the degradations, rendering the proposed method compact in its solution.

In Chapter 3 the first discrete model that is examined in this dissertation, the Rigid Body Spring Network model, is presented. The model is based on a physical concept rather than a mathematical one, mainly in that it divides the structure into rigid bodies that are connected with springs. It falls into the general category of Lattice models. In order to model the elastic properties of the continuum properly a random initial distribution of points is chosen. Using the Voronoi diagram and dividing the domain into convex polygons the basis of the model is formulated. These Voronoi polygons form the rigid bodies of the model and are interconnected with springs. In this work, these springs behave following the Bouc – Wen hysteretic model.

In Chapter 4 the Material Point Method (MPM) for the hysteretic analysis of structures is developed. Starting from a brief theory of continuum mechanics, the final form of the governing equations of motion are derived. In order to solve these equations, the weak form is derived, and the Material Point Method is established. The main algorithm of the MPM is developed in an explicit time integration scheme. The method renders itself to

different implementation choices and different formulations, which are investigated in this work. Similar to Finite Element Method the MPM uses shape functions. Linear and B-Spline shape functions are examined and compared regarding their accuracy and efficiency. The general triaxial Bouc – Wen model with stiffness degradation and strength deterioration is incorporated into the method making it efficient in simulating a wide range of hysteretic behavior.

In Chapter 5 numerical examples both for the RBSN model and the MPM are presented. These range from simple one – dimensional (1D) examples to verify and validate the formulation and computer implementations, to more complex examples examining the behavior of structures in cyclic loading and yield.

Finally, in Chapter 6 some conclusions and remarks are provided, with further suggestions for future work. Three appendices are included. Appendix 1 involves the Von Mises yield criterion and its gradient. Appendix 2 presents Drucker and Il'iyshin's plasticity postulates. Appendix 3 presents some basic elements of continuum mechanics concerning the deformation gradient employed in MPM.

2 BOUC – WEN HYSTERETIC MODEL

2.1 Introduction

A first approximation to material behavior begins with the theory of linear elasticity. This theory is robust and can provide accurate results provided no permanent deformations develop. However, after some level of loading, materials start to behave in a nonlinear manner. This nonlinear material behavior is usually mathematically tackled through a constitutive nonlinear equation. In general, many phenomena manifest material nonlinearity, among these are:

- Viscoplasticity (Rate Dependent plasticity) [28, 78]. Permanent deformations are manifested.
- Rate Independent plasticity [116, 22, 132]. Behavior is the same regardless of the rate of the applied loads.
- Thermo – plasticity [101]. The material is loaded so that not only plastic strains develop but also the temperature is changed.
- Non – linear elasticity [13]. In this case the stresses are not linearly related to strains, but deformation is recoverable. The system is conservative and does not lose any energy. An example of such case is the hyper-elastic behavior.
- Creep. Nonlinear phenomenon that is rate dependent. Permanent deformation under constant stresses.
- Stress relaxation. Decrease of stresses under constant strain conditions.

Two examples of nonlinear stress – strain diagrams are presented in Figure 2.1, i.e. the case of nonlinear elasticity and elastoplasticity. In this work, the Bouc – Wen model that is employed, falls into the category of rate – independent plasticity. A vast majority of engineering materials exhibit elastoplastic behavior. This means that while for the initial elastic region any strain is recoverable, after a certain level of stress, the yield stress, material undergoes plastic deformations. Plastic strains are not recoverable, the system is

not conservative, and the current configuration is path dependent. This can be seen as analogous to classical thermodynamics [3], where a process is irreversible if it exhibits hysteresis.

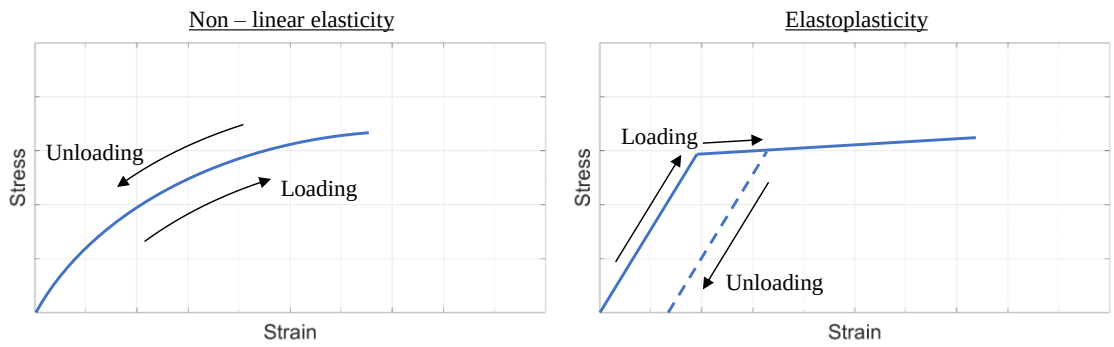

Figure 2.1: Nonlinear stress – strain behavior.

Hysteresis is a highly nonlinear phenomenon and can be found in many scientific fields. A system is considered to be hysteretic when the state of the system depends not only on its current state but on its history. This is especially true in inelastic – plastic materials, where the current deformation depends on the complete history of the loading. On the contrary, in elastic materials the state of strain depends only on the final state of stress.

Over the last decades, there has been significant development of mathematical hysteretic models especially in the phenomenological approach of hysteresis. These models started with the work of Massing [91] and Preisach [104] and became popular more recently through the work of Bouc [22] and Wen [132, 133]. Some notable modifications and extensions have been proposed since then, such as the Baber – Noori model [8] and the Sivaselvan – Reinhorn model [115]. A common characteristic of the aforementioned models is that they are smooth hysteretic models. They are capable of simulating a vast range of hysteretic and plastic behavior through a single smooth hysteretic function. This is a great improvement over the multi – segmental models that demand a complicated bookkeeping mechanism and model the behavior with many linear segments.

In the past decades, the smooth hysteretic model of Bouc-Wen has been widely utilized. Hysteretic models incorporating stiffness degradation, strength deterioration, and pinching phenomena have been effective in simulating the real behavior of various materials such as reinforced concrete, steel and wood (Foliente [54], Sivaselvan and Reinhorn [115]). Some deficiencies and inconsistencies of the Bouc-Wen model regarding displacement drifts, thermodynamic admissibility etc., have been identified (Thyagarajan and Iwan [122], Erlicher and Bursi [51]) whereas recovering of the violation of plasticity postulates (Charalampakis and Koumousis [32]) has been recently tackled [26]. In addition, it has been successfully applied to model hysteretic behavior in plane stress [125], shell [94], plate [93] and beam [128] Finite Elements [127], as well as to model RC flexural failure employing a fiber approach [59]. It has also been applied successfully in the dynamic analysis of composite materials [124] using a multiscale formulation.

The Bouc-Wen model introduces internal variables that are governed by evolution equations. These are expressed in rate form and are derived from the endochronic theories of plasticity (Valanis [129]) expressing the phenomenological behavior at the elemental level. Many researchers [36, 72] have employed the Bouc-Wen model as a robust and accurate method to simulate the hysteretic behavior of various materials. Moreover, efficient algorithms were developed for the identification of the Bouc-Wen model parameters [84, 112, 136, 30], using advanced analytical techniques (Chatzi and Smyth [33]) or evolutionary identification approaches (Charalampakis and Koumousis [31]).

2.2 The hysteretic loops and the concept of hysteresis

In Figure 2.2, a single degree of freedom (s.d.o.f.) oscillator is presented, consisting of a mass and a spring. The material behavior, considering stresses and strains, is considered to be elastic – perfectly plastic and the yield stress is σ_y .

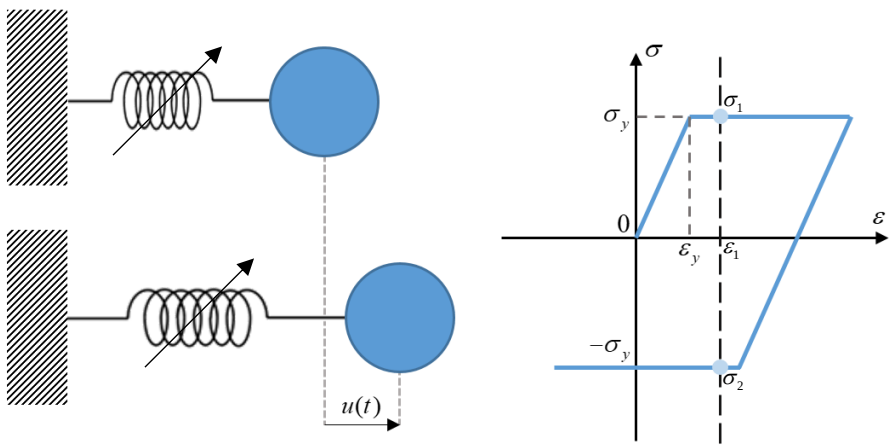

Figure 2.2: Single degree of freedom (s.d.o.f) oscillator and cyclic material behavior.

Initially, when the oscillator is first being loaded, its response is linear, and the material behavior is following Hooke's law. The response remains linear as long as the stresses are smaller than the yield stress. This can be written mathematically as:

$$\sigma(\varepsilon) = E\varepsilon \qquad |\sigma| \le \sigma_y \tag{2.1}$$

where E is the material Young's modulus. With further loading and increase of strains, stresses approach the yield stress and remain at the yield stress for all strains exciding the yield strain ε_y (since there is no hardening considered). This can be formulated as:

$$\sigma(\varepsilon) = \sigma_y \qquad |\varepsilon| > \varepsilon_y \tag{2.2}$$

After this point, when considering cyclic behavior, unloading occurs (where the unloading branch is parallel to the initial elastic one) and reloading at the other direction

until new yielding. This leads to the following observation: For a given level of stain larger than the yield strain (marked as ε_1 in Figure 2.2), there are at least two possible stress states in the range: $\sigma \in \left[-\sigma_y, \sigma_y\right]$ (marked as σ_1 and σ_2 in Figure 2.2). Consequently, there does not exist a function $\sigma(\varepsilon)$ that can uniquely map the current level of strain to the current level of stress.

Hysteresis, through its mathematical foundation and theory, tries to define an output function for the stresses that has the strains as a given input function, in such a way as the derived solution coincides with the stress-strain curve presented in Figure 2.2.

2.3 The uniaxial Bouc – Wen model

In this paragraph the uniaxial Bouc-Wen hysteretic model is presented. Through the explanation of the mathematical theory and its mechanical analogue, the properties and expected behavior of the model can be explained. As previously mentioned, it is a smooth hysteretic model and its mathematical description for a s.d.o.f. dynamic system is as follows:

$$\begin{cases} m\ddot{u} + c\dot{u} + F^{BW} = p \\ F^{BW} = F^{el} + F^{pl} = aku + \left(1-a\right)kz \\ \dot{z} = \dot{u}\left[1 - \left|\dfrac{z}{z_y}\right|^n \left(\beta + \gamma \operatorname{sgn}\left(z\dot{u}\right)\right)\right] \end{cases} \tag{2.3}$$

where m is the mass of the system, c is the damping coefficient, p is the external force acting on the system, F^{BW} is the Bouc-Wen restoring force, z is the introduced hysteretic displacement parameter with $\dot{z}$ being its derivative with respect to time, sgn is the signum function, n, β, γ are parameters that control the shape of the hysteretic loops, u is the systems displacement, $\dot{u}$ its velocity, $\ddot{u}$ its acceleration and a is the ratio of the

post yield stiffness k_{pl} to the initial elastic stiffness k:

$$a = \frac{k_{pl}}{k} \tag{2.4}$$

The model is based on a first order nonlinear differential equation with respect to z i.e. the hysteretic parameter. For a s.d.o.f. system the restoring force consists of an elastic F^{el} and an inelastic hysteretic F^{pl} part as:

$$F = F^{el} + F^{pl} = F_y \left[a\frac{u}{u_y} + (1-a)\frac{z}{u_y} \right] = \alpha ku + (1-\alpha)kz \tag{2.5}$$

The mechanical analogue of the Bouc Wen formulation can be visualized as two elements connected in parallel, one being linear with reduced stifness ak and the other nonlinear as presented in Figure 2.3.

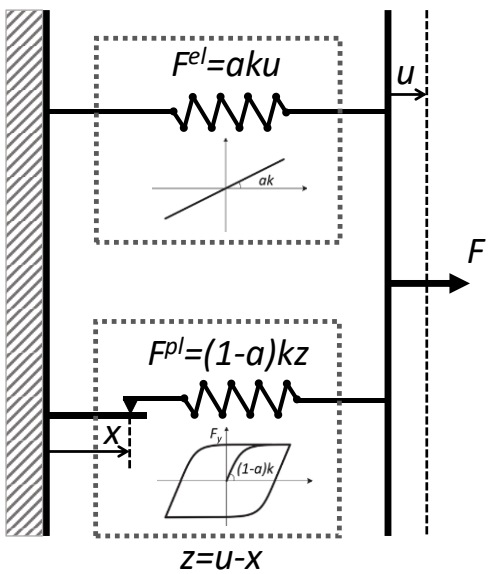

Figure 2.3: Bouc-Wen parallel model mechanical analogue.

The initial stifness of the nonlinear element is $(1-a)k$, the yield force is F_y and the element consists of a linear spring and a slider that are connected in series. If the force acting on the system is smaller than F_y then the system behaves elastically with stifness k since the elastic stifness of the two parallel springs is ak and $(1-a)k$. On the other

hand if the system force exceeds the yield force then the nonlinear spring force remains constant and equal to F_y and the linear spring provides the additional hardening with a slope of the hardening branch given by parameter a.

Similalry, if the force acting on the system is smaller than the yield force then no sliding occurs $x = 0$ and the relative displacement of the nonlinear element is equal to the total displacement u. When the yield force is reached sliding occurs and the relative displacement of the nonlinear spring in the second element remains constant. This means that the following relation holds regarding the hysteretic parameter z:

$$z = \begin{cases} u, & x \le x_y \\ z_y, & x > x_y \end{cases} \tag{2.6}$$

However x is an internal variable and is not easy or even possible to be identified in most systems. For this reason, instead of the relative displacement, the total displacement at which the sliding occurs can be used:

$$z = \begin{cases} u, & u \le u_y \\ u_y, & u > u_y \end{cases} \tag{2.7}$$

The corresponding response from a hysteretic system employing the Bouc-Wen model can be seen in Figure 2.4.

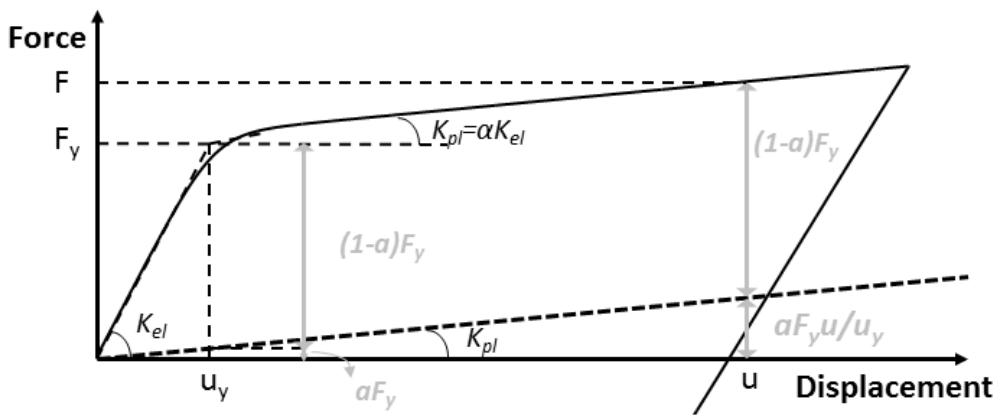

Figure 2.4: Bouc-Wen hysteretic response in terms of force-displacement

2.4 Hysteretic model parameters

Regarding the parameters of the previous formulation n is a scalar that controls the smoothness of the transition from the elastic to the inelastic regime. As n increases, the response approaches the bilinear behavior, while for small values of n smooth transition can be obtained (Figure 2.5)

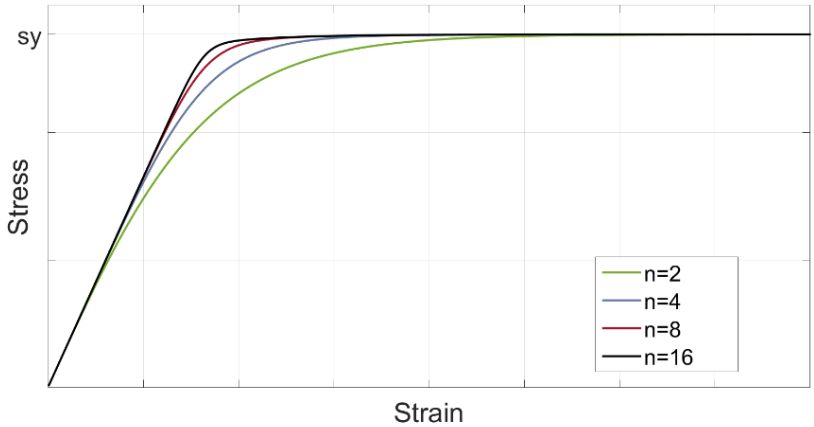

Figure 2.5: Effect of parameter n

Parameters β and γ are shape factors that affect the shape of the hysteretic loops during unloading. For the model to be thermodynamically admissible these parameters should satisfy [52]: $-\beta \le \gamma \le \beta$ and $\beta + \gamma = 1$. Their effect on the stress strain curve can be seen in Figure 2.6.

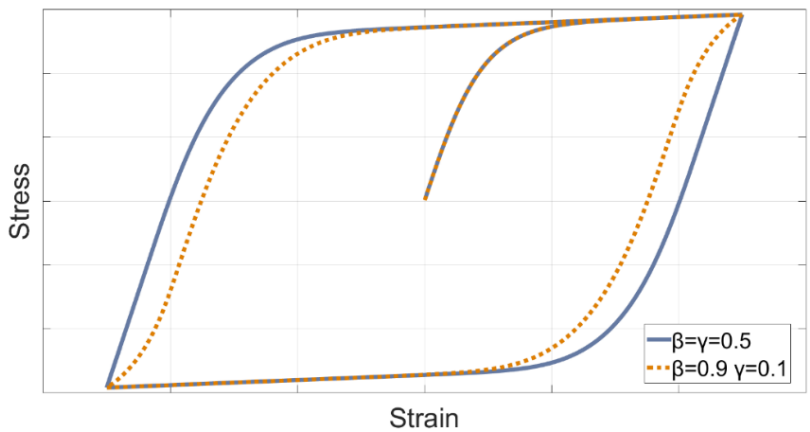

Figure 2.6: Effect of parameters β and γ on stress strain curves

2.5 The generalized triaxial case

An elastic material has no memory of the previous stress – strain state it has reached and upon unloading it returns to a state of zero stress – strain. However, most materials undergo permanent deformation after a level of loading is surpassed. There is a surface, i.e. the yield surface that bounds the elastic domain in the stress space, and is defined by a yield function with the following form:

$$\Phi\left(\{\sigma\},\sigma_y^0\right)=f\left(\{\sigma\}\right)-\sigma_y^0=0 \tag{2.8}$$

where σ_y^0 in the initial yield stress. In every case, all admissible stress states must satisfy the condition: $\Phi \le 0$.

Further loading leads to yielding (or plastic flow) and plastic strains are manifested as permanent strains upon unloading. Based on the theory of classical plasticity the governing equations are the flow rule, the yield condition, the consistency condition and the hardening rule. The plastic flow rule is given by the following relation:

$$\left\{\dot{\varepsilon}^{pl}\right\}=\dot{\lambda}\frac{\partial Q\left(\{\sigma\}\right)}{\partial\{\sigma\}} \tag{2.9}$$

where $Q\left(\{\sigma\}\right)$ is the plastic potential function, $\dot{\lambda}$ is the rate of the plastic multiplier, which can be zero or positive, and the dot indicates time derivative. In the case of associative plasticity, the plastic potential function equates with the yield function $Q\left(\{\sigma\}\right)=\Phi\left(\{\sigma\}\right)$ [39]. The plastic strain tensor is denoted as $\left\{\varepsilon^{pl}\right\}$ and can be expressed in rate form in terms of the yield function Φ as:

$$\left\{\dot{\varepsilon}^{pl}\right\}=\dot{\lambda}\frac{\partial \Phi\left(\{\sigma\}\right)}{\partial\{\sigma\}} \tag{2.10}$$

The Kuhn-Tucker optimality conditions state that:

$$\dot{\lambda} \geq 0 \quad \Phi \leq 0 \quad \dot{\lambda}\Phi = 0 \tag{2.11}$$

This means that there is a complementarity condition that requires either the yield function to be zero or that the plastic multiplier is zero (signifying there is no plastic flow). The total strain tensor can be decomposed to an elastic and a plastic component (assumption of additive decomposition). Therefore, the corresponding rate form can be also stated as:

$$\{\dot{\varepsilon}\} = \{\dot{\varepsilon}^{el}\} + \{\dot{\varepsilon}^{pl}\} \tag{2.12}$$

The stress rate tensor is expressed by the elastic part of the strain rates with the use of the elasticity tensor as:

$$\{\dot{\sigma}\} = [D]\{\dot{\varepsilon}^{el}\} = [D]\left(\{\dot{\varepsilon}\} - \{\dot{\varepsilon}^{pl}\}\right) \tag{2.13}$$

Substituting equation (2.10) to (2.13) the following relation is derived:

$$\{\dot{\sigma}\} = [D]\left\{\{\dot{\varepsilon}\} - \dot{\lambda}\frac{\partial\Phi(\{\sigma\})}{\partial\{\sigma\}}\right\} \tag{2.14}$$

Moreover, hardening is described by the evolution of the yield surface and thus the yield surface can undergo expansion (in the case of isotropic hardening) and/or translation (in the case of kinematic hardening).

When isotropic hardening is considered, the yield surface is expanded uniformly, and this is expressed as:

$$\Phi(\{\sigma\}, \sigma_y) = f(\{\sigma\}) - \sigma_y(\varepsilon_{ps}) = 0 \tag{2.15}$$

The initial constant yield stress σ_y^0 from equation (2.8) is replaced by a variable yield stress $\sigma_y(\varepsilon_{ps})$ that depends on the equivalent plastic strain ε_{ps} [39]:

$$\varepsilon_{ps} = \int \dot{\varepsilon}_{ps} \tag{2.16}$$

This results from the accumulated plastic strain rates as:

$$\dot{\varepsilon}_{ps} = \sqrt{\frac{2}{3}}\left(\dot{\varepsilon}^{pl} : \dot{\varepsilon}^{pl}\right)^{1/2} = \dot{\lambda} B \tag{2.17}$$

where:

$$B = \sqrt{\frac{2}{3}}\left(\frac{\partial \Phi\left(\{\sigma\}\right)}{\partial \{\sigma\}} : \frac{\partial \Phi\left(\{\sigma\}\right)}{\partial \{\sigma\}}\right)^{1/2} \tag{2.18}$$

where, in the case of the Von-Mises (VM) yield criterion: $B = 1$ [39].

On the contrary, when kinematic hardening is considered the yield function assumes the following form:

$$\Phi\left(\{\sigma\}, \sigma_y^0\right) = f\left(\{\sigma\} - \{a\}\right) - \sigma_y^0 = 0 \tag{2.19}$$

where $\{a\}$ is the back-stress tensor. In this form the kinematic hardening is capable of simulating the Bauschinger effect and the yield surface is not expanded as in the isotropic case, but instead its center is translated in the stress space. The evolution of the back-stress tensor is a function of the plastic multiplier $\dot{\lambda}$ and the hardening function $\{G\}$:

$$\{\dot{a}\} = \dot{\lambda}\{G\} \tag{2.20}$$

This relation in general can be non-linear. In this work the case of linear kinematic hardening is considered, through Prager's relations that assume a linear relationship between the back-stresses and the rate of plastic strains of the following form:

$$\{\dot{a}\} = C_p\left\{\dot{\varepsilon}^{pl}\right\} = C_p\left(\dot{\lambda}\frac{\partial \Phi\left(\{\sigma\}\right)}{\partial \sigma}\right) = \dot{\lambda}\left(C_p\frac{\partial \Phi\left(\{\sigma\}\right)}{\partial \sigma}\right) = \dot{\lambda}\{G\} \tag{2.21}$$

where C_p is defined as the hardening constant.

In a more general case, one can consider the combination of kinematic and isotropic hardening [39, 92]. This means that the yield surface can both translate and expand in the stress space. It is achieved by considering a scalar m within the range $0 \le m \le 1$. This scalar represents the percentage of plastic strains that are associated with the isotropic hardening response, while $1-m$ represents the percentage accounting for kinematic hardening. This way the previous relations are modified as follows:

$$\dot{\varepsilon}_{ps}^{iso} = m\dot{\varepsilon}_{ps} = m\sqrt{\frac{2}{3}}\left(\dot{\varepsilon}^{pl} : \dot{\varepsilon}^{pl}\right)^{1/2} = m\dot{\lambda}B \tag{2.22}$$

and:

$$\left\{\dot{a}^{kin}\right\} = (1-m)\dot{\lambda}\left\{G\right\} \tag{2.23}$$

The final expression of the yield surface then becomes:

$$\Phi = f\left(\left\{\sigma\right\} - \left\{a^{kin}\right\}\right) - \sigma_y\left(\varepsilon_{ps}^{iso}\right) = 0 \tag{2.24}$$

In Figure 2.9 different responses that can be achieved for different values of m regarding hardening are presented. For $m=0$ kinematic hardening is considered, for $m=1$ isotropic hardening is valid, while values in-between result in a mixed isotropic-kinematic hardening formulation. The consistency condition states that the stresses must remain on the yield surface during plastic flow and so:

$$\dot{\lambda}\dot{\Phi} = 0 \Rightarrow \dot{\lambda}\left(\left(\frac{\partial\Phi}{\partial\left\{\sigma\right\}}\right)^T\left\{\dot{\sigma}\right\} + \left(\frac{\partial\Phi}{\partial\left\{a^{kin}\right\}}\right)^T\left\{\dot{a}^{kin}\right\} + \frac{\partial\Phi}{\partial\varepsilon_{ps}^{iso}}\dot{\varepsilon}_{ps}^{iso}\right) = 0 \tag{2.25}$$

When at yield $\dot{\Phi} = 0$, $\dot{\lambda} > 0$ and relation (2.25) can be written:

$$\left(\left(\frac{\partial\Phi}{\partial\left\{\sigma\right\}}\right)^T\left\{\dot{\sigma}\right\} + \left(\frac{\partial\Phi}{\partial\left\{a^{kin}\right\}}\right)^T\left\{\dot{a}^{kin}\right\} + \frac{\partial\Phi}{\partial\varepsilon_{ps}^{iso}}\dot{\varepsilon}_{ps}^{iso}\right) = 0 \tag{2.26}$$

In order to derive the expression of the plastic multiplier, relation (2.14) is premultiplied by the flow vector $\left\{\partial\Phi / \partial\{\sigma\}\right\}^{\mathrm{T}}$ and using equation (2.26) one obtains:

$$\dot{\lambda} = \lambda_1 \left(\frac{\partial\Phi}{\partial\{\sigma\}} \right)^T [D]\{\dot{\varepsilon}\} \tag{2.27}$$

where:

$$\lambda_1 = \left(-(1-m)\left(\frac{\partial\Phi}{\partial\{a^{kin}\}} \right)^T \{G\} - m\frac{\partial\Phi}{\partial\varepsilon_{ps}^{iso}} B + \left(\frac{\partial\Phi}{\partial\{\sigma\}} \right)^T [D] \frac{\partial\Phi}{\partial\{\sigma\}} \right)^{-1} \tag{2.28}$$

If the Von Mises (VM) yield criterion is employed and linear kinematic hardening is considered the previous relation can be written as:

$$\lambda_1 = \left((1-m)\frac{3}{2}C_p + mH' + \left(\frac{\partial\Phi}{\partial\{\sigma\}} \right)^T [D] \frac{\partial\Phi}{\partial\{\sigma\}} \right)^{-1} \tag{2.29}$$

where:

$$H' = \frac{E_y}{\left(1 - \frac{E_y}{E}\right)} \tag{2.30}$$

E being the Young's modulus, E_y the tangent modulus in the plastic region and $C_p = 2/3H'$.

The previous equation for the plastic multiplier holds only when yielding has occurred. In order to smooth the transition from the elastic to the inelastic regime and generalize the plastic multiplier expression in the whole domain of the stress space [123, 126], the following Heaviside type functions are introduced:

$$H_1(\Phi)=\begin{cases}1 & \Phi=0\\ 0 & \Phi<0\end{cases}\quad,\qquad H_2(\Phi)=\begin{cases}1 & \dot{\Phi}=0\\ 0 & \dot{\Phi}<0\end{cases} \tag{2.31}$$

and are plugged into the plastic multiplier equation directly:

$$\dot{\lambda}=H_1H_2\lambda_1\left(\frac{\partial\Phi}{\partial\{\sigma\}}\right)^T[D]\{\dot{\varepsilon}\} \tag{2.32}$$

This way a single expression is established for the plastic multiplier neglecting the need for a piecewise approach for the domains of the Kuhn-Tucker condition [126]. This is similar to a Bouc-Wen approach [22, 27], and the Heaviside functions can then be smoothed according to the following relations:

$$\begin{aligned}H_1&=\left|\frac{f\left(\{\sigma\}-\{a^{kin}\}\right)}{\sigma_y\left(\varepsilon_{ps}^{iso}\right)}\right|^n\\ H_2&=\beta+\gamma sign\left(\left\{\frac{\partial\Phi}{\partial\{\sigma\}}\right\}^{\mathrm{T}}[D]\{\dot{\varepsilon}\}\right)\end{aligned} \tag{2.33}$$

where n controls the smoothness from the transition from the elastic region to the inelastic, β and γ are model parameters that control the shape of the unloading branches and are explained in detail in the previous paragraph. Finally substituting the plastic multiplier into equation (2.14) the following relation can be obtained relating stress and strain rates:

$$\begin{aligned}\{\dot{\sigma}\}&=[E_t]\{\dot{\varepsilon}\}\\ [E_t]&=[D]\left([I]-H_1H_2[R]\right)\end{aligned} \tag{2.34}$$

where $[R]$ is the interaction matrix that correlates the interaction of the stress components at yield:

$$[R] = \lambda_1 \left\{ \frac{\partial \Phi}{\partial \{\sigma\}} \right\} \left\{ \frac{\partial \Phi}{\partial \{\sigma\}} \right\}^{\mathrm{T}} [D] \tag{2.35}$$

Thus, the tangent matrix can be obtained in the following form:

$$\begin{aligned} [E_t] = [D] \Bigg([I] - H_1 H_2 \Bigg((1-m)\frac{3}{2} C_p + mH' + \\ + \left(\frac{\partial \Phi}{\partial \{\sigma\}} \right)^T [D] \frac{\partial \Phi}{\partial \{\sigma\}} \Bigg)^{-1} \left\{ \frac{\partial \Phi}{\partial \{\sigma\}} \right\} \left\{ \frac{\partial \Phi}{\partial \{\sigma\}} \right\}^T [D] \Bigg) \end{aligned} \tag{2.36}$$

where H_1 and H_2 are given from equation (2.33).

This tangent matrix replaces the elastic one from equation (2.13) that relates stresses and strains in rate form, and can express the total material behavior in a unified manner following the evolution of the Bouc-Wen model.

In Figure 2.7 the Heaviside function values at different stages in a cyclic stress-strain diagram are presented. At the initial stage the material is elastic and H_1 is close to zero (point A). When the stresses approach the locus of the yield function, H_1 begins to increase until it takes the maximum value of one (point B). If this transition where to happen instantaneously the result would be a bilinear diagram. The material is then further loaded until point C where a load reversal occurs and unloading begins. Up until this moment H_2 is equal to unity in the loading stage. During unloading H_2 becomes zero until further reloading. H_1 is reducing during this stage, but since it is multiplied by H_2 the whole product is zero. At point D the same behavior is again manifested in a cyclic manner.

In Figure 2.8 the various values of the plastic multiplier, the yield function and the yield gradient are presented similar to the previous analysis. The points are different positioned in Figure 2.8 compared to Figure 2.7. In Figure 2.7 points A and B are slightly apart to

signify the smooth transition from the elastic to the inelastic region that the model is capable of simulating together with the smooth evolution of H_1.

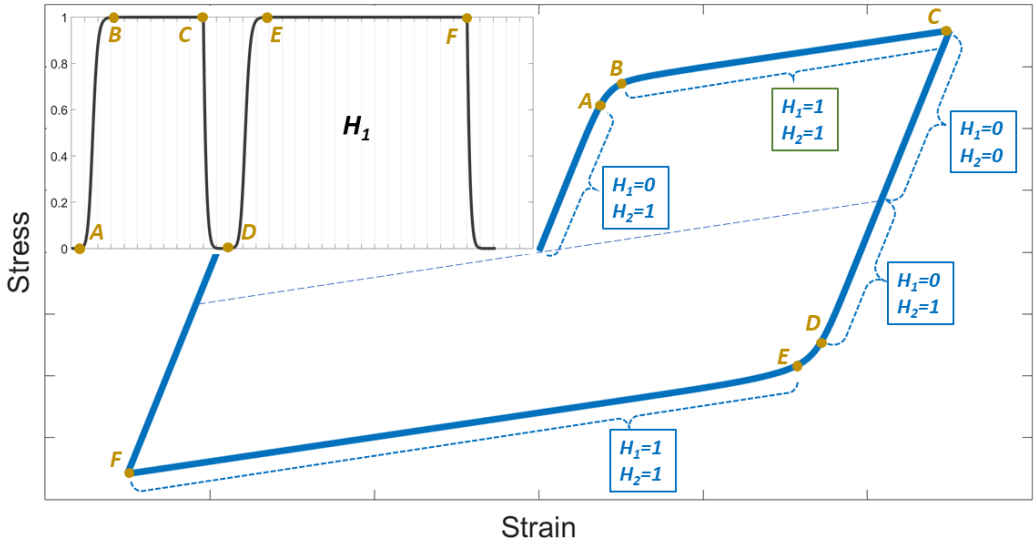

Figure 2.7: Heaviside functions schematic behavior

On the contrary, in Figure 2.8 the regions have been selected in such a way as to better illustrate the various signs of the plastic multiplier, yield function and yield function gradient in each phase of the cyclic hysteretic loop. In the initial elastic stage (AB) the plastic multiplier is zero, then material yields, and the plastic multiplier becomes positive (BC). During unloading the plastic multiplier is zero. Recall from the Kung Tucker optimality conditions (equation (2.11)) that the plastic multiplier is larger or equal to zero and that the yield function must be zero or negative. This can be seen in (AB) region where it is negative and in (BC) region where it takes its maximum value of zero.

Finally, in order to investigate the effect of parameter m controlling mixed hardening, a specimen under uniaxial strain-controlled loading is considered. Material parameters and BW model parameters are presented in Table 2-1

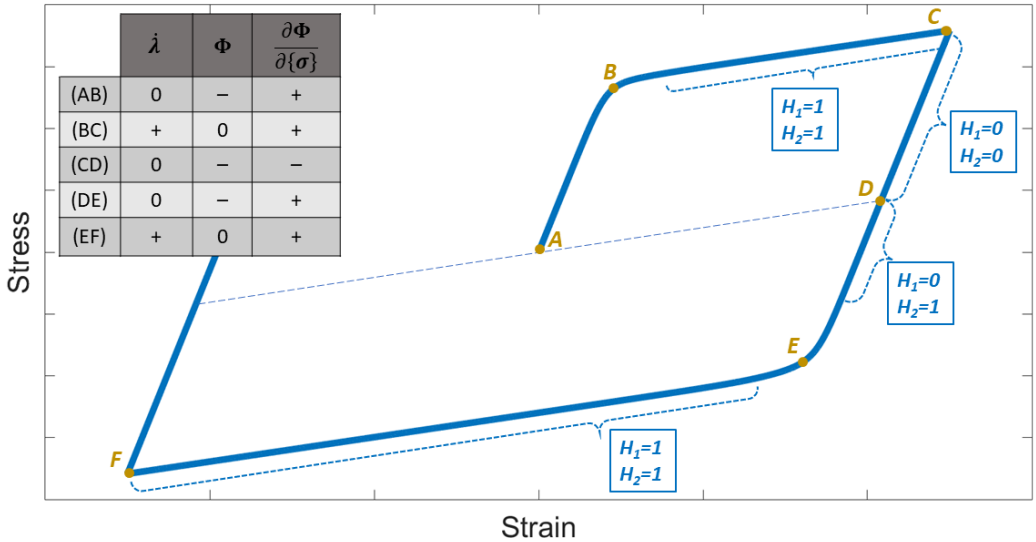

	$\dot{\lambda}$	Φ	$\frac{\partial \Phi}{\partial \{\sigma\}}$
(AB)	0	–	+
(BC)	+	0	+
(CD)	0	–	–
(DE)	0	–	+
(EF)	+	0	+

Figure 2.8: Cyclic behavior of plastic multiplier, yield function and yield gradient

Description	Symbol	Value
Young's modulus	E	30 GPa
Yield stress	σ_y	240 MPa
Post yield slope	a	5%
Smoothness of the transition from elastic to inelastic branch	n	2
Kinematic hardening - Case a)	m	0
Mixed hardening - Case b)	m	0.2
Isotropic hardening - Case d)	m	1

Table 2-1: Parameters of uniaxial model investigating hardening

In Figure 2.9 the effect of the parameter m in the hysteretic loops is presented. Figure 2.9 (a) presents the response for a sinusoidal strain-controlled loading and kinematic hardening ($m=0$). Kinematic hardening signifies the translation of the yield surface and in this form is able to simulate the Bauschinger effect. In addition, the loops are symmetric as expected. In Figure 2.9 (b) a mixed hardening law is used with parameter $m=0.2$.The yield surface in this case is both translating and expanding with the percentage of each case given by parameter m. Finally, in Figure 2.9 (c) the case of isotropic hardening is presented, where the yield surface is expanding and $m=1$. The isotropic model defines that if the yield stress is initially the same both in tension and compression, then the yield

surface is symmetric about the stress axes. As the yield surface then expands then the yield stress in tension and compression remain equal. This behavior can be seen in the Figure 2.9 c) through the enlargement of the yield stress in successive cycles and the symmetrical form of the hysteretic loops.

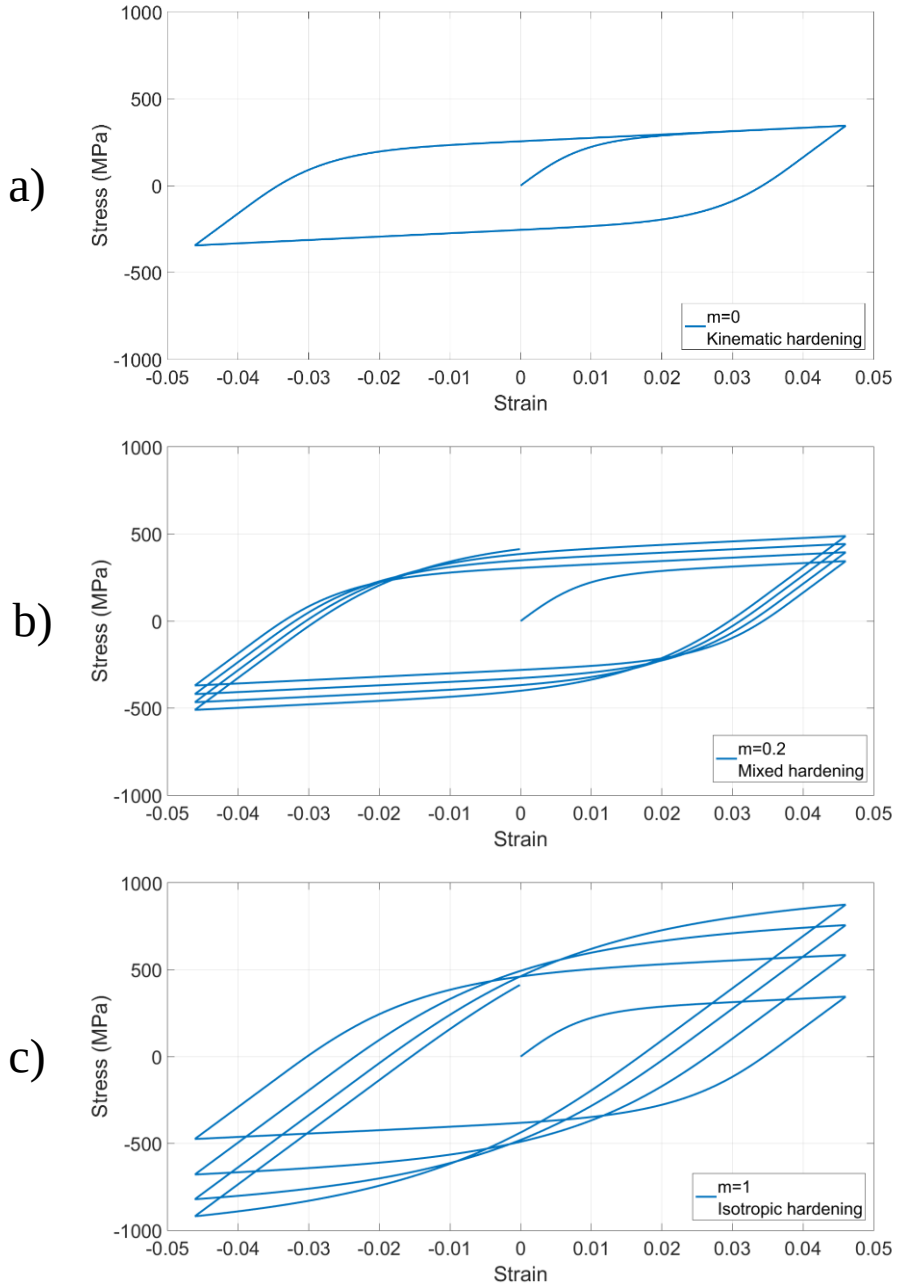

Figure 2.9: Effect of parameter *m* controlling mixed hardening in stress strain curves

2.6 Stiffness and Strength Degradation

During strong dynamic excitations structural members are designed to dissipate energy through a number of mechanisms such as inelastic behavior, friction, crack opening etc. Moreover, during cyclic loading, degradation phenomena can be manifested. These alter the properties of the structure and have to be taken into consideration for the accurate modeling and analysis, especially for later stages of cyclic response. Two main degradation phenomena are usually manifested, mainly stiffness degradation and strength deterioration. Stiffness degradation is the gradual loss of stiffness in successive loading cycles whereas strength deterioration is the reduction of the level of strength for a cross section when loading to the same level of strain. These phenomena are manifested in concrete structures through the formation and propagation of cracks and in steel structures after bolt failure in steel member connections.

The Bouc-Wen model can be extended to account for stiffness degradation and strength deterioration. This is achieved by introducing two additional parameters into the model [9] and equation (2.3) is modified as:

$$\dot{z} = \frac{\dot{u}}{n_s}\left[1 - v_s\left|\frac{z}{z_y}\right|^n \left(\beta + \gamma\,\mathrm{sgn}\left(z\dot{u}\right)\right)\right] \tag{2.37}$$

These parameters, n_s for stiffness degradation and v_s for strength deterioration are based on the accumulated hysteretic energy due to plastic energy dissipation e^h and are increasing functions of time given by the following formulas:

$$\begin{aligned} n_s &= 1 + c_n e^h \\ v_s &= 1 + c_v e^h \end{aligned} \tag{2.38}$$

where $c_n \geq 0$ and $c_v \geq 0$ are model parameters that need to be data fitted or experimentally identified. The aforementioned hysteretic energy is the area enclosed in the hysteretic loops and can be calculated as:

$$e^h = \int (1-a)Ez(t)d\varepsilon \tag{2.39}$$

Erlicher and Bursi [51] studied the thermodynamic admissibility of Bouc-Wen models with stiffness degradation and strength deterioration and concluded that for a thermodynamically admissible degradation rule the following relation must hold:

$$\dot{\eta} \leq \eta v \dot{\xi} \tag{2.40}$$

where η is a function controlling the stiffness degradation and v is a function controlling strength deterioration. Based on endochronic theory [129], ξ is the intrinsic time of the model. This is defined in rate form by the following relation:

$$\dot{\xi} = \left(1 + \frac{\beta}{\gamma}\operatorname{sgn}\left(z\dot{u}\right)\right)\left|\dot{u}\right|\left(\frac{z}{z_y}\right)^{n-1} \tag{2.41}$$

where z is the hysteretic parameter and z_y the value of the hysteretic parameter at yield. The functions for stiffness degradation and strength deterioration are given respectively as [51]:

$$\begin{aligned} \dot{\eta} &= c_\eta \left(\frac{1}{\eta}\right)^{m_u} \beta v_s \dot{\xi} \\ v_s &= 1 + c_v e^h \end{aligned} \tag{2.42}$$

where c_n and $m_u \geq 0$ are model parameters for stiffness degradation and c_v is the parameter controlling strength deterioration.

2.6.1 One dimensional example

In this section, a simple one-dimensional case is considered in order to investigate the effect of the degradation parameters in the overall shape of the hysteretic loops, their evolution and the evolution of the hysteretic energy through time. The material has an elastic modulus equal to 210*GPa* and a yield stress of 235*MPa*. The values of the model parameters are presented in the following Table 2-2:

Description	Symbol	Value
Hardening constant	a	0.03
Smoothness of the transition from elastic to inelastic branch	n	16
Hysteretic loop shape factors	β γ	0.5 0.5
Stiffness degradation parameter	c_η	30
Stiffness degradation parameter	m_u	1.0
Strength deterioration parameter	c_v	0.001
Yield strain	z_y	0.00112

Table 2-2: 1-D example parameter values

The loading is a sinusoidal straining load with 3 cycles over a total time of 36 sec with a maximum strain amplitude of 0.6%. In Figure 2.10 the resulting stress – strain diagram is presented. It can be observed that the stiffness is decreasing in each cycle due to the increase of the hysteretic energy (Figure 2.11). In the same Figure the effect of strength deterioration can also be observed. Moreover, in Figure 2.12 the evolution of the stiffness degradation parameter from equation (2.42) is presented.

Following both the evolution of the stiffness degradation parameter and the hysteretic loops, the following observations can be made. Firstly, stiffness degradation parameter is, as expected, an increasing function over time. Secondly, during unloading and during the elastic phase of loading, it remains constant, since no hysteretic energy is being accumulated.

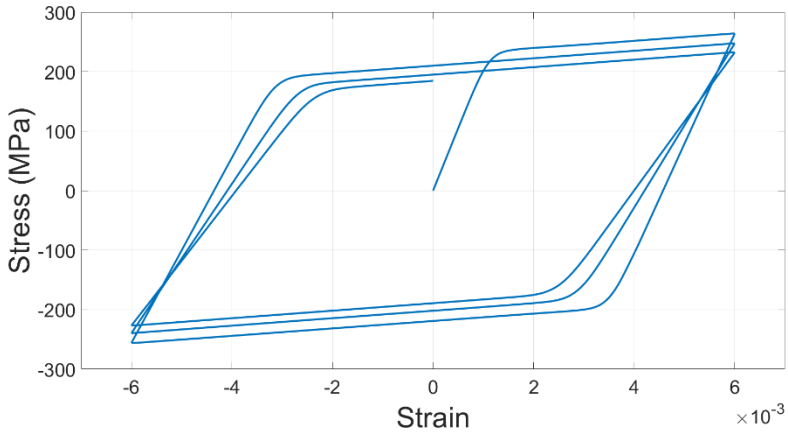

Figure 2.10: Stress – strain hysteretic loop with stiffness and strength deterioration

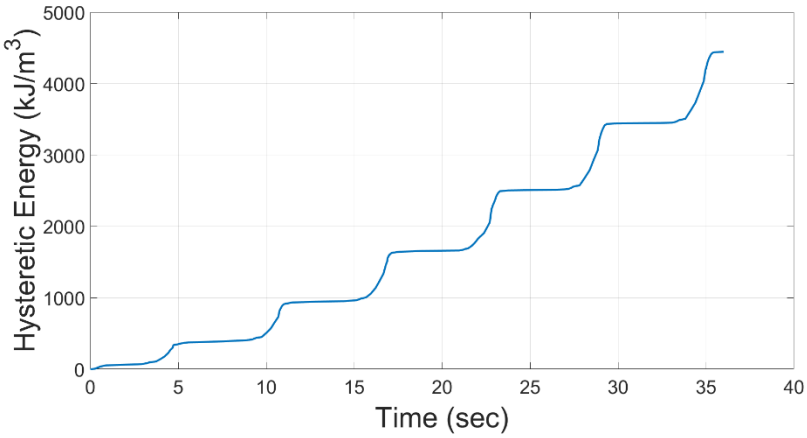

Figure 2.11: Evolution of hysteretic energy

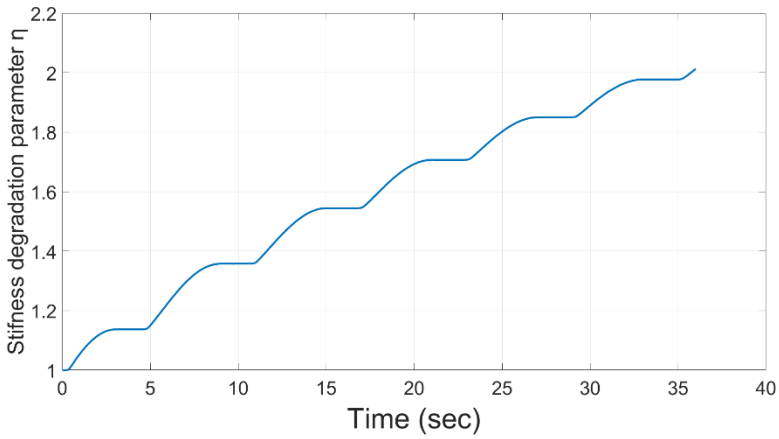

Figure 2.12: Evolution of the stiffness degradation function η

In the next stress - strain diagrams the effect of changing the parameters, on the hysteretic loops produced is presented, in order to showcase the wide range of hysteretic degrading behavior the model can produce. In Figure 2.13 the hysteretic loops produced for different values of the stiffness degradation parameter c_η are presented. It can be observed that as the stiffness degradation parameter increases the reduction of stiffness in each cycle is larger, altering the shape of the hysteretic loops. Furthermore, in Figure 2.14 the effect that the stiffness degradation parameter m_u has on the stress - strain diagram is presented. The main difference between these two parameters is that c_η controls the actual value of the reduction between the cycles while m_u affects the rate of the evolution of the stiffness degradation phenomenon. Finally the effect of the strength deterioration parameter c_v can be seen in Figure 2.15. The reduction of the maximum stress reached in each consecutive cycle can be observed. As the value of the parameter increases, the rate of this reduction also increases. It should be noted that the actual values of the aforementioned parameters should be identified through the verification with experimental data through either numerical or real experiments. There are three additional parameters that need to be identified in addition to the Bouc – Wen model parameters, giving an advantage to this formulation against others that rely on more parameters. Moreover, it is common for the unloading branches to be straight lines. This means that for the Bouc-Wen model one can take $\beta = \gamma = 0.5$ and the other parameters remaining to be identified would be the post yield to initial stiffness ratio a and how smooth the transition should be, n.

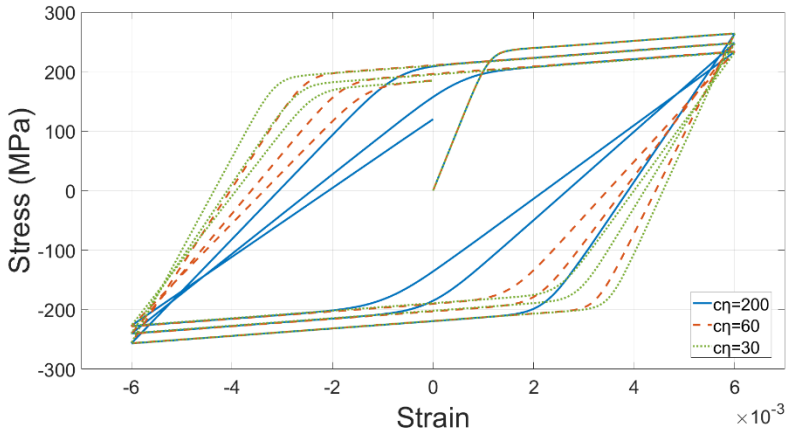

Figure 2.13: Hysteretic loops for various stiffness degradation parameters c_η

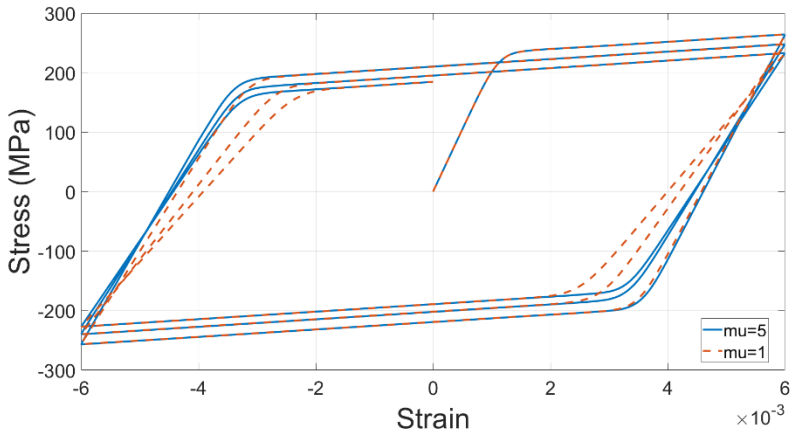

Figure 2.14: Hysteretic loops for various stiffness degradation parameter m_u

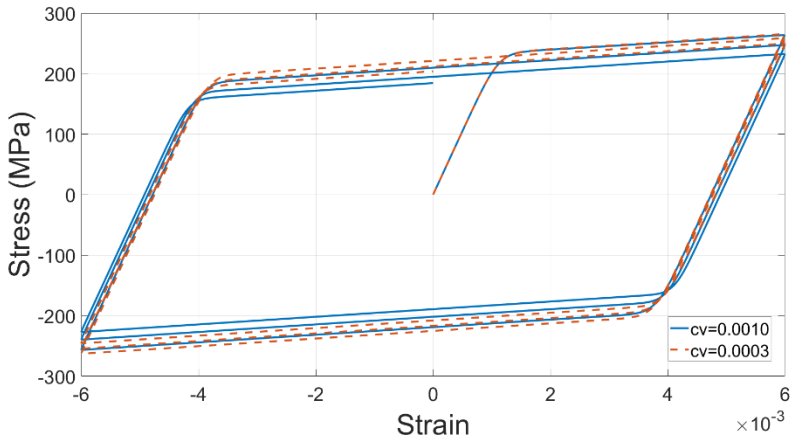

Figure 2.15: Hysteretic loops for various values of the strength deterioration parameter c_v

2.6.2 Three-dimensional stress space generalization

Previous relations hold for single degree of freedom systems, or for systems that the degrees of freedom are uncoupled from each other when hysteresis is considered. To extend the aforementioned model in the stress space, equation (2.34) now incorporates the stiffness degradation and strength deterioration parameters and becomes:

$$\{\dot{\sigma}\} = \frac{1}{n_s}[D]\left([I] - v_s H_1 H_2 [R]\right)\{\dot{\varepsilon}\} \tag{2.43}$$

The hysteretic energy can be calculated as:

$$e^h = \int \{\sigma\} d\left\{\varepsilon^{pl}\right\} \tag{2.44}$$

The intrinsic time can now be written as:

$$\dot{\xi} = \beta H_1 \left(1 + \frac{\gamma}{\beta}\operatorname{sgn}\left(\{\sigma\}^T \{\dot{\varepsilon}\}\right)\right)\left|\{\sigma\}^T \{\dot{\varepsilon}\}\right| \tag{2.45}$$

The final form of the equations accounting for stiffness degradation and strength deterioration in stress space [123] are now taking the following form:

$$\{\dot{\sigma}\} = [D]\frac{1}{\eta}\left([I] - v_s H_1 H_2 [R]\right)\{\dot{\varepsilon}\}$$

$$\dot{\eta} = c_\eta \left(\frac{1}{\eta}\right)^{m_u} \beta H_1 \left(1 + \frac{\gamma}{\beta}\operatorname{sgn}\left(\{\sigma\}^T \{\dot{\varepsilon}\}\right)\right)\left|\{\sigma\}^T \{\dot{\varepsilon}\}\right|$$

$$v_s = 1 + c_v e^h \tag{2.46}$$

$$H_1 = \left|\frac{f\left(\{\sigma\} - \{a^{kin}\}\right)}{\sigma_y\left(\varepsilon_{ps}^{iso}\right)}\right|^n$$

$$H_2 = \beta + \gamma sign\left(\left\{\frac{\partial \Phi}{\partial \{\sigma\}}\right\}^{\mathrm{T}} [D]\{\dot{\varepsilon}\}\right)$$

The tangent stiffness matrix with stiffness degradation and strength deterioration for the general triaxial stress case can then be defined as:

$$\left[E_t^{DEGR}\right]=\left[D\right]\frac{1}{\eta}\left(\left[I\right]-v_s\left|\frac{f\left(\left\{\sigma\right\}-\left\{a^{kin}\right\}\right)}{\sigma_y\left(\varepsilon_{ps}^{iso}\right)}\right|^n H_2\left[R\right]\right) \tag{2.47}$$

where $\left[R\right]$ is the interaction matrix defined previously in equation (2.35) using (2.29).The effect of the degradation parameters on the stress strain diagrams can be seen in Figure 2.16.

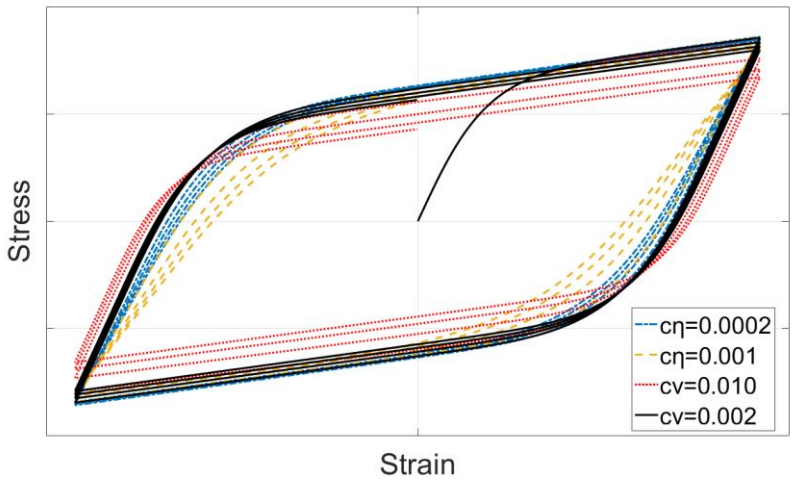

Figure 2.16: Effect of degradation parameters for the three – dimensional case

The main advantage of the above formulation is that stiffness and strength degradation are incorporated into a single additional evolution equation that needs to be solved together with the Bouc – Wen hysteretic equations.

The actual solution process is different for the two numerical methods that are investigated in the present work. In the Rigid Body Spring Network model, in Chapter 3, an implicit solver is used based on Runge-Kutta and Livermore algorithms [106]. The structures stiffness matrices are expanded with hysteretic matrices and the whole system is solved together with the evolution equations. In the Material Point Method in Chapter

4 an explicit time marching algorithm is employed, and the solution of the equations is done in a Forward – Euler scheme. The solvers are presented in greater detail in their respective Chapters.

3 RIGID BODY SPRING NETWORK MODEL

3.1 Introduction

Lattice spring models (LSM) have been widely used for numerical simulations in many scientific fields, ranging from the atomic level [87] to the motion of planets [80]. Engineers have used these models in structural mechanics to simulate a broad range of physical phenomena such as fracture [18], elastic wave propagation [139], fluid dynamics [88, 35], heat diffusion [62] and viscoplasticity [79]. They represent a continuum solid by a discrete system. Spring networks, although discrete in nature, are capable of simulating continuum systems by modeling them with lattices, much coarser than the atomic ones, reducing the total degrees of freedom needed for the analysis. The lattice or spring network model idea combines the physical structure of matter at the very small scale with the more general engineering approach of modelling masses interacting with spring systems.

The concept of a Rigid Body Spring Network model was first proposed by Kawai [77]. The main idea, based on a physical model rather than a mathematical one, was to divide the structure into discrete rigid bodies interconnected with springs and hence reducing the computational effort needed for dynamic analysis compared to the Finite Element Method. This observation was based on the fact that the elemental stiffness matrices in RBSN have dimensions of 6x6 irrespective of beam plate, shell or solid elements and thus the total degrees of freedom could be reduced compared to FEM.

The RBSN model has been used widely in structural engineering and has been used efficiently in the simulation of structural concrete [48, 143] and the modelling of fracture [19, 21, 49]. In addition it has recently been used to simulate brittle fracture in rocks using a Cohesive Zone Model [107]. Bolander and Saito [20] proposed the scaling of elemental stiffness according to Voronoi tessellation of the domain in order to ensure elastic uniformity and maximize the isotropy of crack path propagation, since crack movement

is confined within the boundaries between particles and is therefore strongly affected by the implemented meshing strategy. Their work is based on static loading, which was applied incrementally in concrete specimens in order to investigate the crack path. Voronoi scaling has been also used to simulate concrete fracture under dynamic loading using viscoplastic damage models to describe the rate dependency [79, 68]. Recently, Eliáš [47] studied the boundary layer effect of random geometry Voronoi tessellation discrete models. An explicit time integration scheme has also been developed for RBSN [137]. However, a rate independent plasticity model such as the Bouc Wen model of hysteresis, has not yet been applied to the Rigid Body Spring Network framework to model plasticity related phenomena.

3.2 Voronoi tessellation

Discretizing a domain with Voronoi diagrams is a powerful meshing tool and plays a dominant role in the RBSN formulation. This technique has been applied successfully both in two- and three-dimensional high complexity geometries. The first step in creating a Voronoi diagram is to distribute points inside the domain. These points are going to be the nodes of the Voronoi diagram and can be regularly or randomly placed. For each node there exists an area that is called a cell of the Voronoi diagram. Cell i is defined as the area that encloses all the points that are closer to the node i than any other node in the mesh. This consists a basic property of Voronoi diagrams and discretizes space into a sum of curved polygons. The cell that corresponds to node i is:

$$V(X_i) = \bigcap_{j \neq i} \left\{ X \mid d(X_i, X) \leq d(X_j, X) \right\} \tag{3.1}$$

where X_i are the coordinates of node i, $d(X_i, X)$ is the distance between X_i and position X and the intersection refers to the set of points for $j = 1, ..., n$, except the case

where $j = i$. The previous equation (3.1) defines that every point belonging to a cell of a Voronoi diagram is closer to the node of this cell than any other node in the mesh (Figure 3.1). A set of two nearest neighbors makes up the edges of the Voronoi diagram. The set of three or more nearest neighbors makes up the vertices of the diagram.

Voronoi diagrams are the dual graphs of Delaunay triangulation. Delaunay triangulation for a given set P of discrete points in a plane, is a triangulation $DT(\mathrm{P})$ such that no point in P is inside the circumcircle of any triangle in $DT(\mathrm{P})$. Delaunay triangulations maximize the minimum angle of all the angles of the triangles in the triangulation.

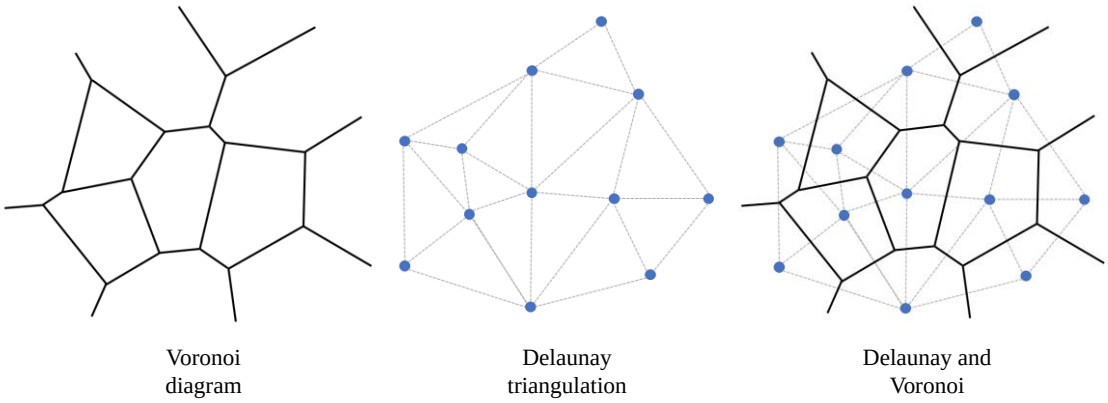

Figure 3.1: Voronoi diagram and its equivalent Delaunay triangulation

Several algorithms have been developed that apply Voronoi tessellation and automate the process for complicated domains and uniform or random distributions of points. For orthogonal domains creating the boundaries is achieved with the use of 4 auxiliary points for every node. These auxiliary points lie outside the domain as can been seen in Figure 3.3.

The Voronoi diagram is then constructed for all the points, both the initial points as well as their quadruplet auxiliary points as can been seen in Figure 3.2. This way the boundaries of the orthogonal domain are automatically generated. The points that lie outside the orthogonal domain are then being discarded.

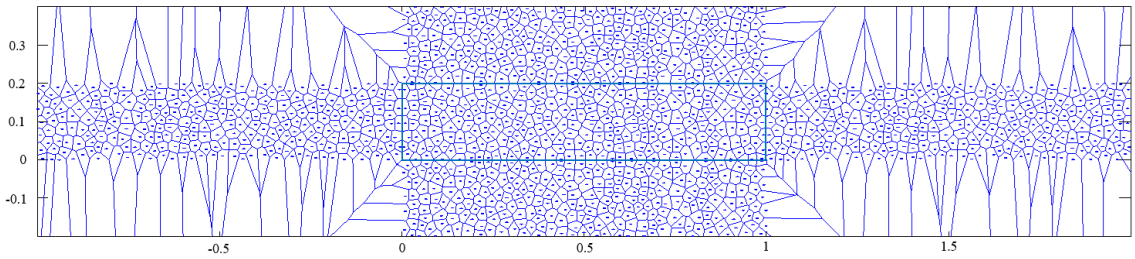

Figure 3.2: Voronoi tessellation of an initial orthogonal domain and the auxiliary points needed for boundary formation

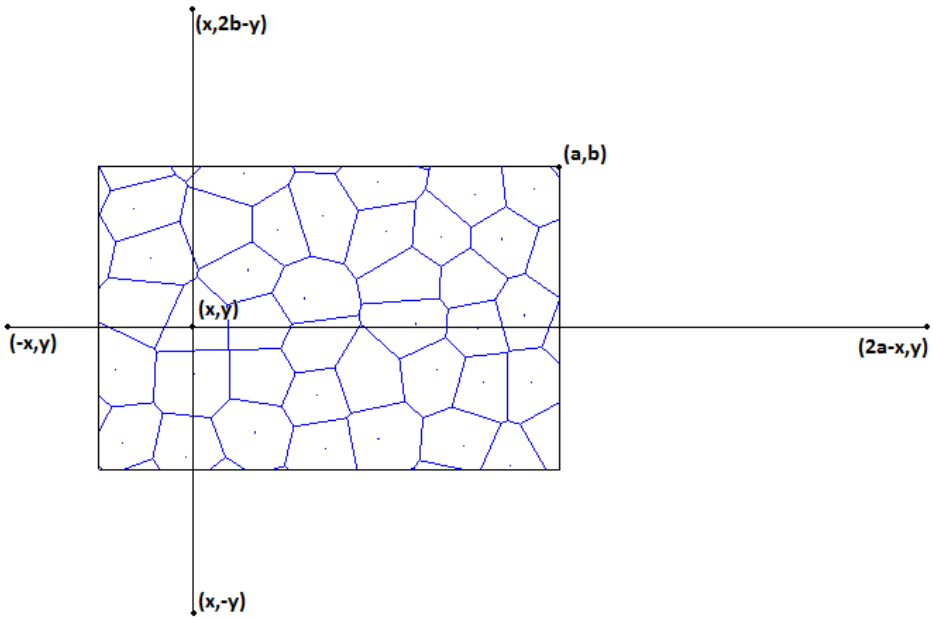

Figure 3.3: Auxiliary points for constructing domain boundaries

3.3 The Rigid Body Spring Network Model

3.3.1 The case of homogeneous isotropic material

In the RBSN framework the structure is divided into a set of rigid particles, which are considered interconnected along their common boundaries with zero length springs (Figure 3.4). Structure deformation is based solely on the localized deformations of these internal springs. Particles or cells are assumed to be rigid in the sense that they don't deform but, depending on loading, they can separate or overlap.

This predetermined set of points act as the nuclei used to define the Voronoi diagram (Preparata and Shamos [105]). The Voronoi diagram mainly divides the domain into convex polygons i.e. the Voronoi cells that define the rigid particles of the model. Voronoi cell *I* is defined as the set of points that are closer to its generator node *I* than any other node in the system. Each individual element consists of two rigid particles and their common facet as shown in Figure 3.4, where by definition the line connecting the computational points 1 and 2 will be perpendicular to the common facet connecting the generated points 3 and 4.

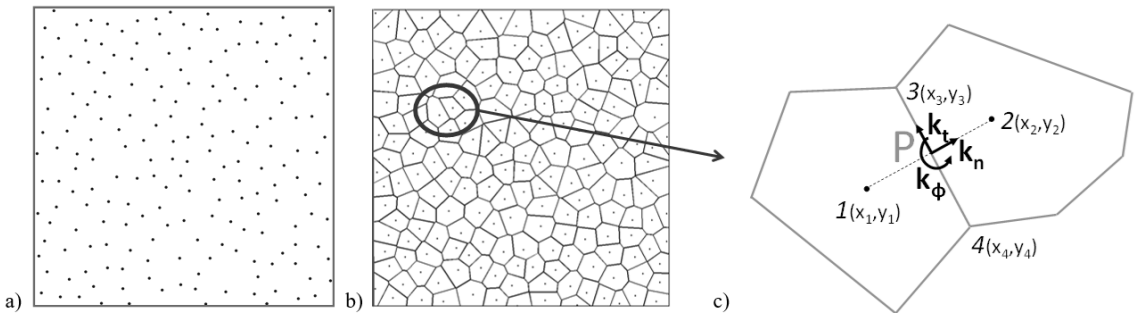

Figure 3.4: Rigid Body Spring Network structure discretization, a) random initial point distribution, b) Voronoi tessellation, c) single element

Let the coordinates of the computational points be (x_1, y_1) and (x_2, y_2) for the two particles and (x_3, y_3), (x_4, y_4) the coordinates of the end points of their common boundary edge. The displaced position of an arbitrary point, with coordinates (x, y), that lies inside particle *1* (Figure 3.4) can be calculated from:

$$\begin{aligned} u &= u_1 - (y - y_1)\theta_1 \\ v &= v_1 - (x - x_1)\theta_1 \end{aligned} \tag{3.2}$$

where u_1, v_1 and θ_1 are the translational displacements and the rotation of particle *1* computational point. At the middle of this common boundary edge (their interface, point P in Figure 3.4) lie three zero length springs with stiffness k_n, k_t and k_φ in the normal,

tangential and rotational sense respectively (in the local coordinate system). Therefore, the diagonal matrix of these uncoupled stiffnesses can be defined as:

$$[D]=\begin{bmatrix} k_n & 0 & 0 \\ 0 & k_t & 0 \\ 0 & 0 & k_\varphi \end{bmatrix} \tag{3.3}$$

Considering the relative displacements at point *P* in the facet local system:

$$\{d\}^T=\begin{bmatrix}\delta_n & \delta_t & \varphi\end{bmatrix} \tag{3.4}$$

and the global nodal displacements of the two computational points - nodes:

$$\{u_e\}^T=\begin{bmatrix}u_1 & v_1 & \theta_1 & u_2 & v_2 & \theta_2\end{bmatrix} \tag{3.5}$$

These are interrelated through:

$$\{d\}=[B]\{u_e\} \tag{3.6}$$

where $[B]$ is a purely geometrical matrix with dimensions (3×6) and expressed as [20]:

$$[B]=\frac{1}{l_{43}}\begin{bmatrix} y_{43} & -x_{43} & (-x_{43}x_{P1}-y_{43}y_{P1}) & -y_{43} & x_{43} & (x_{43}y_{P2}+y_{43}y_{P2}) \\ x_{43} & y_{43} & (y_{43}x_{P1}-x_{43}y_{P1}) & -x_{43} & -y_{43} & (-y_{43}x_{P2}+x_{43}y_{P2}) \\ 0 & 0 & -l_{43} & 0 & 0 & l_{43} \end{bmatrix} \tag{3.7}$$

where $x_{ij}=x_i-x_j$, $y_{ij}=y_i-y_j$ and l_{ij} is the Euclidean distance between points i and j. Point P is located at the middle of the common boundary and the terms in Equation (3.7) are given as: $x_{pi}=(x_{4i}+x_{3i})/2$, $y_{pi}=(y_{4i}+y_{3i})/2$. In addition, the internal forces of the springs $\{q\}$ are evaluated in the elastic case using the relation:

$$\{q\}=\begin{Bmatrix} F_n \\ F_t \\ M \end{Bmatrix}=[D]\{d\} \tag{3.8}$$

where F_n, F_t are the spring forces along the normal, tangential direction respectively and M the moment of the rotational spring. In order to approximate the elastic properties of the continuum, spring stiffnesses are scaled based on the Voronoi discretization diagram and in order to approximate the elastic properties of the continuum, they are given from the following equations [77, 20]:

$$k_n = \frac{Etl_{43}}{\left(1-\nu^2\right)h}$$
$$k_t = \frac{Etl_{43}}{\left(2\left(1+\nu\right)\right)h} \tag{3.9}$$
$$k_\varphi = \frac{k_n l_{43}^2}{12}$$

For plane stress conditions and, E being the elastic modulus, ν the Poisson ratio, t the thickness of the domain and h the distance of the two nodes. In order to obtain the elemental stiffness matrix, the principle of virtual work is applied [20] and the following $\left(6\times 6\right)$ matrix is derived:

$$[K]_e = \left[B\right]^T \left[D\right]\left[B\right] \tag{3.10}$$

All elemental stiffness matrices of every two-particle system are then combined using the direct stiffness method [12] to form the global stiffness matrix of the structure $\left[K\right]_s$. This global matrix has dimensions of $\left(3n\times 3n\right)$ where n is the total number of nodes.

The motion of each discrete rigid particle is determined by the displacements of its centroid, which in the two-dimensional case consists of 3 components. If $\left(u_1, v_1, \theta_1\right)$ are the displacements of the particle's centroid, an arbitrary point on the particle with coordinates $\left(x, y\right)$, assuming small rotations, will be displaced as follows:

$$u = u_1 - (y - y_1)\theta_1$$
$$v = v_1 - (x - x_1)\theta_1 \tag{3.11}$$

Relation (3.11) is used also to express the inertia forces with respect to the computational points. For the dynamic equation of motion, the formation of mass and damping matrices is essential. Let m and I_c be the mass and the mass moment of inertia of a given cell about its center of mass. These are expressed about the computational point as in the following Equation, forming the elemental mass matrix:

$$[M_e] = \begin{bmatrix} m & 0 & -y_c m \\ 0 & m & x_c m \\ -y_c m & x_c m & I_c + mr^2 \end{bmatrix} \tag{3.12}$$

where x_c, y_c are the coordinates of the center of mass from the computational point and $r = \sqrt{x_c^{\,2} + y_c^{\,2}}$ is the distance between the two. The final mass matrix of the system $[M]_s$ is assembled from all the individual cell mass matrices by combining the values that correspond to each degree of freedom and has a size of $(3n \times 3n)$ prior to the enforcement of boundary conditions. The damping matrix $[C]_s$ has the form of a Rayleigh damping matrix [37] and is assumed to be proportional to the mass and stiffness matrices and has also dimensions $(3n \times 3n)$ in the global level. For static problems the following relation has to be solved:

$$[K]_s \{u\} = \{F\} \tag{3.13}$$

And for the dynamic problem:

$$[M]_s \{\ddot{u}\} + [C]_s \{\dot{u}\} + [K]_s \{u\} = \{F(t)\} \tag{3.14}$$

where $F(t)$ is the vector of the external loads with dimensions of $(3n \times 1)$, n being the total number of nodes.

3.3.2 State space formulation

In order to solve the dynamic problem, the system of equations is formulated in state space form. State space formulation is used to convert a system of differential equations into a set of matrix equations. For most differential equations in engineering, there are terms that can be interpreted as inputs to a system and terms that can be interpreted as outputs of the system with the system itself being described by its state variables (Figure 3.5).

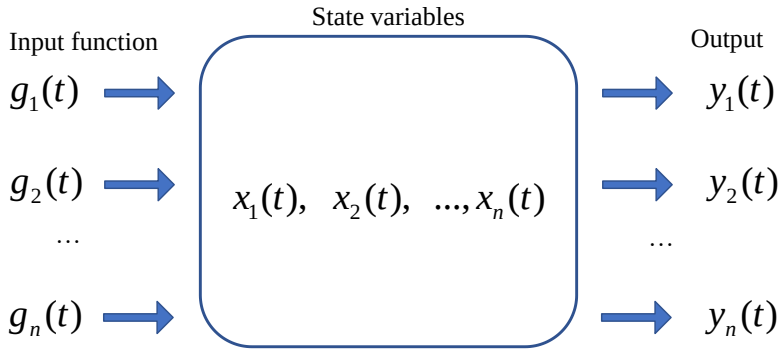

Figure 3.5: State Space formulation of a system

The equation of motion (3.14) is a set of second order ordinary differential equations that has the following general form:

$$[A_1]\{\ddot{x}\}+[A_2]\{\dot{x}\}+[A_3]\{x\}=\{F(t)\} \tag{3.15}$$

where:

- $\{x\}$ being the vector of the generalized coordinates(displacements $\{U\}$ in (3.14),
- $[A_1]$, $[A_2]$, $[A_3]$ are matrixes describing the independent of time characteristics of the system (mass $[M]_s$, damping $[C]_s$ and stiffness matrices $[K]_s$ respectively),

- $\{F\}$ is the vector function of time that contains the external forcing functions acting on the dynamic system.

The mass matrix is symmetrical which simplifies the procedure. However, if the mass matrix was not symmetrical [57] it is possible to rearrange the equations of motion, by writing the matrices as the sum of a symmetrical and a skew-symmetrical matrix, and then proceed as follows.

In RBSN the total number of degrees of freedom is $3n$ with n being the number of nodes. A set of $3n$ second order differential equations can be expressed in the form of a set of $2 \cdot 3n$ first order equations and the solution in dynamics is usually done in the first derivatives. The state variables of the system are the independent variables and the equations can be written as [57]:

$$\{\dot{z}\} = [A]\{z\} + [B]\{g\} \tag{3.16}$$

where:

- $\{z\}$ is a vector of dimensions $(2 \cdot 3n \times 1)$ that holds the state variables,
- $[A]$ is a matrix with dimensions $(2 \cdot 3n \times 2 \cdot 3n)$ which does not depend on time and is called the dynamic matrix.
- $\{g\}$ is a vector function of time that holds the input functions of the system, and its dimensions are the same as the number of inputs of the system n_{inp} .
- $[B]$ is a matrix that correlates the inputs with the equations. Its dimensions are $(2 \cdot 3n \times n_{inp})$.

In the above equation $\{z\}$ is actually a column matrix that can be described as a vector in the $(2\cdot 3n)$-dimensional space. This space is called the state space of the system, signifying that each point belonging to this space correlates to a given state of the system. To transform the system into the state space, a set of $(3n)$ auxiliary variables must be introduced. By choosing the generalized velocities as auxiliary unknown then:

$$\{z\} = \begin{Bmatrix} \{\dot{x}\} \\ \{x\} \end{Bmatrix} \tag{3.17}$$

An equation that relates the generalized velocities and coordinates must be added. Assigning $\{v\} = \{\dot{x}\}$ then the set of $(2\cdot 3n)$ equations corresponding to (3.15) takes the form:

$$\begin{cases} \{\dot{v}\} = -[A_1]^{-1}[A_2]\{v\} - [A_1]^{-1}[A_3]\{x\} + [A_1]^{-1}\{F(t)\} \\ \{\dot{x}\} = \{v\} \end{cases} \tag{3.18}$$

Or expressing it in terms of the RBSN system:

$$\begin{cases} \{\dot{v}\} = -[M]_s^{-1}[C]_s\{v\} - [M]_s^{-1}[K]_s\{u\} + [M]_s^{-1}\{F(t)\} \\ \{\dot{u}\} = \{v\} \end{cases} \tag{3.19}$$

This way the dynamic matrix $[A]$ and matrix $[B]$ from equation (3.16) can be expressed as:

$$\begin{aligned} [A] &= \begin{bmatrix} -[M]_s^{-1}[C]_s & -[M]_s^{-1}[K]_s \\ \mathrm{I} & 0 \end{bmatrix} \\ [B] &= \begin{bmatrix} [M]_s^{-1} \\ 0 \end{bmatrix} \end{aligned} \tag{3.20}$$

Since the external forces acting on the system are the input functions of the system, then the vector function that holds them is simply:

$$\{g\} = \{F(t)\} \tag{3.21}$$

and finally, equation (3.16) becomes:

$$\{\dot{z}\} = \begin{bmatrix} -[M]_s^{-1}[C]_s & -[M]_s^{-1}[K]_s \\ \mathrm{I} & 0 \end{bmatrix} \{z\} + \begin{bmatrix} [M]_s^{-1}\{F(t)\} \\ 0 \end{bmatrix} \tag{3.22}$$

In this above form the linearity of the equations means that a unique solution exists, and the equations have been transformed into a set of first order differential equations, that can be solved. The state space form of the equation of motion and the evolution equations of Bouc – Wen are presented in Paragraph 3.4 together with the incorporation of the hysteretic model into the RBSN.

3.3.3 Mesh generation procedure

Considering a two dimensional rectangular domain, according to Bolander and Saito [20] the maximum number of points that can be placed using a random distribution process and a minimum distance criterion, is $\hat{n} = 0.68ab / d_m^2$ where a and b are the height and width of the rectangular domain respectively and d_m is the user defined minimum allowable distance between points. By choosing $n \to \hat{n}$ the mesh becomes more regular and the points are distributed more uniformly. It should be noted that parameter $\hat{n}$ comes from numerical experimentation.

The necessity for this formulation is that Voronoi scaling of the spring constants essentially renders the structure elastically uniform for simple modes of straining as shown in [20] and [16]. If the structure is discretized using a Voronoi diagram and the nuclei of the Voronoi diagram define the computational nodes of the model, then the RBSN model is elastically uniform. In that regard, the use of the Voronoi diagram is not just an efficient method meshing technique. The spring constants that are assigned are

uniquely defined by the local structure of the network. In this way discretization becomes more natural in a sense that is capable of expressing a directional uniformity of the response. This property renders itself useful for the formulation presented in the next paragraphs, in the case where plasticity is concerned and with regards to fracture representation, by maximizing isotropy regarding potential crack direction.

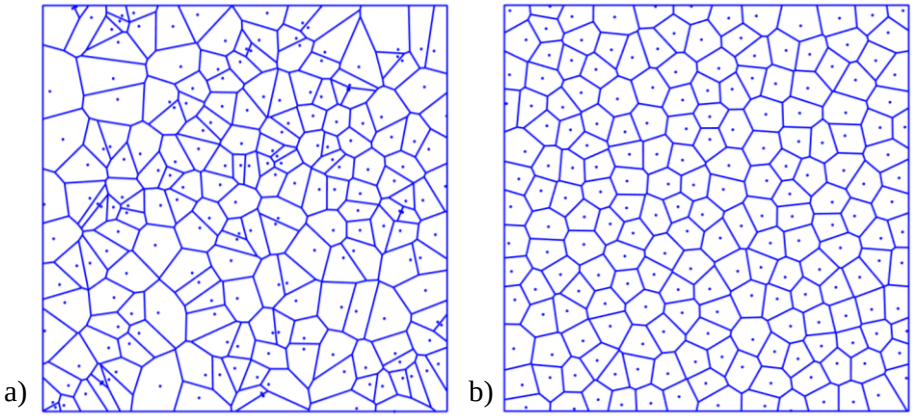

Figure 3.6: Different mesh generation procedures for the Voronoi diagrams, a) without a minimum distance criterion, b)with the criterion

3.3.4 Equivalency to beam element

The Rigid Body Spring Network can be considered as a special type of beam spring network. In general, the elemental stiffness matrices that are formed are different from those of ordinary beam elements. There is, however, a case where they can be made the same that manifests in the case of a regular square lattice.

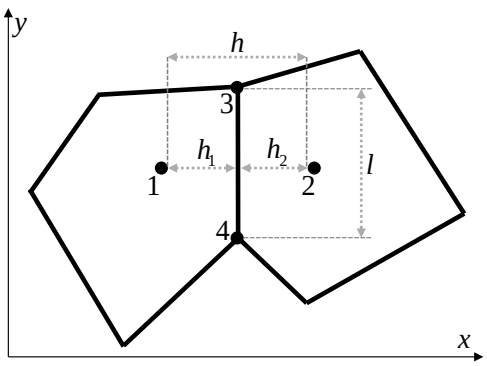

Figure 3.7: Single element aligned with global axes

Consider the single element depicted in Figure 3.7 that consists of two particles that align with the global axis in the *x*-direction and their interface is aligned with the axis in the *y*-direction. Then $y_{p1} = y_{p2} = x_{43} = 0$ and $y_{43} = l_{43}$. Also, for the sake of clarity let $l_{43} = l$, then:

$$x_{p1} = (x_{41} + x_{31})/2 = ((x_4 - x_1) + (x_3 - x_1))/2 = (h_1 + h_1)/2 = h_1 \tag{3.23}$$

and

$$x_{p2} = (x_{42} + x_{32})/2 = ((x_4 - x_2) + (x_3 - x_2))/2 = (-h_2 - h_2)/2 = -h_2 \tag{3.24}$$

This leads to $[B]$ matrix of equation (3.7) simplifying to:

$$[B] = \frac{1}{l}\begin{bmatrix} l & 0 & 0 & -l & 0 & 0 \\ 0 & l & lh_1 & 0 & -l & -lh_2 \\ 0 & 0 & -l & 0 & 0 & l \end{bmatrix} \tag{3.25}$$

and the following elemental stiffness matrix is formed:

$$\underset{(6\times 6)}{[K_e]} == \begin{bmatrix} K_{11} & K_{12} \\ K_{12} & K_{22} \end{bmatrix} \tag{3.26}$$

where:

$$K_{11} = \begin{bmatrix} -\dfrac{Etl}{(1-v^2)h} & 0 & 0 \\ 0 & \dfrac{Etl}{2(1+v)h} & \dfrac{Etlh_1}{2(1+v)h} \\ 0 & \dfrac{Etlh_1}{2(1+v)h} & \left(\dfrac{Etlh_1^2}{2(1+v)h} + \dfrac{Etl^3}{(1-v^2)12h}\right) \end{bmatrix} \tag{3.27}$$

and:

$$K_{12}=\begin{bmatrix} -\dfrac{Etl}{\left(1-v^2\right)h} & 0 & 0 \\ 0 & \dfrac{Etl}{2\left(1+v\right)h} & \dfrac{Etlh_2}{2\left(1+v\right)h} \\ 0 & -\dfrac{Etlh_1}{2\left(1+v\right)h} & \left(\dfrac{Etlh_1h_2}{2\left(1+v\right)h}-\dfrac{Etl^3}{\left(1-v^2\right)12h}\right) \end{bmatrix} \tag{3.28}$$

and:

$$K_{22}=\begin{bmatrix} \dfrac{Etl}{\left(1-v^2\right)h} & 0 & 0 \\ 0 & \dfrac{Etl}{2\left(1+v\right)h} & -\dfrac{Etlh_2}{2\left(1+v\right)h} \\ 0 & -\dfrac{Etlh_2}{2\left(1+v\right)h} & \left(\dfrac{Etlh_2^2}{2\left(1+v\right)h}+\dfrac{Etl^3}{\left(1-v^2\right)12h}\right) \end{bmatrix} \tag{3.29}$$

Assuming further that the network is square, $h=l$, $h_1=h_2=h/2$ and that Poison ratio is zero $v=0$, and setting $A=tl$, $I=tl^3/12$ then the beam element stiffness matrix is derived:

$$\left[K_e\right]=\begin{bmatrix} \dfrac{EA}{L} & 0 & 0 & -\dfrac{EA}{L} & 0 & 0 \\ & \dfrac{12EI}{L^3} & \dfrac{6EI}{L^2} & 0 & -\dfrac{12EI}{L^3} & \dfrac{6EI}{L^2} \\ & & \dfrac{4EI}{L} & 0 & -\dfrac{6EI}{L^2} & \dfrac{2EI}{L} \\ & & & \dfrac{EA}{L} & 0 & 0 \\ & \text{SYM} & & & \dfrac{12EI}{L^3} & -\dfrac{6EI}{L^2} \\ & & & & & \dfrac{4EI}{L} \end{bmatrix} \tag{3.30}$$

This leads to the conclusion that the RBSN for the strict conditions mentioned above, and a square beam element network are essentially identical.

3.4 Incorporation of Bouc – Wen model in RBSN

The spring forces at the middle of the facet (Figure 3.4) are equilibrated at the computational nodes by F_x, F_y and M, which are expressed using the relation:

$$\begin{Bmatrix} F_x^1 \\ F_y^1 \\ M^1 \\ F_x^2 \\ F_y^2 \\ M^2 \end{Bmatrix} = [B]^T \begin{Bmatrix} F_n \\ F_t \\ M \end{Bmatrix} \tag{3.31}$$

According to Bouc-Wen model spring forces can be decomposed into an elastic and a hysteretic part:

$$\begin{aligned} F_n &= ak_n\delta_n + (1-\alpha)k_n z_n \\ F_t &= ak_t\delta_t + (1-\alpha)k_t z_t \\ M &= ak_\varphi\varphi + (1-\alpha)k_\theta z_\varphi \end{aligned} \tag{3.32}$$

or in matrix form:

$$\begin{Bmatrix} F_n \\ F_t \\ M \end{Bmatrix} = \begin{bmatrix} ak_n & 0 & 0 \\ 0 & ak_t & 0 \\ 0 & 0 & ak_\varphi \end{bmatrix} \begin{Bmatrix} \delta_n \\ \delta_t \\ \varphi \end{Bmatrix} + \begin{bmatrix} (1-a)k_n & 0 & 0 \\ 0 & (1-a)k_t & 0 \\ 0 & 0 & (1-a)k_\varphi \end{bmatrix} \begin{Bmatrix} z_n \\ z_t \\ z_\varphi \end{Bmatrix} \tag{3.33}$$

where the hysteretic forces are:

$$\{F^h\} = \begin{Bmatrix} F_n^h \\ F_t^h \\ M^h \end{Bmatrix} = \begin{bmatrix} (1-a)k_n & 0 & 0 \\ 0 & (1-a)k_t & 0 \\ 0 & 0 & (1-a)k_\varphi \end{bmatrix} \begin{Bmatrix} z_n \\ z_t \\ z_\varphi \end{Bmatrix} \tag{3.34}$$

Considering equations (3.6), (3.33) and substituting into (3.31) the following relation can be derived:

$$\begin{Bmatrix} F_x^1 \\ F_y^1 \\ M^1 \\ F_x^2 \\ F_y^2 \\ M^2 \end{Bmatrix} = [B]^T \begin{bmatrix} ak_n & 0 & 0 \\ 0 & ak_t & 0 \\ 0 & 0 & ak_\varphi \end{bmatrix} [B] \begin{Bmatrix} u_1 \\ w_1 \\ \theta_1 \\ u_2 \\ w_2 \\ \theta_2 \end{Bmatrix} + [\mathrm{B}]^T \begin{bmatrix} (1-a)k_n & 0 & 0 \\ 0 & (1-a)k_t & 0 \\ 0 & 0 & (1-a)k_\varphi \end{bmatrix} \begin{Bmatrix} z_n \\ z_t \\ z_\varphi \end{Bmatrix} \quad (3.35)$$

where the hysteretic part is following a Bouc-Wen nonlinear first order differential equation of the form:

$$\begin{cases} \dot{z}_n = \dot{\delta}_n \left[1 - \left| \dfrac{z_n}{z_y^n} \right|^n \left(\gamma + \beta \operatorname{sgn}\left(z_n \dot{\delta}_n \right) \right) \right] \\ \dot{z}_t = \dot{\delta}_t \left[1 - \left| \dfrac{z_t}{z_y^t} \right|^n \left(\gamma + \beta \operatorname{sgn}\left(z_t \dot{\delta}_t \right) \right) \right] \\ \dot{z}_\varphi = \dot{\varphi} \left[1 - \left| \dfrac{z_\varphi}{z_y^\varphi} \right|^n \left(\gamma + \beta \operatorname{sgn}\left(z_\varphi \dot{\varphi} \right) \right) \right] \end{cases} \quad (3.36)$$

The hysteretic matrix is defined as

$$[H] = [B]^T \begin{bmatrix} (1-a)k_n & 0 & 0 \\ 0 & (1-a)k_t & 0 \\ 0 & 0 & (1-a)k_\varphi \end{bmatrix} \quad (3.37)$$

where parameters n, α, β, γ are considered the same for all springs, but in general may be different. The formulation takes into account the coupling of axial and shear forces and moments through the inherent equilibrium coupling. One way to treat interaction of internal variables during plasticity is through the evaluation of the yield parameters z_y^n, z_y^t and z_y^φ. The interaction of these parameters can be implicitly accounted for, through the evaluation for example, of the bending yield parameter for the anticipated level of axial forces, considering axial-bending interaction. A more formal formulation would be to employ the interaction matrix of equation (2.35) together with a yield criterion

expressed in terms of hysteretic forces which results in the following modification of equations (3.36):

$$\begin{Bmatrix} \dot{z}_n \\ \dot{z}_t \\ \dot{z}_\varphi \end{Bmatrix} = \left([I] - H_1 H_2 [R] \right) \begin{Bmatrix} \dot{\delta}_n \\ \dot{\delta}_t \\ \dot{\delta}_\varphi \end{Bmatrix} \tag{3.38}$$

with I being a 3×3 identity matrix. The evolution equations of the hysteretic forces are expressed as:

$$\left\{ \dot{F}^h \right\} = \begin{Bmatrix} \dot{F}_n^h \\ \dot{F}_t^h \\ \dot{M}^h \end{Bmatrix} = [\mathrm{B}]^T \begin{bmatrix} (1-a)k_n & 0 & 0 \\ 0 & (1-a)k_t & 0 \\ 0 & 0 & (1-a)k_\varphi \end{bmatrix} \left([I] - H_1 H_2 [R] \right) \begin{Bmatrix} \dot{\delta}_n \\ \dot{\delta}_t \\ \dot{\delta}_\varphi \end{Bmatrix} \tag{3.39}$$

In the above equations H_1 and H_2 are evaluated as:

$$\begin{aligned} H_1 &= \left\| \Phi\left(F_n^h \quad F_t^h \quad M^h \right) + 1 \right\|^n \\ H_2 &= \gamma + \beta \operatorname{sgn}\left(\left\{ F_n^h \quad F_t^h \quad M^h \right\} \begin{Bmatrix} \dot{\delta}_n \\ \dot{\delta}_t \\ \dot{\delta}_\varphi \end{Bmatrix} \right) \end{aligned} \tag{3.40}$$

and Φ is the yield criterion such that:

$$\Phi\left(\left\{ F^h \right\} \right) - 1 \le 0 \tag{3.41}$$

Finally, the interaction matrix can be expressed as:

$$[R] = \left[\left(\frac{\partial \Phi}{\partial \left\{ F^h \right\}} \right)^T [E] \left(\frac{\partial \Phi}{\partial \left\{ F^h \right\}} \right) \right]^{-1} \left[\left(\frac{\partial \Phi}{\partial \left\{ F^h \right\}} \right) \left(\frac{\partial \Phi}{\partial \left\{ F^h \right\}} \right)^T [E] \right] \tag{3.42}$$

Combining all the elements hysteretic stiffness matrices the structure hysteretic matrix $[H]_s$ can be derived, with dimensions $(3\times n, 3\times n_{el})$ where n_{el} is the number of elements and n is the number of nodes. The dynamic equation of motion has the following form:

$$[M]_s\{\ddot{u}\}+[C]_s\{\dot{u}\}+[K]_s\{u\}+[H]_s\{z\}=\{P(t)\} \tag{3.43}$$

The equation of motion together with the differential equations of Bouc-Wen type are solved simultaneously. The linear equations of motion with respect to the displacement vector $\{u\}$ can be solved using Newmark's method together with a Runge-Kutta integrator for the nonlinear evolution equations in coupled form. An alternative approach is to transform the system into state-space form by introducing as additional unknown the vector of nodal velocities $\{\dot{u}\}$. This way the dynamic equilibrium equations are transformed into a set of linear differential equations of first order coupled with the nonlinear first order Bouc-Wen evolution equations.

$$\begin{Bmatrix}\{\dot{u}\}\\ \{\ddot{u}\}\end{Bmatrix}=\begin{bmatrix}0 & I & 0\\ -[M]^{-1}[K] & -[M]^{-1}[C] & -[M]^{-1}[H]\end{bmatrix}\begin{Bmatrix}\{u\}\\ \{\dot{u}\}\\ \{z\}\end{Bmatrix}+\begin{Bmatrix}0\\ \{P(t)\}\end{Bmatrix} \tag{3.44}$$

with the nonlinear hysteretic equations being in the form of:

$$\{\dot{z}\}=f\left(\{\dot{u}\},\{z\}\right) \tag{3.45}$$

Combined the previous relations lead to the following augmented system to be solved

$$\{\dot{x}\}=G\left(\{x\}\right)+\{F(t)\} \tag{3.46}$$

where the matrix G is a state dependent operator and has the form:

$$G\left(\{x\}\right)=\begin{bmatrix}0 & I & 0\\ -[M]^{-1}[K] & -[M]^{-1}[C] & -[M]^{-1}[H]\\ 0 & Y\left(\{\dot{u}\},\{z\}\right) & 0\end{bmatrix} \tag{3.47}$$

and $\{x\}$ is the augmented vector:

$$\{x\} = \begin{bmatrix} \{u\} \\ \{\dot{u}\} \\ \{z\} \end{bmatrix} \tag{3.48}$$

In relation (3.47) evolution equations are in implicit form in the third row for all elements. The above system of differential equations, for a given dynamic loading and initial conditions can be integrated using robust numerical integrators such as Runge-Kutta or Livermore algorithms [106]. In this work a variable order solver based on numerical differentiation formulas is used [111] that is proved more efficient. In addition, since the differential equations of each element are uncoupled, they can be solved in parallel allowing for effective use of massively parallel supercomputers and faster calculations.

The entire formulation focuses on the displacement field and the forces and moments developed at the rigid cells. In this respect the stress field is concentrated at the facets while at the cells is circumvented rendering the method appropriate for the contemporary displacement based and performance-based design procedures.

3.5 Fracture representation in RBSN

There are three modes of fracture depicted in Figure 3.8. They are distinguished based on the stress that drives the crack opening. In Mode I the crack tip is propagating due to tensile stress, normal to the crack surface. In Mode II, there is shear stress driving the crack movement that is parallel to the crack surface. Mode III is a tearing mode in a sense that the shear stress acting on the crack is out of the plane of the crack surface.

Several criteria have been proposed for the simulation of initiation and propagation of the crack as well as to best determine its path. [76]. In Linear Elastic Fracture Mechanics, the most common used criteria are the Maximum Tangential Stress criterion (MTS [50]), the

Minimum Strain Energy Density (MSED [113]) criterion and the Maximum Energy Release Rate (MERR [100]) criterion.

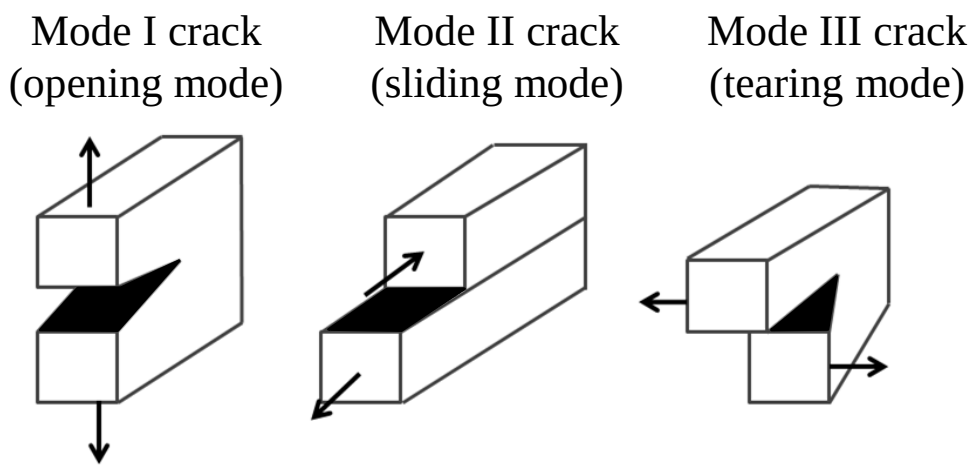

Figure 3.8: Three fracture models.

In numerical methods the models simulating crack initiation and propagation can be divided into three main categories:

- Continuum damage models.
- Discrete models of fracture.
- Models based on variational principles.

The RBSN model provides a discrete representation of the structure. Crack opening and crack propagation is therefore bound to develop at the interfaces of the cells. This means that crack movement is directly affected by the local shape of the tessellation. According to [110] regular meshing strategies create a bias of fracture movement towards the predetermined cracking directions. A triangular lattice for example offers three distinct directions for crack movement. Some authors have developed adaptive algorithms for remeshing the area around the crack tip in finite element [70] and boundary element [29] methods. When adaptive strategies are not implemented or the fracture is not localized, random mesh design is an effective strategy for minimizing bias towards crack movement.

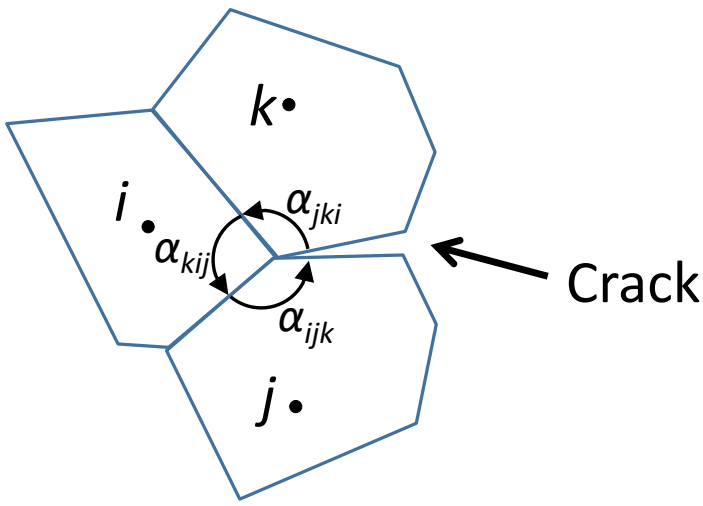

Figure 3.9: Typical three cell Voronoi assembly and crack opening at the interface of two cells *k* and *j*.

Using the Voronoi tessellation, the edges of the cells that are created are met, except under special conditions, in triple junctions as in Figure 3.9. Because Voronoi tessellation divides the domain into convex polygons all the angles at the junctions will be smaller than 180°. For a random distribution of points using the minimum distance criterion and the number of points approaching $\hat{n}$ as previously mentioned the mean value of the angles α that are formed is 120° with smaller variance. This leads to a greater degree of isotropy regarding possible crack movement.

Several spring braking rules have been proposed by authors mainly based on critical energy or critical stress [73]. In this work a simpler approach is utilized. Both crack initiation and crack propagation obey simple cut-off rule in combination with a Mohr-Coulomb type of criterion for normal and tangential stresses, following the work in [20]. In each computational cycle the stress of the normal and tangential (s_n and s_t respectively) springs are calculated as:

$$s_n = \frac{q_n}{(S_{ij}t)}, \qquad s_t = \frac{q_t}{(S_{ij}t)} \tag{3.49}$$

where S_{ij} is the length of the common facet of particles i and j, t is the thickness of the structure, q_n and q_t are the normal and tangential forces acting on the respective local springs. These are then used to calculate r as:

$$r = \sqrt{\left(s_n^{\ 2} + s_t^{\ 2}\right)} \tag{3.50}$$

i.e. the distance from the origin in the normal and tangential stress space, and are compared to the fracture surface with the criterion:

$$R = \frac{r}{r_f} > 1 \tag{3.51}$$

where r_f defines the area in the stress field, inside which every pair of normal ant tangential stresses don't lead to fracture, and can be seen in Figure 3.10.

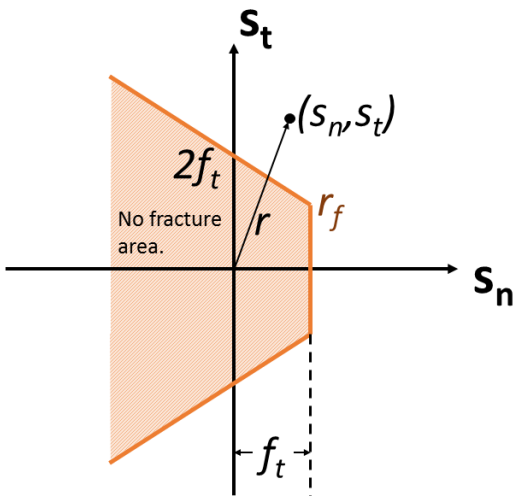

Figure 3.10: Mohr-Coulomb type of criterion with cut-off for normal stresses

If the fracture criterion is satisfied then for this surface, and therefore element, brittle fracture is assumed. This means that the element spring forces are released and the local spring stiffnesses are set to zero. Only one fracture event is allowed for each computational cycle and that is the element with highest R. In order to advance to the next computational step all stresses must lie within the fracture surface. In addition, the

criterion assumes traction free cracks and although, using the Voronoi tessellation the mesh bias regarding crack movement is minimized, crack propagation is not objective with different mesh sizes. Although simple in its apprehension and implementation, the fracture criterion should be extended to account for proper fracture energy calculation.

3.6 RBSN – Single element verification

3.6.1 Plasticity

For this first example a 1x0.5*m* domain is discretized with 2 nodes and 1 element as shown in Figure 3.11 using the RBSN model. This demonstrates the hysteretic behavior at the elemental level, which is easier to follow, as in models with a large number of elements the overall behavior is reflected. The material is steel S235 with an elastic modulus of 210*GPa*, the Poisson ratio is set to 0.3 and the thickness of the model is assumed to be 0.02*m*. The first node is fixed and a sinusoidal force of increasing amplitude with a maximum value of 2700*kN* is applied to the second node in the horizontal direction as in Figure 3.12. The analytical expression of the applied force time history is as follows.

$$P(t) = 2700\frac{t}{T_{end}}\sin(3\pi t) \tag{3.52}$$

The analysis run for T_{end}=5*sec*. The Bouc-Wen parameters are set to $n = 8$ and $\beta = \gamma = 0.5$. The ratio of the inelastic to the elastic stiffness, i.e. the slope of the post yield branch is considered to be 5%.

The resulting force-displacement diagram is shown in Figure 3.13. The results display the hysteretic loops due to the dynamic external loading exceeding the yield force of 2350*kN* and the slope of the post elastic regime is at 5% of the initial elastic stiffness validating the numerical code.

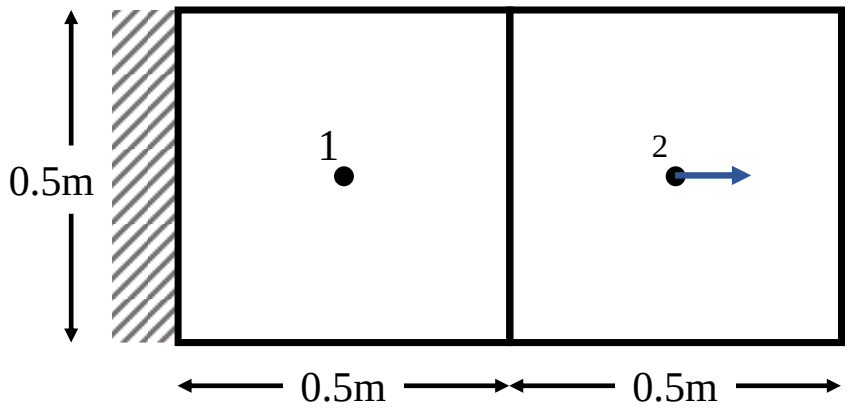

Figure 3.11: Single element geometry for plasticity

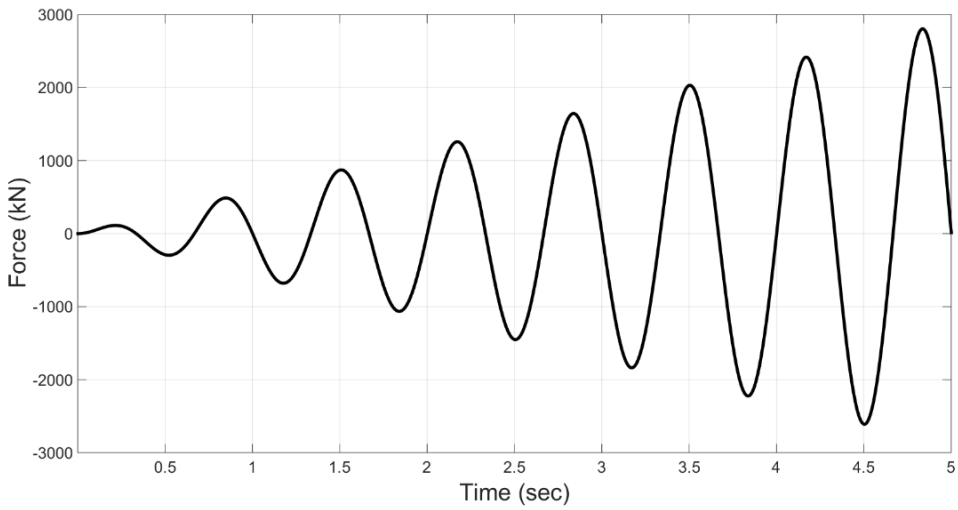

Figure 3.12: Applied load time history

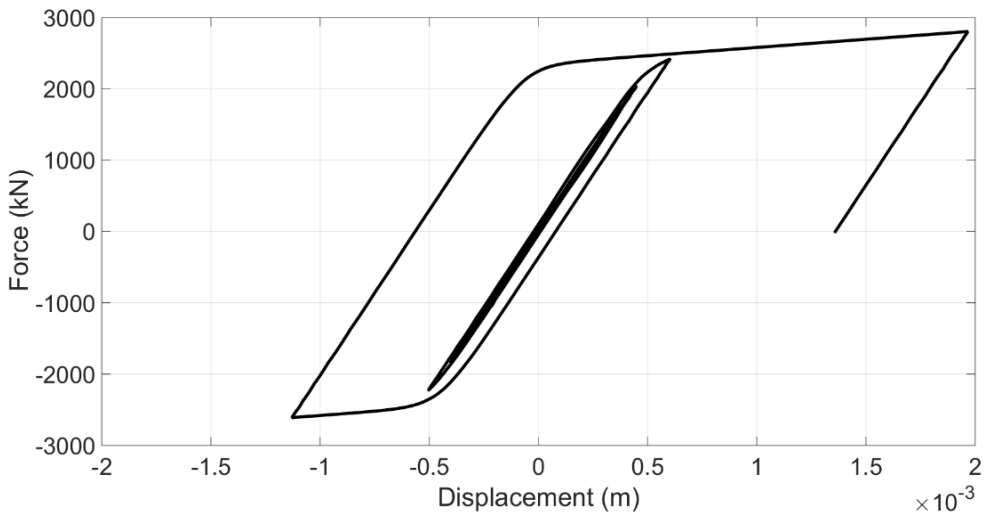

Figure 3.13: Force-Displacement diagram

3.6.2 Plasticity and fracture

For a second example a 1x0.1*m* domain is discretized with 2 nodes and 1 element as shown in Figure 3.14 and the thickness of the model is 0.05*m*:

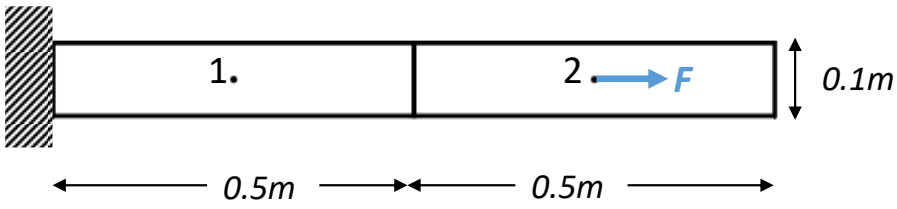

Figure 3.14: Single element geometry for plasticity and fracture

This example demonstrates the hysteretic behavior and fracture propagation at elemental level and is used to verify the methodology and the developed codes. The material parameters are depicted in the following Table:

Description	Symbol	Value
Elastic modulus	E	$210GPa$
Yield stress	σ_y	16
Hysteretic loop shape factors	$\beta = \gamma$	0.5
Smoothness parameter	n	8
Post yield stiffness ratio	a	2%
Yield strain	z_y	0.00112

Table 3-1: Parameters of single element example with plasticity and fracture

The specimen is fixed on one side and the force is pseudo static applied in the x direction on the other side. The yield force for this simple tensile case can be evaluated analytically as:

$$F_y = \sigma_y \cdot \mathrm{A} = 240000\left(kN/m^2\right)\cdot 0.1(m)\cdot 0.05(m) = 1200kN \qquad (3.53)$$

Fracture is considered at $1.15\sigma_y = 1320kN$. A monotonically increasing force is applied with maximum value of $1400kN$. Force – displacement results are shown in Figure 3.15. As expected, yielding occurs around $1200kN$ while fracture occurs at $1318kN$ denoted in Figure 3.15 by the red dot. After that time the algorithm followed a straight line since the

stiffnesses of the internal springs where released and thus the structures stiffness matrix was singular.

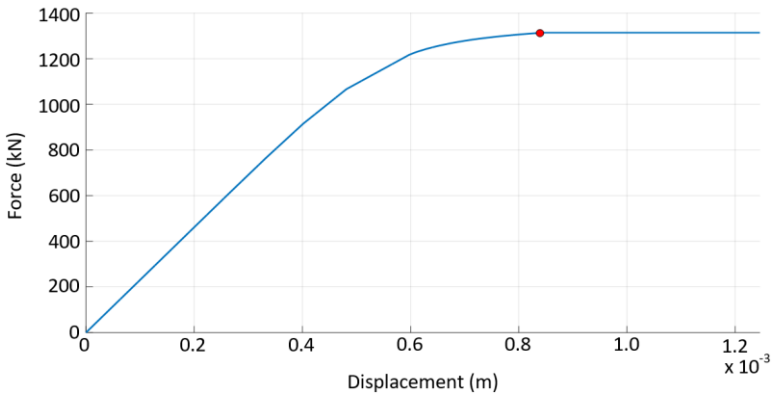

Figure 3.15: Single element force displacement curve with fracture at the red dot

3.7 Mesh sensitivity in RBSN

3.7.1 Elasticity

In this analysis, the effect the RBSN mesh density has on the overall solution, is examined. To this end, a cantilever beam is assumed with dimensions of 1x0.1m. The beam is considered elastic and is loaded at its free end. For this case, the analytical solution is known for the deflection of the free end and is given by the following formula:

$$\delta = \frac{Pl^3}{3EI} \tag{3.54}$$

Assuming the Young's modulus, load and depth of the beam are $E=400000\ N/m^2$, $P=1N$ and $b=1m$ respectively, then from Equation 1, the deflection of the beam is calculated as $0.01m$. For the RBSN a Poisson ration of 0.3 is additionally considered. Eight set of analyses were run. In each set a different minimum distance criterion is chosen starting from $0.05m$ for a crude mesh to $0.005m$ for a very fine mesh. Moreover, since the point generation is random, three analyses are carried out in each set. The eight minimum distances studied, as well as an indicative discretization for each case, are shown in Figure

3.16. At the two ends of the beam the points are strategically placed in a uniform manner in order to facilitate the imposition of essential boundary conditions and loads. Results regarding the deflection of tip of the beam are presented in Figure 3.17 as well as in Table 3-2, together with the number of nodes and number of elements for each model. As it can be observed, the RBSN approaches the correct solution and can reach satisfactory results even with the crude mesh. However, as the minimum distance is lowered, the mesh becomes finer, and results appear to deviate from the correct solution, with the overall structure becoming less stiff. This mesh dependency is a characteristic of lattice systems in general. The ability of a lattice model to be used as an idealization of a structure should be investigated further and validated.

Minimum distance (m)	Case	Deflection (m)	Number of cells	Number of elements
0.050	A	0.009212	40	78
	B	0.009529	43	86
	C	0.009448	42	82
0.040	D	0.009528	63	138
	E	0.009501	63	137
	F	0.009542	61	130
0.030	G	0.010029	97	224
	H	0.009999	92	212
	I	0.010677	96	221
0.025	J	0.010559	130	313
	K	0.010511	128	307
	L	0.010421	129	310
0.020	M	0.010299	193	487
	N	0010569	194	489
	O	0.010701	189	473
0.015	P	0.010684	326	862
	Q	0.010829	335	882
	R	0.010738	331	873
0.010	S	0.011433	705	1931
	T	0.011407	725	1992
	U	0.011623	715	1958
0.005	V	0.011728	2765	7784
	W	0.011683	2760	7769
	X	0.011651	2770	7791

Table 3-2: Elastic analyses results

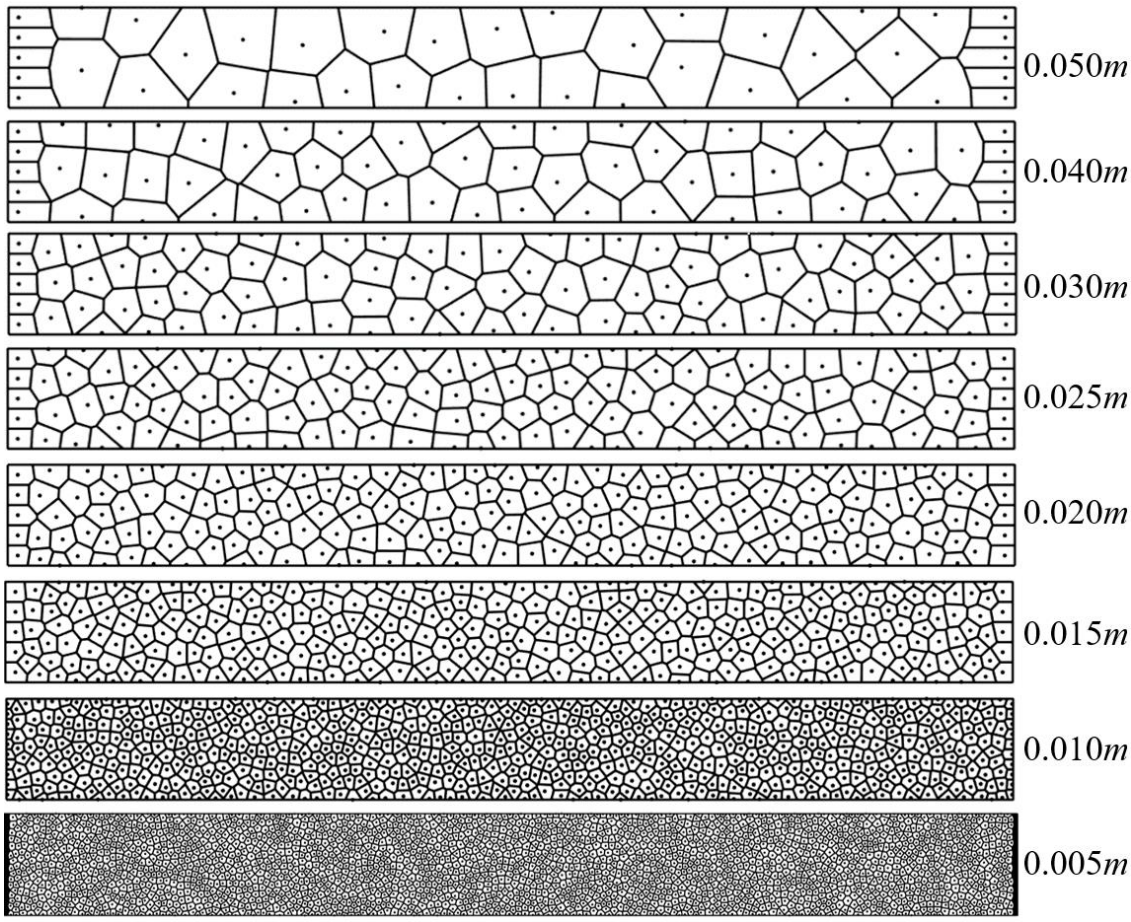

Figure 3.16: Minimum distances and resulting meshes

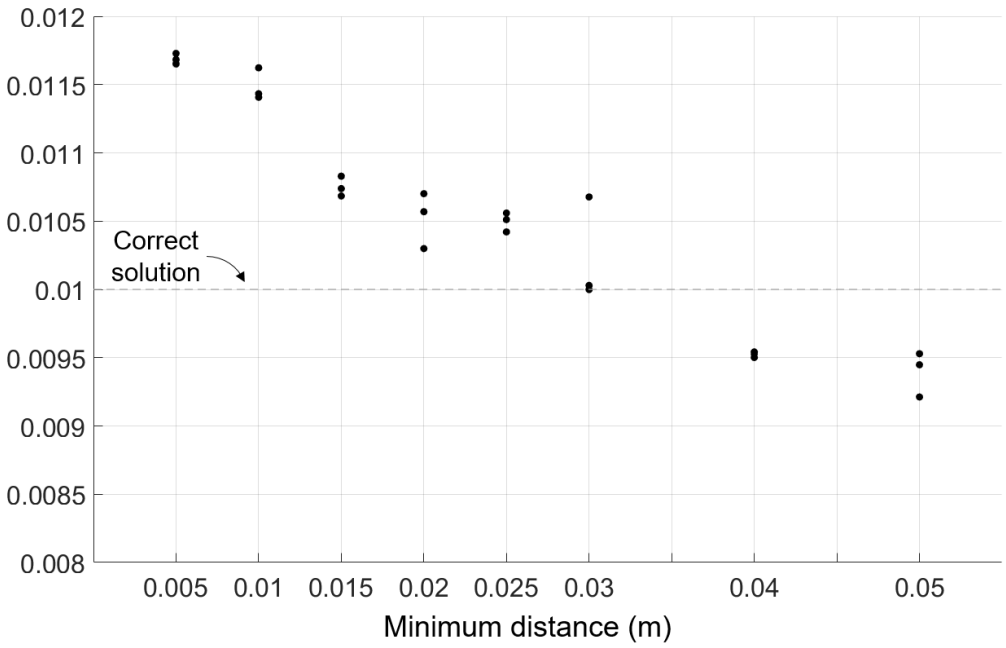

Figure 3.17: Cantilever beam tip displacement for all analyses

3.7.2 Plasticity

In order to investigate the mesh dependency of RBSN when plasticity is concerned two cases are being investigated. In the first case, a steel beam with dimensions 1x0.2m is examined. The beam is loaded with a sinusoidal load that leads to the beam exciding its yield point. Firstly, results are compared with Finite Element codes for the dynamic problem to ensure and verify the accuracy of the proposed formulation. Secondly, 10 more analyses are being carried out. In these analyses the total number of nodes that the beam is discretized is kept the same. This explores how the randomness of the directions of the facets affects the results in hysteretic simulations.

For the second case an aluminum plate with a central hole is studied. The load is a constantly increasing one that leads to the plates yielding. In this case the plate is discretized with a various number of nodes and different minimum distance criteria. The structure is discretized with 53, 109 and 315 nodes. This is to investigate how mesh and element size affects the numerical results, which are compared with results from Finite Element codes.

3.7.3 Random node positions, fixed beam,

This example refers to the dynamic response of a beam with dimensions 1x0.2*m* and *0.02m* thickness, to a sinusoidal excitation. Material is steel S235 with 5% hardening and *5%* damping. Beam discretization is presented in Figure 3.18.

The number of nodes is 64 for this first analysis and the number of elements is 146 with a minimum distance of 5*cm*. The force at the end of the beam is harmonic and acts in the vertical direction with a maximum value of 75*kN*. In ANSYS [6] a bilinear model with kinematic hardening is used with 1cm quadrilateral elements. In Figure 3.18 the plastic

regions developed in the beam at the final instance of the applied dynamic loading are presented. These are concentrated as expected near the fixed support.

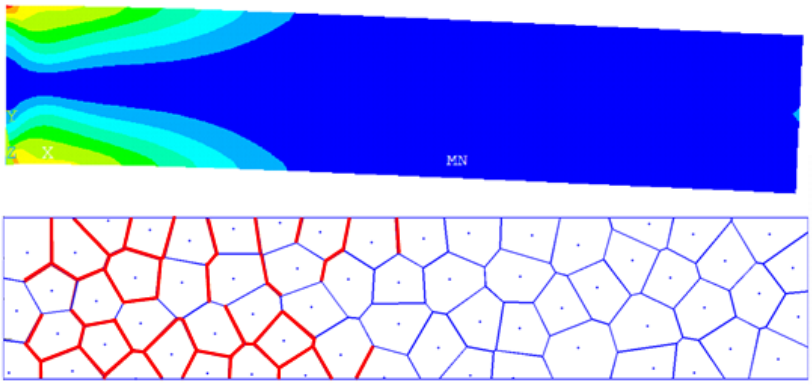

Figure 3.18: Beam plastic regions (ANSYS up vs RBSN model down)

The regions that underwent plasticity are similar in both cases for this specific coarse discretization, although in the Rigid Body Spring Network model with Bouc-Wen they seem to extend further along the length of the beam. In Figure 3.19 the displacements of the free end of the beam are compared between ANSYS and the proposed formulation. The results are in good agreement considering the differences of the two methods. It is apparent that the proposed method is capable of expressing the main characteristics of the hysteretic behavior.

In addition to the previous analysis, the same structure is discretized 10 different times using, for all cases, the same minimum distance criterion of 5cm. Since the node generation is based on a random procedure, each discretization will be slightly different from one another, resulting in different shaped elements and various facet orientations. The purpose of this analysis is to examine the effect of the randomness of discretization in the overall behavior of the structure when hysteresis is involved, for similar element numbers. In Figure 3.20 the different discretization of the beam for the 10 different cases are presented while the corresponding results are all plotted in Figure 3.21. They are presented in the form of the displacements of the free end of the beam.

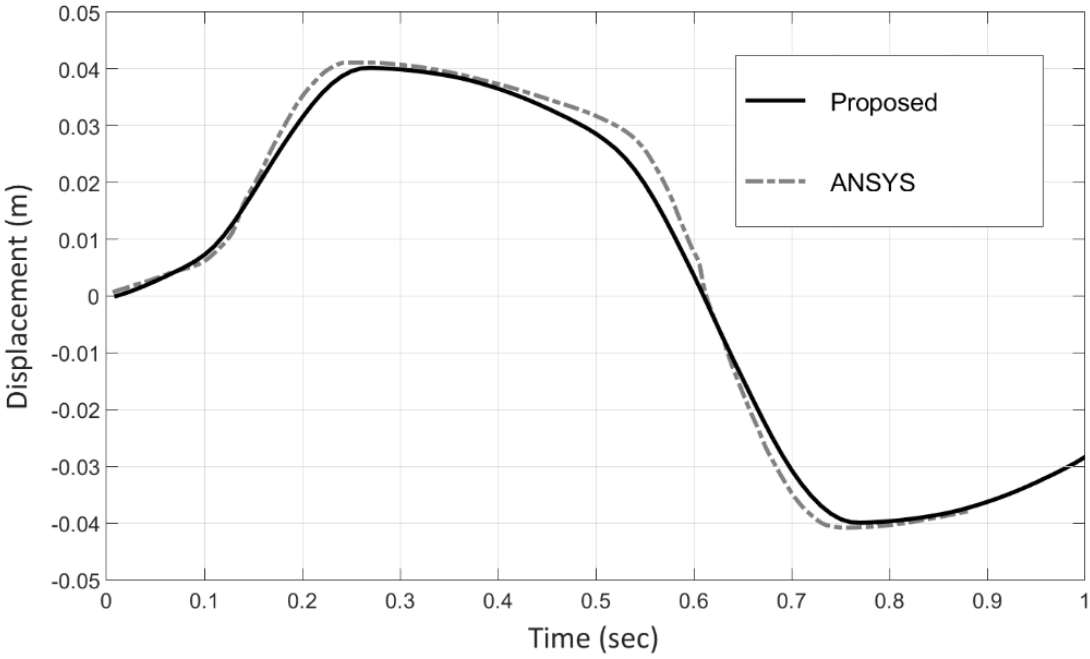

Figure 3.19: Beam free end displacement vs time

It can be observed that the global behavior of the structure is indeed slightly affected for this crude discretization criterion similarly to the results from the elastic static analyses of Paragraph 3.7.1. In the next example, the effect of the mesh element size on the overall hysteretic response is going to be investigated.

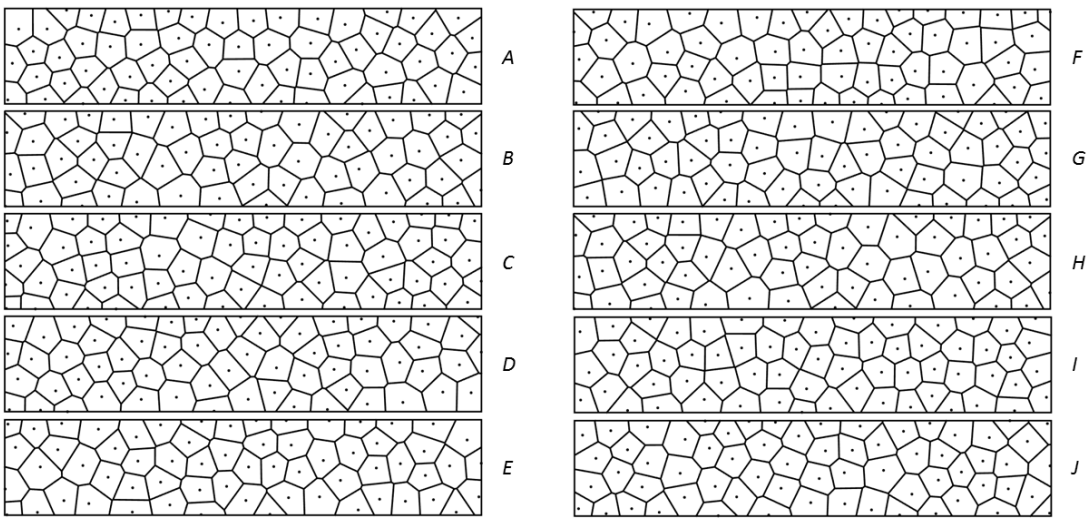

Figure 3.20: Different discretization with same minimum distance criterion of 5cm

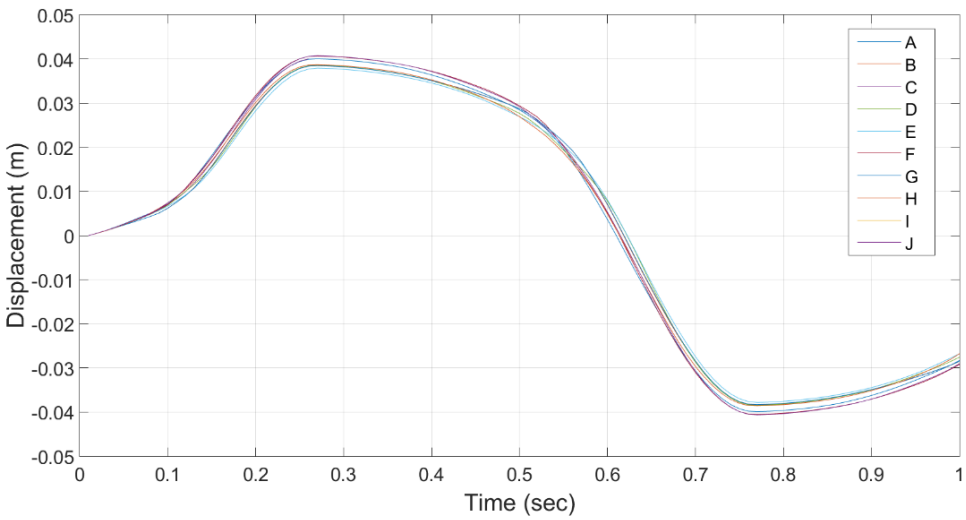

Figure 3.21: Beam free end displacement vs time for 10 different discretization schemes

3.7.4 Increasing number of elements, perforated sheet

In this example, an aluminum plate with a central circular hole is examined. Material parameters are $E = 72\,GPa,\ v = 0.22$, $\sigma_y = 262\,MPa,\ a = 0.002$. Bouc-Wen parameters used are $\beta = \gamma = 0.5$ and $n = 8$. Due to symmetry of the model only a quarter is analyzed with the boundary conditions and loads applied on nodes. The geometry is presented in Figure 3.22, while the reduced discretized model due to symmetry, with the appropriate support conditions are schematically presented in Figure 3.23.

Three analyses are carried out. For the first analysis the minimum distance between nodes is set to 5cm. This way the total number of nodes for the simulation is 53, while the number of elements is 128. For the second case the minimum distance is set to 3cm thus creating 109 nodes and 289 elements and for the third a minimum distance of 2cm resulting in 315 nodes and 873 elements. In all cases the nodes along the perimeter are manually placed, while interior nodes are placed automatically following the minimum distance rule.

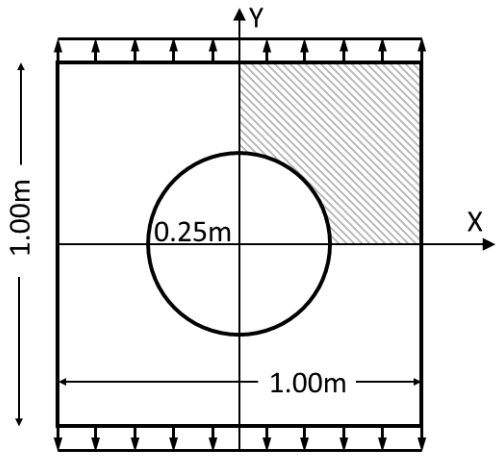

Figure 3.22: Geometry of metal sheet with central hole

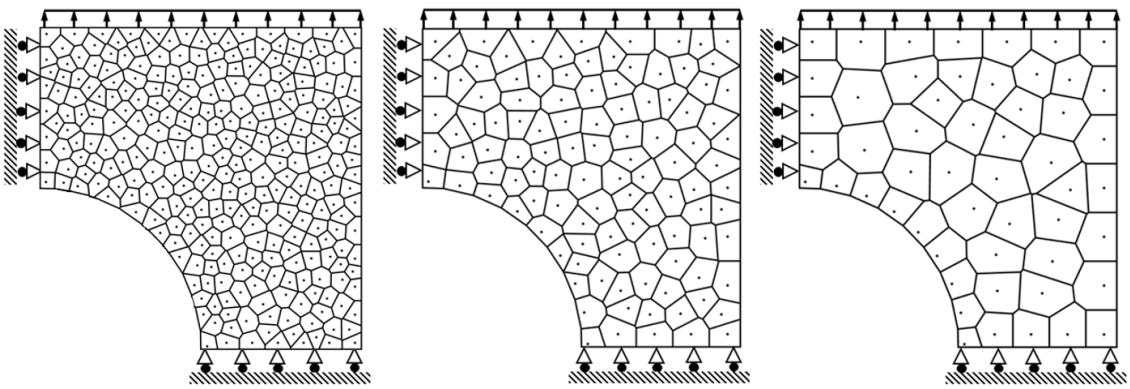

Figure 3.23: Different discretization (873, 289 and 128 elements) for the reduced model

The displacement of the upper left node of the model is examined and the force-displacement diagram is presented in Figure 3.24. Results are compared with those obtained using the elastoplastic Finite Element HYPLAS code [97] as well as in [126]. The solution obtained from the proposed formulation is in good agreement with the other solutions, showing the model's ability to simulate hysteretic behavior of various plane structures. There are some differences present in the transition from the elastic to the inelastic branch for the discretization with 5cm minimum distance criterion (128 elements). For this case, the load – displacement curve of the proposed model appears to

be smoother and yielding seems to occur at a smaller load. This can be attributed to the coarse discretization due to the larger minimum distance criterion used.

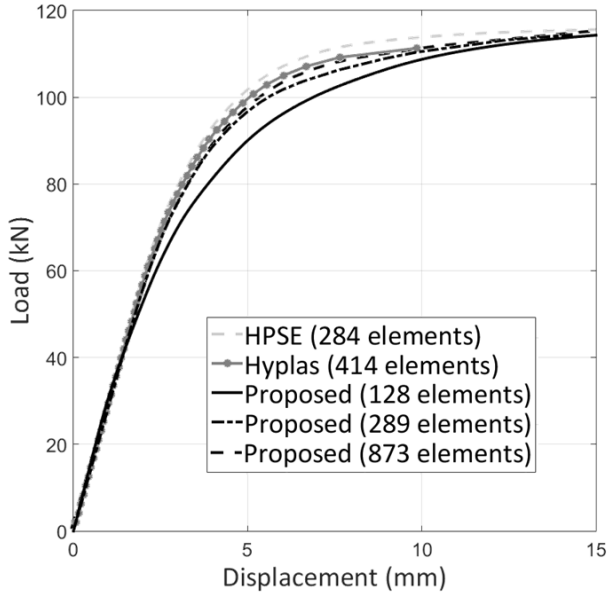

Figure 3.24: Load displacement curves comparison

By reducing the minimum distance, the structure is discretized with more nodes and elements and gives better results. This indicates the mesh density dependency of the RBSN models. However even with coarser discretization numerical results approach the correct solution in an effective manner

4 Material Point Method

4.1 Introduction

The Material Point Method (MPM) is a hybrid method in a sense that it employs both a Lagrangian and an Eulerian description. It is also a discrete method in a sense that all the information is carried by the particles and the mesh is only used for calculations. The Material Point Method can be considered as a successor of Particle-In-Cell (PIC) methods. The first PIC formulation was developed in 1955 by Harlow [63, 65, 64] and was mainly used in fluid mechanics problems. In PIC both Lagrangian and Eulerian descriptions are employed, in a sense that the fluid is discretized with Lagrangian particles but the computational mesh is Eulerian. The Lagrangian particles in PIC carry some material properties like position and mass. The method can be divided into two distinct phases for each computational step. The first phase is the Lagrangian one, where all the variables are updated. This includes the nodal positions of the mesh. In the second phase, the Eulerian one, the computational mesh is reset to its original position and the particles remain at their updated positions. In PIC some information is stored in the computational grid while particles carry only mass and positional information. The main issue of the PIC method was numerical dissipation, because of the mapping process from the particles to the grid and vice versa. This was later solved in 1986, by Brackbill and Ruppel with the formulation and development of the FLIP method, the Fluid Implicit Particle method [23, 24]. In this method, the particles are fully Lagrangian, all the information is stored in the particles, including energy and momentum and thus convective transport, the largest source of computational diffusion in calculations of fluid flow is removed. The FLIP has been later modified and extended for applications in solid mechanics in 1994 by Sulsky et al. [120] and the Material Point Method has been formed.

MPM has a significant advantage over FLIP for the simulation of history dependent materials, in a sense that stresses and strains are stored in the particles, and not in the

element centers as in FLIP. Moreover, the MPM is formulated in the weak form, similar to FEM, and thus bears many similarities with existing FEM procedures. The particles in MPM hold the full physical state of the material such as position, mass, velocity, acceleration, stress, strains etc. The MPM employs both kinematic descriptions similar to PIC algorithms, which are the use of Lagrangian material points that carry all the physical information, and a background Eulerian grid used for the discretization of continuous fields (i.e., displacement field). Therefore, the MPM combines the advantages of both Eulerian and Lagrangian methods.

Considering the Lagrangian description, the material points and the background grid are attached and deform together during loading in a similar manner to FEM. This means that since each material point carries the deformation gradient and stresses, as well as history variables, modeling of history-dependent materials is straightforward. The grid is reset at the end of each time step to its original configuration. This means that the grid does not become distorted in large deformation problems. MPM employs a grid from an Eulerian point of reference that is fixed in space and the material points that move along the mesh.

The mathematical formulation of MPM from the basics of continuum mechanics to the weak form and spatial discretization are presented in the subsequent paragraphs.

4.1.1 Continuum Mechanics

In order to proceed with the formal mathematical description of the Material Point Method, several fundamental notions of continuum mechanics [141] will be presented in the following paragraphs. We start by considering a continuum body that is moving (Figure 4.1). The body is its initial undeformed configuration is occupying a region Ω at time $t = 0$. Within this body we isolate a material point or particle that moves from its original position. The initial position of the particle is P at time $t = 0$ with coordinates

given by vector $\boldsymbol{X}$, while its current position is p at time t with coordinates given by vector $\boldsymbol{x}$.

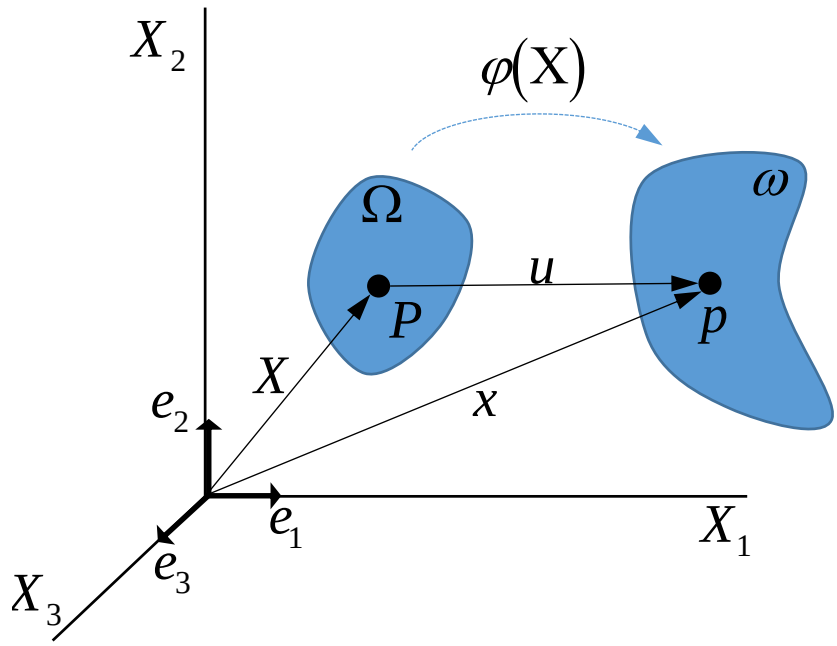

Figure 4.1: Initial and deformed configuration

The coordinates are given by:

$$\boldsymbol{X} = X_i \boldsymbol{e}_i , \qquad i = 1,2,3 \tag{4.1}$$

where $\boldsymbol{e}_i$ is the unit vector of the spatial coordinate system (which is considered the same both for the material and the spatial coordinates). The region of space that the body occupies at time t is called the current – deformed configuration, ω. One configuration should be chosen as the reference configuration, meaning the configuration to which the motion will be referred to. Usually the initial configuration is chosen as the reference configuration.

The deformation of the body is defined by a smooth one-to-one function φ:

$$\varphi : \Omega \rightarrow \omega \tag{4.2}$$

which maps each material particle from its original position P to its current position p:

$$\boldsymbol{x} = x_i \boldsymbol{e}_i = \varphi(\boldsymbol{X}), \qquad i = 1,2,3 \tag{4.3}$$

where, as presented in Figure 4.1, $\boldsymbol{X}$ is the position vector of a particle in the reference configuration. The coordinates X_i are the material (Lagrangian) coordinates while x_i are the spatial (Eulerian) coordinates.

In the Lagrangian description, an observer is standing in the body-frame and observes the changes in the position and physical properties as the continuum body moves in space with time, which is commonly used in solid mechanics. These physical properties are described in terms of the material coordinates $\boldsymbol{X}$ and the reference configuration is the initial one. The body motion is given as:

$$\boldsymbol{x} = \boldsymbol{x}(\boldsymbol{X}, t) \tag{4.4}$$

signifying the mapping from the initial configuration Ω to the current one ω. The displacement field can then be expressed as:

$$\boldsymbol{u} = \boldsymbol{x}(\boldsymbol{X}, t) - \boldsymbol{X} \tag{4.5}$$

which is in terms of the material coordinates.

The Eulerian description on the other hand, is focused on what is occurring at a fixed point in space as time progresses. The current configuration is the reference configuration and the description is in terms of spatial coordinates $\boldsymbol{x}$ .Therefore, no history-dependency is considered in the Eulerian description. This approach is commonly used in fluid mechanics. The body motion is given as:

$$\boldsymbol{X} = \boldsymbol{X}(\boldsymbol{x}, t) \tag{4.6}$$

signifying that the particle with position vector x in the current configuration is the same that had position vector $\boldsymbol{X}$ in the undeformed one. The displacement field can then be expressed as:

$$\boldsymbol{u} = \boldsymbol{x} - \boldsymbol{X}\left(\boldsymbol{x}, t\right) \tag{4.7}$$

which is in terms of the material coordinates.

In order to obtain the velocity and acceleration field, the partial derivative of $\boldsymbol{x}$ with respect to time has to be calculated with $\boldsymbol{X}$ being constant:

$$\dot{\boldsymbol{x}} = \frac{\partial \boldsymbol{u}\left(\boldsymbol{X}, t\right)}{\partial t} \tag{4.8}$$

and:

$$\ddot{\boldsymbol{x}} = \frac{\partial^2 \boldsymbol{u}\left(\boldsymbol{X}, t\right)}{\partial t^2} \tag{4.9}$$

4.1.2 Strong form

In this section the equations that govern the mechanical problems are presented and are derived from an updated Lagrangian approach [141,53], which is common in MPM. In the updated Lagrangian approach, the stress and strain measures are defined with respect to the current configuration.

The continuum must satisfy the conservation laws of thermodynamics. These are the conservation of mass, the conservation of momentum and finally energy conservation. Moreover, a constitutive equation is required, relating stresses and strains together with initial and boundary conditions.

4.1.2.1 Conservation of mass

The total mass of the body remains constant and thus the conservation of mass can be written as:

$$p\left(\boldsymbol{X}, t\right) J\left(\boldsymbol{X}, t\right) = p_0\left(\boldsymbol{X}\right) \tag{4.10}$$

where p is the current density at a local region of the body while p_0 is the local density of the body referring to the initial configuration and J is the Jacobian. In the MPM the mass of each material point remains constant during the analysis, and the volume it represents and its density vary, thus the conservation of mass is automatically satisfied.

4.1.2.2 Conservation of momentum

The conservation of linear momentum represents the motion of the body, i.e. Newton's second law of motion. Conservation of momentum is given by:

$$p\ddot{\boldsymbol{x}} - p\boldsymbol{b} - \boldsymbol{\sigma} \cdot \nabla = 0 \tag{4.11}$$

where $\ddot{x}$ is the acceleration, $\boldsymbol{b}$ is the vector of the body forces per unit mass acting on the body, $\boldsymbol{\sigma}$ is the stress and ∇ stands for the gradient operator. This represents a dynamic formulation since acceleration and inertia terms are taken into account. The equation of conservation of linear momentum relates the forces acting on a body (internal and external) with its kinematics. In the previous relation $\boldsymbol{\sigma} \cdot \nabla$ is the internal force while $p\boldsymbol{b}$ are the external forces acting on the body

4.1.2.3 Conservation of energy

If E is the internal energy per unit mass and ε the strains, the mechanical energy conservation equation is written as

$$p\dot{E} = \boldsymbol{\sigma} : \dot{\boldsymbol{\varepsilon}} + pv \cdot \boldsymbol{b} \tag{4.12}$$

In the previous equation thermal energy and heat effects are neglected. The only source of energy is mechanical work.

4.1.2.4 Initial and boundary conditions

The initial conditions are given for the displacements, velocities and stresses as:

$$\dot{\boldsymbol{u}}(\boldsymbol{X},\mathrm{t}=0)=\dot{\boldsymbol{u}}_{\boldsymbol{0}}(\boldsymbol{X}),\quad \boldsymbol{u}(\boldsymbol{X},\mathrm{t}=0)=\boldsymbol{u}_{\boldsymbol{0}}(\boldsymbol{X})\quad \boldsymbol{\sigma}(\boldsymbol{X},\mathrm{t}=0)=\boldsymbol{\sigma}_{\boldsymbol{0}}(\boldsymbol{X}) \tag{4.13}$$

While the boundary conditions are given in equation (4.14):

$$\dot{\boldsymbol{u}}(\boldsymbol{X},\mathrm{t}=0)=\dot{\boldsymbol{u}}_{\boldsymbol{0}}(\boldsymbol{X}),\quad \boldsymbol{u}(\boldsymbol{X},\mathrm{t}=0)=\boldsymbol{u}_{\boldsymbol{0}}(\boldsymbol{X})\quad \boldsymbol{\sigma}(\boldsymbol{X},\mathrm{t}=0)=\boldsymbol{\sigma}_{\boldsymbol{0}}(\boldsymbol{X}) \tag{4.14}$$

4.1.2.5 Constitutive relation

In order to completely describe the material behavior, a constitutive relation is needed, relating the stresses $\boldsymbol{\sigma}$ and strains $\boldsymbol{\varepsilon}$ in a simple form, or in a more general case relating the stresses of a body with some of it kinematics variables (such as the velocity gradient etc.):

$$\dot{\boldsymbol{\sigma}}=\boldsymbol{f}\left(\boldsymbol{\sigma},\dot{\boldsymbol{\varepsilon}},etc.\right) \tag{4.15}$$

This relation can take many forms for different formulations, materials or problems. The Cauchy stress can be used to express stresses, but its rate $\dot{\boldsymbol{\sigma}}$ is not objective. For this reason, the Jaumann stress rate $\dot{\boldsymbol{\sigma}}^{J}$ can be employed, which is objective and is given from:

$$\dot{\boldsymbol{\sigma}}^{J}=\dot{\boldsymbol{\sigma}}+\boldsymbol{\sigma}\cdot\boldsymbol{\Omega}-\boldsymbol{\Omega}\cdot\boldsymbol{\sigma} \tag{4.16}$$

where $\boldsymbol{\Omega}$ is the spin tensor (or rate of rotation).

4.1.3 Weak form and spatial discretization

The previous equations can completely describe the kinematics of a body and form a group of partial differential equations (PDEs). The solution of these differential equations analytically, is not trivial except for some simple cases. For this reason, they have to be solved numerically. There are mainly two categories of numerical methods for the solution of partial differential equations. The first, tries to find an approximate solution of the differential equations directly together with their boundary and initial conditions.

A notable example in this category is the finite difference method (FDM). The second category establishes a weak form of the PDEs, using test functions. The weak form is equivalent to the original PDEs, and is solved numerically. The MPM belongs in the second category and is based on the weak form formulation similar to FEM. The momentum equation (4.11) is multiplied by a test function which is the virtual displacements vector δu_i and after rearranging:

$$\int_{\Omega} \delta u_i \left(\sigma_{ij,j} - p\ddot{x}_i + pb_i \right) d\Omega = 0 \tag{4.17}$$

or:

$$\int_{\Omega} \delta u_i \sigma_{ij,j} d\Omega - \int_{\Omega} \delta u_i p\ddot{x}_i d\Omega + \int_{\Omega} \delta u_i pb_i d\Omega = 0 \tag{4.18}$$

The first term of equation (4.18) is given by the following equation:

$$\int_{\Omega} \delta u_i \sigma_{ij,j} d\Omega = \int_{\Omega} (\delta u_i \sigma_{ij})_{,j} d\Omega - \int_{\Omega} \delta u_{i,j} \sigma_{ij} d\Omega \tag{4.19}$$

Using the divergence theorem (Gauss theorem) the first term on the right-hand side of equation (4.19) can be written as:

$$\int_{\Omega} (\delta u_i \sigma_{ij})_{,j} d\Omega = \int_{\partial\Omega_t} \delta u_i t_i dS \tag{4.20}$$

where the traction boundary is denoted as $\partial\Omega_t$ and dS is the surface integral which is zero everywhere except the traction boundary and t_i is the vector containing the components of tractions.

Substituting equations (4.19) and (4.20) into (4.18), leads to the weak form of the momentum equation with traction boundary conditions:

$$\int_{\partial\Omega_t} \delta u_i t_i dS - \int_{\Omega} \delta u_{i,j} \sigma_{ij} d\Omega - \int_{\Omega} \delta u_i p\ddot{x}_i d\Omega + \int_{\Omega} \delta u_i pb_i d\Omega = 0 \tag{4.21}$$

and after rearranging:

$$\int_{\Omega} \delta u_{i,j} \sigma_{ij} d\Omega + \int_{\Omega} \delta u_i p \ddot{x}_i d\Omega = \int_{\Omega} \delta u_i p b_i d\Omega + \int_{\partial\Omega_t} \delta u_i t_i dS \tag{4.22}$$

Which signifies the virtual work balance:

$$\delta w^{int} + \delta w^{kin} = \delta w^{ext} \tag{4.23}$$

where δw^{int} is the virtual work of the internal forces, δw^{ext} is the virtual work of the external forces and δw^{kin} is the virtual work of the inertial terms:

$$\begin{aligned} \delta w^{ext} &= \int_{\Omega} \delta u_i p b_i d\Omega + \int_{\partial\Omega_t} \delta u_i t_i dS \\ \delta w^{int} &= \int_{\Omega} \delta u_{i,j} \sigma_{ij} d\Omega \\ \delta w^{kin} &= \int_{\Omega} \delta u_i p \ddot{x}_i d\Omega \end{aligned} \tag{4.24}$$

4.2 The MPM Algorithm

In the Material Point Method, a body is discretized into a number of material points (particles) that move through an Eulerian background grid (Figure 4.2). The material domain Ω can be represented by N_p number of material points. Each material point represents a subdomain Ω_p and holds all the properties such as mass m_p, position x_p, velocity v_p, strain ε_p and stress σ_p. The Eulerian background grid is employed to solve the equations of motion and to calculate the spatial gradient terms with N_g number of nodes. Since the total mass is divided into the material point set and the material points have constant mass through the simulation, the mass conservation is fulfilled. The strain rate is expressed in terms of the gradient velocity as:

$$\frac{d\varepsilon}{dt} = \frac{1}{2}\left(\nabla v + \left(\nabla v\right)^T\right) \tag{4.25}$$

and for the linear elastic case the constitutive equation relating stress rates and strain rates can be expressed using the constitutive matrix D as:

$$\frac{d\sigma}{dt} = D\frac{d\varepsilon}{dt} \tag{4.26}$$

where D in the general case, is the fourth-order elasticity tensor or in the case of plasticity the tangent stiffness matrix.

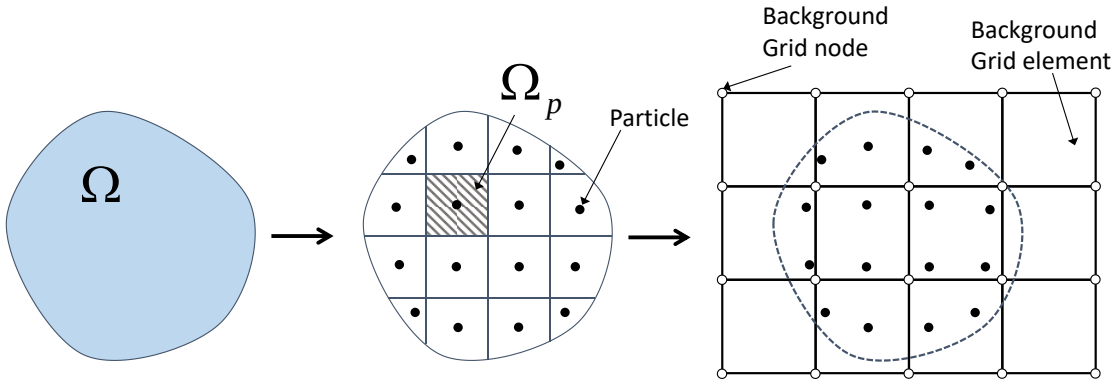

Figure 4.2: MPM discretization

In the Material Point Method each particle represents a sub-domain of the whole domain Ω . Using the Dirac delta function δ the mass density can be expressed as a function of the material point masses and the material point positions as:

$$p = \sum_{i=1}^{N_p} m_p \delta\left(x - x_p\right) \tag{4.27}$$

Substituting equation (4.27) into the weak form equation (4.22) results in:

$$\begin{aligned}\sum_{p=1}^{N_p} m_p \sigma_{ij}(x_p)\delta u_{i,j}(x_p) + \sum_{p=1}^{N_p} m_p \ddot{x}_i(x_p)\delta u_i(x_p) = \ldots \\ \ldots \sum_{p=1}^{N_p} m_p b_i(x_p)\delta u_i(x_p) + \sum_{p=1}^{N_p} m_p \frac{t_i(x_p)}{h}\delta u_i(x_p)\end{aligned} \tag{4.28}$$

Equation (4.27) plays an important role in the MPM since volume integrals can be converted to the sums of values of the integrand evaluated at each particle position and multiplied with the particle volume as:

$$\int f(x,y,z)dxdydz = \sum_{p=1}^{N_p} g(\chi_p, \psi_p, \zeta_p)V_p \tag{4.29}$$

Similar to the Finite Element Method, the material gradient terms are calculated on a background computational grid. Shape functions are used to approximate the solution and the velocity and acceleration of any material point are expressed in terms of the nodal accelerations of the grid as:

$$v\left(x_p\right) = \sum_{i=1}^{N} v_i N_i \tag{4.30}$$

and:

$$\alpha\left(x_p\right) = \sum_{i=1}^{N} \frac{dv_i}{dt} N_i \tag{4.31}$$

where in both relations the summation refers to the nodes of the element of the background grid that the material point resides in. In general, using shape functions the particle displacement $u_i(x_p)$ and virtual displacement $\delta u_i(x_p)$ can be calculated from the grid nodal displacement values as:

$$\begin{aligned} u_i(x_p) &= N_I(x_p)u_i(x_I) \\ \delta u_i(x_p) &= N_I(x_p)\delta u_i(x_I) \end{aligned} \tag{4.32}$$

Finally using equations (4.32) and (4.28) the momentum equation is retrieved in its discrete form at each grid node:

$$\sum_{i=1}^{N_g} m_i \frac{dv_i}{dt} = F_i^{\text{int}} + F_i^{ext} \tag{4.33}$$

The internal and the external forces are defined as:

$$F_i^{\text{int}} = -\sum_{i=1}^{N_p} \frac{m_{p,i}}{p_i} \sigma_{p,i} \nabla N_i \tag{4.34}$$

and:

$$F_i^{ext} = \tau_i + b_i \tag{4.35}$$

where the subscript p,i denotes the material point i.

In this work two types of shape functions are employed, either linear, for cases where the material points stay inside their original elements, or cubic B-Splines [4, 56, 117] for large deformation problems. A comparison between the two shape functions is investigated in Paragraph 4.6. In addition, for some benchmark problems a moving mesh MPM method is employed. For the majority of the presented examples though B-Splines are used. They have been shown to reduce the quadrature errors and the grid crossing errors associated with discontinuous shape function gradients when a material point crosses from an element to a neighbor one, and also prove to be superior in terms of stress calculations.

Many implementations are possible [118] and are explained in detail in the following Paragraph. The main algorithm of the MPM is described below and show schematically in Figure 4.3:

The structure is discretized into a set of material points and the relevant properties are given to the initial particle distribution including initial conditions. For each time step the following procedure is followed:

- The background structured mesh is generated.
- The shape functions and their derivatives are calculated.
- The state variables needed for the analysis are mapped from the material points to the background grid nodes.

- Momentum equation is solved at the background grid nodes.
- Material point state variables are updated.

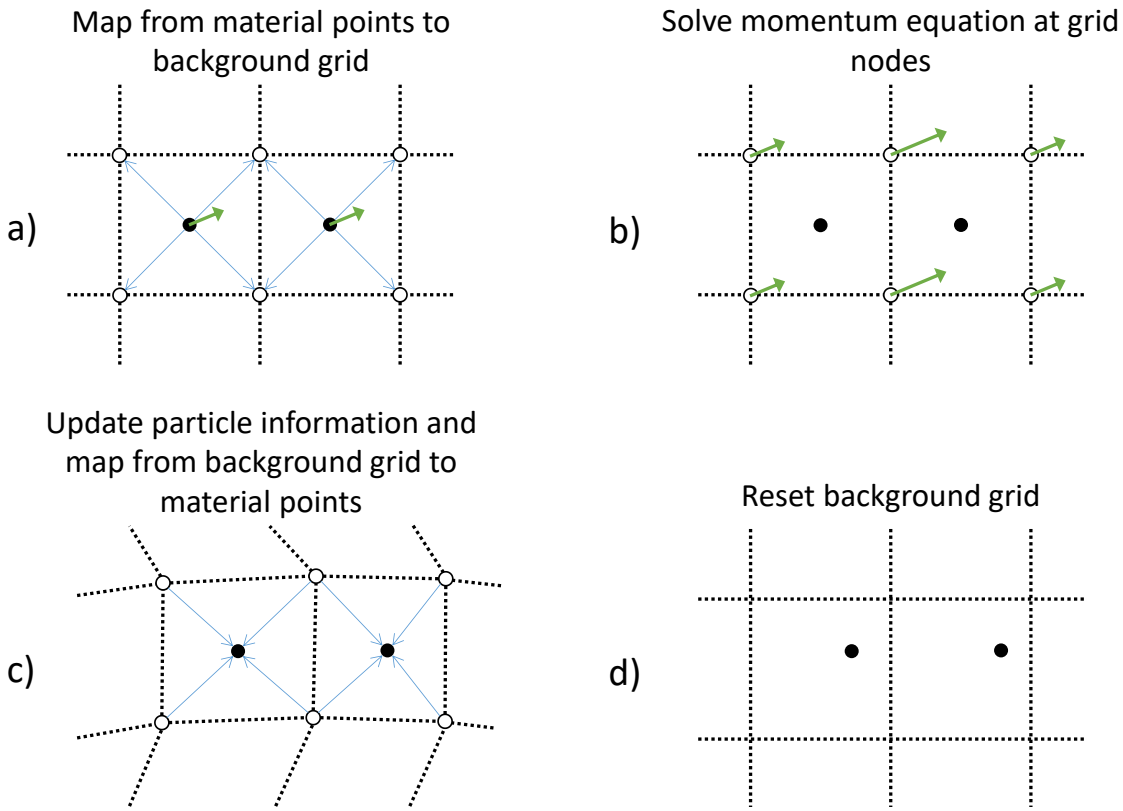

Figure 4.3: Schematic illustration of one MPM computational step

In this work the following algorithm is used for each time step in more detail, following a MUSL (Modified Update Stress Last) approach, which is explained in more detail in Paragraph 4.4:

1. Background grid is reset, and all its variables are set to zero (mass, momentum, forces).
2. The element number that each material point lies in is identified (which is trivial for a structured grid).
3. The shape functions and their derivatives are calculated. For each material point in 2D, 16 shape function values are calculated and 32 derivatives, since every material point maps its properties to 16 nodes when the cubic B-Splines shape

functions are used. The properties are mapped not only to the nodes of the cell the material point resides in but also in the surrounding cells. Instead, for the linear shape functions, 4 values are calculated and 8 derivatives. In this case the material points map their properties to the 4 nodes of the cell they reside in.

4. The material point mass, momentum and internal forces are mapped to the nodes of the background grid according to:

$$
\begin{aligned}
m_i &= \sum_{p=1}^{N_p} M_p N_i \\
(mv)_i &= \sum_{p=1}^{N_p} (Mv)_p N_i \\
F_i^{\text{int}} &= -\sum_{p=1}^{N_p} \frac{M_p}{p_p} \sigma_p \nabla N_i
\end{aligned}
\tag{4.36}
$$

5. The external forces are mapped to the grid nodes according to the following relation:

$$F_i^{ext} = \sum_{p=1}^{N_p} N_i b_{ip} \tag{4.37}$$

6. The total grid force vector is calculated.

$$F_i = F_i^{ext} + F_i^{int} \tag{4.38}$$

7. The grid momenta are updated as:

$$(mv)_i = (mv)_i + F_i dt \tag{4.39}$$

8. Essential boundary conditions are applied to the grid nodes.
9. From the updated momenta at the grid nodes the positions and velocities of particles are updated:

$$
\begin{aligned}
v\left(x_p\right) &= v\left(x_p\right) + \left(\sum_{i=1}^{N} \frac{F_i N_i}{m_i}\right) dt \\
x_p &= x_p + \left(\sum_{i=1}^{N} \frac{\left(mv\right)_i N_i}{m_i}\right) dt
\end{aligned}
\tag{4.40}
$$

10. Employing the Modified Update Stress Last (MUSL) scheme the final step is to recalculate the grid nodal momentum based on the new particle velocities and from there calculate the particle strain and stress increments as:

$$
\begin{aligned}
\left(mv\right)_i &= \sum_{p=1}^{N_p} M_p v\left(x_p\right) N_i \\
v_i &= \frac{\left(mv\right)_i}{m_i} \\
\Delta\varepsilon_p &= \sum_{i=1}^{N} v\left(x_p\right) \nabla N_i dt \\
\Delta\sigma_p &= \left[D\right] \Delta\varepsilon_p
\end{aligned}
\tag{4.41}
$$

4.3 Considerations and implementation choices

In this section, the various formulations and modification to the original MPM method are presented. Firstly, some problematic behavior of the Material Point Method algorithm is discussed in Paragraph 4.3.1. It consists of grid crossing instabilities when a particle crosses between elements, and numerical fracture when two material points are farther than one cell distance away. Several shape functions and modifications to the original MPM algorithm have been proposed to overcome these problems and are discussed in Paragraph 4.3.2. Moreover, a discussion comparing the use of Cartesian structured grid versus unstructured grid is presented in paragraph 4.3.3. Implementations regarding the time integration are presented in 4.3.4 distinguishing between explicit and implicit algorithms. Finally in Paragraph 4.3.5 the critical time step is calculated which is essential for the stability of the explicit time integration algorithm.

4.3.1 Grid crossing error and numerical fracture

It has already been mentioned that there is a source of numerical instability inherent in the MPM when the shape functions have C^0 continuity, which is the grid crossing error. It manifests, as the name suggests, when a material point crosses from one element to a neighbor one. The problem lies with the calculation of the internal forces. For this calculation, the gradient of the shape functions is needed as in equation (4.36). If the shape functions are C^0 continuous, then the gradient of the shape functions is discontinuous and a discontinuous function has to be integrated. Schematically the error can be seen in Figure 4.4 and is explained as follows.

Let's isolate the internal forces of node 2 of Figure 4.4. These are calculated from the contribution of the four material points that lie in elements 2 and 3. In addition, suppose that the stress field is uniform and all the material points have the same equal stress state, the same mass and the same density. Then from (4.36) the internal forces are:

$$\begin{aligned} F_2^{\text{int}} &= -\sum_{p=1}^{N_p} \frac{M_p}{p_p} \sigma_p \nabla N_i \Rightarrow \\ F_2^{\text{int}} &= -\frac{M_1}{p_1}\sigma_1 \nabla N_2 - \frac{M_2}{p_2}\sigma_2 \nabla N_2 + \frac{M_3}{p_3}\sigma_3 \nabla N_2 + \frac{M_4}{p_4}\sigma_4 \nabla N_2 \Rightarrow \\ F_2^{\text{int}} &= 0 \end{aligned} \tag{4.42}$$

Since all the material points have the same mass, density and stresses then $M_1 = M_2 = M_3 = M_4 = m$, $p_1 = p_2 = p_3 = p_4 = p$ and $\sigma_1 = \sigma_2 = \sigma_3 = \sigma_4 = \sigma$. The shape function gradients have a positive value for the material points on element 2 and a negative value for the material points in element 3 (Figure 4.4 b). This means that the internal force of node 2 is zero.

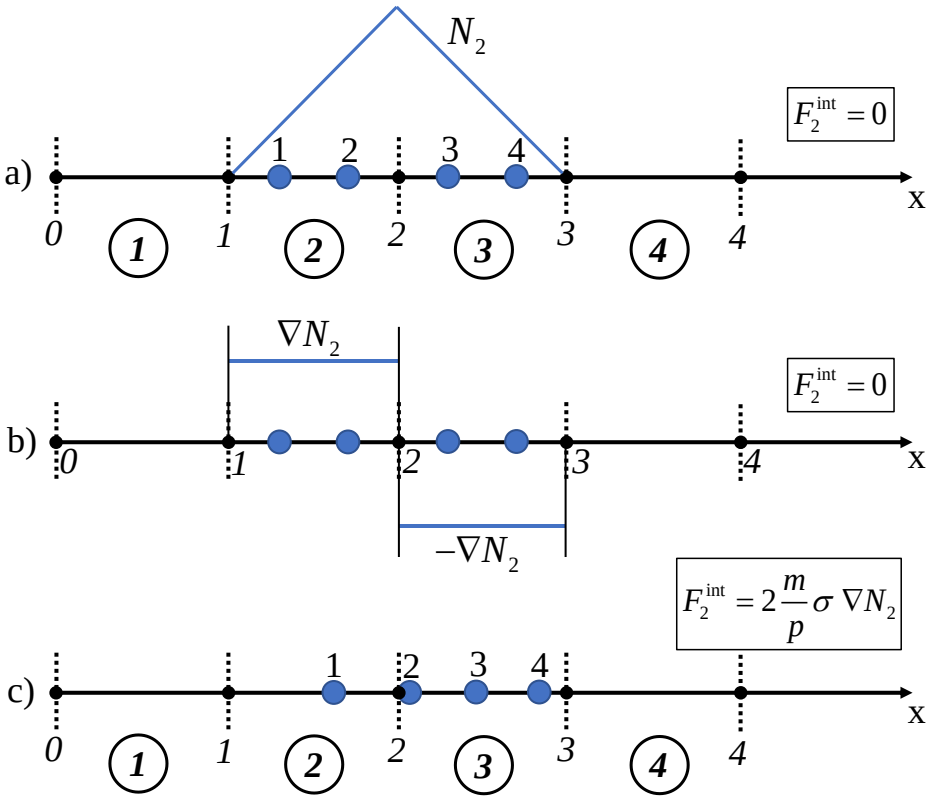

Figure 4.4: Grid crossing error illustration

However, supposing material point 2 moves and crosses from element 2 to element 3 (Figure 4.4 c) then a sudden change of the internal force of node 2 is occurring as shown in Equation (4.43):

$$
\begin{aligned}
F_2^{\text{int}} &= -\sum_{p=1}^{N_p} \frac{M_p}{p_p} \sigma_p \nabla N_i \Rightarrow \\
F_2^{\text{int}} &= -\frac{M_1}{p_1}\sigma_1 \nabla N_2 + \frac{M_2}{p_2}\sigma_2 \nabla N_2 + \frac{M_3}{p_3}\sigma_3 \nabla N_2 + \frac{M_4}{p_4}\sigma_4 \nabla N_2 \Rightarrow \\
F_2^{\text{int}} &= 2\frac{m}{p}\sigma\,\nabla N_2
\end{aligned}
\tag{4.43}
$$

Generally, when the material point volumes are constant, every unequal distribution of material points between elements will create these errors. The use of higher order shape functions that have smooth gradients without discontinuities can remedy this problem. This is one of the reasons that cubic B-Splines are used in this work, as is explained in more detail in a subsequent paragraph.

Another numerical issue present in the Material Point Method is numerical fracture. This means that the solid is separated and appears to fracture without any fracture or damage law specified. It occurs when two particles (in 1D for example) are separated by such a length so that they can no longer interact through the background grid. For linear shape functions the distance is the length of the element as shown in Figure 4.5.

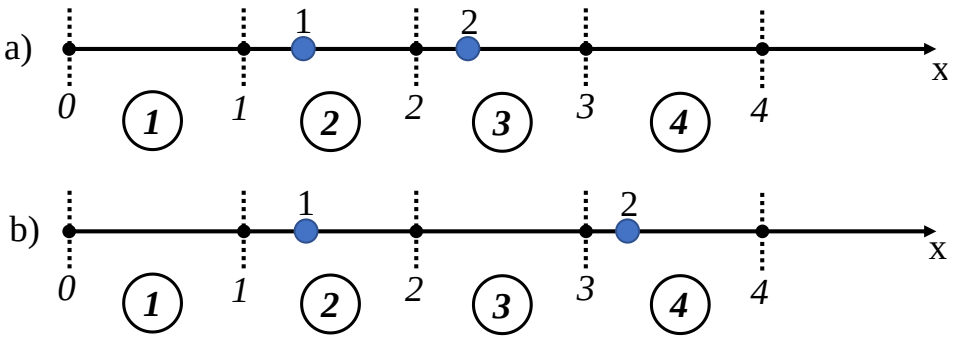

Figure 4.5: Numerical fracture illustration

In case a), material point 1 maps its properties to element 2 with nodes 1 and 2 while material point 2 maps its properties to element 3with nodes 2 and 3. Since the interactions are carried out through the background grid these material points will interact through their common node 2 when the grid momentum will be updated (Equation (4.39). On the contrary the particles cannot interact in case b) of Figure 4.5, since they don't share a common node.

4.3.2 Use of different shape functions

In the original MPM, the shape functions used are linear shape functions similar to those in FEM. Linear shape functions have C^0 continuity, resulting in grid-crossing errors when particles cross the cell boundaries. These errors become larger the finer the mesh, although accuracy in other variables such as stresses etc. may improve.

A modification in order to overcome this problem and improve quadrature in MPM was proposed by Bardenhagen and Kober [11], introducing the generalized interpolation

material point (GIMP) method. The main difference is that in standard MPM particles are considered to be points with no dimensions, while in GIMP they have sizes that represent their volume. This results in C^1 continuous functions that improve accuracy and remedy the grid crossing errors.

An extension of GIMP is the Convected Particle Domain Interpolation (CPDI) method that was developed by Sadeghirad et al [108]. In CPDI particle domains are tracked as parallelograms or quadrilaterals in 2D with better accuracy. There are other formulations also developed that can be distinguished by the spatial discretization they employ (quadrilaterals, triangles, tetrahedra for 3D etc.) [99, 114, 109, 98]. Another formulation worth mentioning is the Dual Domain MPM [140, 41] in which constant gradient fields are reproduced exactly at material points thus rendering the energy error second order in time and space discretization.

Finally, B-Splines [67] have been presented for MPM [117, 56]. Recently they have been employed in unstructured triangular grids [81]. The B-splines Material Point Method (BSMPM) has been programmed in Matlab and is used in this work and will be presented in more detail in Paragraph 4.6, where a more extensive comparison with linear shape functions is made.

4.3.3 Cartesian grid versus unstructured grid

The vast majority of MPM publications and research employs a regular Cartesian grid. When using a uniform grid, the identification of which cell each material point lies in is straightforward and computationally inexpensive. Avoiding a taxing nearest neighbor search algorithm constitutes a computational advantage of the method over other meshless methods. However unstructured grids have been employed in the context of MPM, especially in geotechnical engineering applications [140, 134, 17, 74].

Unstructured grids have the same drawback with meshless methods, which is a computationally expensive search, in order to determine the element that a material point belongs to. On the upside, they facilitate the enforcement of complex boundary conditions, straight into the nodes of the computational grid.

4.3.4 Explicit and implicit time integration schemes

In MPM the most common implementation is an explicit time integration scheme. It is easier to implement, and as explained in the next paragraph, if the chosen time step is smaller than a critical value, the algorithm is unconditionally stable. Implicit solvers have also been developed in the context of MPM, allowing for a more efficient simulation of static or quasi-static loadings. For a single time step, implicit solvers are more computationally expensive than explicit ones. However they can become more efficient as they can solve for larger time steps.

Implicit version of MPM can be found in the literature. Guilkey and Weiss [60] employed the similarities of MPM and FEM to develop an implicit solution scheme. In their work, Guilkey and Weiss form the tangent stiffness matrix and solve the equilibrium equations using a Newmark integration scheme, similar to FEM. Sulsky and Kaul [119] avoid the formulation of a tangent stiffness matrix, which is computationally expensive and used a matrix free Newton – Krylov algorithm. Finally, Beuth [17] developed an implicit MPM formulation with higher order elements used in quasi-static problems.

4.3.5 Critical time step - Stability

In general, the explicit time integration used in MPM is unconditionally stable if the time step is less than a critical value Δt_{cr} .This is a convergence criterion named after Courant–Friedrichs–Lewy and it is known as CFL condition [38]. It arises when numerical solvers

are used for partial differential equations that are formed in explicit time integration scheme. The condition implies that the time step size has to be lower than the time it takes for a wave to travel across the smallest element of the mesh [12]. For the one-dimensional case the CFL condition is:

$$\frac{v\Delta t}{\Delta x} \leq 1 \Leftrightarrow \Delta t \leq \frac{\Delta x}{v} \tag{4.44}$$

In FEM, the smallest period of any element is always larger than or equal to the smallest natural period in the system [71]. Therefore, the following relation holds:

$$\Delta t_{cr} = \min \frac{l^e}{c} \tag{4.45}$$

where l^e signifies that the critical time step has to be calculated for all elements, where c is the speed of sound in the material. For a linear elastic material, the sound speed is given from [141]:

$$c = \sqrt{\frac{E(1-\nu)}{(1+\nu)(1-2\nu)\rho}} \tag{4.46}$$

For a nonlinear system the time step is usually chosen as a fraction of the Δt_{cr} of the linear system usually in the range of 80%-98% [141].

However, in MPM the background grid is not deforming, and only material points are moving. This means that particle velocity has to be accounted for when calculating the critical time step [5]. Eq. (4.45) can now be reformulated as (for an orthogonal background grid with element length of l^g):

$$\Delta t_{cr} = \frac{l^g}{\max\left(c_p + |v_p|\right)} \tag{4.47}$$

where c_p is the sound speed of particle p and v_p is its velocity.

4.4 Different MPM Formulations

Three main formulations that have been developed for explicit MPM, mainly the Update Stress Last (USL), the Modified Update Stress Last (MUSL), that is being used in this thesis and was presented in Paragraph 4.2, and the Update Stress First (USF) [10] formulation. Their similarities and differences are being presented schematically in Figure 4.6:

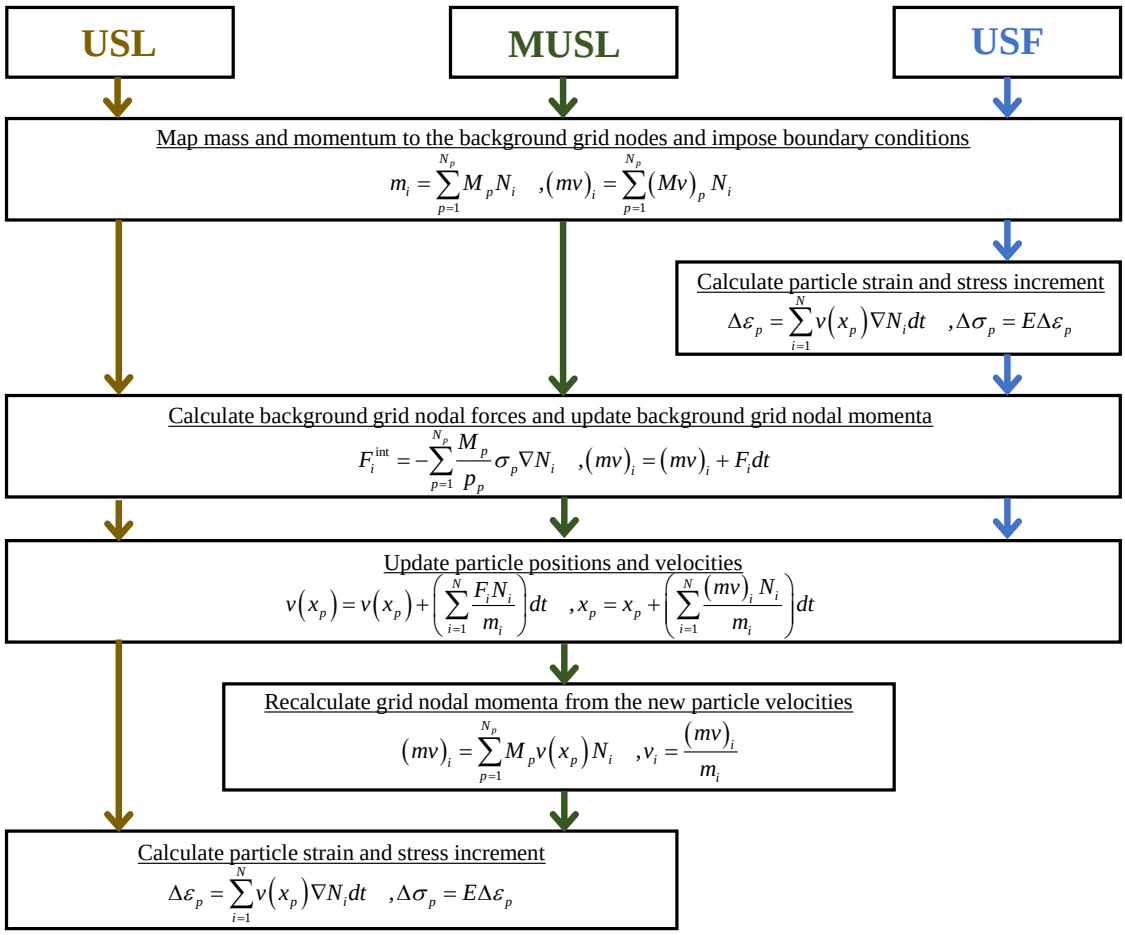

Figure 4.6: Different MPM explicit time integration formulations

The main difference between USF and USL formulation is the calculation of grid nodal velocities. In USF they are calculated at the beginning of the time step straight from the grid nodal momenta. This means that equation (4.36) is modified as:

$$
\begin{aligned}
m_i &= \sum_{p=1}^{N_p} M_p N_i \\
(mv)_i &= \sum_{p=1}^{N_p} (Mv)_p N_i \\
v_i &= \frac{(mv)_i}{m_i} = \sum_{p=1}^{N_p} \frac{M_p v_p N_i}{m_i}
\end{aligned}
\tag{4.48}
$$

USF schemes are found to be conservative while USL schemes are dissipative according to [10]. Also, MUSL and USF lead to generally improved energy calculations compared to USL schemes as reported in [95].

4.5 Advantages and disadvantages of MPM

The Material Point Method inherits the positive features of both Lagrangian and Eulerian descriptions and has some advantages that are outlined below:

- Mesh distortion and element entanglement problems are eliminated, since the background grid is not moving and remains fixed. Only the material points move through the computational grid and so there is no mesh deformation. This implies also that no remeshing is needed, which is usually encountered in FEM simulations with large displacements, and it can be the source of numerical errors and an increase in computational time [83].
- Connectivity between particles is achieved through the background grid. If it is a structured orthogonal grid, then the identification of which element every material point lies in, is trivial. This renders the method generally faster than meshfree methods that usually employ neighbor search algorithms for connectivity, since these algorithms usually take up significant amount of computational time in each time step.

- A no-slip contact algorithm is inherent in MPM. The method can handle this type of contact problems without any additional computational cost or complexity. The contact is inherent in MPM since the material points share the same velocity field. If two material points map their properties to the same node of the computational grid, then contact is bound to occur. However, this contact is based on the grid resolution and there is ongoing research to improve and expand the MPM contact procedures [96, 66].
- The discretization of the structure is relatively easy and fast. It is algorithmically and computationally efficient to distribute points inside a bounded volume or area of any arbitrary geometrical shape. Converting images or 3D models [61] to numerical models for simulation is therefore effortless.
- Can be easily programmed for parallel, distributed-memory computers [44] since each material point is independent of others and through decomposition of the computational domain.

The main disadvantages of MPM are summarized below

- The MPM is slower in its explicit formulation than FEM. This is due to the fact that in each computational cycle the MPM has to perform extra calculations of the mapping from and to the computational grid. In addition, the shape functions are not constant like in FEM but have to be recalculated every time a material point changes its position.
- Grid crossing error and numerical fracture that have been discussed in previous paragraph.
- Lower accuracy than FEM, since the material points can be positioned anywhere inside an element and not at the optimal positions required for numerical integration (such as Gauss points in FEM). In order to circumvent this problem

higher order shape functions must be used and larger particle densities, which lead to higher computational cost for the same accuracy.

4.6 Shape function investigation

In this section the use of different shape functions in MPM, linear and cubic B-splines, is considered. In order to investigate the computational accuracy of the aforementioned shape functions two cases are examined. In the first case the calculation of gradient velocity is examined, in this paragraph, while for the second one, the quadrature accuracy during plasticity is studied in paragraph 4.7.2.

Owing to their compact support, ease of computation, and partition of unity property, piecewise linear shape functions are probably the most commonly used choice in MPM algorithms as they are in FEM. Their plot together with their formula for the 1D case is shown in Figure 4.7 both for the shape functions and for their derivatives Moreover, in Figure 4.9 plots of linear shape function for the two dimensional case are presented. These linear basis functions are the same as in many low-order FEMs, but in MPM the discontinuous nature of ∇N is important as it is a mixed Lagrangian–Eulerian method and is the reason grid crossing errors occur.

In FEM, integration over the domain is decomposed into the sum of integrals over elements with quadrature points remaining fixed within elements at optimal positions. In MPM, however, particles act as quadrature points and are allowed to move freely through the domain and across these discontinuities in ∇N. Therefore, grid-crossing errors occur when shape functions with discontinuous gradients are used. The main difference between MPM and meshfree particle methods (SPH, EFG and RKPM) is that the equations of motion are solved on the background grid and material points are used as the quadrature points to approximate nodal forces and nodal masses, while in meshfree

methods the equations of motion are solved on the material points and a background mesh is constructed for quadrature purposes to approximate the nodal forces.

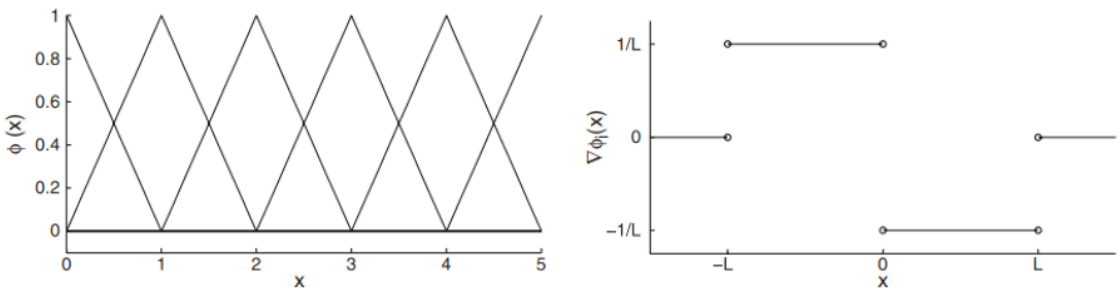

$$\phi_i(x) = \begin{cases} 1+(x-x_i)/h, & x_i - h \leqslant x < x_i \\ 1-(x-x_i)/h, & x_i \leqslant x \leqslant x_i + h \\ 0 & \text{otherwise} \end{cases}$$

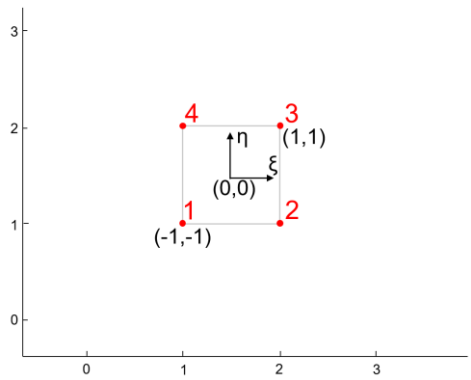

Figure 4.7: Piecewise-linear functions [117], their derivatives and single element.

Cubic B-Splines are presented in Figure 4.8 as well as their derivatives for the one-dimensional case as well as a single element. It should be noted that the cubic spline interpolation is used for each individual material point and each m.p. maps its values to nodes that lie a maximum distance of two grid nodes away in either direction. In two dimensions, this means that each material point maps its properties to 16 neighboring nodes, both for the element it resides in but also for the neighboring ones, as shown in Figure 4.8.

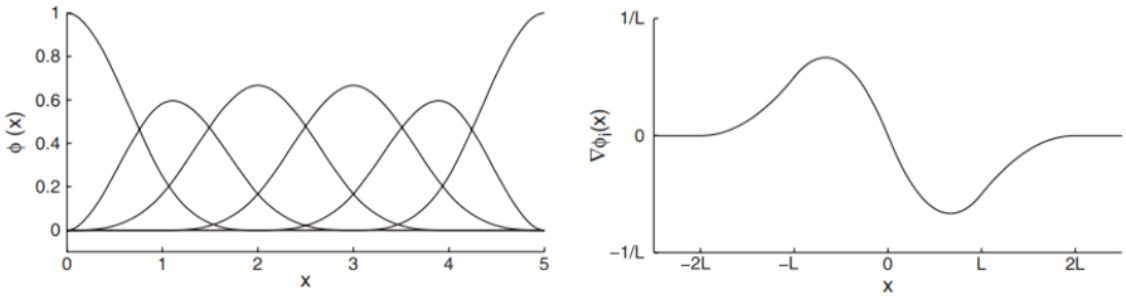

$$\phi(x)=\begin{cases}\frac{1}{6h^3}x^3+\frac{1}{h^2}x^2+\frac{2}{h}x+\frac{4}{3}, & -2h\leqslant x\leqslant -h\\ -\frac{1}{2h^3}x^3-\frac{1}{h^2}x^2+\frac{4}{3}, & -h\leqslant x\leqslant 0\\ \frac{1}{2h^3}x^3-\frac{1}{h^2}x^2+\frac{4}{3}, & 0\leqslant x\leqslant h\\ -\frac{1}{6h^3}x^3+\frac{1}{h^2}x^2-\frac{2}{h}x+\frac{4}{3}, & h\leqslant x\leqslant 2h\\ 0 & \text{otherwise}\end{cases}$$

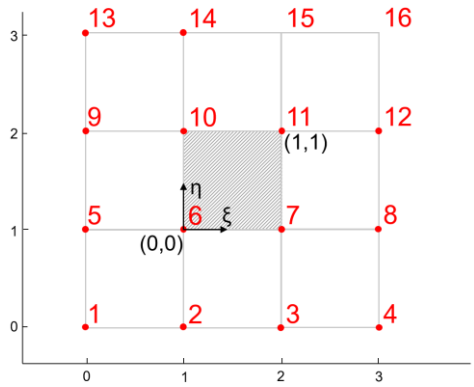

Figure 4.8: Cubic B-spline functions [117], their derivatives and single element.

The values of the cubic B-Spline shape functions for the two-dimensional case are presented in Figure 4.10. In order to obtain two-dimensional or three-dimensional shape functions the tensor product of the different one-dimensional shape functions has to be calculated. In FEM B-Splines are used to improve the representation of complex geometries. In MPM however, since the background grid is static and orthogonal, they are used to provide better quadrature results and smooth derivatives that improve strain calculations.

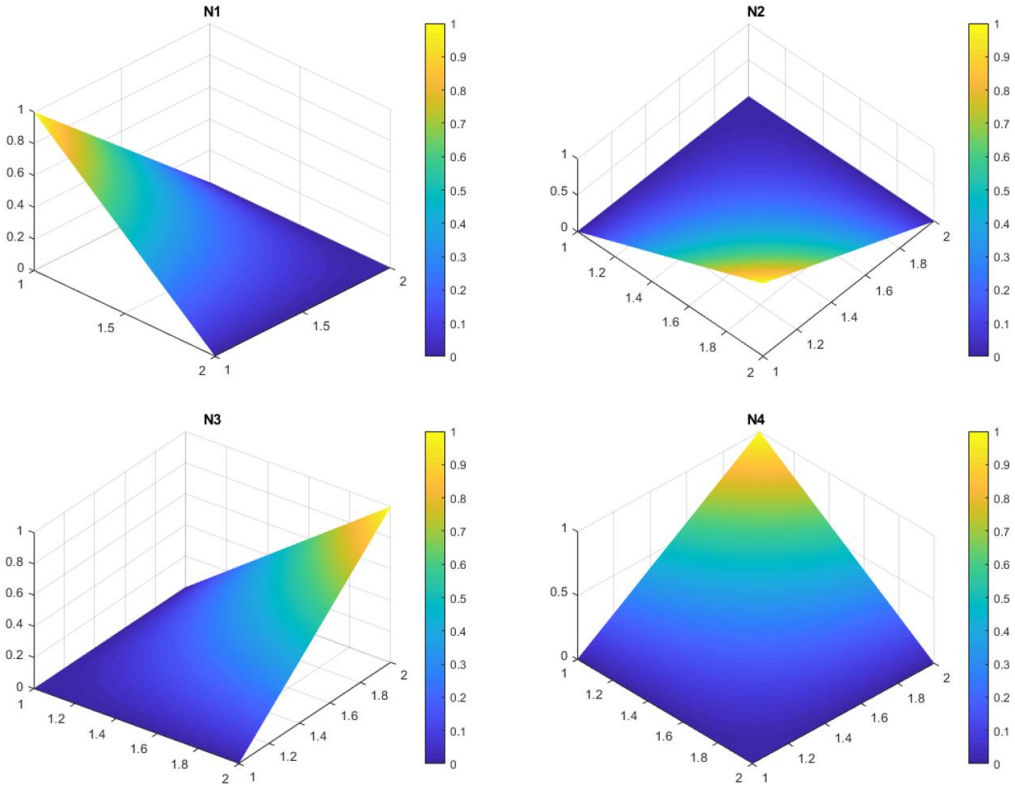

Figure 4.9: Linear shape function values at each element node.

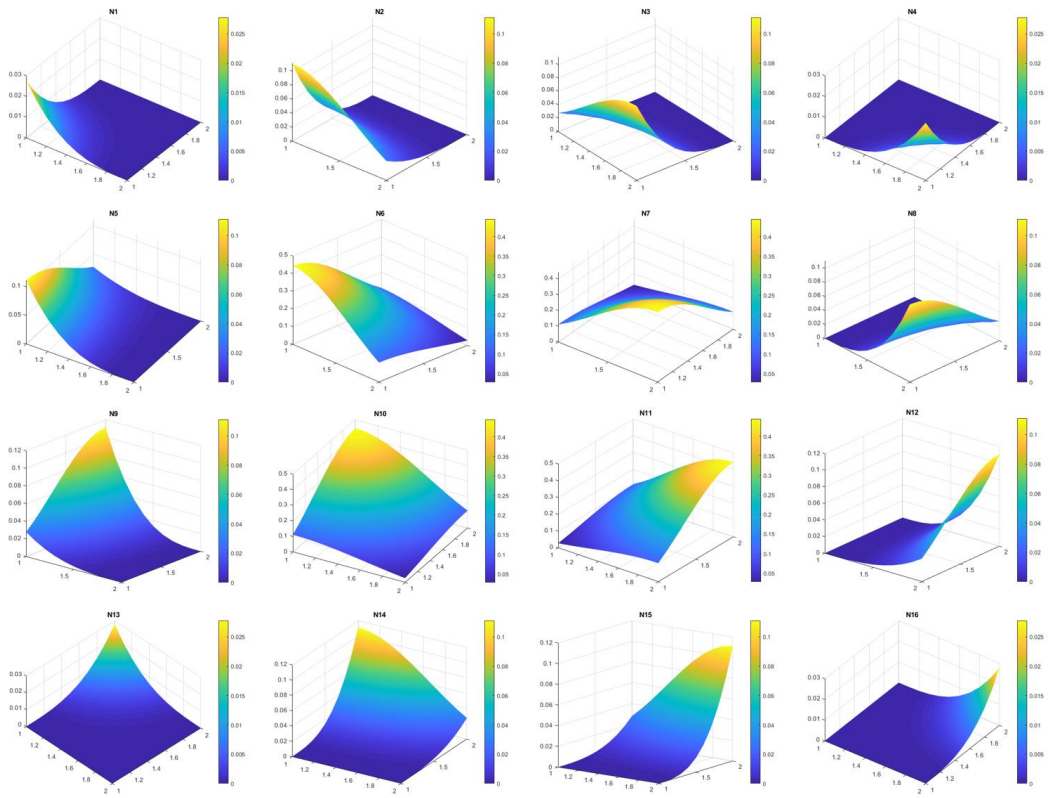

Figure 4.10: Cubic B-spline shape functions values at each element node

4.6.1 1-D Domain

For this analysis a pseudo 1D domain as depicted in Figure 4.11 is considered with dimensions $0.5m \times 5.0m$. Several analyses are carried out where the domain is discretized with various number of elements and particles per element. In the first set of analyses the number of elements is kept constant while the number of particles per element is increased. The number of points per element varies from 1, 4, 9 and 16 and the total number of elements changes from 10 to 20 and finally 40 elements. In all analyses an initial sinusoidal velocity field is applied:

$$pVEL = 0.01\cos\left(\frac{\pi}{5}(x_p - 0.5)\right) \tag{4.49}$$

For this velocity field the gradient velocity can be analytically calculated:

$$L_p = (0.01\frac{\pi}{5})\sin\left(\frac{\pi}{10} - \frac{\pi}{5}x_p\right) \tag{4.50}$$

and is compared with the MPM calculation. The geometry of the domain is presented in Figure 4.11. The total length is $5m$, the height is $0.5m$ and the depth is considered to be $1m$, with $E = 10000Pa$, $v = 0$, and the density is $1000kg/m^3$.

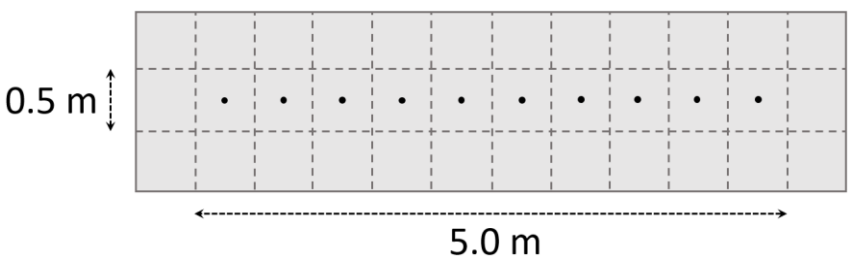

Figure 4.11: Pseudo 1-D Domain

Results are presented in the following Figures and Tables. In Table 4-1 results regarding computational time as well as accuracy are presented. The baseline with regard to the computational time is considered the first case where the domain is discretized with 10

elements containing 1 particle per element. Cubic B-Splines are used as shape functions. It can be observed in the third column of the table that the computational time for each analysis is almost analogous to the number of material points used. This is expected since the explicit MPM algorithm used, spends most of the computational time in loops that have the length of the total number of material points and in its current formulation avoids the unnecessary calculation of inactive background grid cells. For example, if one calculates the total material points used for the last analysis (in the last row of the table) there are $40 \cdot 16 = 640$ material points which is 64 times larger than the $10 \cdot 1$ material points used in the baseline analysis. The computational time is 62.62 times larger in this case than the baseline. Similarly, for the case of 20 elements and 4 points per element 8 times more material points are used and the computational time is 7.73 times larger.

N. elements	**Particles per element**	**Computational time (x)**	**L2 norm**
10	1	1	0.0193
10	4	3.86	0.0166
10	9	8.73	0.0164
10	16	15.36	0.0164
20	1	1.97	0.004225
20	4	7.73	0.004111
20	9	17.76	0.004108
20	16	30.88	0.004106
40	1	4.03	0.0010319
40	4	15.8	0.0010282
40	9	35.02	0.0010280
40	16	62.62	0.0010280

Table 4-1: Computational time and accuracy for different discretization

In Figure 4.12, Figure 4.13 and Figure 4.14 in the net pages, the results are plotted and compared with the analytical solution. In Table 4.1 the L2 error norms are presented for

each case in the last column. As can be expected increasing either the number of elements or the number of material points per element generally increases the accuracy of the solution. However, the benefits of increasing the material points per element are negligible compared to increasing the number of elements, when taking into account the additional computational time. For example, the case of 10 elements and 16 material points per element has almost the same computational time as 40 elements and 4 material point per element (15.36 vs 15.8). However, the 40 element discretization gives much better accuracy. In Figure 4.15 the same conclusion can be reached from the plotted MPM calculations.

CONSTANT NUMBER OF 10 ELEMENTS

Case for 1 particle per element:

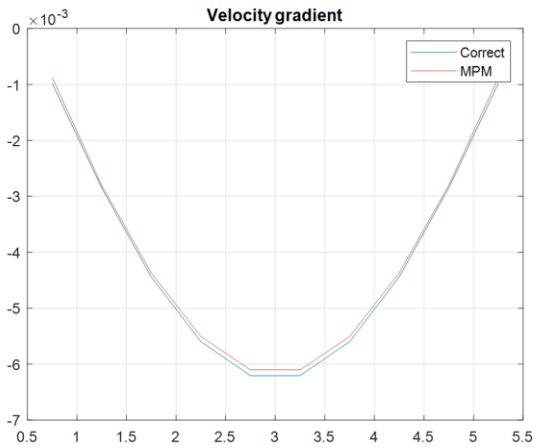

Case for 4 particle per element:

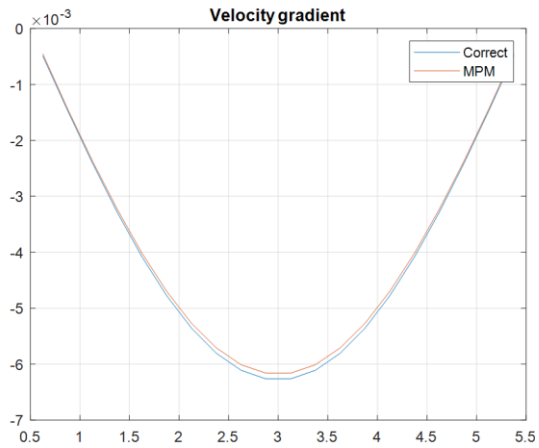

Case for 9 particle per element:

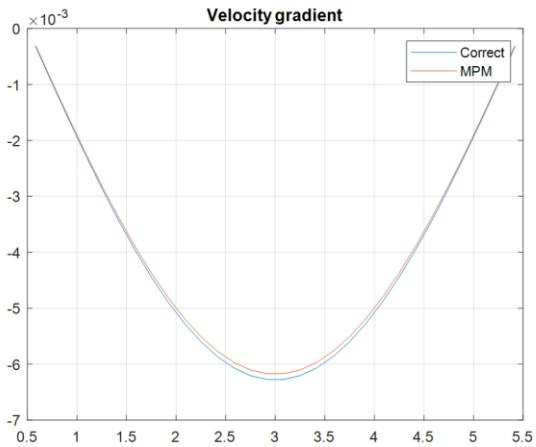

Case for 16 particle per element:

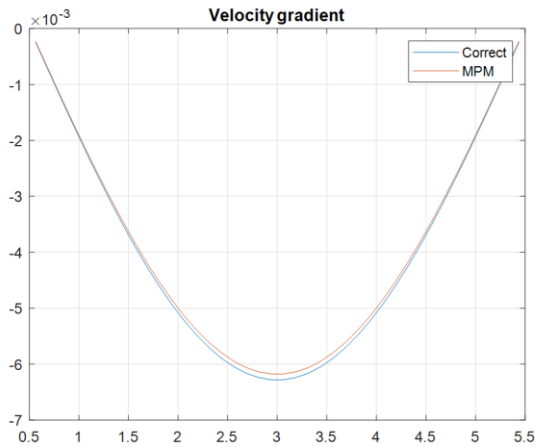

Figure 4.12: Discretization with 10 elements results

CONSTANT NUMBER OF 20 ELEMENTS

Case for 1 particle per element:

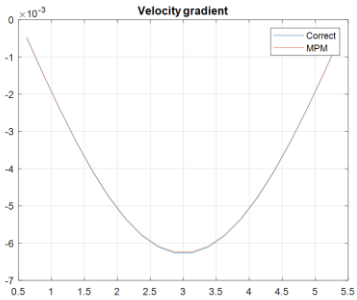

Case for 4 particle per element:

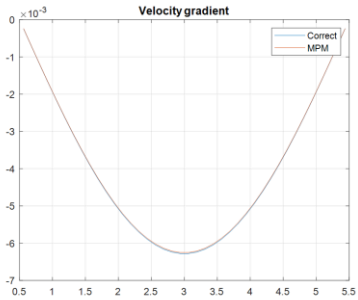

Case for 9 particle per element:

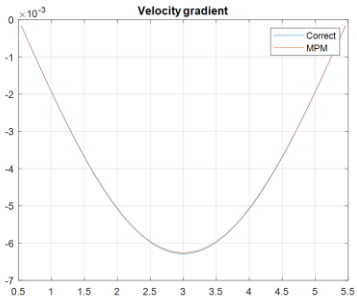

Case for 16 particle per element:

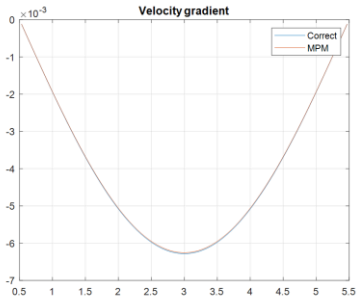

Figure 4.13: Discretization with 20 elements results

CONSTANT NUMBER OF 40 ELEMENTS

Case for 1 particle per element:

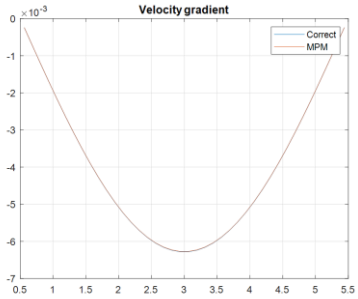

Case for 4 particle per element:

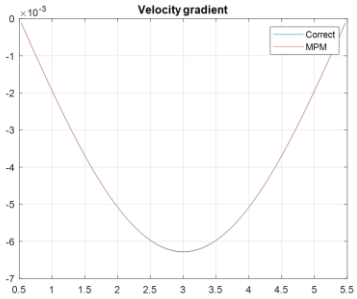

Case for 9 particle per element:

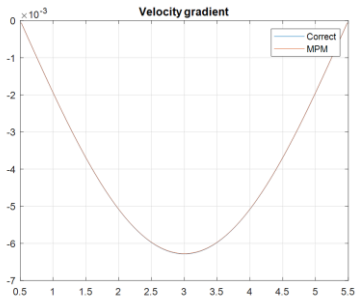

Case for 16 particle per element:

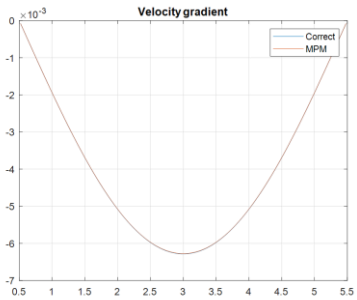

Figure 4.14: Discretization with 40 elements results

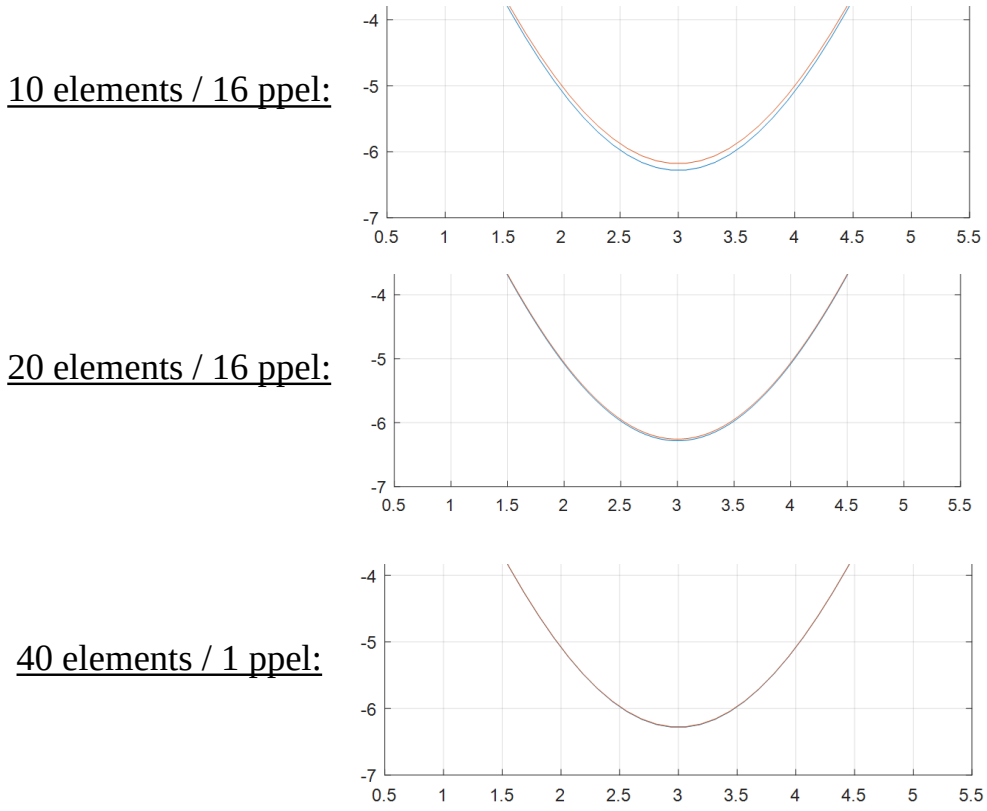

Figure 4.15: Different number of elements accuracy

All the analyses so far employed the cubic B-Splines shape functions. For the next analyses the linear shape functions are used and the same problem is analyzed. In Figure 4.16 and Table 4-2 the results and L2 error norms are presented for a discretization with 10 elements and an increasing number of material points, for linear shape functions. Several remarks can be made from these results. Firstly, when using linear shape functions and 1 material point per element, the quadrature and projections give increased accuracy. This is attributed to the fact that the material point lies on the center of the background grid node element in its optimum position, similar to using 1 Gauss point quadrature in FEM. However, when more material points per element are present the linear shape functions cannot capture the correct solution and only present a constant velocity gradient within each element, therefore degrading the accuracy of the solution. This is attributed to the linear shape unction gradient that is a constant value and discontinuous across elements.

LINEAR SHAPE FUNCTIONS

Case for 1 particle per element:

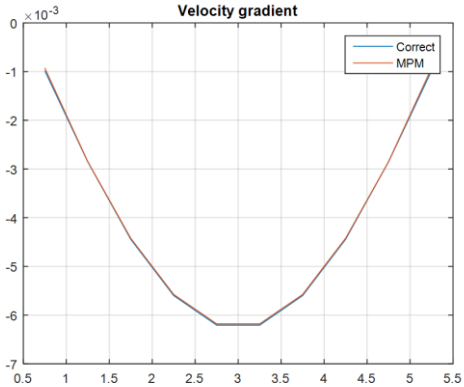

Case for 4 particle per element:

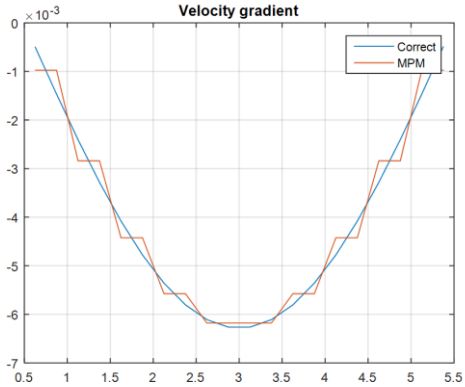

Case for 9 particle per element:

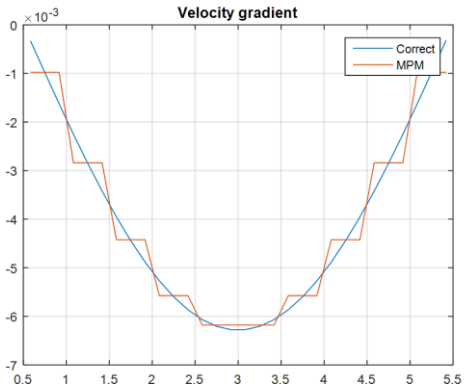

Case for 16 particle per element:

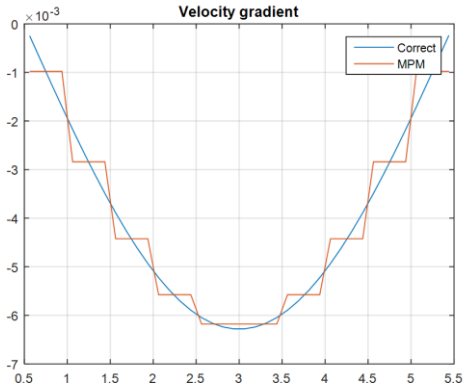

Figure 4.16: Discretization with 10 elements results – linear shape functions

N. elements	Particles per element	L2 linear s.f.	L2 B-Splines s.f.
10	1	0.0070	0.0193
10	4	0.0785	0.0166
10	9	0.0854	0.0164
10	16	0.0877	0.0164

Table 4-2: L2 error norms for different shape functions

In addition, as can been observed from Figure 4.17, when using linear shape functions, if the material point does not lie in the center of the background grid element (which in a general simulation will be the case most of the time), it cannot correctly represent the velocity gradient correct solution and results appear to diverge as the material point leaves its optimum position.

LINEAR SHAPE FUNCTIONS

Move points 5cm left:

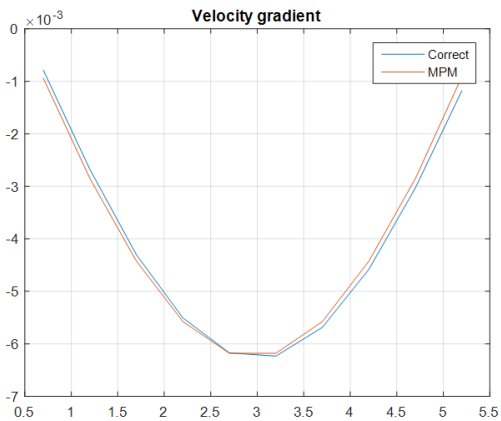

Move points 10cm left:

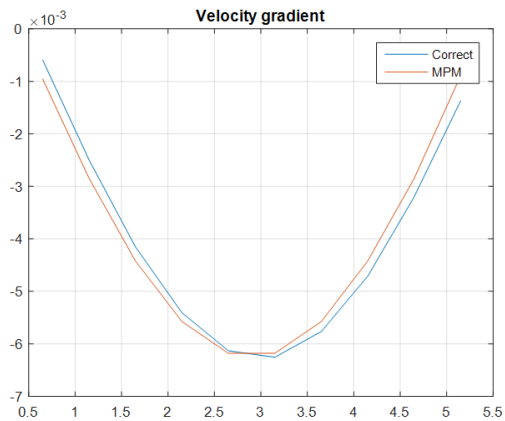

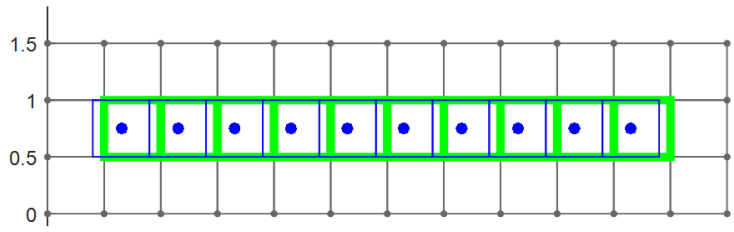

Figure 4.17: Linear shape functions, 1 material point per element in displaced positions

4.7 Bouc – Wen implementation in MPM

4.7.1 Tangent modulus and algorithm modifications

The tangent stiffness matrix that was previously developed in Chapter 2, is evaluated at every material point and has a dominant role in the proposed MPM formulation as it is used in relation (2.36). Thus, the updated stresses at the end of each time step can be calculated on the basis of the total strains. The main algorithm is presented in Figure 4.18 for the case where no degradations are considered. For the calculation of the tangent stiffness matrix with no degradations the following relations hold:

$$
\begin{aligned}
&[E_t] = [D]\left([I] - H_1 H_2 [R]\right) \\
&H_1 = \left| \frac{f\left(\{\sigma\} - \{a^{kin}\}\right)}{\sigma_y\left(\varepsilon_{ps}^{iso}\right)} \right|^n \\
&H_2 = \beta + \gamma sign\left(\left\{ \frac{\partial \Phi}{\partial \{\sigma\}} \right\}^{\mathrm{T}} [D]\{\dot{\varepsilon}\} \right) \\
&[R] = \lambda_1 \left\{ \frac{\partial \Phi}{\partial \{\sigma\}} \right\} \left\{ \frac{\partial \Phi}{\partial \{\sigma\}} \right\}^{\mathrm{T}} [D] \\
&\lambda_1 = \left((1-m)\frac{3}{2} C_p + mH' + \left(\frac{\partial \Phi}{\partial \{\sigma\}} \right)^T [D] \frac{\partial \Phi}{\partial \{\sigma\}} \right)^{-1}
\end{aligned}
\tag{4.51}
$$

In the context of MPM the tangent stiffness matrix presented above relates strain increments with stress increments and has dimensions of (*3x3*) for 2D simulations. It can encapsulate isotropic, kinematic or mixed hardening and various yield functions providing a smooth representation of the hysteretic loops. In the case where stiffness and strength degradation are considered, the tangent stiffness matrix is calculated as:

$$
\begin{aligned}
&[E_t] = [D]\frac{1}{\eta}\left([I] - v_s H_1 H_2 [R]\right) \\
&H_1 = \left| \frac{f\left(\{\sigma\} - \{a^{kin}\}\right)}{\sigma_y\left(\varepsilon_{ps}^{iso}\right)} \right|^n \\
&H_2 = \beta + \gamma sign\left(\left\{ \frac{\partial \Phi}{\partial \{\sigma\}} \right\}^{\mathrm{T}} [D]\{\dot{\varepsilon}\} \right) \\
&[R] = \lambda_1 \left\{ \frac{\partial \Phi}{\partial \{\sigma\}} \right\} \left\{ \frac{\partial \Phi}{\partial \{\sigma\}} \right\}^{\mathrm{T}} [D] \\
&\lambda_1 = \left((1-m)\frac{3}{2} C_p + mH' + \left(\frac{\partial \Phi}{\partial \{\sigma\}} \right)^T [D] \frac{\partial \Phi}{\partial \{\sigma\}} \right)^{-1}
\end{aligned}
\tag{4.52}
$$

For every particle $p = 1, 2, \ldots$ given: $\underset{(1x1)}{C_p}$ $\underset{(1x1)}{H'}$ $\underset{(3x1)}{\{\Delta\varepsilon^t\}}$ $\underset{(3x1)}{\{a^{t-1}\}}$ $\underset{(3x1)}{\{\varepsilon^{t-1}\}}$ $\underset{(3x3)}{[D]}$ $\underset{(3x1)}{\{\sigma^{t-1}\}}$ $\underset{(1x1)}{\lambda^{t-1}}$:

1. Calculate effective stresses using the back stress tensor. For the Von Mises yield criterion for kinematic hardening (for isotropic hardening the back stress tensor is 0). This signify the movement of the yield surface in the stress space:	$\begin{cases} \sigma_{xx}^{\text{eff}} = \sigma_{xx} - a_{xx} \\ \sigma_{yy}^{\text{eff}} = \sigma_{yy} - a_{yy} \\ \sigma_{xy}^{\text{eff}} = \sigma_{xy} - a_{xy} \\ \sigma_{zz}^{\text{eff}} = 0 - \left(-a_{xx} - a_{xy}\right) \end{cases}$
2. Calculate the variable yield stress for isotropic hardening (in case of the Von Mises yield criterion $\varepsilon_{ps} = \lambda^{t-1}$):	$\sigma_y^{\text{var}} = \sigma_y + mH'\varepsilon_{ps}$
3. Evaluate H_1, which for the Von Mises yield criterion is:	$\underset{(1x1)}{H_1} = \left\lvert \frac{\left(\sqrt{\left(\left(\sigma_{xx}^{\text{eff}} - \sigma_{yy}^{\text{eff}}\right)^2 + \left(\sigma_{xx}^{\text{eff}} - \sigma_{zz}^{\text{eff}}\right)^2 + \left(\sigma_{yy}^{\text{eff}} - \sigma_{zz}^{\text{eff}}\right)^2 + 6\cdot\left(\sigma_{xy}^{\text{eff}}\right)^2\right)/2}\right)}{\sigma_y^{\text{var}}} \right\rvert^n$
4. Calculate:	$\underset{(3x1)}{\frac{\partial\Phi(\{\sigma\})}{\partial\{\sigma\}}}$
5. Calculate H_2:	$\underset{(1x1)}{H_2} = \beta + \gamma\, sign\left(\left\{\frac{\partial\Phi}{\partial\{\sigma\}}\right\}^{\mathrm{T}}[D]\{\dot{\varepsilon}\}\right)$
6. Compute:	$\underset{(1x1)}{\lambda_1} = \left(\mathrm{H}' + \left(\frac{\partial\Phi}{\partial\{\sigma\}}\right)^T [D] \frac{\partial\Phi}{\partial\{\sigma\}}\right)^{-1}$
7. Calculate:	$\underset{(3x3)}{[R]} = \lambda_1 \left\{\frac{\partial\Phi}{\partial\{\sigma\}}\right\}\left\{\frac{\partial\Phi}{\partial\{\sigma\}}\right\}^{\mathrm{T}}[D]$
8. And finally:	$\underset{(3x3)}{[E_t]} = [D]([I] - H_1 H_2 [R])$
9. Finally update variables for next time step:	$\begin{cases} \underset{(3x1)}{\{\Delta\varepsilon_{pl}{}^t\}} = H_1 H_2 [R]\{\Delta\varepsilon^t\}^T \\ \underset{(3x1)}{\{\Delta a^t\}} = (1-m) C_p \{\Delta\varepsilon_{pl}{}^t\} \\ \underset{(1x1)}{\Delta\lambda^t} = H_1 H_2 \lambda^{t-1} \left\{\frac{\partial\Phi(\{\sigma\})}{\partial\{\sigma\}}\right\}^T [D]\{\Delta\varepsilon^t\} \\ \underset{(1x1)}{\lambda^t} = \lambda^{t-1} + \Delta\lambda^t \\ \underset{(3x1)}{\{a^t\}} = \{a^{t-1}\} + \{\Delta a^t\} \end{cases}$
10. Update stresses and strains:	$\begin{cases} \underset{(3x1)}{\{\Delta\sigma^t\}} = [E_t]\{\Delta\varepsilon^t\} \\ \underset{(3x1)}{\{\sigma^t\}} = \{\sigma^{t-1}\} + \{\Delta\sigma^t\} \\ \underset{(3x1)}{\{\varepsilon^t\}} = \{\varepsilon^{t-1}\} + \{\Delta\varepsilon^t\} \end{cases}$

Figure 4.18: MPM pseudocode for kinematic, isotropic or mixed hardening

Where the degradation parameters are calculated from:

$$\dot{\eta} = c_\eta \left(\frac{1}{\eta}\right)^{m_u} \beta H_1 \left(1 + \frac{\gamma}{\beta}\operatorname{sgn}\left(\{\sigma\}^T\{\dot{\varepsilon}\}\right)\right)\left|\{\sigma\}^T\{\dot{\varepsilon}\}\right| \tag{4.53}$$

$$v_s = 1 + c_v e^h$$

The tangent stiffness matrix of equation (4.52) is calculated for every material point. Equation (4.53) has to be solved simultaneously in incremental form in the explicit time integration MPM scheme. The model can simulate hysteretic behavior with kinematic, isotropic or mixed hardening with stiffness degradation and strength deterioration.

An advantage of the proposed formulation is that the whole hysteretic behavior, is enclosed in the calculation of the tangent stiffness matrix. The model can be easily incorporated into existing MPM codes. In addition, the calculation of the tangent stiffness matrix can be done in parallel computations for massive simulations taking advantage the discrete nature of the method.

4.7.2 Shape functions in plasticity

In order to investigate the use of different shape functions when plasticity is concerned, a simply supported beam is subjected to a concentrated tip load on its middle (Figure 4.19). Material is steel with a Young's modulus of 210*GPa*, a yield stress of 240*MPa* and a mass density of 7850kg/m^3. Kinematic hardening is considered with a 5% ratio. For the beam discretization 1280 material points were used corresponding to 4 points per element (4ppel). The background grid elements have a length of 0.025m. The load is applied gradually in small increments over a long time period of 20 seconds until its maximum value to simulate quasi-static conditions within the present MPM explicit dynamic formulation. Two analyses are carried out one with the use of linear shape functions and the second using cubic B-Splines.

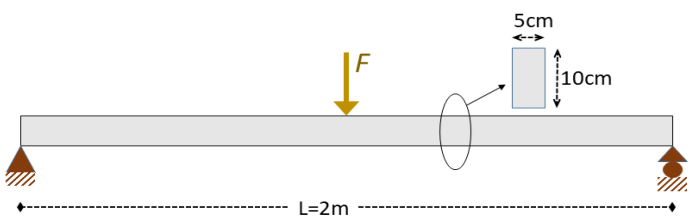

Figure 4.19: Simply supported beam

In Figure 4.20 the normal stress- normal strain diagrams are presented. It can be observed that for the linear shape functions, oscillations and noise begin to appear when the stresses approach the yield stress. For cubic B-Splines the diagram is smooth revealing their superior properties. In addition, it can be noticed that both shape functions produce stress contours for normal stresses that are in good agreement, with minor differences (Figure 4.21). However, for shear stresses, presented in Figure 4.22, the linear shape functions fail to capture the real distribution of stresses and exhibit a saw tooth pattern similar to FEM.

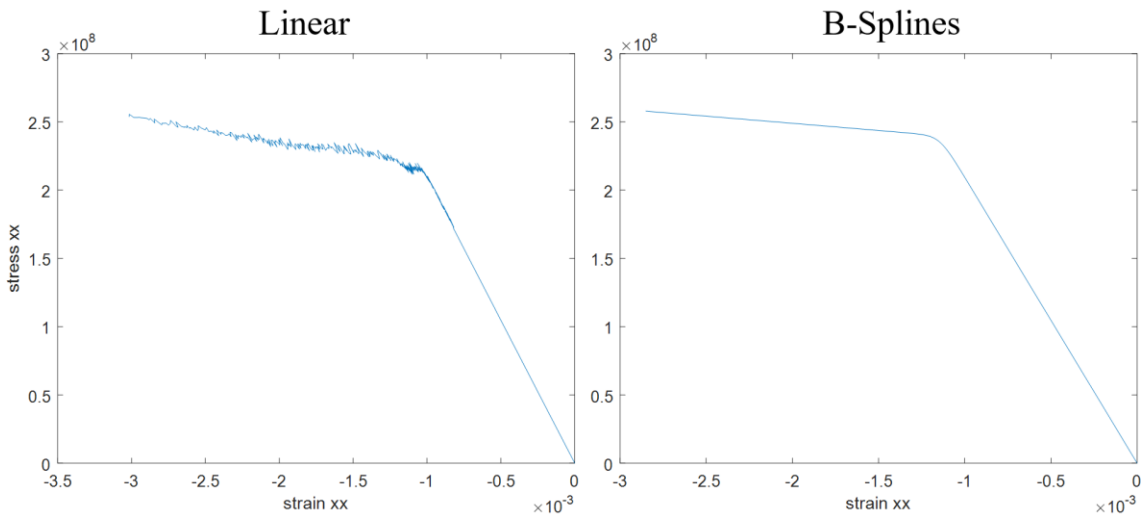

Figure 4.20: Normal stress – strain curves for linear and B-Spline shape functions

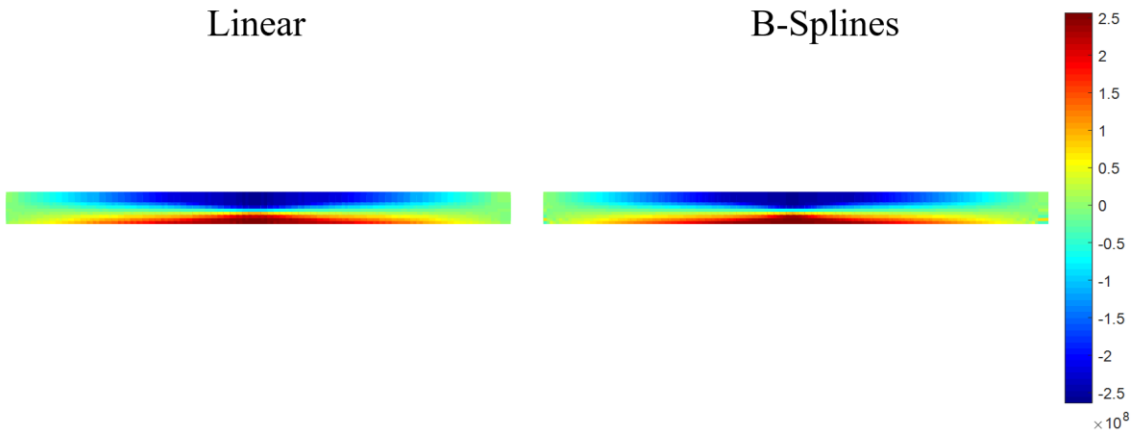

Figure 4.21: Normal stress contours for linear and B-Spline shape functions

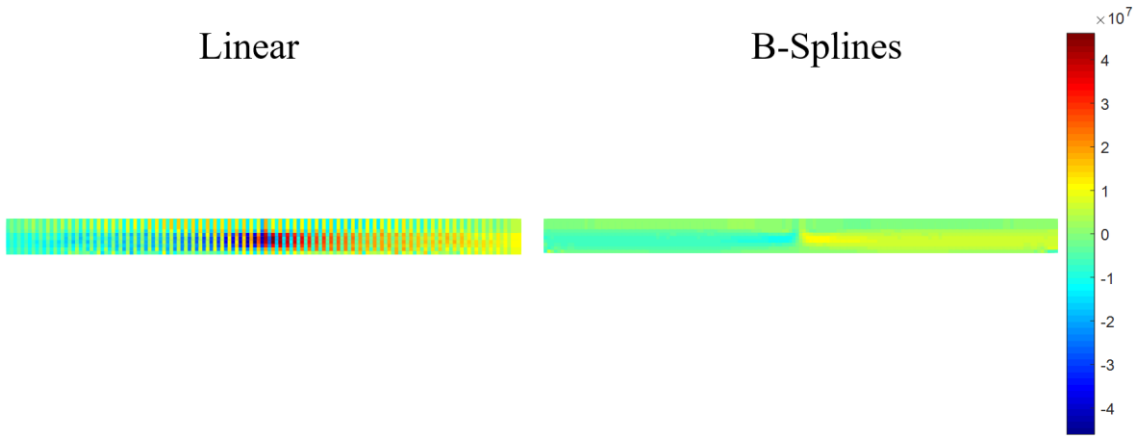

Figure 4.22: Shear stress contours for linear and B-Spline shape functions

When elastoplasticity is considered, using linear shape functions can lead to unrealistic stresses at individual material points, and stress oscillations after yielding. There can also be cases where material points reach yielding due to the non-physical stress variation within a linear element. As a result of this, the material behavior is not modelled correctly and higher order shape functions such as cubic B-Splines is advisable to be used.

4.7.3 Different discretization in plasticity

In this paragraph different mesh sizes are investigated when plasticity is concerned. A steel cantilever beam is considered with dimensions 1x0.2m. The support conditions are simply supported for the middle of the beam and rollers for all the other points, and the load is distributed in all the points lying in the edge. The various parameter values used in the analyses are given in Table 4-3. A vertical load is applied at the free end of the beam. In order to simulate static conditions, the load is applied gradually over the timespan of 1sec.

	Symbol	Value
Young's modulus	E	210GPa
Yield stress	σ_y	240MPa
Post yield stiffness/elastic	a	10%
BW shape parameters	$\beta=\gamma$	0.5
BW smoothness parameter	n	16

Thickness	t	$0.06m$
Load	F	$160kN$

Table 4-3: Parameters of cantilever beam

Analyses are carried out with various mesh sizes. Starting from a crude mesh size with elements of $0.1m$ edge length up to a fine mesh with elements of $0.02m$ length. In addition, analyses are carried out with various number of material points per element. Results are presented in the following Figures. In Figure 4.23, the stress strain diagram the normal stresses and normal strains are presented for the material point that is closest to the fixed base and at the further end from the centerline. As expected, with finer meshes and more points per element, this material lies closer to the corner of the beam, where the maximum stress is theoretically expected. This means that the maximum stress that the material reaches should increase with smaller mesh sizes.

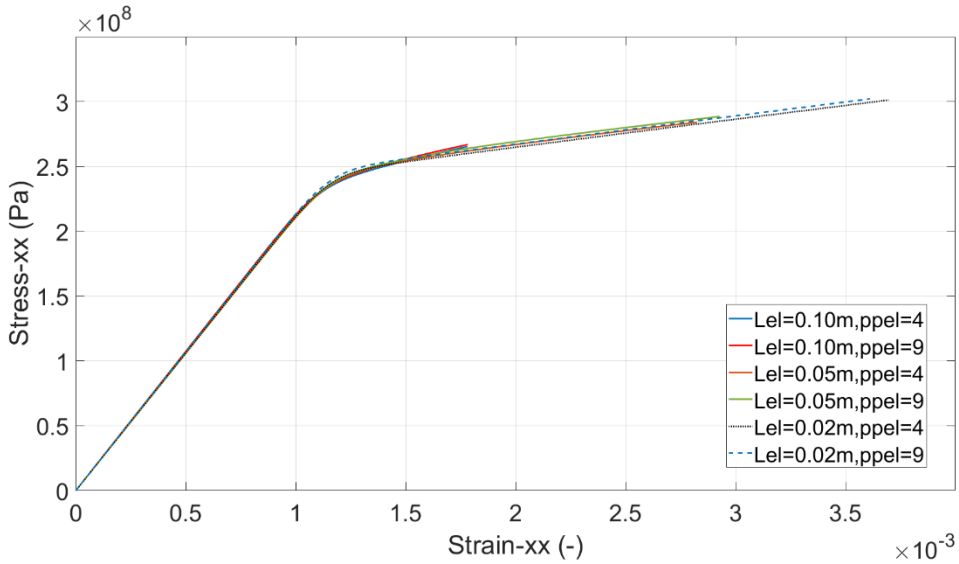

Figure 4.23: Stress –strain diagram for various mesh sizes and point per element

Moreover, in Figure 4.24 the final Von Mises stress distributions are plotted for the various mesh sizes and points per element. Figure 4.24 a) refers to an element length of 0.1m and 4 points per element (ppel), b) is 0.1m and 9ppel, c) is 0.05m and 4 ppel, d) is 0.05m and 9 ppel, e) is 0.02m and 4 ppel and finally f) is 0.02m and 9 ppel respectively.

The present formulation is able to capture the correct stress distribution with better resolution for finer meshes.

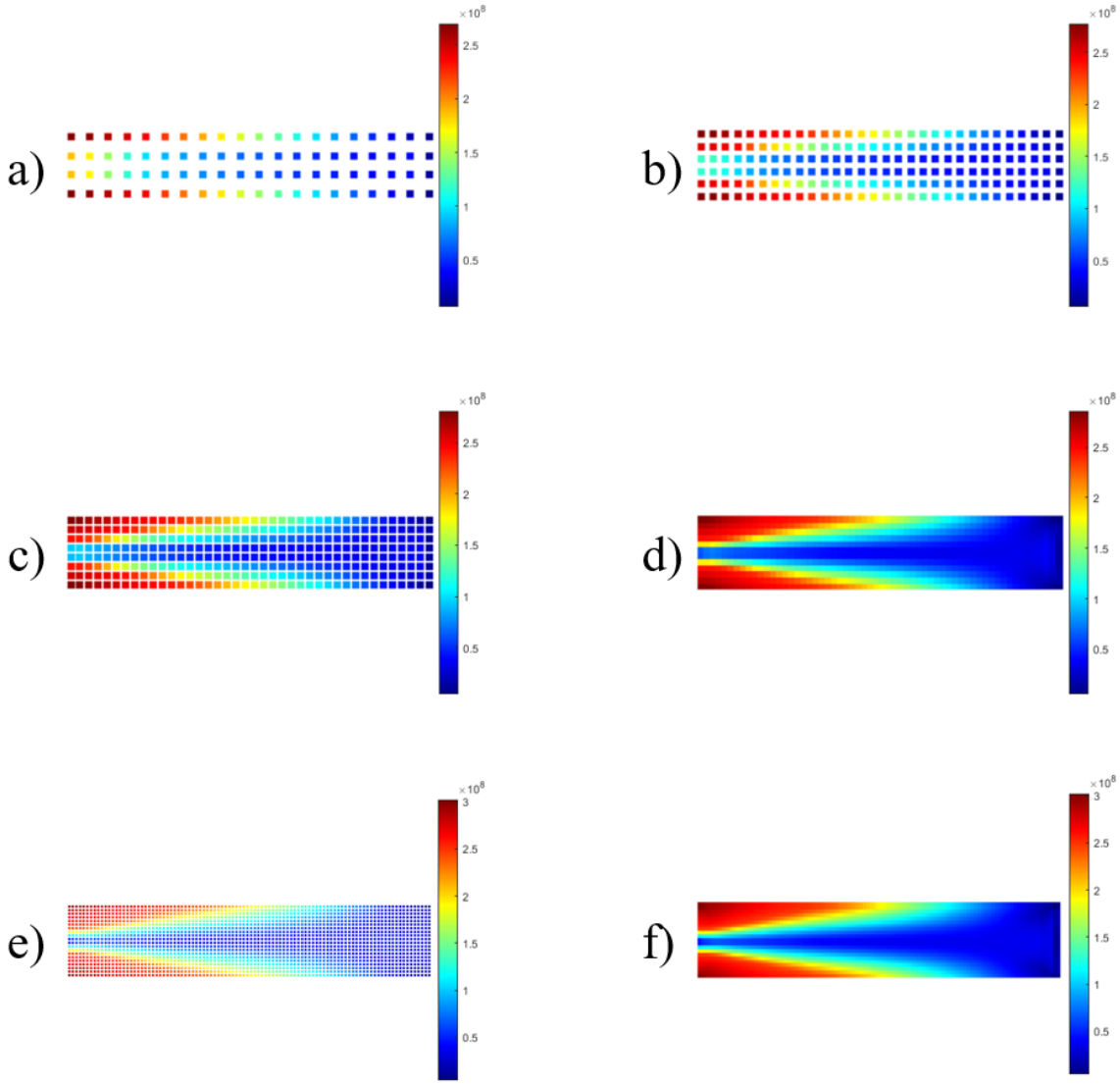

Figure 4.24: Von Mises stress distribution at final step for different mesh sizes and points per element

5 NUMERICAL EXAMPLES

The following paragraphs provide several examples both for RBSN and MPM in order to verify and validate the proposed methodologies as well as examine their accuracy and ability to simulate hysteretic phenomena and plasticity. All the examples presented are solved using Matlab codes developed for this thesis.

5.1 RBSN – Cantilever beam with tip load

In this example a cantilever beam with a concentrated load applied at the free end, is examined. Material is considered as elastic – perfectly plastic (with parameter a set to *0*), Young's modulus is $E = 210GPa$, Poisson ratio is set to *0.3*, material yield stress is $\sigma_y = 240MPa$, beam thickness is 5*cm* and Bouc-Wen parameters are set to $\beta = \gamma = 0,5$ and $n = 8$. Beam geometry is presented in Figure 5.1 and for the discretization a minimum distance of 5*cm* and 3*cm* is used, resulting in two different discretization schemes.

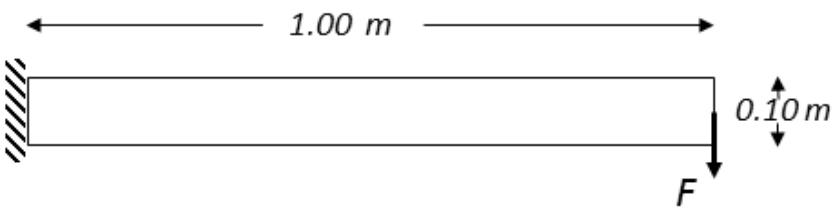

Figure 5.1: Cantilever beam geometry

The applied concentrated load is monotonically increased. For beams with span/depth ratios larger than 3 the initial yield load and a lower bound for the ultimate load can be calculated analytically [85] by Equation (5.1) with the following results:

$$P_y = \frac{\sigma_y b h^2}{6L} = 20kN$$
$$P_u = \frac{\sigma_y b h^2}{4L} = 30kN \tag{5.1}$$

In Figure 5.2, the tip load – tip vertical deflection curve is presented. For this analysis the beam is discretized in two different ways, one using 39 nodes and 78 elements resulting from the 5*cm* minimum distance criterion and the other using 94 nodes and 219 from the 3*cm* distance criterion. Results are compared with those from Hysteretic Bouc-Wen Plane Stress Element (HPSE) [126] using 328 elements and those obtained from Abaqus code [1] using 2094 CPS3 elements. Abaqus implements the full Newton-Raphson scheme for the solution, while HPSE employs the Livermore solvers for ordinary differential equation [106]. Results are in good agreement and indicate the proposed hysteretic RBSN model's ability to simulate the smooth transition from the elastic to the inelastic regime, as well as to predict the correct yield load of the beam. For the discretization with 39 nodes yielding seems to occur at a higher displacement. This can be attributed to the small number of nodes and the resulting few elements along the height of the beam.

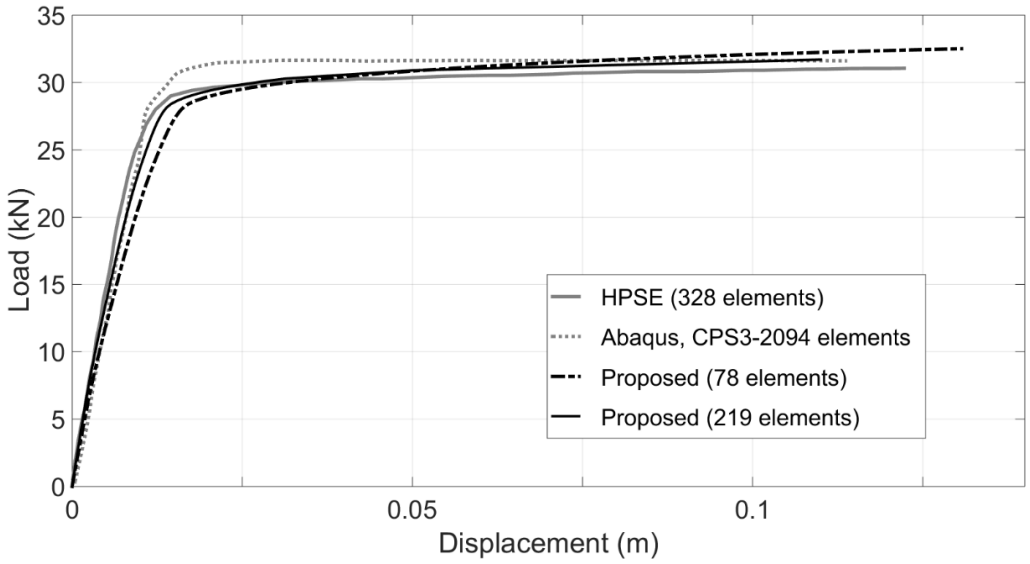

Figure 5.2: Tip load – tip deflection curves for cantilever beam

In Figure 5.3, the distribution of Von Mises stresses is presented at the final state where all the facets near the fixed support are approaching their ultimate plastic state. Results are presented in normalized form and are compared with HPSE in Figure 5.4.

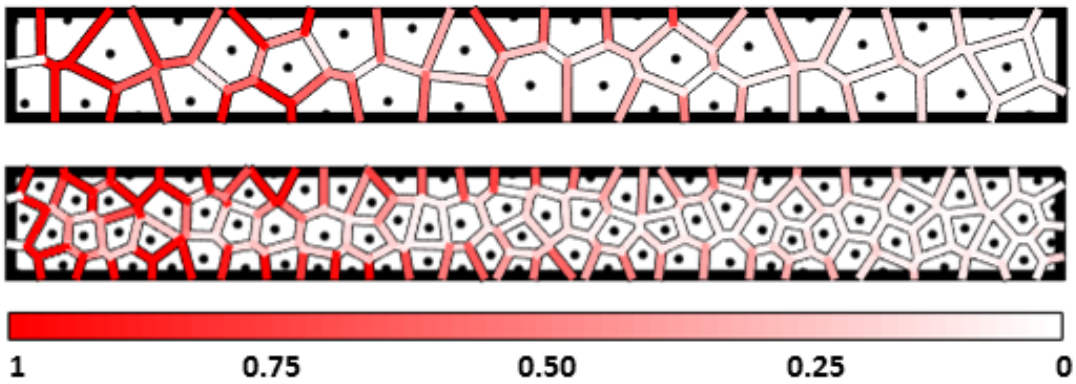

Figure 5.3: Normalized Von Mises yield criterion for proposed method

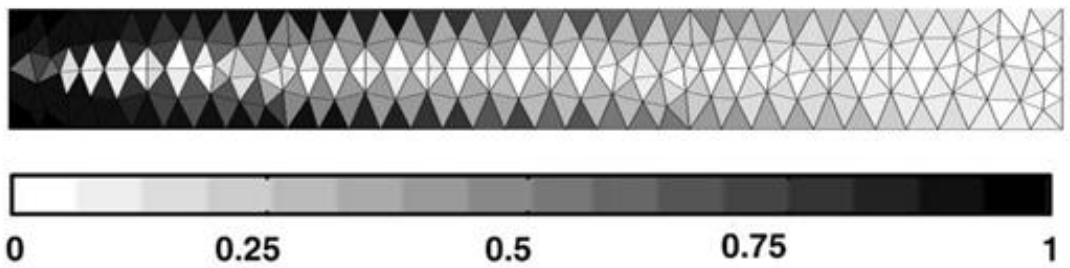

Figure 5.4: Normalized Von Mises yield criterion for HPSE [126]

5.2 RBSN – Plasticity and fracture

In this example a simply supported beam with a load at its middle is examined. Two different discretization schemes are employed using 275 and 689 nodes. Material is elastic, concrete C20/25 with a Young's modulus of $E=29Gpa$, Poisson ratio $v=0.2$ and the dimensions of the beam are 1x0.2m. The tensile strength is 2MPa and the shear strength 6MPa. The final configuration of the deformed beam together with the developed cracks are presented in Figure 5.5. The model is able to predict the correct form and shape of the cracks with one major crack developing as expected in the middle of the simply supported beam. Other cracks are also developing although they are smaller in magnitude.

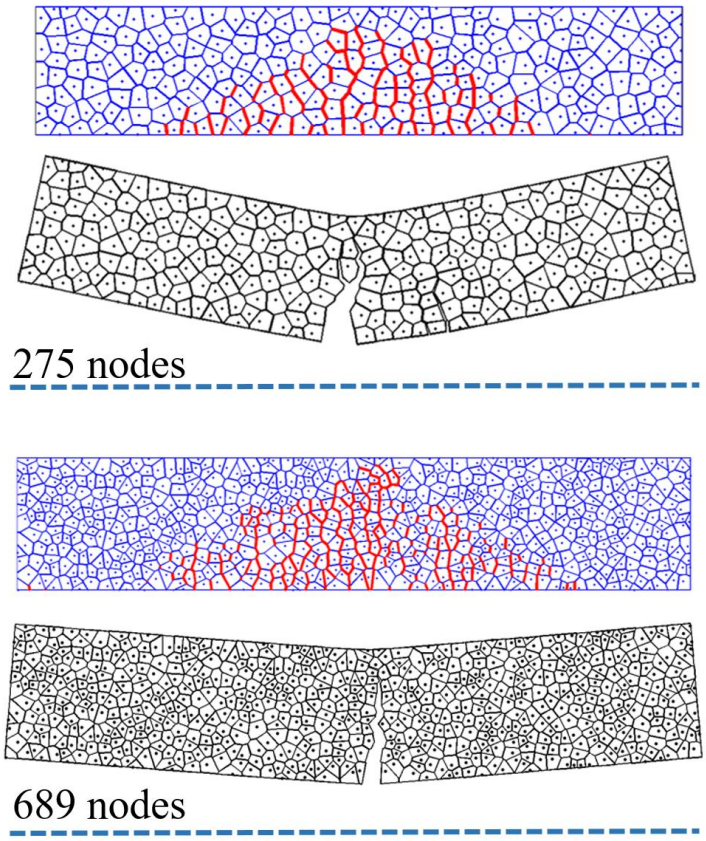

Figure 5.5: Crack patterns in simply supported beam

For a second example a cantilever beam with a concentrated load at the free end is examined. This time both plasticity and fracture are considered. The beam geometry together with the discretization can be seen in Figure 5.6. For this example, the beam was discretized with 94 nodes producing 219 elements.

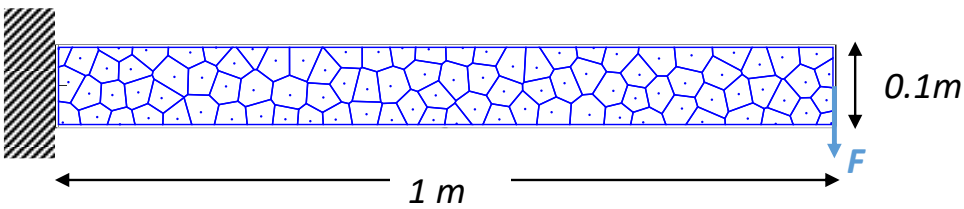

Figure 5.6: Beam geometry and discretization

Material is steel with $\sigma_y=240MPa$ and Young's modulus is $E=210Gpa$ while Poisson ratio is ν=0.3. Beam thickness is 0.05m and the Bouc-Wen parameters are $n=8$ and $\alpha=\beta=0.5$ while the ratio of the post yielding branch to the initial elastic one is set to 2%

hardening. Since the beam has a span to depth ratio larger than 3, the beam yield load and ultimate load can be calculated analytically as in Equation (5.1).

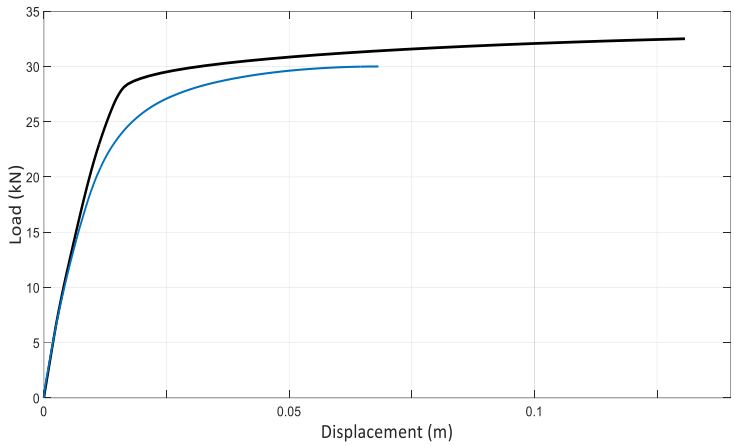

Figure 5.7: External load-tip displacement diagram

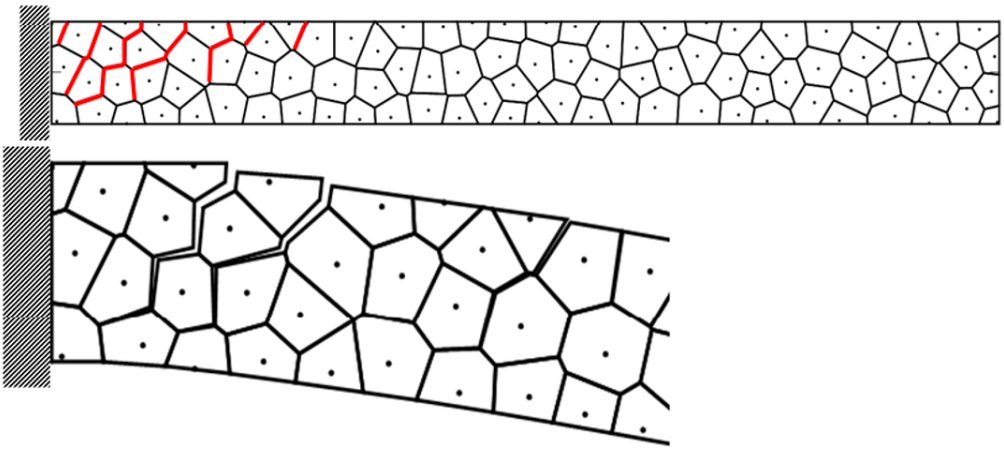

Figure 5.8: Magnified crack pattern

In Figure 5.7, results obtained from two analyses are presented. In the first analysis, only plasticity is considered for the internal springs and no fracture is involved (black line). In the second analysis fracture was also taken into account (blue line). Results show that after initial yield some elements near the support rupture, resulting in a gradual stiffness loss until the external force reached around *30kN* when most of the cross section has lost its stiffness and essentially became a plastic hinge. In Figure 5.8 the crack patterns developed in the beam are also presented. The red lines denote the facets in which the

springs have ruptured. Also, in the same figure the base of the beam near the support is presented magnified in order to show the main cracks developed and their propagation through the beam.

5.3 RBSN – Plastic fracturing of a titanium alloy plate

In this example, the plastic fracture of a titanium alloy plate is examined. Experimental procedures, as well as simulations using a discretized virtual internal bond (DVIB) technique are conducted in Ding et al. [42]. The same problem is also analyzed in [142] using a distinct lattice spring model (DLSM) with a modified Drucker – Prager plasticity model, that is simplified to a Von Mises one. The elastic modulus of the titanium alloy is 115 *GPa*, Poisson's ratio is 0.28, and the tensile strength σ_t is 1007 *MPa* while the yield stress is σ_y=955 *MPa*. These parameters are directly taken from [42] and are obtained from an experimental uniaxial tension test. These experimental measured stress strain curves in uniaxial tension and RBSN simulation are presented in Figure 5.9. The Bouc Wen model in RBSN is able to predict the elastoplastic behavior at elemental level, up to the point where softening behavior is manifested.

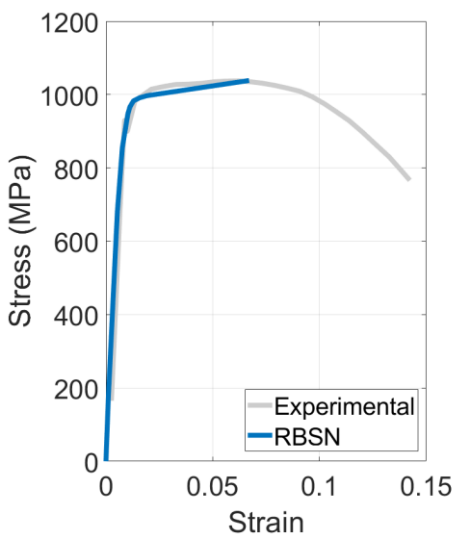

Figure 5.9: Uniaxial tensile stress-strain curve (simulated vs experimental)

Two measurement points are tracked, marked with red dots in Figure 5.10, in order to record the corresponding Crack Opening Displacement (COD). The COD versus reaction force curve recorded in the experimental test [42] is used for verification, and the results from RBSN simulations are compared with those from the other numerical methods. In RBSN simulations the force is gradually applied in a dynamic simulation framework during a large timespan. Results are presented in Figure 5.11.

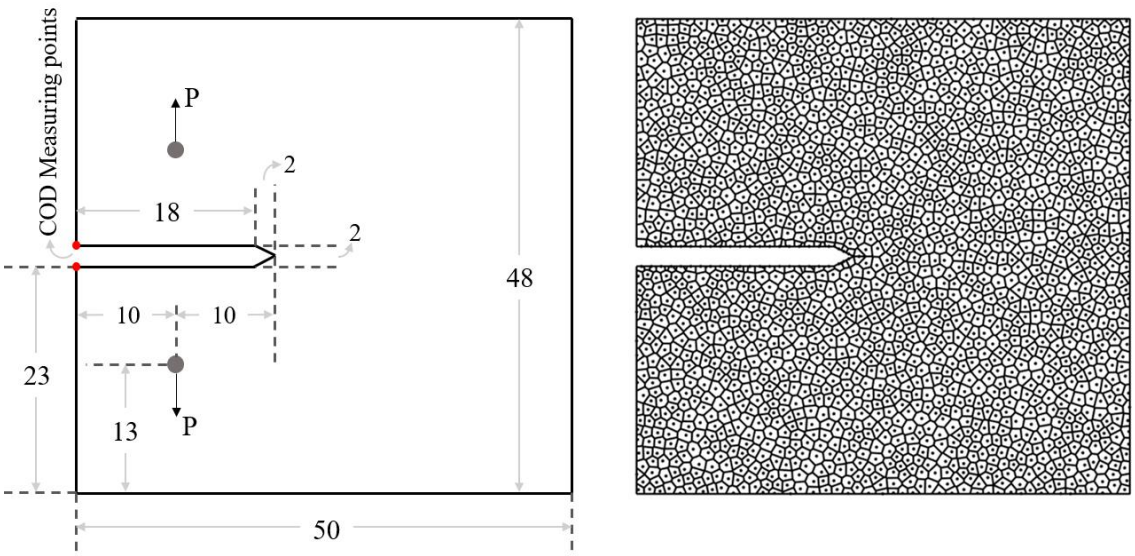

Figure 5.10: Titanium alloy plate geometry and RBSN discretization

In RBSN two meshing schemes are adopted, one using a 3mm minimum distance criterion and one using a 0.9mm criterion. This leads to 218 and 1949 nodes for each model respectively and the initial discretization with 1949 nodes is presented in Figure 5.10.

In Figure 5.11 results are presented for the elastic model as well as the elastoplastic one comparing with an elastoplastic DLSM model. The model appears to be less stiff for the RBSN formulation and as explained in previous Chapters its stiffness is slightly affected by the discretization scheme. The 218 nodes model appears to be closer to the DLSM method (that employs a particle size of 0.5mm) in terms of initial stiffness.

From Figure 5.12, it can be seen that the simulated load-COD curves of the RBSN model considering both plasticity and fracture, agree reasonably with the tested results. Different mesh size schemes give slightly different results regarding the load-COD curve. However, the fracture pattern remains consistent. The fracture pattern is presented in Figure 5.13 together with results from the DVIB method, the DLSM method as well as experimental results.

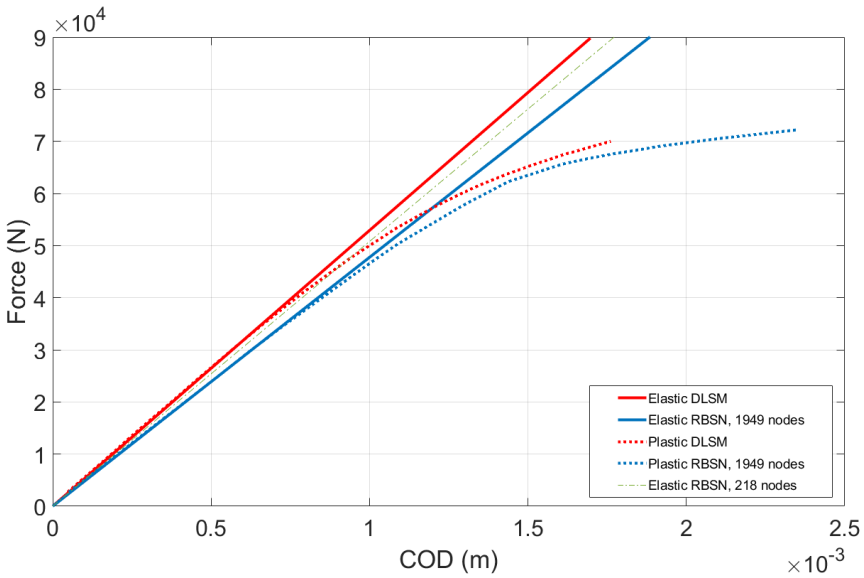

Figure 5.11: Comparison of simulation and experimental results

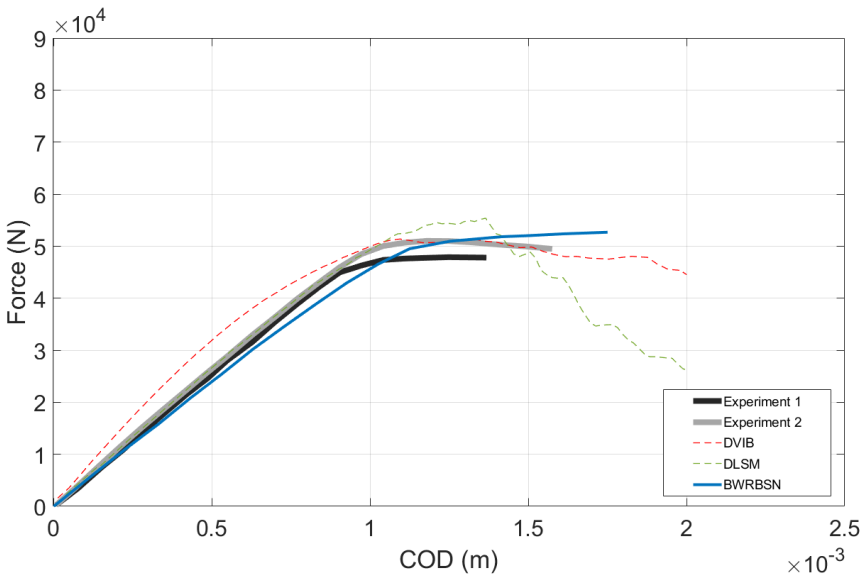

Figure 5.12: Comparison of simulation and experimental results

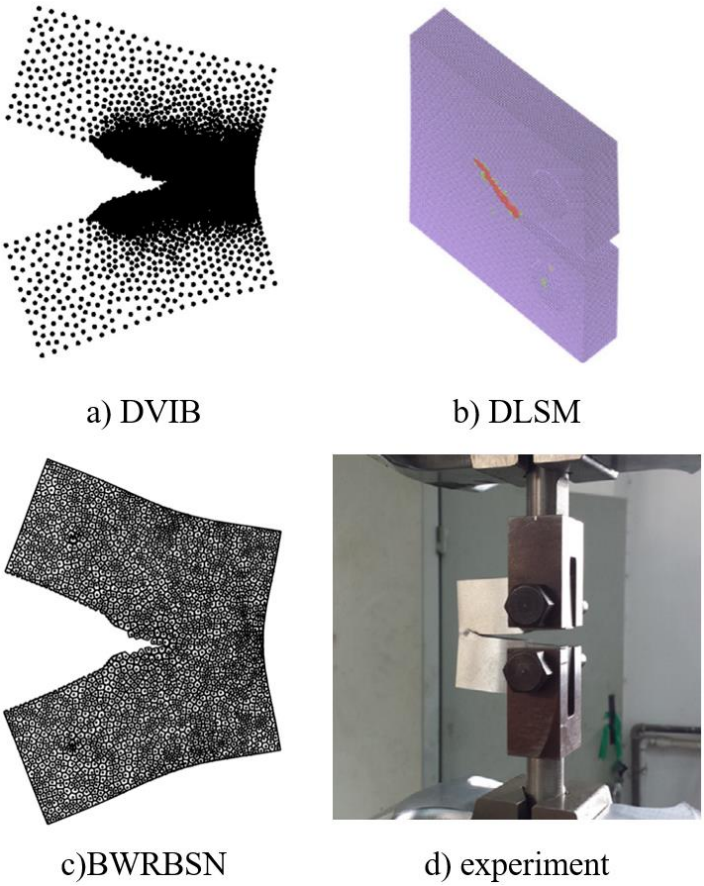

Figure 5.13: a), c): Magnified (10times) crack opening, b) Fracture pattern in DLSM and d) experiment

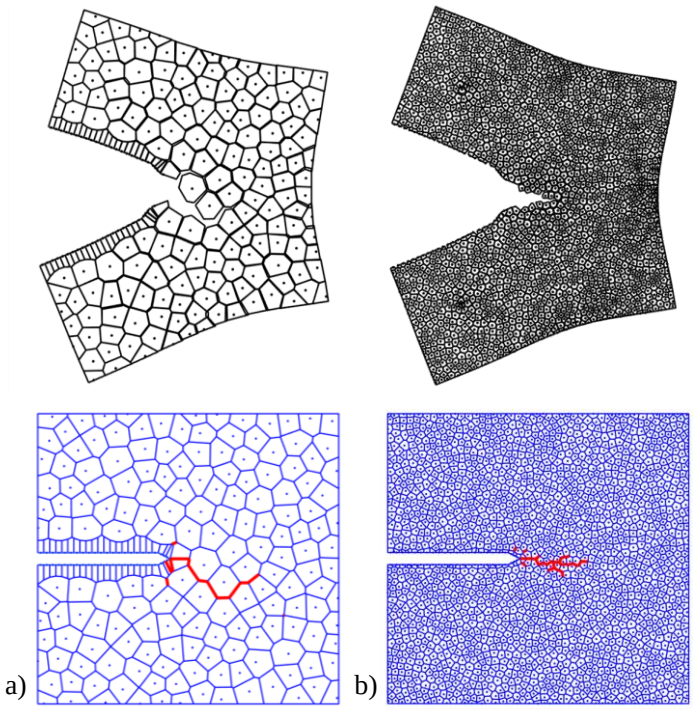

Figure 5.14: RBSN fracture patterns for a) 218 and b) 1949 nodes

Finally, in Figure 5.14 the fracture patterns are presented for a crude discretization with 218 nodes and a mode refined with 1949 nodes. This simulation results signify that the present RBSN method with plasticity and fracture can quantitatively simulate the plastic fracture in this titanium alloy plate.

5.4 MPM – Square patch under tension

As a first numerical example concerning the Material Point Method, the benchmark [119] of a square patch under tension is examined and extended for the inelastic regime. The square patch is attached to a rigid body on the right end and is fixed on the other. Two loading cases are considered. The first refers to a constant velocity applied on the rigid body, while in the second case a sinusoidal velocity is applied. This is essentially a displacement control analysis. The square dimensions are $0.3m \times 0.3m$, and is discretized either with *9* elements and *4* material points per element (*37* material points, Figure 5.15), or *36* elements and *16* material points per element (*576* material points, Figure 5.16). The rigid body has dimensions of $0.1m \times 0.3m$, with *4* material points per element. The Young's modulus is $E = 1000Pa$, and the density is set to $p = 10kg/m^3$. The velocity is imposed on the *x*-direction of the rigid body for both load cases. For the first case the velocity is $v_x = 0.001m/\sec$, while for the second case is given by the following formula: $v_x = 0.015\cos\left(4\pi t / T_{end}\right)$. The analysis is run for $T_{end} = 10.34\sec$. In both cases the yield stress is set at $\sigma_y = 25MPa$ and the hardening ratio at 10%. For the proposed model the parameters used were $n = 32$ to approach bilinear behavior and $\beta = \gamma = 0.5$. Various time step sizes are investigated, and no degradations are considered for this example. Since this is a small deformation problem, linear shape functions were chosen to verify the proposed model in the original MPM formulation. For the case were 36 elements were used and 16 material points per element, to avoid the grid crossing errors, the background

grid was displaced, following the deformation of the square patch (moving mesh MPM [130]).

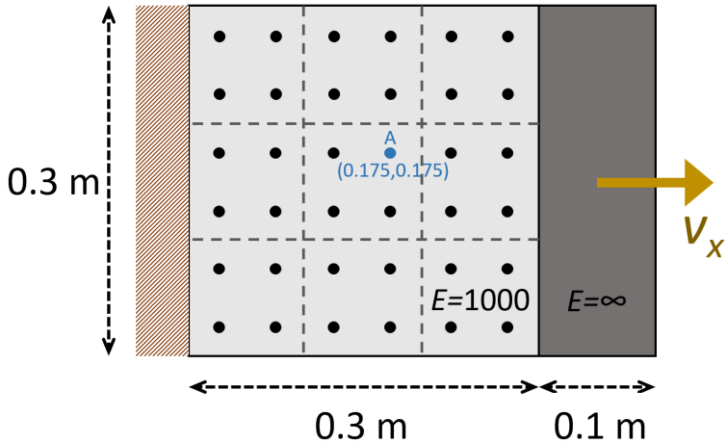

Figure 5.15: Square patch in tension benchmark geometry (9 elements and 4 particles per element)

The results are presented and compared with FEM results [6] from a fine mesh (the FEM elements have dimensions of $0.0125m \times 0.0125m$). In more detail, for the constant velocity and quasi static conditions, the evolution of Von Mises stress is presented in Figure 5.17, regarding the point A with coordinates $x = y = 0.175m$ (as marked in Figure 9) for the discretization with 9 elements and 4 material point per element. The final difference in VM stress is 0.42% and the time step used was $dt = 0.01\text{sec}$ in both analyses.

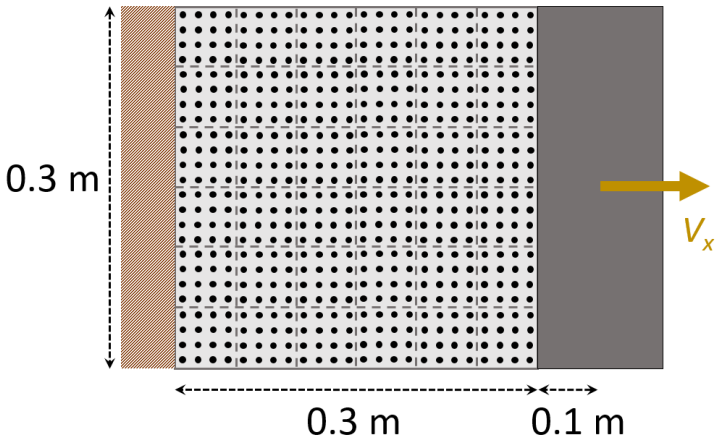

Figure 5.16: Square patch in tension benchmark geometry (36 elements and 16 particles per element)

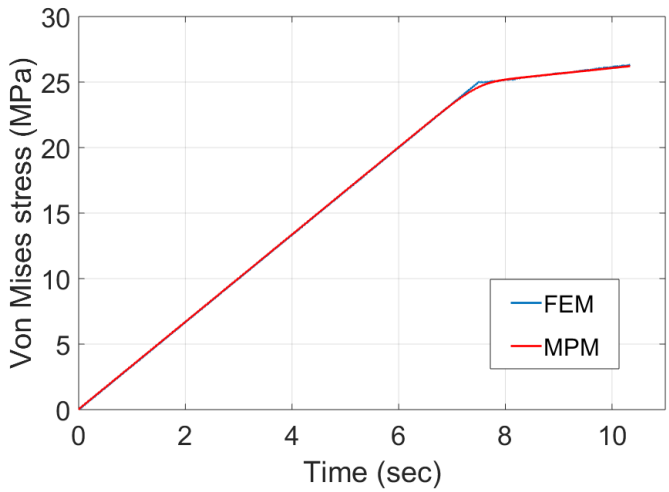

Figure 5.17: Time evolution of Von Mises stress – constant velocity loading case

In addition, the final displacement and stress distribution in the square patch are compared with FEM results (for a discretization with 36 elements and 16 material points per element in the MPM) and are presented in Figure 5.18. Results are in very good agreement, especially for the displacements, while for the stresses, the maximum Von Mises stress developed in the square patch is $26.36MPa$ in MPM and $26.42MPa$ in FEM and the minimum VM stress is $25.34MPa$ and $25.21MPa$ respectively, showing small differences.

It should be noted that for this structure stress concentrations are located at the 4 corner nodes, which increases the maximum stresses as the mesh is refined. This behavior is observed both in FEM and MPM analyses. For this reason, a more refined analysis was conducted using a very fine mesh of plane stress elements with dimensions $0.001m \times 0.001m$ for the FEM and the MPM model. In MPM 4 particles per element were employed for a total of 3600 material points. The results considering the Von Mises stresses for the central region (omitting the 4 corners where stress concentrations manifest) with dimensions $0.3m \times 0.25m$ are presented in Figure 5.19.

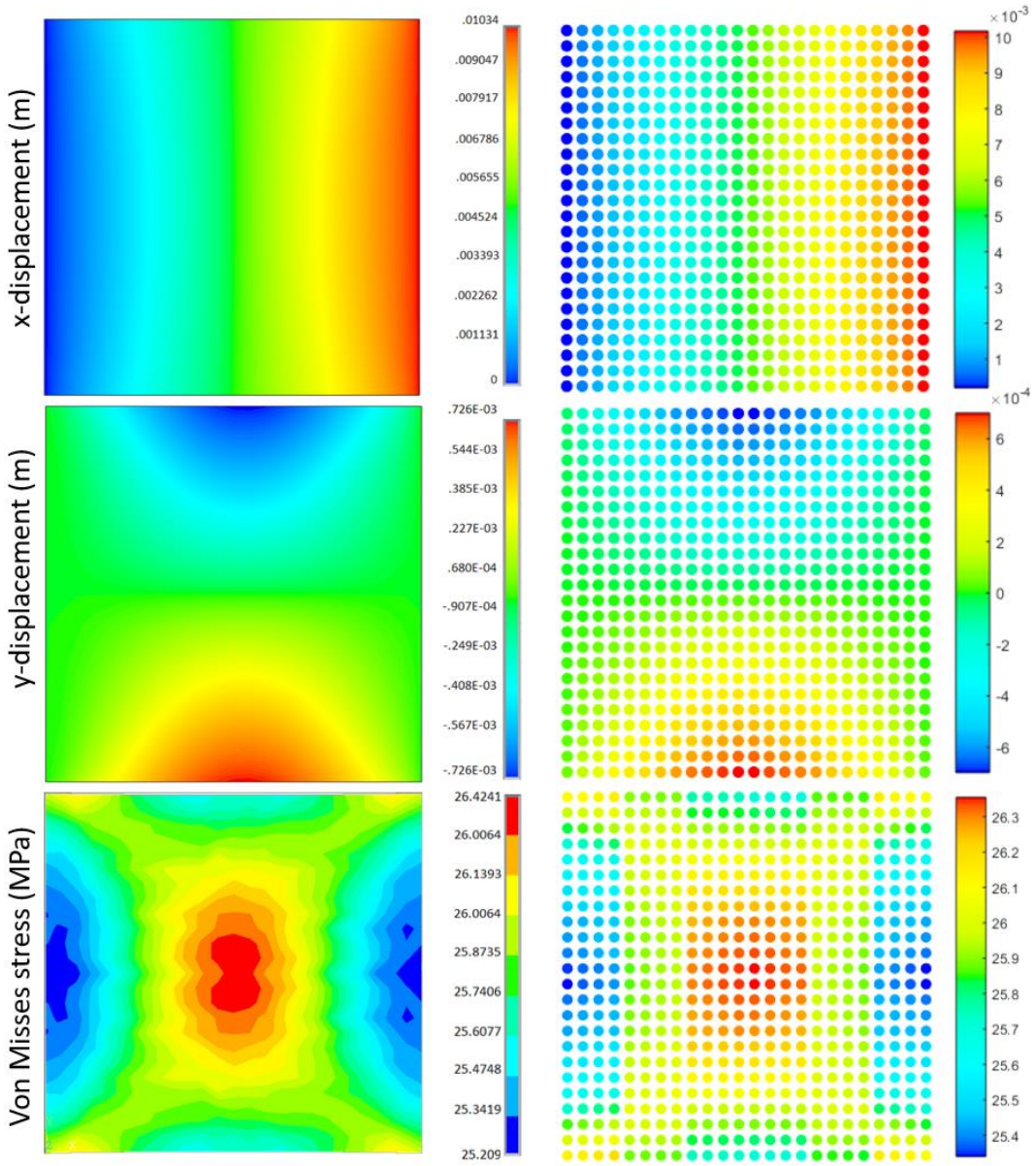

Figure 5.18: Square patch final displacement profiles and Von Mises stress distribution comparison at final time step (Left FEM – right MPM)

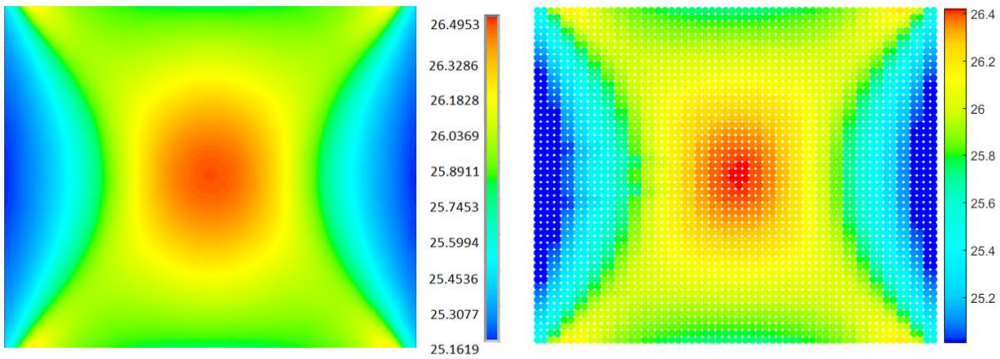

Figure 5.19: Von Mises stress distribution - central region (left FEM – right MPM)

Finally, in order to examine the error in satisfying the yield criterion using a Forward Euler explicit scheme for plasticity, the time evolution of the H_1 function, representing the yield criterion is plotted for different time steps in Figure 5.20.

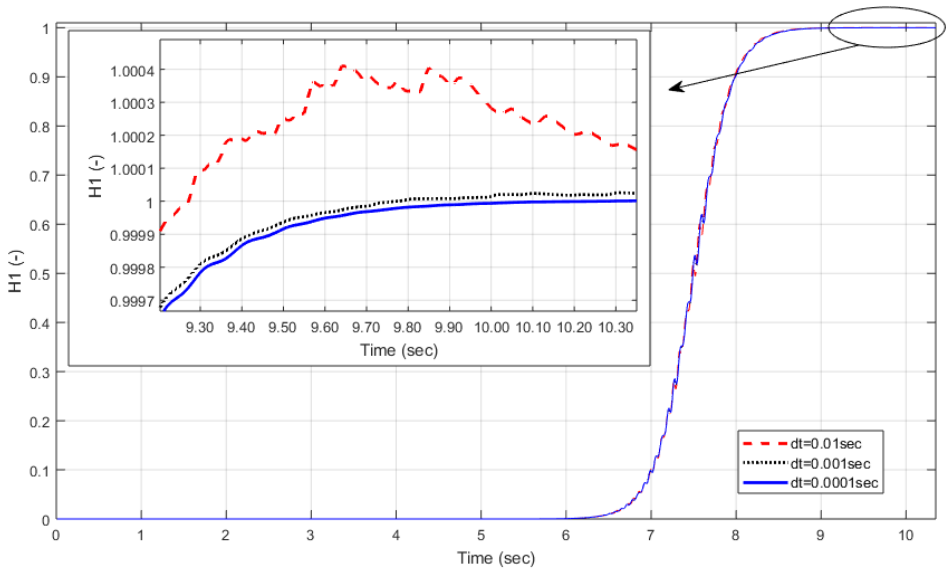

Figure 5.20: Time evolution of H_1 function (yield criterion) for different time steps for constant velocity

This function takes values between zero and one with one representing a fully yielded material. Three different time step sizes are used namely: $dt = 0.01\text{sec}$, $dt = 0.001\text{sec}$ and $dt = 0.0001\text{sec}$. The maximum errors recorded where: $err_{0.01} = 4.09\times10^{-4}\%$ $err_{0.001} = 2.62\times10^{-5}\%$ $err_{0.0001} = 1.14\times10^{-6}\%$ respectively. It can be observed that even with the highest time step dictated by the CFL condition of $dt = 0.01\text{sec}$, the error remained low for this problem. In addition, even for the highest time step H_1 tends to return to its theoretical value of one (1) as time increases. This will be more evident in next part of this example when a sinusoidal velocity is applied.

In the second part of this benchmark example the sinusoidal velocity is applied to study the dynamic behavior of the square patch. Again, the velocity is imposed on the rigid

body in the x direction. All the parameters are the same as in the previous case and two different cases are considered one for isotropic and one for kinematic hardening. Stress and strain results are presented in Figure 5.22 for the point with coordinates $x = y = 0.175m$ (as marked in Figure 5.15) and are compared with FEM. As it can be observed, for this small deformation problem, the results are essentially identical between the two methods verifying the proposed model ability to accurately simulate hysteretic behavior. Moreover, the evolution of the H_1 function, representing the yield criterion is plotted for different time steps in Figure 5.21. As it can be observed the accuracy is better for smaller time steps and even for the highest time step of $dt = 0.01\text{sec}$, the error is low at $err_{0.01} = 2.9 \times 10^{-3}\%$. The error is observed at the first instances when the material reaches the yield surface and as time evolves it returns to the correct value. It should be emphasized here that this behavior manifests for higher values of n, where the response approaches the bilinear behavior. For smaller values and smoother transition from the elastic to the inelastic regime the error is lower. For example, if $n = 8$ the maximum error was $err_{0.01} = 0.59 \times 10^{-3}\%$.

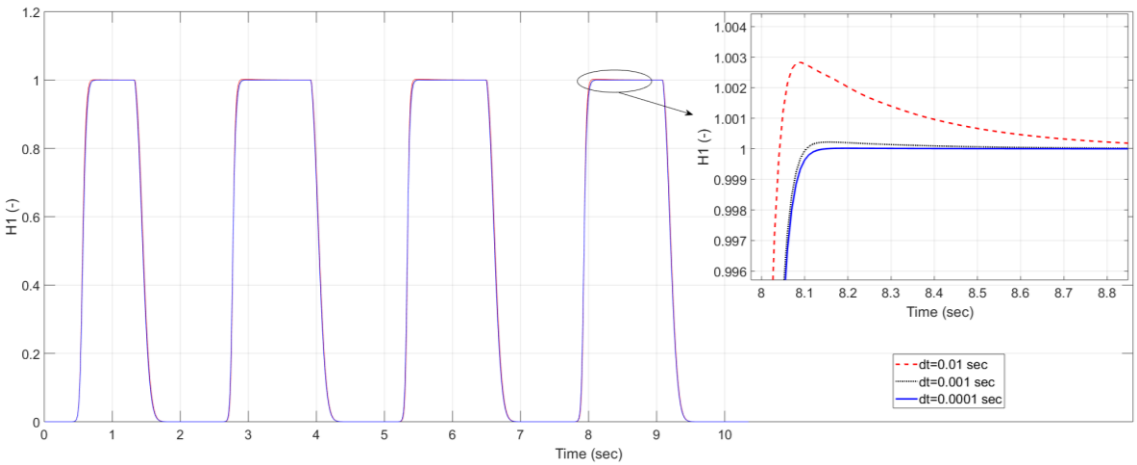

Figure 5.21: Time evolution of H_1 function (yield criterion) for different time steps for sinusoidal velocity and kinematic hardening

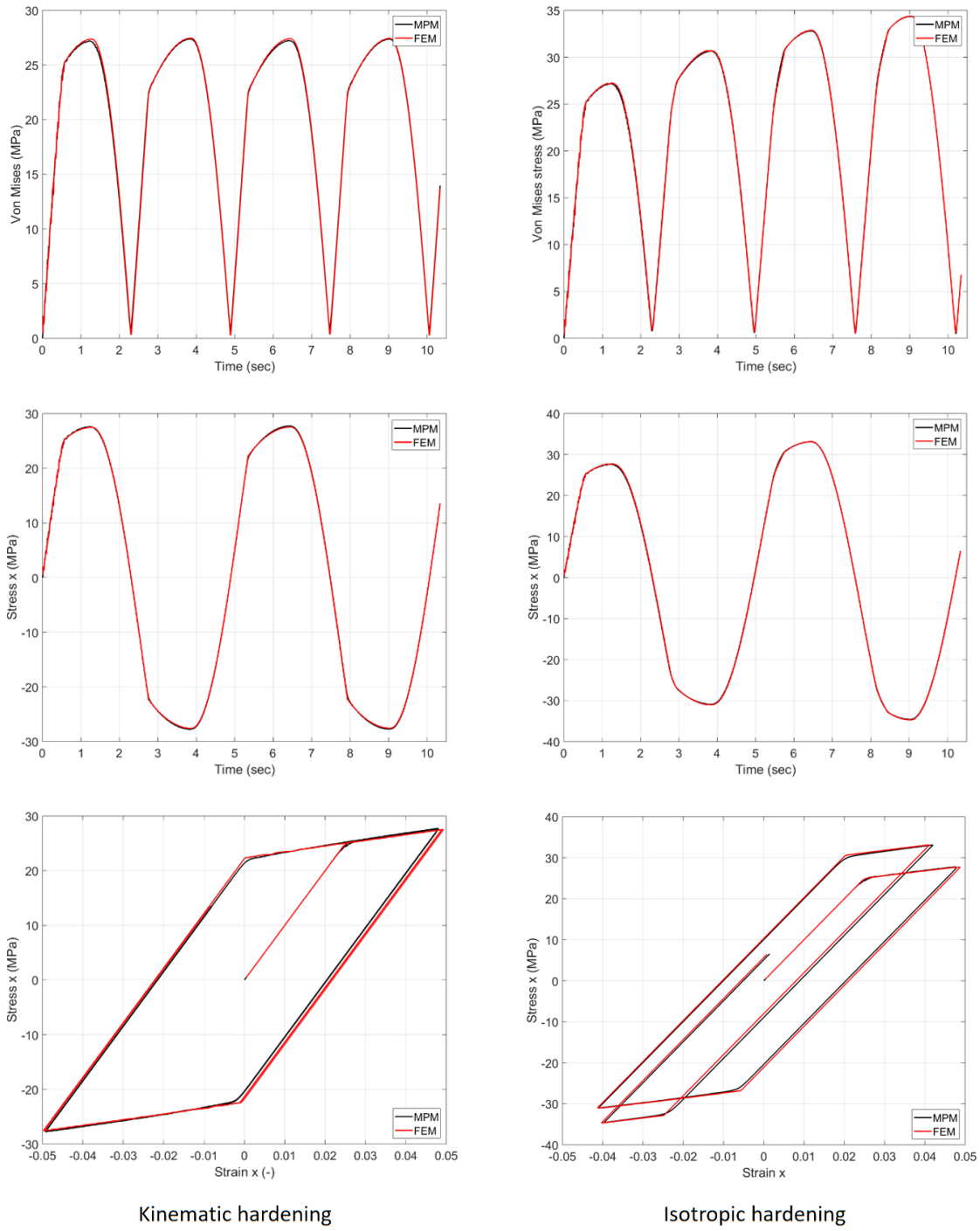

Figure 5.22: Results comparison for sinusoidal load case

5.5 MPM – Hysteretic simply supported beam

In this example, a simply supported beam is subjected to a concentrated tip load on its middle as depicted in Figure 5.23. The material is structural steel with Young's modulus $E = 210GPa$, yield stress of $\sigma_y = 240MPa$ and a mass density of $p = 7850kg/m^3$.

Material is considered as elastic – perfectly plastic. The beam has a length of $2m$ and a height of $0.1m$, while the width is $0.05m$. For the beam discretization 1280 material points were used corresponding to 4 points per element (4ppel). The background grid elements have a length of $0.025m$. The load is applied gradually in small increments over a long time period of 20 sec until its maximum value to simulate quasi-static conditions within the present MPM explicit dynamic formulation. The time step is chosen as $dt = 5 \cdot 10^{-6}$ sec, which although bigger than the one suggested from the CFL condition i.e. $dt_{CFL} = 4.15 \cdot 10^{-6}$, offers quite satisfactory and stable results.

The force-displacement diagram of the free end of the beam is presented in Figure 5.24 and is compared with results from Finite Element code [6]. Finally, the Von Mises stress contour plot for the beam is presented in Figure 5.25 and compared with the results from FE model. Results are essentially identical with an exception near the boundary corners of the beam, due to B-Spline shape functions used in this example. This has been observed also by other researchers in [56] and [4] regarding discrepancies in stress calculations near the boundaries attributed to B-Spline shape functions. However, since the plasticity dominates the central part of the beam this does not affect the overall behavior and final stress state of the beam. Using more particles per element and more elements theses discrepancies become smaller. The hysteretic MPM model can predict accurately the nonlinear response of the beam as well as its stress state.

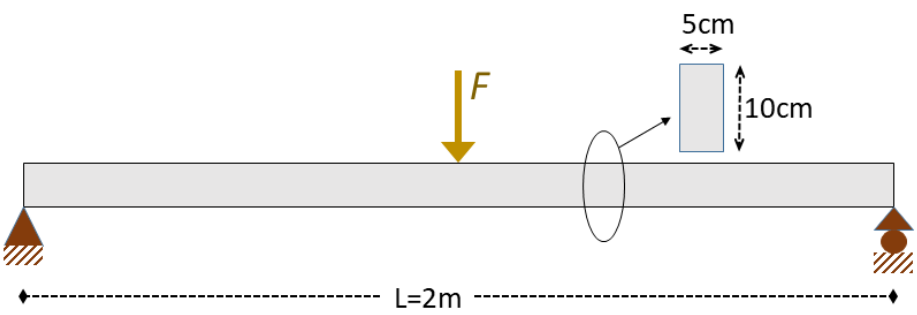

Figure 5.23: Geometry of simply supported beam

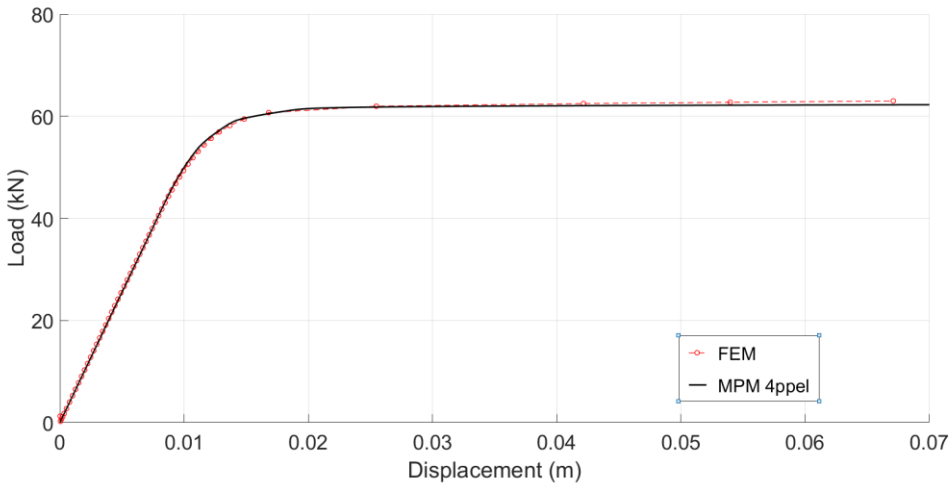

Figure 5.24: Force-displacement diagrams for the middle of the beam

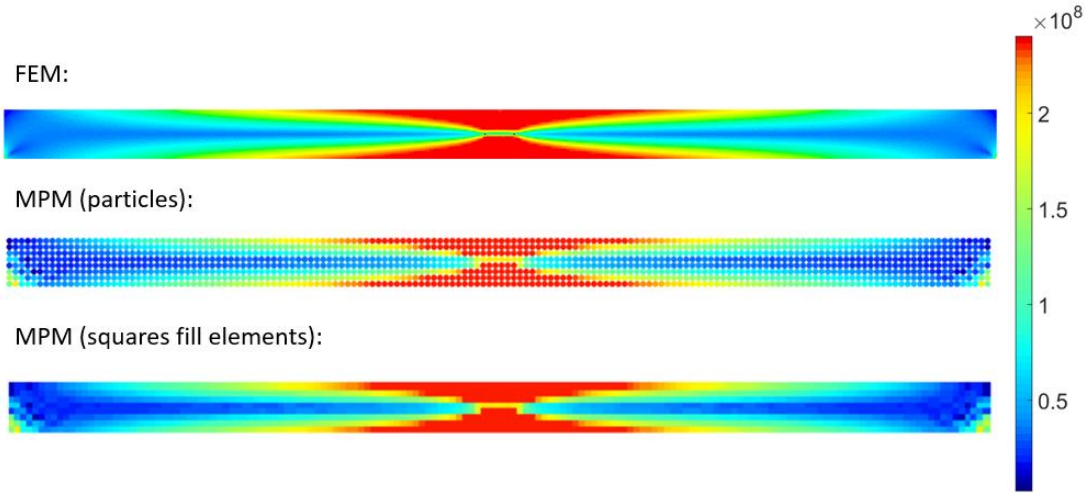

Figure 5.25: Von Mises stress distribution

Furthermore, a second analysis has been performed concerning the dynamic inelastic response of the beam under a sinusoidal load and a hardening of 5%. The imposed sinusoidal dynamic load has a duration of 6 sec and an amplitude of 60kN. It is applied at the middle of the simply supported beam like in the previous example. The analytical expression for the load is: $F = 60\sin(\pi t)$. In Figure 5.26 the time history of the displacement of the middle beam is presented and compared with results from FEM code. Analyses were carried out both for isotropic and kinematic hardening. In addition, the stress strain curves regarding the normal stresses in the horizontal direction that dominate

the beams response are presented in Figure 5.27 regarding the material point located in the bottom half length of the beam for kinematic and isotropic hardening and are compared with FEM. Results are in good agreement verifying the accuracy of the hysteretic MPM formulation for inelastic dynamic analysis. Finally, results considering stiffness degradation and strength deterioration are presented both for stress – strain diagrams (Figure 5.27) and the beam displacements (Figure 5.28). It can be observed that the reduction in stiffness or strength leads to an increasing amplitude response

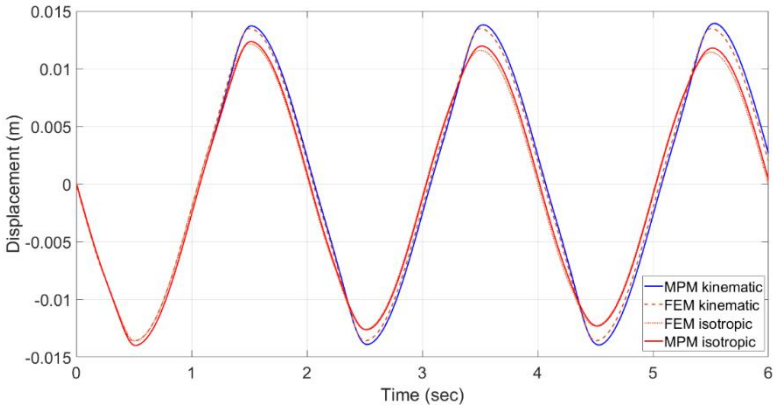

Figure 5.26: Beam displacement time history

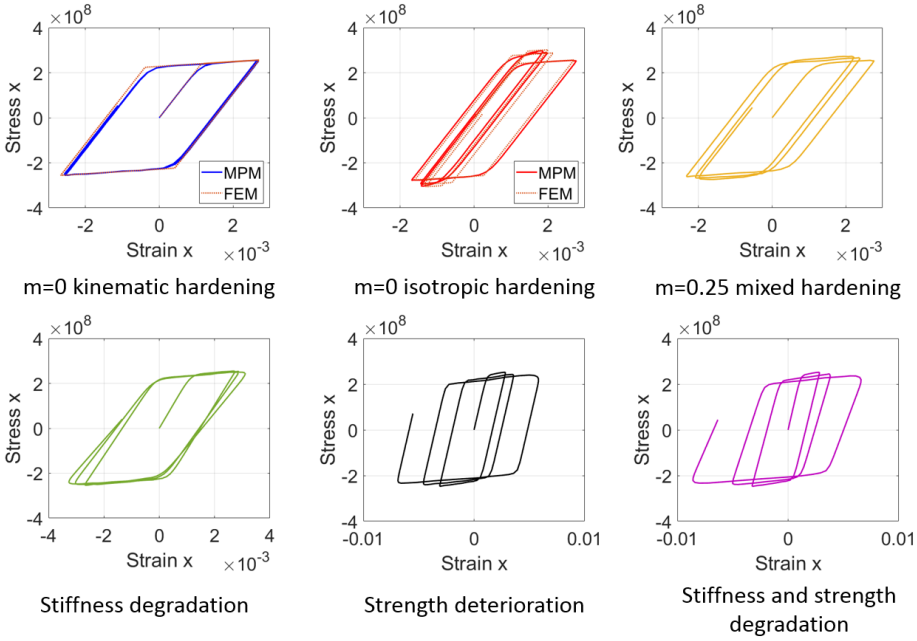

Figure 5.27: Stress strain curves for different hardening and degradation parameters

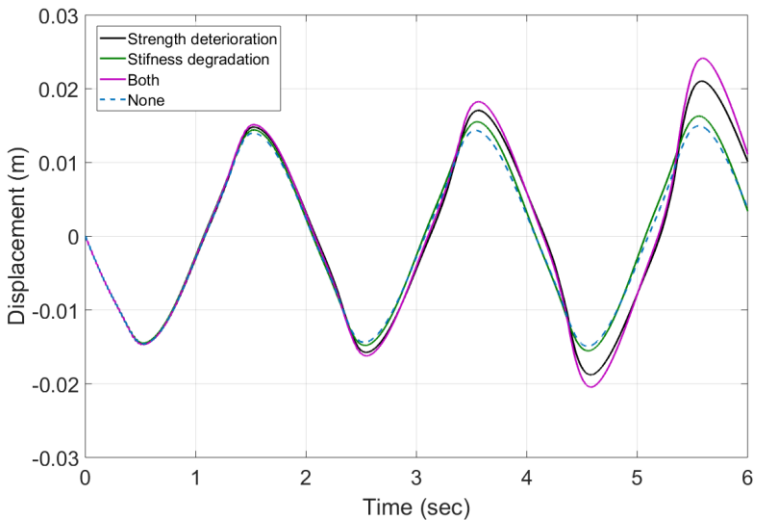

Figure 5.28: Beam displacement time history comparison with degradations

5.6 MPM – Frame corner connection

In this example, the nonlinear response of a frame corner is examined. The experimental setup and the whole investigation is presented in [14]. Both members of the frame connection are made of $\mathrm{W30\times108}$ members and stiffeners and material is steel A36. The geometry and the details of the model can be seen in Figure 5.29. A more detailed discussion of the parameters chosen for the analysis can be found in [138]. In order to simulate the I shaped beams and stiffeners, different thicknesses were assigned to individual material points, namely b_{f} for the flanges and t_w for the web, as can be visualized in Figure 5.29 (left). The grid spacing and the material points per element define the value of the width of the flanges of the I beam t_{f} (represented by the outermost particles). All the other intermediate particles have a depth value of t_w. The moment of inertia of the cross section must remain the same as the original cross section and can be written as the sum of the contributions from the web and the flanges:

$$I_{xx} = I_w + I_{\mathrm{f}} = \frac{t_w\left(D-2t_{\mathrm{f}}\right)^2}{12} + 2b_{\mathrm{f}}t_{\mathrm{f}}\left(\frac{D}{2}-\frac{t_{\mathrm{f}}}{2}\right)^2 + 2\frac{b_{\mathrm{f}}t_{\mathrm{f}}^{\,3}}{12} \tag{5.2}$$

Solving the previous equation for b_f the equivalent flange thickness perpendicular to the 2D domain, that is used in the simulations, is obtained. For the MPM analysis 1296 material points were used with 9 points per element. The force-displacement diagram is presented in Figure 5.30. Results from inelastic MPM simulations are compared against experimental observations as well as results from Meshfree method [138]. The results are in good agreement between the two numerical methods. Differences are observed for both numerical methods with experimental data, after a point where softening behavior is manifested when local buckling of the flanges was reported. It is natural a force controlled numerical model cannot capture this behavior since it only accounts for hardening. However, up to that point the inelastic MPM results follow satisfactory the experimental ones.

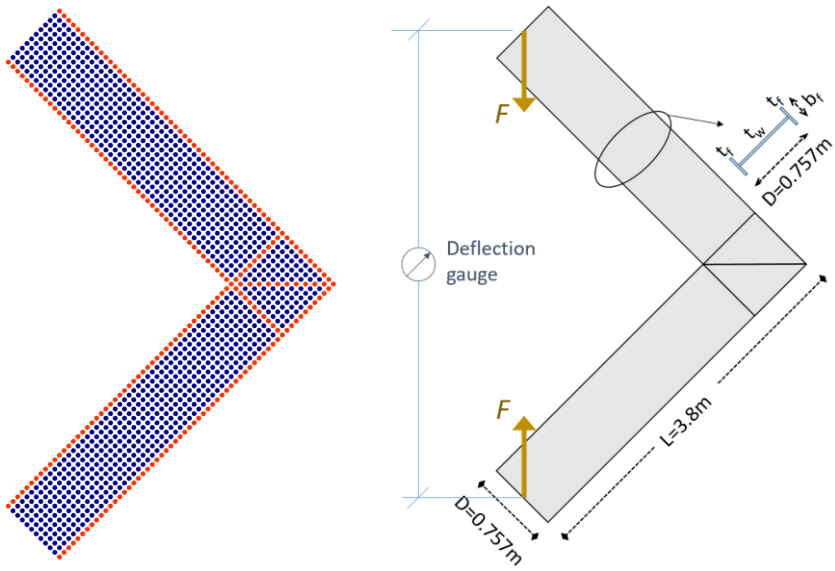

Figure 5.29: Geometry of frame connection

Finally, the stresses developed in the frame corner are plotted in Figure 5.31 and compared against those reported in [138]. They match closely one another, and some observations can be made. A plastic hinge is formed near the corner connection and the beam's neutral axis has shifted towards the flange that is in tension. This is attributed to

the combined axial and bending load state of the beam. These observations are manifested in the numerical results validating the formulation

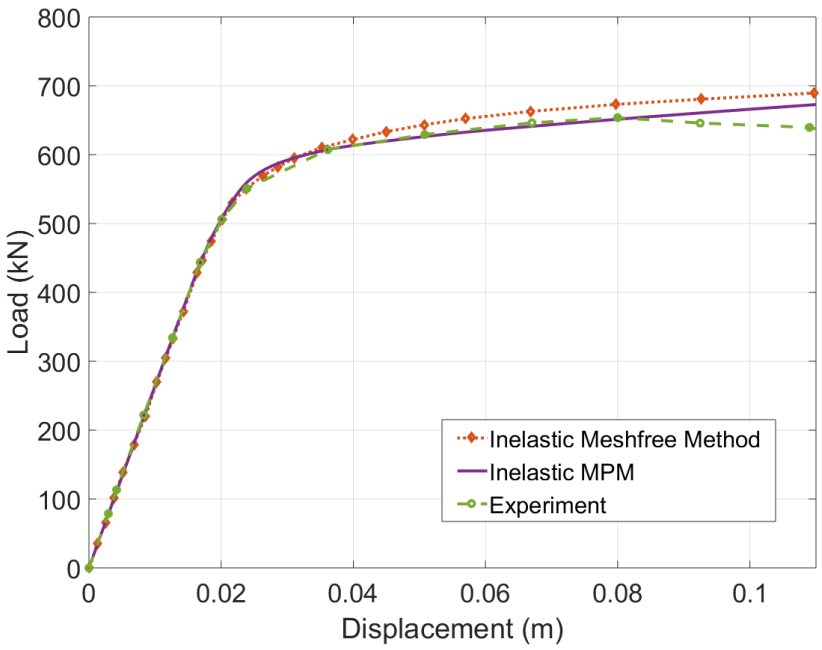

Figure 5.30: Load-displacement diagram for the frame connection

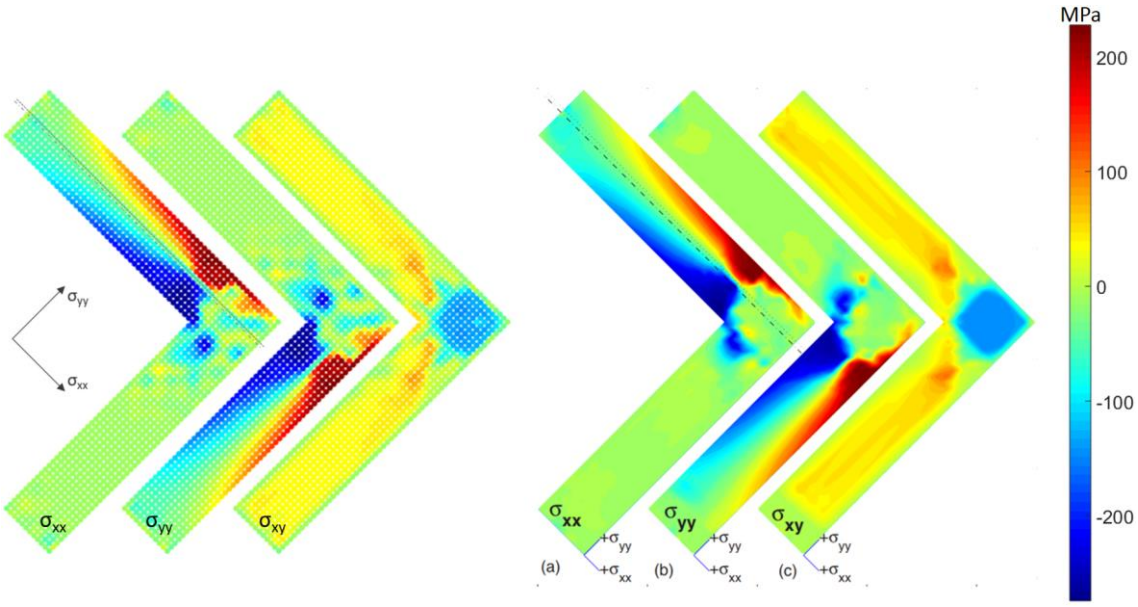

Figure 5.31: Frame corner connection stresses (MPa). Left MPM, right Meshfree Method (adopted from [138])

5.7 MPM – Steel frame

In this example a steel portal frame structure is considered [90]. Material is steel with Young's modulus of 207*GPa*, yield strength of 470*MPa* and a 5% hardening. Both columns of the frame are fixed, and a constant load is applied at the top of the frame with a value of 444.82*kN*. The column cross section is W12x120 while for the beam the cross section is W16x36. Similarly to the previous example, in order to simulate the I beam shape different thicknesses were assigned to material points based on whether they are part of the flanges or the web. Two dynamic analyses are performed, one where the material is considered to be elastic and one for elastoplastic.

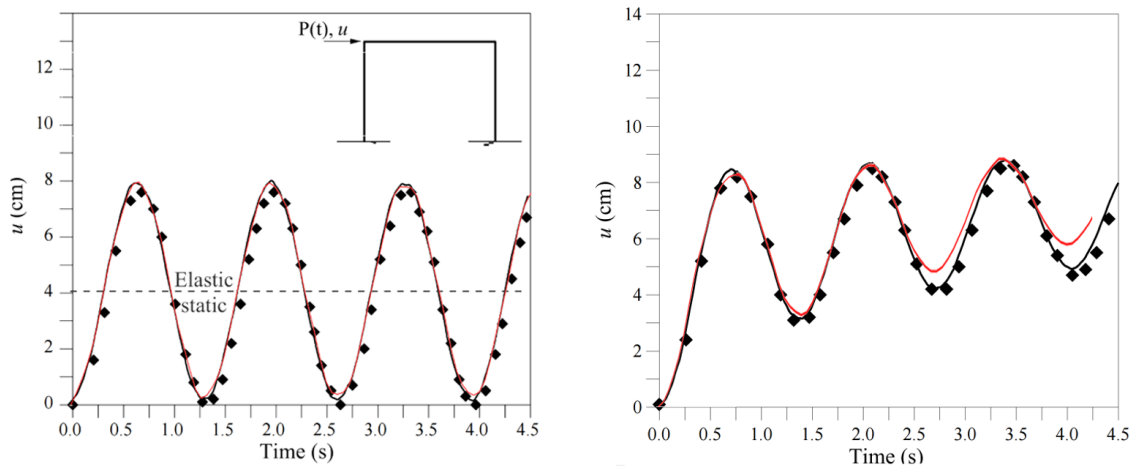

Figure 5.32: Time history of the displacement of the upper left node of the frame (elastic and elastoplastic behavior)

In Figure 5.32, the displacement time history of the top left node of the frame is plotted both when the frame is considered elastic (left) and when plasticity is taken into account (right). Results are compared with an inelastic beam finite element code and appear to be in good agreement [90]. The slight differences that are observed for the inelastic case can be attributed to the difference in the parameter value *n* that controls the smoothness from the elastic to the inelastic region as well as in the fact that in FEM a lumped mass approach is employed. With the black solid line and dots are the results using beam elements while

the MPM results are plotted in red solid lines. Finally, in Figure 5.33 the deformed shape of the frame is presented its maximum amplitude.

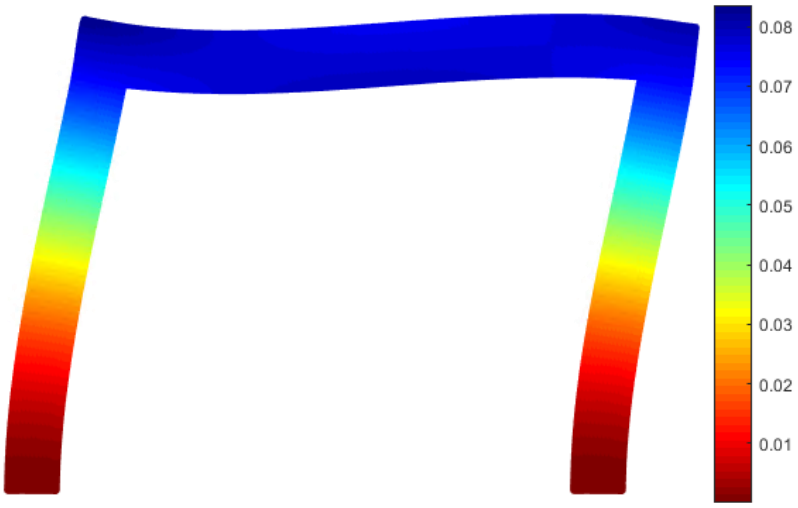

Figure 5.33: Deformed shape for the frame at maximum amplitude

5.8 MPM – Taylor impact test

This example refers to a classical cylinder impact test often referred to as Taylor test. A steel rod is impacting a rigid surface at high velocity. The material of the rod is aluminum 6061-T6 with a density of $p=2700kg/m^3$ and a Young's modulus of $E=78.2GPa$. The Poisson ratio is set to $v=0.3$ and the Von Mises yield stress is $\sigma_y=0.29GPa$ with isotropic hardening. The length of the rod is considered to be three times its radius with its length being $L_o=2.346cm$ and the radius $R_o=0.782cm$. The initial geometry and the MPM discretization are presented in Figure 5.34.

The rod has an initial downwards vertical velocity of $v_0=-373m/sec$. This velocity is applied as an initial velocity to all material points in the MPM algorithm. For the MPM analysis a regular orthogonal grid is chosen with square elements of edge length $L_{el}=0.0782\ cm$. Four material points per element are used in this simulation for a total of

1200 material points. The rigid wall is modelled with roller boundary conditions in the horizontal direction and fixed in the vertical direction.

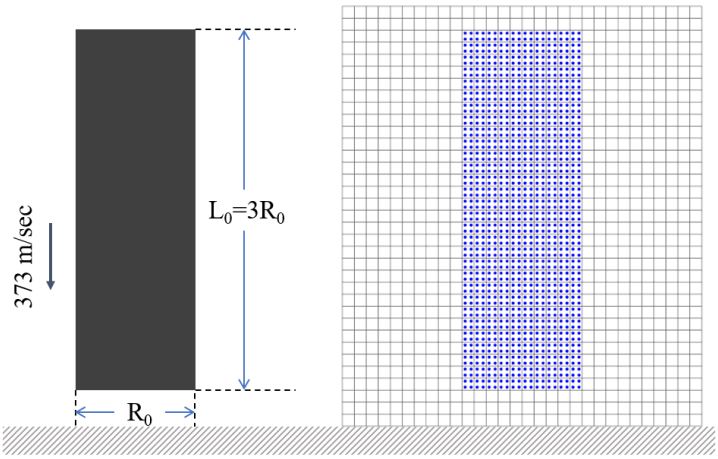

Figure 5.34: Elastoplastic aluminum cylinder initial geometry and MPM discretization

The same problem is analyzed in [121] by Sulsky using an axisymmetric form of the Material Point Method. Results are compared with those from 2D axisymmetric MPM in cylindrical coordinates, as well as other methods also reported in [121] and [103], in Table 5-1, for the final length of the rod L_f and its final diameter D_f. Furthermore, the diameter of the rod at a height 0.25cm from base is also presented, $D_{h=0.25}$ as a measure of the final shape of the rod. For BWMPM (Bouc-Wen Material Point Method) the distances were calculated between the furthest material points, vertically or horizontally, for each case. Since each material point represents an area of the continuum the actual boundaries of the rod are not explicitly tracked by the material points. Results appear to be in good agreement and the BWMPM is able to capture the final deformed shape of the rod. This showcases the ability of the Material Point Method to handle contact problems easily without any modification of the numerical codes and algorithms. Moreover, in Figure 5.35 the final deformed shape of the rod is presented and compared with the deformed shape reported in [121] in Figure 5.35 a) and [103] in Figure 5.35 b) outlined above the BWMPM results. In [121] the coordinates and the problem parameters are normalized in

such a way as $R_o=1$. This implies that that the rod length is $L_o=6$ since half of the rod is actually simulated with symmetric boundary conditions in the middle. All the other units were also made dimensionless by scaling them, for example velocity was scaled using the uniaxial wave speed. In Figure 5.36 the equivalent plastic strains are plotted. As can be expected plasticity is concentrated around the impact area.

	L_f (cm)	D_f (cm)	$D_{h=0.25}$(cm)
FLIP [121]	1.63	1.480	0.98
HEMP [103]	1.652	1.484	1.106
CSQ [103]	1.605	1.440	1.106
Experiment [135]	1.651	-	
BWMPM	1.595	1.452	1.103

Table 5-1: Results regarding the final length of the rod, its final diameter, and its diameter at 0.25cm height for isotropic hardening

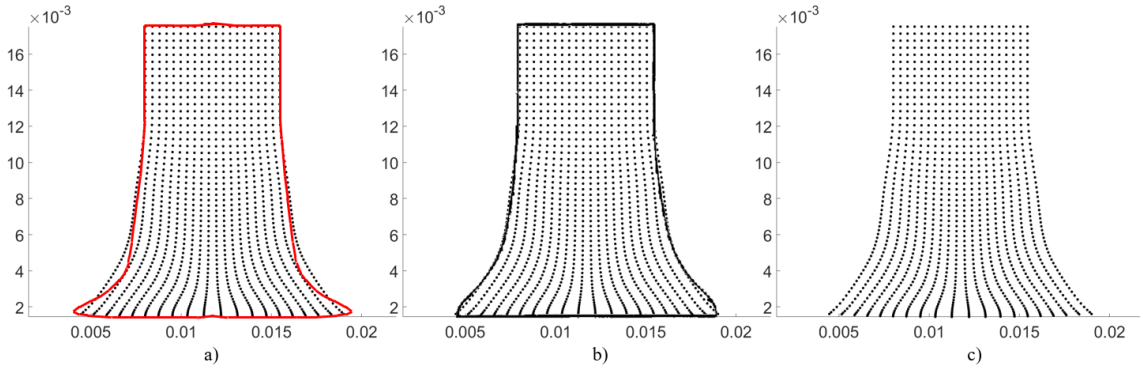

Figure 5.35: Final deformed shape of the rod for isotropic hardening: a) comparison with [121], b) comparison with [103], and c) BWMPM (all units in m)

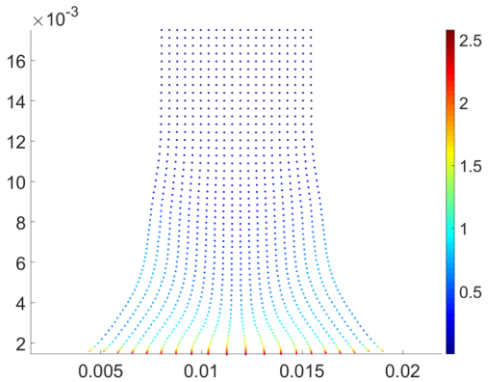

Figure 5.36: Equivalent plastic strains – isotropic hardening

The maximum equivalent plastic strains reported in [121] is 2.732. The BWMPM is able to capture the final shape of the deformed rod with some minor differences regarding the shape of the bulge at 0.25cm height.

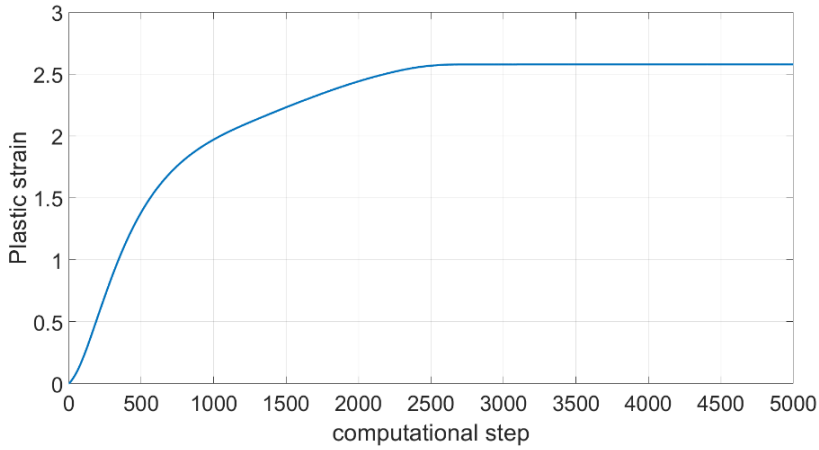

Figure 5.37: Equivalent plastic strain evolution for material point in the middle of the rod impact area.

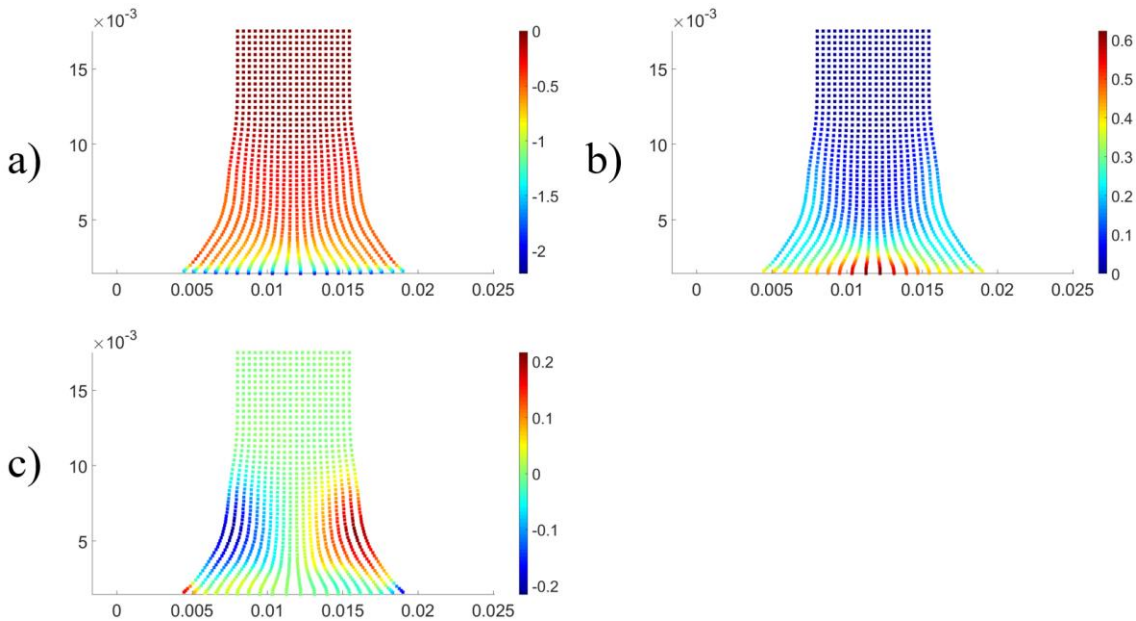

Figure 5.38: Plastic strain distribution, a) ε^{pl}_{xx}, b) ε^{pl}_{yy}, c) ε^{pl}_{xy}

In Figure 5.37 the evolution of the equivalent plastic strains for the material point lying in the middle of the impacting face of the rod are presented. It can be observed that the plastic strains remain unchanged after the 2500 computational step which signifies that

the collision with the rigid wall has occurred and the rod is at rest. Finally, in Figure 5.38 the distribution of normal, tangential and shear plastic strains are presented.

In addition, the same impact problem is analyzed, and the material is considered to be elastic perfectly-plastic. In Table 5-2 results are presented again with regards to the final length of the rod L_f, its final diameter at impact D_f and its final diameter at 0.25cm height $D_{h=0.25}$. In Figure 5.39 the final deformed shape of the rod is presented. In Figure 5.39 a) results from [121] are plotted and in Figure 5.39 b) the black outline represents the final shape of the CSQ results [103] plotted over the BWMPM results. Moreover, in Figure 5.39 c) the deformed shape of the BWMPM alone is presented for clarity. Finally, in Figure 5.40 the equivalent plastic strains are plotted for the case of elastic perfectly plastic material. The maximum plastic strain reported in [121] is 3.559. Results appear to be in good agreement with some shape differences around the impact area of the rod.

	L_f (cm)	D_f (cm)	$D_{h=0.25}$(cm)
FLIP [121]	1.42	1.880	1.00
HEMP [103]	1.479	1.796	1.164
CSQ [103]	1.477	1.652	1.170
BWMPM	1.427	1.753	1.029

Table 5-2: Results regarding the final length of the rod, its final diameter, and its diameter at 0.25cm height for perfectly plastic material

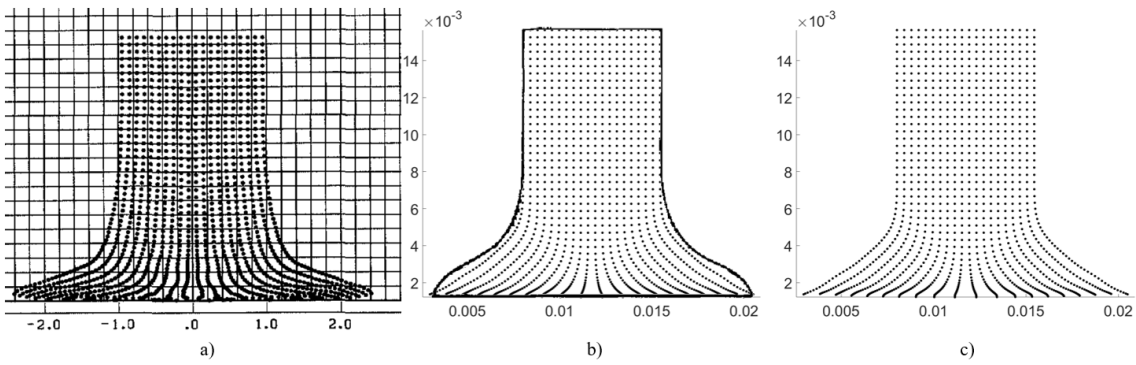

Figure 5.39: Final deformed shape of the rod for perfectly plastic material: a) comparison with [121], b) comparison with [103], and c) BWMPM (all units in m)

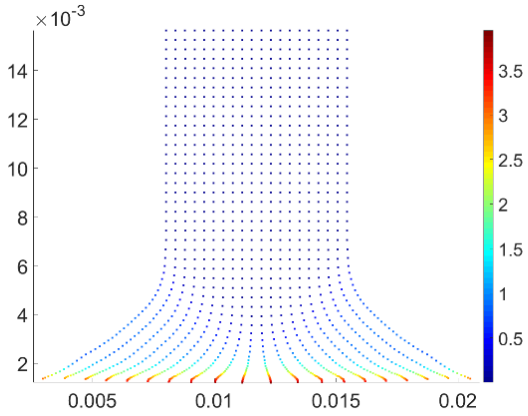

Figure 5.40: Equivalent plastic strains – perfectly plastic

6 CONCLUSIONS - FUTURE RESEARCH

6.1 Summary, comparisons and concluding remarks

In this dissertation, smooth, rate independent Bouc-Wen hysteretic models are derived based on both a physical based approach with a mechanical analogue, as well as on classical plasticity theory concepts. The main advantage of the Bouc-Wen formulation is the use of smooth Heaviside type functions, acting as switches, and controlling all the stages of a hysteretic loop, avoiding the stepwise prediction correction incremental procedure. A single relation is established for the plastic multiplier in rate form that is valid for the entirety of the stress space. The formulation is quite general so as the model can accommodate various yield criteria and hardening laws. Consequently, the Bouc-Wen equations are established in a compact form allowing for isotropic, kinematic and mixed hardening as well as stiffness degradation and strength deterioration. By adjusting the parameters of the hysteretic model, a wide range of inelastic response can be simulated. These parameters are the exponent n, which controls the smoothness of the transition from the elastic to the inelastic regime, β and γ that control the shape of the hysteretic loops during unloading, parameter α that controls the slope of the inelastic branch and c_η, m_u, and c_v that control stiffness degradation and strength deterioration.

The Rigid Body Spring Network method is investigated next. A nonlinear Rigid Body Spring Network element that incorporates the Bouc-Wen hysteretic model is developed, together with effective methods for the solution of the resulting equations of motion in implicit form. An element consists of two rigid cells connected at their common facet. This connection is established using three zero length springs that follow a Bouc-Wen hysteretic behavior. For each spring, the total force is decomposed into an elastic and an inelastic part. Both linear differential equations of motion and the nonlinear hysteretic equations are solved simultaneously by being converted into state space form. A hysteretic matrix is being established for each element rendering the proposed

formulation suitable for incorporation into existing RBSN codes. This is accomplished mainly by evaluating the hysteretic matrices and establishing the evolution equations. Numerical examples are presented that demonstrate the validity of the model in simulating hysteretic behavior. These are compared with Abaqus and Ansys commercial code, as well as the HYPLAS code and results obtained from a hysteretic Bouc-Wen type plane stress finite element approach. From an engineering perspective, a direct physical model that has the ability to incorporate the main characteristics of hysteresis in plane 2D problems has been presented. This provides designers the ability to study the behavior of various structures and identify regions of interest with regards to plastic phenomena to accurately determine the final deformed state of the structure. As such, the entire approach does not account accurately for the stress field within the rigid cells and is more suitable for the contemporary performance based and displacement-based design.

The Material Point Method is addressed next, in an explicit formulation to model dynamic or quasi-static problems, incorporating hysteretic-inelastic behavior. This formulation accounts for a smooth transition from the elastic to the inelastic regime and incorporates isotropic, kinematic and mixed hardening law, accommodating stiffness degradation and strength deterioration for the whole behavior at each material point, employing the Bouc -Wen model. The hysteretic model has been efficiently incorporated into the MPM framework by deriving a tangent modulus for each material point taking into account the interaction between the stress components and a smooth behavior from elastic to inelastic transition. The formulation can accommodate various yield criteria, hardening laws and stiffness degradation and strength deterioration. The model is used in an explicit time integration scheme and the numerical results show that it can be quite effective in a Forward Euler scheme without the need for a predictor – corrector, or radial return algorithm, achieving lower errors for smoother transitions. Numerical examples are presented and compared with results from finite element codes, experimental results and

meshless methods, which validate the proposed model ability to simulate hysteretic inelastic phenomena in the framework of MPM. Since the tangent modulus is calculated for each material point, incorporating the proposed formulation into existing MPM codes is quite straightforward. In addition, these calculations are discrete, rendering the method suitable for the use in massive parallel computations in high performance computing.

	Solver	**Displacement accuracy**	**Stress accuracy**	**Mesh size dependency**	**Ease of mesh generation**
RBSN	Implicit	✓✓✓	✓	✓	✓✓
MPM	Explicit	✓✓✓	✓✓✓	✓✓	✓✓✓

Table 6-1: Comparison of the two discrete methods

Both these methods are termed as discrete. The RBSN employs the Voronoi tessellation as a main characteristic of the method. There are numerous algorithms available in the literature for automatic Voronoi tessellation of complex geometries. This means that the RBSN with Bouc-Wen as presented, provides effective means to effectively identify areas of interest through its discrete representation of plasticity and crack patterns with automated meshing. The MPM can be used for plane stress and plane strain problems involving hysteretic behavior and provide a better resolution of internal variables, such as stresses and strains. In comparison with the RBSN, the MPM is able to provide better results concerning the calculation of stresses in 3D stress space. The accuracy of both methods with regard to the displacement field can be regarded as similar. Both methods are adequate in correctly capturing the displacements of structures during dynamic loadings and when plasticity is manifested.

6.2 Future research

Research directions that further improve the work presented in this dissertation are listed below.

1. Extend the RBSN model with fracture laws that are based on energy calculations both for monotonic and cyclic loadings.
2. In this dissertation, the material response is regarded as independent of the rate of application of loads and/or the timescale of the problems considered. An interesting point of future research could be the use of Bouc-Wen hysteretic model in the case of viscoplasticity (or rate-dependent plasticity).
3. Incorporate Damage laws in Bouc-Wen model in order to model the softening behavior of various materials.
4. Develop a Damage model for the MPM, taking into account localization phenomena and mesh dependencies.
5. In the analysis of elongated structural members, using a rectangular grid results in having a vastly larger number of elements in one direction than in the perpendicular one. This leads to higher computational times. In FEM this can be partially overcome, by discretizing with orthogonal plane stress elements. An interesting study would be to incorporate beam models in the MPM to model part of the elongated structure. Moreover, embedded reinforcement in concrete could be modelled with such beam elements.

7 REFERENCES

1. Abaqus version 6.5 [Computer software]. Dassault Systemes Simulia, Providence

2. Adamatzky, A., Alonso-Sanz, R., and Lawniczak, A. (2008). Automata-2008: Theory and applications of cellular automata. Luniver Press

3. Adkins, C. J. (1983). Equilibrium Thermodynamics. Cambridge University Press, Cambridge, UK

4. Andersen, S., and Andersen, L. (2010). “Analysis of spatial interpolation in the material-point method”. Computers and Structures, 88(7-8), 506–518. doi:10.1016/j.compstruc.2010.01.004

5. Anderson, C. E. (1987). “An overview of the theory of hydrocodes”. International Journal of Impact Engineering, 5(1-4), 33–59. doi:10.1016/0734-743x(87)90029-7

6. ANSYS Mechanical APDL and Mechanical Applications Theory Reference, (2010) ANSYS Release 15.0, ANSYS Inc.

7. Ashby, M. F. (1996). “Modelling of materials problems”. Journal of Computer-Aided Materials Design, 3(1–3), 95–99

8. Baber, T. T., and Noori, Mohammad N. (1985). “Random vibration of degrading, pinching systems”, Journal of Engineering Mechanics 111 (8), pp. 1010-1026.

9. Baber, T. T., and Wen, Y. K. (1980). “Seismic response of hysteretic degrading structures”, Publ. Turk. Natl. Comm. on Earthquake Eng. Volume 7, Turkish National Committee on Earthquake Engineering, Istanbul, Turkey, 457–464.

10. Bardenhagen, S. G. (2002). Energy Conservation Error in the Material Point Method for Solid Mechanics. Journal of Computational Physics, 180(1), 383–403. doi:10.1006/jcph.2002.7103

11. Bardenhagen, S., and Kober, E. (2004). “The generalized interpolation material point method”. CMES - Computer Modeling in Engineering and Sciences, 5(6), 477–496

12. Bathe, K. (1996). Finite Element Procedures, Prentice-Hall, New Jersey

13. Beatty, M. F. (1996). Introduction to Nonlinear Elasticity. Nonlinear Effects in Fluids and Solids, 13–112. doi:10.1007/978-1-4613-0329-9_2

14. Beedle, L. S., Christopher, R. (1963) “Tests of steel moment connections”. AISC Eng. J., 1(4), 116–125

15. Belyschko, T., Liu, W. K., and Moran, B. (2000). Nonlinear Finite Elements for Continua and Structures, John Wiley and Sons, New York

16. Berton, S. (2003) “Numerical simulation of the durability mechanics of cement-based materials”. Ph.D. thesis, Civil and Environmental Engineering, University of California, Davis

17. Beuth, L., Więckowski, Z., and Vermeer, P. A. (2010). “Solution of quasi-static large-strain problems by the material point method”. International Journal for Numerical and Analytical Methods in Geomechanics, n/a–n/a. doi:10.1002/nag.965

18. Bolander, J. E., and Berton, S. (2004). “Cohesive zone modeling of fracture in irregular lattices”. Fracture Mechanics of Concrete Structures. Proc. of FRAMCOS-5:989- 994

19. Bolander, J. E., and Hong, G. S. (2002). “Rigid-Body-Spring Network modeling of prestressed concrete members”. ACI Structural Journal, 99(5):595-604

20. Bolander, J. E., and Saito, S. (1998). “Fracture analyses using spring networks with random geometry”. Engineering Fracture Mechanics, 61(5-6), 569–591. doi:10.1016/s0013-7944(98)00069-1

21. Bolander, J. E., Moriizumi, K., Kunieda, M. and Yip, M. (2001). “Rigid-Body-Spring Network modeling of cement-based composites”. Fracture Mechanics of Concrete Structures, 773-780

22. Bouc, R. (1967). “Forced vibration of mechanical systems with hysteresis”, Proceedings of the Fourth Conference on Non-linear oscillation, Prague, Czechoslovakia

23. Brackbill, J. U., and Ruppel, H. M. (1986). “FLIP: A method for adaptively zoned, particle-in-cell calculations of fluid flows in two dimensions”. Journal of Computational Physics, 65(2), 314–343. doi:10.1016/0021-9991(86)90211-1

24. Brackbill, J. U., Kothe, D. B., and Ruppel, H. M. (1988). “Flip: A low-dissipation, particle-in-cell method for fluid flow”. Computer Physics Communications, 48(1), 25–38. doi:10.1016/0010-4655(88)90020-3

25. Cakmakci, M., Sendur G. K., and Durak, U. (2017). Simulation-Based Engineering. In: Mittal S., Durak U., Ören T. (eds), Guide to Simulation-Based Disciplines. Simulation Foundations, Methods and Applications. Springer, Cham

26. Carli, F. (1999). “Nonlinear response of hysteretic oscillator under evolutionary excitation”. Advances in Engineering Software, 30(9-11), 621–630. doi:10.1016/s0965-9978(98)00111-2

27. Casciati, F. (1995) “Stochastic dynamics of hysteretic media”. Probabilistic Methods in Applied Physics. Lecture Notes in Physics, vol 451. Springer, Berlin, Heidelberg

28. Chaboche, J. L. (1989). “Constitutive equations for cyclic plasticity and cyclic viscoplasticity”. International Journal of Plasticity, 5(3), 247-302

29. Chahrour, A. H., and Ohtsu, M. (1994). “Crack growth prediction in scaled down model of concrete gravity dam”. Theoretical and Applied Fracture Mechanics, 21(1), 29–40. doi:10.1016/0167-8442(94)90006-x

30. Charalampakis, A. E. (2014). “The response and dissipated energy of Bouc–Wen hysteretic model revisited”. Archive of Applied Mechanics, 85(9-10), 1209–1223. doi:10.1007/s00419-014-0937-8

31. Charalampakis, A. E., and Koumousis, V. K. (2008). “Identification of Bouc–Wen hysteretic systems by a hybrid evolutionary algorithm”, Journal of Sound and Vibration, Vol. 314, Issues 3-5, pp. 571-585.

32. Charalampakis, A. E., and Koumousis, V. K., (2009). “A Bouc Wen Model compatible with plasticity postulates”, Journal of Sound and Vibration, Vol. 322, Issues 4-5, pp. 954-968.

33. Chatzi, E. N., and Smyth, A. W. (2009). “The unscented Kalman filter and particle filter methods for nonlinear structural system identification with non-collocated heterogeneous sensing”, Structural Control and Health Monitoring 16(1), pp. 99-123.

34. Chen, S., and Doolen, G. D. (1998). “LATTICE BOLTZMANN METHOD FOR FLUID FLOWS”. Annual Review of Fluid Mechanics, 30(1), 329–364. doi:10.1146/annurev.fluid.30.1.329

35. Chen, S., Wang, Z., Shan, X., and Doolen, G. D. (1992). “Lattice Boltzmann computational fluid dynamics in three dimensions”. Journal of Statistical Physics, 68(3-4), 379–400. doi:10.1007/bf01341754

36. Choi, S. B., and Lee, S. K. (2001). “A hysteresis model for the field dependent damping force of a magnetorheological damper”, Journal of Sound and Vibration 245(2), 375-383.

37. Chopra, A. (2009). Dynamics of Structures. Prentice Hall, New York

38. Courant, R., Friedrichs, K., and Lewy, H. (1967). On the Partial Difference Equations of Mathematical Physics. IBM Journal of Research and Development, 11(2), 215–234. doi:10.1147/rd.112.0215

39. Crisfield, M. A. (1991). Non-linear Finite Element Analysis of Solids and Structures. Volume 1: Essentials. Wiley, New York

40. Cundall, P. A. (1971). “A computer model for simulating progressive, large scale movements in blocky rock systems”. Proceedings of the Symposium of the International Society for Rock Mechanics, Society for Rock Mechanics (ISRM), France, II-8, 129–136.

41. Dhakal, T. R., and Zhang, D. Z. (2018). “Combining dual domain material point method with molecular dynamics for thermodynamic nonequilibriums”. Journal of Computational Physics. doi:10.1016/j.jcp.2018.08.007

42. Ding, J., Zhang, Z., Yang, F., Zhao, Y., and Ge, X. (2017). “Plastic fracture simulation by using discretized virtual internal bond”. Engineering Fracture Mechanics, 178, 169–183. doi:10.1016/j.engfracmech.2017.04.032

43. Donea, J., Giuliani, S., and Halleux, J. P. (1982). “An arbitrary lagrangian-eulerian finite element method for transient dynamic fluid-structure interactions”. Computer Methods in Applied Mechanics and Engineering, 33(1-3), 689–723. doi:10.1016/0045-7825(82)90128-1

44. Dong, Y., Wang, D., and Randolph, M. F. (2015). “A GPU parallel computing strategy for the material point method”. Computers and Geotechnics, 66, 31–38. doi:10.1016/j.compgeo.2015.01.009

45. Drucker, D. C. (1959). “A definition of a stable inelastic material”. ASME Journal of Applied Mechanics, 26, 101-195

46. Drucker, D. C. (1960). “Plasticity. Structural Mechanics”. Proc. 1st Symposium of Naval Structural Mechanics. New York: Pergamon Press, pp 407-55

47. Eliáš, J. (2017). Boundary Layer Effect on Behavior of Discrete Models. Materials, 10(2), 157. doi:10.3390/ma10020157

48. Eliáš, J., and Vořechovský, M. (2011). “The Effect of Mesh Density in Lattice Models for Concrete with Incorporated Mesostructure”. Key Engineering Materials, 488-489, 29–32. doi:10.4028/www.scientific.net/kem.488-489.29

49. Eliáš, J., Vořechovský, M., Skoček, J., and Bažant, Z. P. (2015). “Stochastic discrete meso-scale simulations of concrete fracture: Comparison to experimental data”. Engineering Fracture Mechanics, 135, 1–16. doi:10.1016/j.engfracmech.2015.01.004

50. Erdogan, F., and Sih, G. C. (1963). “On the Crack Extension in Plates Under Plane Loading and Transverse Shear”. Journal of Basic Engineering, 85(4), 519. doi:10.1115/1.3656897

51. Erlicher, S., and Bursi, O. S. (2009). “Bouc–Wen-Type Models with Stiffness Degradation: Thermodynamic Analysis and Applications”, Journal of Engineering Mechanics, Vol. 134, No. 10, 843 – 855.

52. Erlicher, S., and Point, N. (2004). “Thermodynamic admissibility of Bouc Wen type hysteresis models”, C. R. Mecanique, Vol. 332, pp. 51-57

53. Fern, J., Rohe, A., Soga, K., and Alonso, E., (2019) The Material Point Method for Geotechnical Engineering: A Practical Guide, CRC Press

54. Foliente, G. C (1995). “Hysteresis modeling of Wood Joints and Structural Systems”, Journal of Structural Engineering, 121(6), pp. 1013-1022.

55. Frank, R. M., and Lazarus, R. B. (1964). “Mixed Eulerian – Lagrangian method”. in: B. Alder, S. Fernbach M.Rotenberg (Eds.), Methods in Computational Physics,Vol.3: Fundamental Methods in Hydrodynamics, AcademicPress, NewYork, pp.47–67

56. Gan, Y., Sun, Z., Chen, Z., Zhang, X., and Liu, Y. (2017). “Enhancement of the material point method using B-spline basis functions”. International Journal for Numerical Methods in Engineering, 113(3), 411–431. doi:10.1002/nme.5620

57. Genta, G. (2012). Introduction to the mechanics of space robots. Springer. 10.1007/978-94-007-1796-1_6

58. Gingold, R. A., and Monaghan, J. J. (1977). “Smoothed particle hydrodynamics: theory and application to non-spherical stars”. Monthly Notices of the Royal Astronomical Society, 181(3), 375–389. doi:10.1093/mnras/181.3.375

59. Gkimousis, I., and Koumousis, V. (2018). “Modeling RC column flexural failure modes under intensive seismic loading”. Earthquake Engineering & Structural Dynamics, 47(9), 1942–1962. doi:10.1002/eqe.3050

60. Guilkey, J. E., and Weiss, J. A. (2003). “Implicit time integration for the material point method: Quantitative and algorithmic comparisons with the finite element method”. International Journal for Numerical Methods in Engineering, 57(9), 1323–1338. doi:10.1002/nme.729

61. Guilkey, J. E., Hoying, J. B., and Weiss, J. A. (2006). “Computational modeling of multicellular constructs with the material point method”. Journal of Biomechanics, 39(11), 2074–2086. doi:10.1016/j.jbiomech.2005.06.017

62. Guo, Z., and Zhao, T. S. (2005). “A LATTICE BOLTZMANN MODEL FOR CONVECTION HEAT TRANSFER IN POROUS MEDIA”. Numerical Heat

Transfer, Part B: Fundamentals, 47(2), 157–177. doi:10.1080/10407790590883405

63. Harlow, F. H., (1955). “A machine calculation method for hydrodynamic problems”, Tech. Rep. LAMS- 1956, Los Alamos Scientific Laboratory.

64. Harlow, F. H., (1957). “Hydrodynamic problems involving large fluid distortions”, Journal of the ACM 4 (1) 137–142

65. Harlow, F. H., (1964). “The particle-in-cell computing method for fluid dynamics”, Methods in Computational Physics 3,319–343

66. Huang, P., Zhang, X., Ma, S., and Huang, X. (2010). “Contact algorithms for the material point method in impact and penetration simulation”. International Journal for Numerical Methods in Engineering, 85(4), 498–517. doi:10.1002/nme.2981

67. Hughes, T. J. R., Cottrell, J. A., and Bazilevs, Y. (2005). “Isogeometric analysis: CAD, finite elements, NURBS, exact geometry and mesh refinement”. Computer Methods in Applied Mechanics and Engineering, 194(39-41), 4135–4195. doi:10.1016/j.cma.2004.10.008

68. Hwang, Y. K., Bolander, J. E., and Lim, Y. M. (2016). “Simulation of concrete tensile failure under high loading rates using three-dimensional irregular lattice models”. Mechanics of Materials, 101, 136–146. doi:10.1016/j.mechmat.2016.08.002

69. Il’iushin, A. A. (1961) “On the postulate of plasticity”. Prikl Math Mekh; 25:503-7

70. Ingraffea, A. R., and Saouma, V. (1985). “Numerical modeling of discrete crack propagation in reinforced and plain concrete”. Fracture Mechanics of Concrete: Structural Application and Numerical Calculation, 171–225. doi:10.1007/978-94-009-6152-4_4

71. Irons, B. M. (1970). “Applications of a theorem on eigenvalues to finite element problems”. (CR/132/70), Tech. Rep., University of Wales, Department of Civil Engineering, Swansea,

72. Ismail, M., Ikhouane, F., and Rodellar, J. (2009). “The Hysteresis Bouc-Wen Model, a Survey”. Archives of Computational Methods in Engineering, 16(2), 161–188. doi:10.1007/s11831-009-9031-8

73. Jagota, A., and Bennison, S. J. (1995). Element breaking rules in computational models for brittle fracture. Modelling and Simulation in Materials Science and Engineering, 3(4), 485–501. doi:10.1088/0965-0393/3/4/005

74. Jassim, I., Stolle, D., and Vermeer, P. (2012). “Two-phase dynamic analysis by material point method”. International Journal for Numerical and Analytical Methods in Geomechanics, 37(15), 2502–2522. doi:10.1002/nag.2146

75. Kakouris, E. G., and Triantafyllou, S. P. (2017). “Phase-field material point method for brittle fracture”. International Journal for Numerical Methods in Engineering, 112(12), 1750–1776. doi:10.1002/nme.5580

76. Kakouris, E. G., and Triantafyllou, S. P. (2019). “Phase-Field Material Point Method for dynamic brittle fracture with isotropic and anisotropic surface energy”. Computer Methods in Applied Mechanics and Engineering, 357, 112503. doi:10.1016/j.cma.2019.06.014

77. Kawai, T. (1978). “New discrete models and their application to seismic response analysis of structures”. Nucl Eng Des, 48(1):207-29

78. Khan, A. S., and Huang, S. (1995). “Continuum Theory of Plasticity”. New York, WileyInterscience 1995,440

79. Kim, K., and Lim, Y. M. (2011). “Simulation of rate dependent fracture in concrete using an irregular lattice model”. Cement and Concrete Composites, 33(9), 949–955. doi:10.1016/j.cemconcomp.2011.01.002

80. Kirshner, R. (1997). “Cosmology: the universe as a lattice”. Nature 385(6612):112-113

81. Koster, P., Tielen, R., Wobbes, E. and Moller, M. (2020) “Extension of B-spline Material Point Method for unstructured triangular grids using Powell–Sabin splines”. Computational. Particle. Mechanics. (2020). https://doi.org/10.1007/s40571-020-00328-3

82. Landau, L. D., and Lifshitz, E. M. (1959). Theory of Elasticity. Pergamon Press, Oxford

83. Lee, N.-S., and Bathe, K.-J. (1994). “Error indicators and adaptive remeshing in large deformation finite element analysis”. Finite Elements in Analysis and Design, 16(2), 99–139. doi:10.1016/0168-874x(94)90044-2

84. Li, S. J., Yu, H., and Suzuki, Y. (2004). “Identification of non-linear hysteretic systems with slip”. Computers & Structures, 82(2-3), 157–165. doi:10.1016/j.compstruc.2003.10.005

85. Lubliner, J. (2008). Plasticity theory. Dover, New York

86. Lucy, L. B. (1977). “A numerical approach to the testing of the fission hypothesis”. The Astrophysical Journal 8 (12), 1013–1024

87. Ludlam, J. J., Stadelmann, T. O., Taraskin, S. N. and Elliott S. R. (2001) Numerical analysis of the vibrational eigenmodes of a 2D disordered lattice. Journal of Non-Crystalline Solids 293:676-681

88. Luo, L. S. (2000). “Theory of the lattice Boltzmann method: lattice Boltzmann models for nonideal gases”. Phys Rev E 62(4):4982-4996

89. Maghous, S., Dormieux, L., and Barthélémy, J. F. (2009). “Micromechanical approach to the strength properties of frictional geomaterials”. European Journal of Mechanics - A/Solids, 28(1), 179–188. doi:10.1016/j.euromechsol.2008.03.002

90. Marur, S. R., and Kant, T. (1994). “A stress correction procedure for the analysis of inelastic frames under transient dynamic loads”. Computers & Structures, 50(5), 603–613. doi:10.1016/0045-7949(94)90419-7

91. Masing, G. (1926). “Eigenspannungen Und Verfestigung Beim Messing”, Procceedings of the Second International Congress for Applied Mechanics, Zurich, Switzerland, pp. 332-335 (in German).

92. Moysidis, A. N., and Koumousis V. K. (2015). “Hysteretic Plate Finite Element”, J Eng mech. https://doi.org/10.1061/(ASCE)EM.1943-7889.0000918

93. Moysidis, A. N., and Koumousis, V. K. (2015). “Hysteretic Plate Finite Element”. Journal of Engineering Mechanics, 141(10), 04015039. doi:10.1061/(asce)em.1943-7889.0000918

94. Moysidis, A. N., and Koumousis, V. K. (2019). “Hysteretic Shell Finite Element”. Journal of Engineering Mechanics, 145(5), doi:10.1061/(ASCE)EM.1943-7889.0001589

95. Nairn, J. A. (2003). “Material Point Method Calculations with Explicit Cracks”. Computer Modeling in Engineering and Sciences, 4(6):649–663

96. Nairn, J. A., Hammerquist, C. C., and Smith, G. D. (2020). “New material point method contact algorithms for improved accuracy, large-deformation problems, and proper null-space filtering”. Computer Methods in Applied Mechanics and Engineering, 362, 112859. doi:10.1016/j.cma.2020.112859

97. Neto de Souza, E. A., Peric, D. Owen, D. R. J. (2008). Computational methods for plasticity theory and applications. Wiley, West Sussex

98. Nguyen, V. P., and Nguyen, G. D. (2016). “A Voronoi Cell Material Point Method for Large Deformation Solid Mechanics Problems”. Applied Mechanics and Materials, 846, 108–113. doi:10.4028/www.scientific.net/amm.846.108

99. Nguyen, V. P., Nguyen, C. T., Rabczuk, T., and Natarajan, S. (2017). “On a family of convected particle domain interpolations in the material point method”. Finite Elements in Analysis and Design, 126, 50–64. doi:10.1016/j.finel.2016.11.007

100. Nuismer, R. J. (1975). “An energy release rate criterion for mixed mode fracture”. International Journal of Fracture, 11(2), 245–250. doi:10.1007/bf00038891

101. Perzyna, P., and Sawczuk, A. (1973). “Problems of thermoplasticity”. Nuclear Engineering and Design, 24(1), 1–55. doi:10.1016/0029-5493(73)90017-4

102. Poschel, T., and Schwager, T. (2005). Computational granular dynamics: models and algorithms. Springer

103. Predebon, W. W., Anderson, C. E., and Walker, J. D. (1991). “Inclusion of evolutionary damage measures in Eulerian wavecodes”. Computational Mechanics, 7(4), 221–236. doi:10.1007/bf00370037

104. Preisach, F. (1935). “Über die magnetische Nachwirkung. Zeitschrift Für Physik”, 94(5-6), 277–302. doi:10.1007/bf01349418

105. Preparata, F. P., and Shamos, M. I. (1985). Computational Geometry-An introduction. Springer, New York

106. Radhakrishnan, K., and Hindmarsh, A. C. (1993). “Description and use of LSODE, the Livermore Solver for Ordinary Differential Equations”. LLNL report UCRL-ID-113855, US Dept of Energy, Oak Ridge, TN

107. Rasmussen, L. L., de Farias, M. M., and de Assis, A. P. (2018). “Extended Rigid Body Spring Network method for the simulation of brittle rocks”. Computers and Geotechnics, 99, 31–41. doi:10.1016/j.compgeo.2018.02.021

108. Sadeghirad, A., Brannon, R. M., and Burghardt, J. (2011). “A convected particle domain interpolation technique to extend applicability of the material point method for problems involving massive deformations”. International Journal for Numerical Methods in Engineering, 86(12), 1435–1456. doi:10.1002/nme.3110

109. Sadeghirad, A., Brannon, R. M., and Guilkey, J. E. (2013). “Second-order convected particle domain interpolation (CPDI2) with enrichment for weak discontinuities at material interfaces”. International Journal for Numerical Methods in Engineering, 95(11), 928–952. doi:10.1002/nme.4526

110. Schlangen, E. (1995). “Computational aspects of fracture simulations with lattice models”. Fracture Mechanics of Concrete Structures, Freiburg, Germany, 913

111. Shampine, L. F., and Reichelt M. W. (1997). “The MATLAB ODE Suite,” SIAM Journal on Scientific Computing, Vol. 18, 1997, pp. 1–22

112. Shen, Y., Golnaraghi, M. F., and Heppler, G. R. (2005). “Analytical and Experimental Study of the Response of a Suspension System with a

Magnetorheological Damper". Journal of Intelligent Material Systems and Structures, 16(2), 135–147. doi:10.1177/1045389x05048330

113. Sih, G. C. (1974). "Strain-energy-density factor applied to mixed mode crack problems". International Journal of Fracture, 10(3), 305–321. doi:10.1007/bf00035493

114. Sinaie, S., Ngo, T. D., Nguyen, V. P., and Rabczuk, T. (2018). "Validation of the material point method for the simulation of thin-walled tubes under lateral compression". Thin-Walled Structures, 130, 32–46. doi:10.1016/j.tws.2018.05.014

115. Sivaselvan, M. V., and Reinhorn, A. M. (2000). "Hysteretic Models for deteriorating inelastic structures", Journal of Engineering Mechanics 126 (6), 633-640.

116. Sivaselvan, M. V., and Reinhorn, A. M. (2004). "Nonlinear Structural Analysis Towards Collapse Simulation: A Dynamical Systems Approach". Technical Report MCEER-04-0005, New York

117. Steffen, M., Kirby, R. M., and Berzins, M. (2008). "Analysis and reduction of quadrature errors in the material point method (MPM)". International Journal for Numerical Methods in Engineering, 76(6), 922–948. doi:10.1002/nme.2360 107

118. Steffen, M., Wallstedt, P. C., Guilkey, J. E.,Kirby, R. M., and Berzins, M. (2008). "Examination and analysis of implementation choices within the Material Point Method (MPM)". CMES - Computer Modeling in Engineering and Sciences. doi:10.3970/cmes.2008.031.107

119. Sulsky, D., and Kaul, A. (2004). "Implicit dynamics in the material-point method". Computer Methods in Applied Mechanics and Engineering, 193(12-14), 1137–1170. doi:10.1016/j.cma.2003.12.011

120. Sulsky, D., Chen, Z., and Schreyer, H. L. (1994). A particle method for history-dependent materials. Computer Methods in Applied Mechanics and Engineering, 118(1-2), 179–196. doi:10.1016/0045-7825(94)90112-0

121. Sulsky, D., Zhou, S.-J., and Schreyer, H. L. (1995). “Application of a particle-in-cell method to solid mechanics”. Computer Physics Communications, 87(1-2), 236–252. doi:10.1016/0010-4655(94)00170-7

122. Thyagarajan, R. S., and Iwan, W. D. (1990). “Performance characteristics of a widely used hysteretic model in structural dynamics”, Proceedings of the 4th US National Conference on Earthquake Engineering, EERI, Palm Springs.

123. Triantafyllou P.S. (2011) “Hysteretic Finite Elements and Macro-elements for nonlinear dynamic analysis of structures”. PhD Thesis, NTUA, Athens, Greece

124. Triantafyllou, S. P., and Chatzi, E. N. (2014). “A hysteretic multiscale formulation for nonlinear dynamic analysis of composite materials”. Computational Mechanics, 54(3), 763–787. doi:10.1007/s00466-014-1032-2

125. Triantafyllou, S. P., and Koumousis, V. K. (2012). “An hysteretic quadrilateral plane stress element”. Archive of Applied Mechanics, 82(10-11), 1675–1687. doi:10.1007/s00419-012-0682-9

126. Triantafyllou, S. P., and Koumousis, V. K. (2012). “Bouc-Wen Type Hysteretic Plane Stress Element”. Journal of Engineering Mechanics, 138(3), 235–246. doi:10.1061/(asce)em.1943-7889.0000332

127. Triantafyllou, S. P., and Koumousis, V. K. (2014). “Hysteretic Finite Elements for the Nonlinear Static and Dynamic Analysis of Structures”. Journal of Engineering Mechanics, 140(6), 04014025. doi:10.1061/(asce)em.1943-7889.0000699

128. Triantafyllou, S., and Koumousis, V. (2012). “Small and Large Displacement Dynamic Analysis of Frame Structures Based on Hysteretic Beam Elements”. Journal of Engineering Mechanics, 138(1), 36–49. doi:10.1061/(asce)em.1943-7889.0000306

129. Valanis, K. C. (1971). “A theory of viscoplasticity without a yield surface.” Arch. Mech. Stossowanej, 23(4), 517-551.

130. Wang, B., Karuppiah, V., Lu, H., Komanduri, R., and Roy, S. (2005). “Two-Dimensional Mixed Mode Crack Simulation Using the Material Point Method”.

Mechanics of Advanced Materials and Structures, 12(6), 471–484. doi:10.1080/15376490500259293

131. Wang, B., Vardon, P. J., Hicks, M. A., and Chen, Z. (2016). “Development of an implicit material point method for geotechnical applications”. Computers and Geotechnics, 71, 159–167. doi:10.1016/j.compgeo.2015.08.008

132. Wen, Y. K. (1976). “Method for random vibration of hysteretic systems”. Journal of Engineering Mechanics Division, 102(2), 249-263

133. Wen, Y. K. (1980). “Equivalent linearization for hysteretic systems under random excitation”, Journal of Applied Mechanics, Transactions ASME, 47(1), 150-154

134. Więckowski, Z., Youn, S.-K., and Yeon, J.-H. (1999). “A particle-in-cell solution to the silo discharging problem”. International Journal for Numerical Methods in Engineering, 45(9), 1203–1225. doi:10.1002/(sici)1097-0207(19990730)45:9<1203::aid-nme626>3.0.co;2-c

135. Wilkins, M. L., and Guinan, M. W. (1973). “Impact of cylinders on a rigid boundary”. Journal of Applied Physics, 44(3), 1200–1206. doi:10.1063/1.1662328

136. Wong, C. W., Ni, Y. Q., and Ko, J. M. (1994). “Steady-State Oscillation of Hysteretic Differential Model. II: Performance Analysis”. Journal of Engineering Mechanics, 120(11), 2299–2325. doi:10.1061/(asce)0733-9399(1994)120:11(2299)

137. Yagi, T., and Takeuchi, N. (2015). “An Explicit Dynamic Method of Rigid Bodies-Spring Model”. International Journal of Computational Methods, 12(04), 1540014. doi:10.1142/s0219876215400149

138. Yaw, L. L., Kunnath, S. K., and Sukumar, N. (2009). “Meshfree Method for Inelastic Frame Analysis”. Journal of Structural Engineering, 135(6), 676–684. doi:10.1061/(asce)0733-9445(2009)135:6(676))

139. Yim, H., and Sohn, Y. (2000). “Numerical simulation and visualization of elastic waves using mass-spring lattice model”. IEEE Transactions on Ultrasonics, Ferroelectrics and Frequency control, vol. 47(3):549-558

140. Zhang, D. Z., Ma, X., and Giguere, P. T. (2011). “Material point method enhanced by modified gradient of shape function”. Journal of Computational Physics, 230(16), 6379–6398. doi:10.1016/j.jcp.2011.04.032

141. Zhang, X., Zhen, C, and Yan, L. “The Material Point Method A Continuum-Based Particle Method for Extreme Loading Cases”. Elsevier and Tsinghua University Press, Computational mechanics Series

142. Zhao, G.-F., Lian, J., Russell, A., and Khalili, N. (2019). “Implementation of a modified Drucker–Prager model in the lattice spring model for plasticity and fracture”. Computers and Geotechnics, 107, 97–109. doi:10.1016/j.compgeo.2018.11.021

143. Zhong, X., Zhao, C., Liu, B., Shu, X., and Shen, M. (2018). “A 3-D RBSM for simulating the failure process of RC structures”. Structural Engineering and Mechanics, 65(3), 291–302. https://doi.org/10.12989/SEM.2018.65.3.291

8 APPENDICES

APPENDIX 1 – VON MISES YIELD CRITERION

The Von Mises yield criterion has been widely used to describe the ductile behavior of materials. Its hypothesis is that plastic deformation is manifested when the second invariant of the deviatoric stress reaches a critical value. In three – dimensional stress space the criterion forms the yield surface that is defined by the following relation [85]:

$$\Phi^{VM} = 0 \tag{8.1}$$

where:

$$\Phi^{VM} = \frac{(\sigma_{11}-\sigma_{22})^2+(\sigma_{22}-\sigma_{33})^2+(\sigma_{11}-\sigma_{33})^2+6\left[(\sigma_{12})^2+(\sigma_{23})^2+(\sigma_{13})^2\right]}{2\sigma_y^{\,2}}-1 \tag{8.2}$$

which can also be written using the second invariant of the deviatoric stress tensor as:

$$\Phi^{VM} = \frac{J_2}{2\sigma_y^{\,2}}-1 \tag{8.3}$$

The 3D representation of the Von Mises yield surface in principal stress space can be seen in the Following Figure:

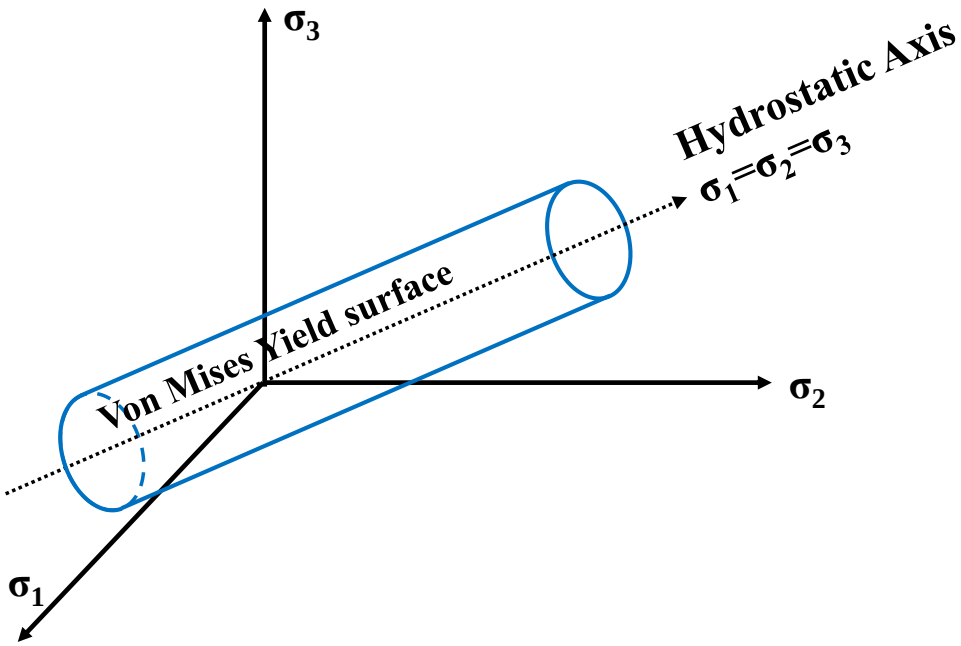

Figure 8.1: Von Mises yield surface

When 2D plasticity is considered, the VM yield surface is given by the following relation:

$$\Phi^{VM} = \frac{\left(\sigma_{11}-\sigma_{22}\right)^2+\left(\sigma_{22}\right)^2+\left(\sigma_{11}\right)^2+6\left(\sigma_{12}\right)^2}{2\sigma_y{}^2}-1 \tag{8.4}$$

In some equations in Chapter 2 the yield gradient must be calculated. This is given for the case of VM plasticity as:

$$\frac{\partial\Phi}{\partial\{\sigma\}} = \left\{ \frac{2\sigma_{11}-\sigma_{22}}{\sigma_y{}^2} \quad \frac{2\sigma_{22}-\sigma_{11}}{\sigma_y{}^2} \quad \frac{6\sigma_{12}}{\sigma_y{}^2} \right\}^T \tag{8.5}$$

APPENDIX 2 – PLASTICITY POSTULATES OF RATE – INDEPENDENT PLASTICITY

In plasticity several postulates have been proposed over the years, mainly to distinguish the plastic part of strains or stresses. These are proposed as mathematical inequalities and the two most well-known are those by Drucker [46,45] and Il'iyshin [69]. They are outlined below.

Drucker's Postulate.

Consider a material volume which is in a homogeneous state of stress and strain. Focusing on the one-dimensional case without loss of generality, the initial stress state is denoted by $\boldsymbol{\sigma}^0$, point A in Figure 8.2. This stress state is general in the sense that the material may have undergone any type of deformation and it may have yielded or not.

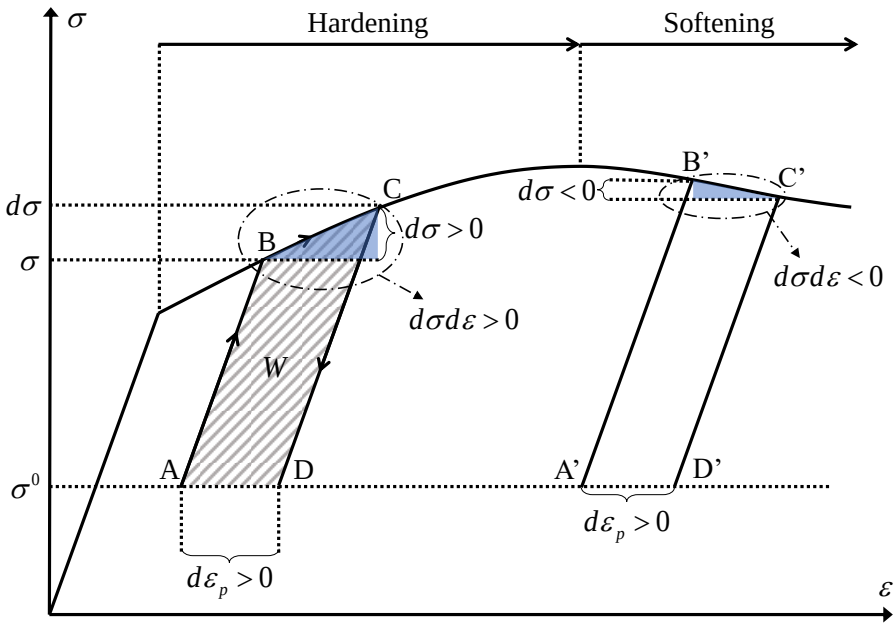

Figure 8.2: Illustration of Drucker' s stability postulate

Applying an additional load (or as is commonly referred to as external agency) the material reaches its current yield stress $\boldsymbol{\sigma}$, at point B. If the stress is increased by a infinitesimal increment $d\boldsymbol{\sigma}$, a change in strain is produced, denoted by $d\boldsymbol{\varepsilon}$ and the material reaches point C. Upon removing the incremental infinitesimal stress (removing the

external agency), the material returns to the original stress state $\boldsymbol{\sigma}^0$ and a strain is recovered. By applying and removing stress a stress cycle is formed [78], i.e. a closed loop. The strain that is recovered depends on whether plastic deformation has occurred.

For softening behavior, the material is loaded and reaches point B'. In order to reach point C' the stress must be reduced. However, this is not feasible in a stress control experiment since unloading from point B'; will lead to elastic unloading near point A'. In order to complete the stress cycle a strain-controlled experiment must be used. In this case the strains will increase, and the stresses will drop by $d\boldsymbol{\sigma} < 0$ bringing the material to point C'. Unloading after that will carry out the stress cycle. If we suppose now that the material is already on point B' so that $\boldsymbol{\sigma} = \boldsymbol{\sigma}^0$, it is not possible for the material to undergo a stress cycle. This distinguishes strain hardening from strain softening materials since a strain softening material cannot in all cases go through a stress cycle.

Drucker' Postulate define a stable material and asserts that the following relation is satisfied:

$$W = \int_{ABCD} \left(\boldsymbol{\sigma}(\boldsymbol{\varepsilon}) - \boldsymbol{\sigma}^0\right) : d\boldsymbol{\varepsilon} \geq 0 \tag{8.6}$$

Where W is the work per unit volume done by the external agency and the integral is evaluated over the stress cycle *ABCD*. This leads to the following statements:

- The work done by the external agency during the loading phase must be positive: $d\boldsymbol{\sigma} : d\boldsymbol{\varepsilon} > 0$
- Over a stress cycle the work done by the external agency must be nonnegative. In case of elastic deformation, the work is zero.

If a material abides by these postulates it is said to be stable. It is also evident that a strain hardening material is stable. For a softening material (or a perfectly plastic one), plastic loading gives a non-positive work $d\boldsymbol{\sigma} : d\boldsymbol{\varepsilon} < 0$. These materials are defined as unstable.

Furthermore, assuming an additive decomposition of strains, $d\boldsymbol{\varepsilon} = d\boldsymbol{\varepsilon}^{el} + d\boldsymbol{\varepsilon}^{pl}$ and noting that the elastic work is recoverable, then, assuming $d\boldsymbol{\sigma}$ is infinitesimal:

$$W = (\boldsymbol{\sigma} - \boldsymbol{\sigma}^0) : d\boldsymbol{\varepsilon}^{pl} + \frac{1}{2} d\boldsymbol{\sigma} : d\boldsymbol{\varepsilon}^{pl} \tag{8.7}$$

If in the first term: $(\boldsymbol{\sigma} - \boldsymbol{\sigma}^0) >> d\boldsymbol{\sigma}$ and so:

$$(\boldsymbol{\sigma} - \boldsymbol{\sigma}^0) : d\boldsymbol{\varepsilon}^{pl} > 0 \tag{8.8}$$

If however $\boldsymbol{\sigma} = \boldsymbol{\sigma}^0$ then Drucker's postulate reduces to:

$$d\boldsymbol{\sigma} : d\boldsymbol{\varepsilon}^{pl} > 0 \tag{8.9}$$

Drucker's postulate relates to the yield surface and states that the yield surface should be convex. If the yield surface were concave then it might be possible to find a stress point inside the yield surface for which $(\boldsymbol{\sigma} - \boldsymbol{\sigma}^0) : d\boldsymbol{\varepsilon}^{pl}$ would be negative and Drucker's postulate would be violated.

Il'iyshin' s Postulate

Il'iyshin' s plasticity postulate is similar to Drucker's postulate, but it is based on a strain cycle instead of a stress cycle. It is stated as: Consider a strain cycle. Assume that the material is in equilibrium and that strain is homogeneous. The material is plastic is, during the cycle, the total work done is positive, and is elastic when the work done is zero. The postulate can be mathematically stated as:

$$W = \int_{ABCD} \boldsymbol{\sigma}(\boldsymbol{\varepsilon}) : d\boldsymbol{\varepsilon} \geq 0 \tag{8.10}$$

Where again the integral is evaluated over the closed cycle of strains ABCD (Figure 8.3). One of the differences with Drucker's postulate is that in Il'iyshin' s plasticity postulate the work done cannot be negative as can be seen in Figure 8.3. It includes both stable and unstable materials and characterizes the behavior of a very large class of materials.

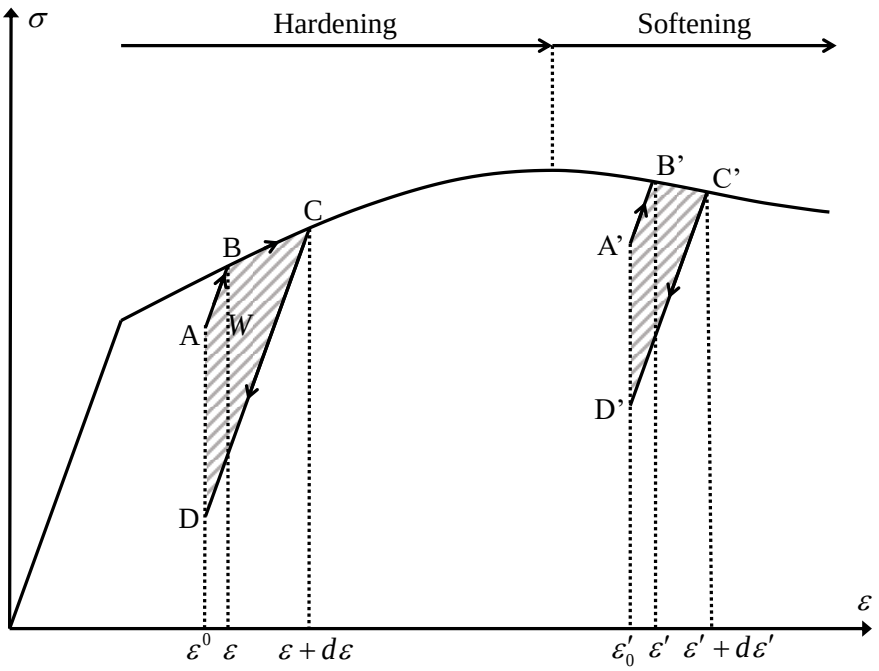

Figure 8.3: Illustration of Il'iyshin' s postulate

APPENDIX 3 – ELEMENTS OF CONTINUUM MECHANICS

Deformation gradient

The deformation gradient is a second order asymmetric tensor that relates to both the reference and current configuration. Considering the motion φ of Figure 8.4 the deformation gradient is:

$$\boldsymbol{F}\left(\boldsymbol{X},t\right)=\nabla\varphi(\boldsymbol{X},t)=\frac{\partial\boldsymbol{x}}{\partial\boldsymbol{X}} \tag{8.11}$$

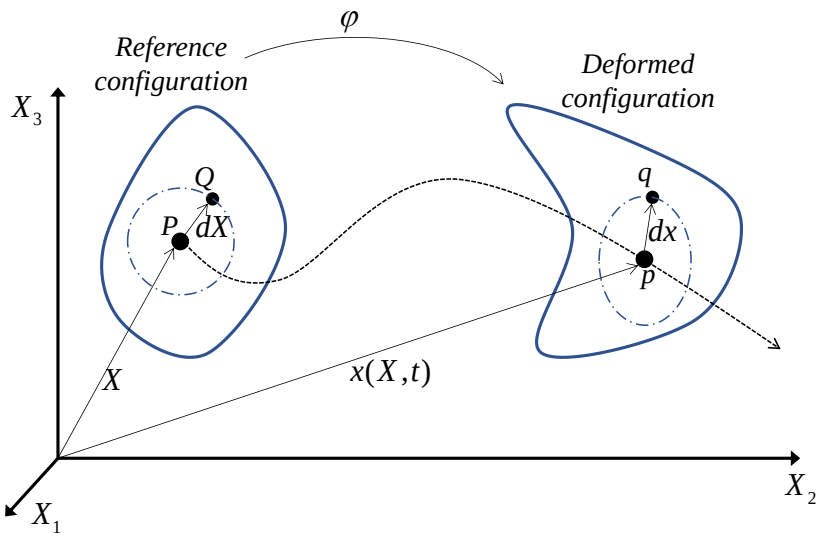

Figure 8.4: The deformation gradient

In Figure 8.4, $d\boldsymbol{X}$ is an infinitesimal linear material fiber that connect the two material particles *P* and *Q*. Particle *P* has a position vector $\boldsymbol{X}$ while *Q* has a position vector of $\boldsymbol{X}+d\boldsymbol{X}$ in the reference configuration. In the current configuration the linear element becomes $d\boldsymbol{x}$ and material particles P and Q are mapped to p and q respectively. The deformation gradient is a linear operator relating infinitesimal linear fibers $d\boldsymbol{X}$ with their deformed counterparts $d\boldsymbol{x}$:

$$d\boldsymbol{x}=\boldsymbol{F}\cdot d\boldsymbol{X} \tag{8.12}$$

The deformation gradient is termed as a two-point tensor in a sense that it acts on vectors in the reference configuration to produce other vectors in the deformed configuration.

When the deformation gradient is independent of the reference configuration $\boldsymbol{X}$ then the deformation gradient is uniform and the deformation is called homogeneous. Rigid body translations and rotations are homogeneous deformations and don't contribute to stress and strain. Another useful quantity is the determinant of the deformation gradient $J = \det \boldsymbol{F}$ that represents the local change of volume after the deformation per unit reference volume:

$$J = \left| \frac{\partial \boldsymbol{x}}{\partial \boldsymbol{X}} \right| = \begin{vmatrix} \frac{\partial x_1}{\partial X_1} & \frac{\partial x_1}{\partial X_2} & \frac{\partial x_1}{\partial X_3} \\ \frac{\partial x_2}{\partial X_1} & \frac{\partial x_2}{\partial X_2} & \frac{\partial x_2}{\partial X_3} \\ \frac{\partial x_3}{\partial X_1} & \frac{\partial x_3}{\partial X_2} & \frac{\partial x_3}{\partial X_3} \end{vmatrix} \tag{8.13}$$

The determinant of the deformation gradient for any deformed configuration of the body should be positive:

$$J > 0 \tag{8.14}$$

<u>*Velocity gradient*</u>

If $\boldsymbol{v}$ is the spatial velocity:

$$\boldsymbol{v}\left(\boldsymbol{X}, t\right) = \dot{\boldsymbol{x}}\left(\varphi^{-1}(\boldsymbol{x}, t), t\right) \tag{8.15}$$

then, we can define the velocity gradient as:

$$\boldsymbol{L} = \frac{\partial \boldsymbol{v}}{\partial \boldsymbol{x}} \tag{8.16}$$

that accounts for the difference between the velocity of a particle P and its neighboring particle P' at time t:

$$d\boldsymbol{v} = \boldsymbol{v}(\boldsymbol{x} + d\boldsymbol{x}, t) - \boldsymbol{v}(\boldsymbol{x}, t) = \boldsymbol{L} \cdot d\boldsymbol{x} \tag{8.17}$$

The velocity gradient can be split into symmetric and skew parts

$$\boldsymbol{L} = \boldsymbol{D} + \boldsymbol{\Omega} \tag{8.18}$$

and the rate of deformation and the spin tensor can then be derived:

$$\begin{aligned} \boldsymbol{D} &= \frac{1}{2}\left(\boldsymbol{L} + \boldsymbol{L}^T\right) \\ \boldsymbol{\Omega} &= \frac{1}{2}\left(\boldsymbol{L} - \boldsymbol{L}^T\right) \end{aligned} \tag{8.19}$$